ELECTROCHEMICAL PROCESSING OF SINGLE-WALLED CARBON NANOTUBES AND RELATED MATERIALS

Stephen Anthony Hodge *MChem (Hons)*

Imperial College London, Department of Chemistry

September 2012

Submitted in partial fulfilment of the requirements for the degree of
Doctor of Philosophy of Imperial College London

Department of Chemistry
Imperial College London
London, SW7 2AZ,
UK

Plagiarism declaration

I hereby declare that this thesis is my own work. All research was performed in the Department of Chemistry, Imperial College London; all other sources used have been completely referenced where appropriate.

This work has not been submitted previously for the reward of a degree course at this or any other university.

Stephen A. Hodge

Acknowledgements

First and foremost I would like to thank Prof. Milo Shaffer for his invaluable supervision over the past three and a half years, without his knowledge and enthusiasm, this thesis would not have been born, and Wilf Corrigan (CEO of LSI Logic Corporation) for the funding of this exciting project. Secondly, but probably just as importantly, I'd like to thank my parents for housing/feeding me during my PhD, and my brother and his family; I am truly grateful for all the love and support. I'd also like to thank my girlfriend Jess for her continuous love and encouragement, and her parents for housing/feeding me almost every weekend!

Imperial College has been a great place to work, everyone in the NanoHAC group has been amazing, I've made some truly special friends. I have a long list of people to thank, but particular mention has to go to "Big" Dave, a true friend with comedic chemistry knowledge, for many useful insights into my project from a physicist's perspective, and Hin Chun, for his great sense of humour and awesome organic chemistry knowledge. Thank you to Robert for his German efficiency and ability to make sense of almost everything, Siân, for her previous research that has created a platform for me to work on, and Musty for his tireless motivation. I'd also like to thank Ainara for being an "ok, not amazing" squash/badminton partner and a great friend, and Brandi and Shane for their invaluable experience and former 'motherly' and 'fatherly' roles in the group. I'd also like to thank MSci/BSc students Cong and Charlene that have helped me collect hundreds of Raman and UV-vis-nIR spectra! I also wish to thank the current and past members of the NanoHAC group, Almudena, Katharine O., Richard, Johann, Sherry, Matt, Jon, Shu, Tomi, Adam, Takuya, Cynthia, Jodie, Andrew, Neil, Colin and Tayyab for their friendship and support. My deepest sympathies go to Hui Huang who is starting to fear electrochemistry as much as I did! At least you will have Darth Vader (glove box) for your PhD!

Not forgetting people outside of the group, I'd like to thank Chris and Tita for their friendship over the years, the lads in Chemistry Stores (Jamie and Paul), the Chemistry Research Technicians, especially Stefanos for constantly fixing/chatting, and Steve Ramsey for his awesome glassblowing skills having made several electrochemical cells for me! Lastly, thanks to the chaps at UCL (Prof. Neal Skipper, Dr. Chris Howard, David Buckley and Patrick Cullen) for useful discussions and collaborations. I hope that's everyone!

Abstract

The remarkable properties of single-walled carbon nanotubes (SWNTs) and potential applications are hindered by current solution-phase processing strategies. The initial dissolution of SWNTs remains a fundamental challenge, reliant on aggressive chemistry or ultrasonication and lengthy ultracentrifugation. In this thesis, a simple non-aqueous electrochemical reduction process that leads to spontaneous dissolution of individualised SWNTs from raw, unprocessed powders is outlined. The intrinsic electrochemical stability and conductivity of these nanoparticles allows their electrochemical dissolution from a pure SWNT cathode to form solutions of well-defined nanoparticle anions with characteristic charge density. Other than a reversible change in redox/solvation state, there is no obvious chemical functionalisation of the structure, suggesting an analogy to conventional atomic electrochemical dissolution. The heterogeneity of as-synthesised SWNT samples leads to the sequential dissolution of distinct fractions over time. Initial preferential dissolution of defective nanotubes and carbonaceous debris provides a simple, non-destructive means to purify raw materials without recourse to the usual, damaging, competitive oxidation reactions. During early stage developments, the process showed remarkable affinity for dissolving metallic SWNTs, providing a potentially scalable route for separation by electronic character, vital for many applications. However, selectivity was lost with significantly increased process yields (complete dissolution) following several optimisations. Subsequently, the electrochemical deposition of SWNTs is proposed as a new route to selectively plate specific SWNT species and avoid unwanted functionalisations that occur when exposing reduced SWNTs to different atmospheres. Finally, the extension of electrochemical processing to related materials including activated and graphitic nanocarbons, metallic and metal chalcogenide nanomaterials was also investigated, with great promise for the development of new applications.

Contents

Figures, Schemes and Tables

III. ELECTROCHEMICAL DISSOLUTION OF SWNTS

IV. ELECTROCHEMICAL DEPOSITION OF SWNTS

V. EXTENSION TO OTHER NANOPARTICLE ANIONS

VI. CONCLUSIONS AND FUTURE STUDIES

VII. APPENDIX

Abbreviations

General abbreviations

ARC	Arc Discharge	MWNT	Multi-Walled Carbon Nanotube
BN	Boron Nitride	NHE	Normal Hydrogen Electrode
BWF	Breit-Wigner-Fano	OCP	Open Circuit Potential
CCVD	Catalytic CVD	OHP	Outer Helmholtz Plane
CNF-PL	Carbon Nanofibre Platelets	OLED	Organic Light Emitting Diode
CNT	Carbon Nanotube	OM	Oosawa–Manning
CVD	Chemical Vapour Deposition	PECVD	Plasma Enhanced CVD
DGU	Density Gradient Ultracentrifugation	POSS	Polysilsesquioxane
DOS	Density Of States	RBM	Radial Breathing Mode
DWNT	Double-Walled Carbon Nanotube	rcf	Relative Centrifugal Force
FET	Field-Effect Transistor	sc-	Semi-conducting
GIC	Graphite Intercalation Compound	SCE	Standard Calomel Electrode
(ER)GO	(Electrochemically Reduced) Graphene Oxide	SET	Single Electron Transfer
HOPG	Highly Ordered Pyrolytic Graphite	SG	Supergrowth
HOMO	Highest Occupied Molecular Orbital	SWNT	Single-Walled Carbon Nanotube
IH	In-house	$SWNT^{n-}$	SWNT anions (nanotubide)
IHP	Inner Helmholtz Plane	TCF	Transparent Conductive Film
ITO	Indium Tin Oxide	TWNT	Triple-Walled Carbon Nanotube
LUMO	Lowest Unoccupied Molecular Orbital	vdW	van der Waals
m-	Metallic	vHSs	Van Hove singularities

Analytical techniques

AFM	Atomic Force Microscopy	SEM	Scanning Electron Microscopy
CITS	Current Imaging Tunnelling Spectroscopy	SERS	Surface Enhanced Raman Scattering
CV	Cyclic Voltammetry	SPM	Scanning Probe Microscopy
EDX	Energy dispersive X-ray spectra	SS-MUGEC	Single-Surfactant Multicolumn Gel Chromatography
EELS	Electron Energy Loss Spectroscopy	STM/STS	Scanning Tunneling Microscopy and Spectroscopy
EPR	Electron Paramagnetic Resonance	TEM	Transmission Electron Microscopy
EXAFS	Extended X-ray Absorption Fine Structure Spectroscopy	TGA	Thermogravimetric Analysis

KF	Karl Fischer	UV-vis-nIR	Ultraviolet-visible-near-Infrared
PL	Photoluminescence	VC-SEM	Voltage Contrast-SEM
PLE	PL Excitation	XPS	X-ray photoelectron spectroscopy
SAED	Selected Area Electron Diffraction	XRD	X-ray Diffraction

Common chemicals and solvents

AN	Acetonitrile	NMP	N-Methylpyrrolidone/ 1-Methyl-2-pyrrolidinone
APTES	3-(Aminopropyl)triethoxysilane	PC	Propylene Carbonate
CHP	1-Cyclohexyl-2-pyrrolidone	PMMA	Poly(methyl methacrylate)
DCB	1,2-Dichlorobenzene	PTFE	Poly(tetrafluoroethylene)
DCM	Dichloromethane	PVP	Poly(vinylpyrrolidone)
DMA	N,N-Dimethylacetamide	SC	Sodium Cholate
DME	1,2-Dimethoxyethane	SDBS	Sodium Dodecylbenzenesulphonate
DMEU	Dimethylethyleneurea / 1,3-Dimethyl-2-imidazolidinone	SDS	Sodium Dodecyl Sulphate
DMF	N,N-Dimethylformamide	STPB	Sodium Tetraphenylborate
DMSO	Dimethylsulphoxide	TAA	Tetraalkylammonium
DOC	Sodium Deoxycholate	TBAP	Tetrabutylammonium Perchlorate
HMPA	Hexamethylphosphoramide	THF	Tetrahydrofuran
IDD	1-Iodododecane	TMS	Tetramethylene sulphone/ Sulpholane
KP	Potassium Perchlorate		

PREFACE

This research endeavour advanced from the fundamental issues surrounding the slow progression towards developing (opto)electronic applications incorporating the outstanding properties of single-walled carbon nanotubes (SWNTs). The widespread use of ultrasonication and centrifugation to disperse and individualise SWNTs has been a major drawback to liquid-phase processing and scalability; the lack of control over nanotube synthesis and challenging post-synthetic sorting strategies are also particular issues in the current context. These problems sparked an interest in mild dissolution techniques based on charged carbon systems, from which an electrochemical methodology was conceived. The ability to finely tune electrochemical potentials to the redox events that occur for carbon nanotubes was foreseen to hypothetically allow the selective dissolution and deposition of SWNTs on a significantly large scale. Preliminary research by Dr. Siân Fogden provided overwhelming evidence for the spontaneous dissolution of active SWNT electrodes following electrochemical reduction in a sodium tetraphenylborate (STPB)/DMF electrolyte. Results also indicated the preferential dissolution of metallic nanotube species over their semi-conducting counterparts. The research outlined in this thesis is a development of this electrochemical system to a fully-fledged process that could have an overwhelming impact on general nanomaterial processing.

In this thesis, the main focus of work involves the electrochemical processing of SWNTs; consequently, the structure, properties (specifically (opto)electronic), synthesis, and post-synthetic processing techniques to achieve control over SWNT type are well reviewed. Characterisation of SWNTs is also of major importance, and consequently explained in detail. In terms of results, the electrochemical dissolution and deposition of SWNTs by reduction and oxidation reactions, respectively, are presented separately. Later on, there is a shift back to the generalisation of the electrochemical dissolution approach to other nanomaterial systems. This research answers many important questions, however, many more possible avenues for further work have also opened, the study of fundamental nanomaterial properties and reactivity, improved processing, and electronic device development, to name a few.

I. INTRODUCTION

I. 1. NANOMATERIALS

Nanomaterials are currently the focus of intense research and development due to their potential for revolutionary technological applications. In recent years, nanomaterials have become increasingly present in our everyday lives; nano- particles, tubes, rods, wires, ribbons, and composites, to name a few, have amassed huge interest due to many exceptional properties and phenomena that arise due to quantum confinement and simple surface area/volume effects at the nanoscale. Nanomaterials have existed for thousands of years, evident in the Roman artefact the 'Lycurgus cup,' that exhibits different colours in reflected and transmitted light due to the presence of gold and silver nanoparticles.[1] Over the last 20 to 30 years, with the increased technology and performance of nanoscale characterisation techniques such as scanning probe and electron microscopies, nanomaterials such as fullerenes, carbon nanotubes, and more recently graphenes, are now able to be synthesised deliberately and fully characterised.

Recent years have witnessed huge worldwide concerns such as climate change, increasing energy and technological demands. Nanotechnology is currently at the forefront to provide solutions to these issues, through the development of carbon capture materials, materials for renewable energies such as solar cells and fuel cells, and materials for large-scale electronic applications such as computer memory and processors, and flexible electronics.

Nanomaterial synthesis is tackled from two different approaches. The first approach requires processing of a bulk material such as graphite, and turning it in to individual atomic sheets, known as graphene, using micromechanical cleavage of highly ordered pyrolytic graphite (HOPG)[2] ('scotch-tape' technique), or liquid-phase exfoliation[3] (ultrasonication/chemical functionalisation). The alternative bottom-up approach requires synthesising nanomaterials from atomic/molecular components. The exfoliation approach is favoured due to its low cost and immediate processability, however, aggressive treatments often lead to materials with surface defects and impurities that present a challenge to device design and fabrication. The bottom-up approach generally produces materials that have a lower defect concentration and a more homogeneous chemical composition, although mechanisms that control structural properties are

complex and difficult to reproduce. In this thesis, the main focus is aimed towards the post-synthetic processing and sorting of single-walled carbon nanotubes, with an overview of many other nanomaterials that are potential candidates for nanoelectronic device applications.

I. 1. 1. Carbon nanomaterials

Historically, carbon has been known to exist in three different forms: amorphous carbon, graphite, and diamond. While diamond and graphite make up the 3D and 2D allotropes of carbon respectively, the discovery[4] of buckminsterfullerene (C_{60}) in 1985, formed *via* the laser ablation of graphite, caused much excitement among researchers. The discovery of C_{60} paved the way for the discovery of other types of fullerenes, C_{70} and C_{80} bearing a slightly elongated shape. These advancements led to the full recognition of 1D structures – carbon nanotubes; single-walled carbon nanotubes (SWNTs) can be conceptualised by wrapping a graphene sheet into a seamless cylinder; diameters are typically close to 1 nm, with aspect ratios (length/diameter, L/d) often around 1000, although much larger values are known.[5] Concentric layers of tubes build up to form double-, triple-, and multi-walled carbon nanotubes (DWNTs/TWNTs/MWNTs respectively) as shown in Fig. I-1.
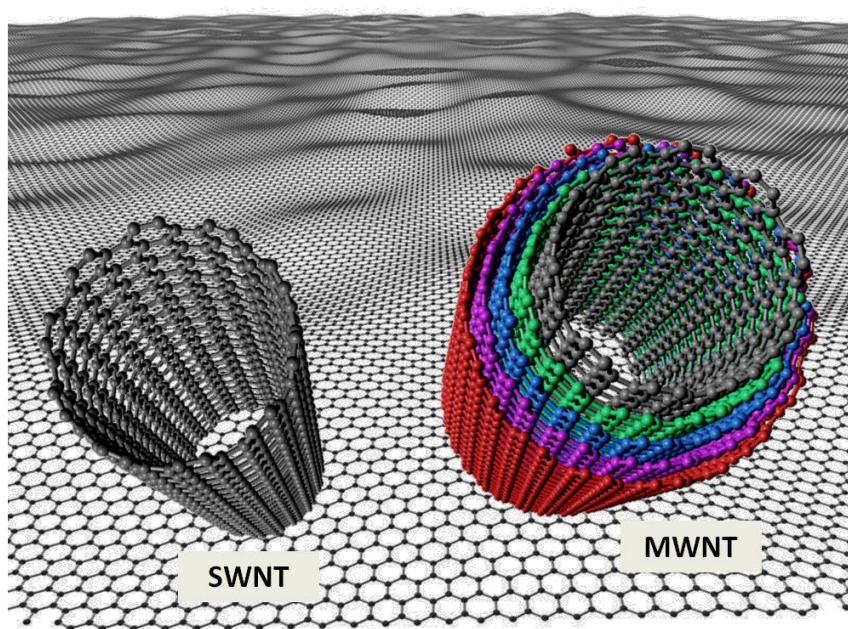
Fig. I-1 The structures of selected carbon nanomaterials. Graphene[6] (background), single- and multi-walled carbon nanotubes (SWNTs/MWNTs). Graphene is one atom thick, although has a rippled surface due to energetic factors.

Recently, a family tree of sp^2 carbon nanomaterials was proposed,[7] incorporating the many different graphitic nanostructures that have been discovered, including nano- ribbons, cones and scrolls following different topological operations (Fig. I-2). Since the early 1990s, great advancements have been made in understanding the morphology and properties of carbon nanomaterials; theoretical models and experimental activity have helped to enhance researchers' knowledge in this field, with many fundamentals now known. Small dimensions and superior electronic, mechanical and thermal properties (section I. 2. 1) make carbon nanotubes highly desirable, however, detailed information regarding pure nanotubes is still limited.
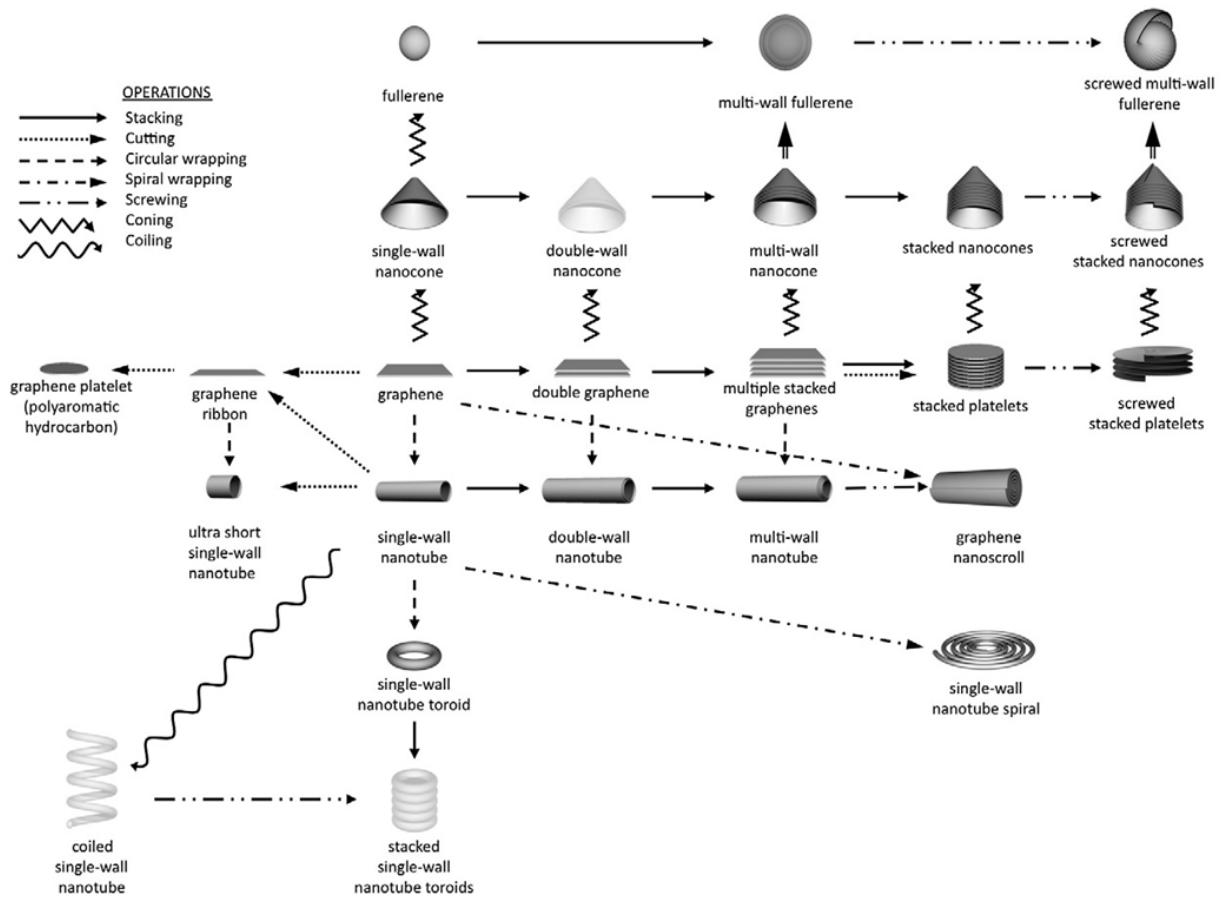
Fig. I-2 "Family tree" of primary carbon nanoforms showing the topological relationships between them. All 1D forms can undergo the same operations as for the single-walled nanotube. Hybrid forms (such as fullerene-filled nanotubes) are not included. Forms which have not been identified experimentally are faded. Reproduced from ref. 7.

As-synthesised SWNTs typically comprise $^1/_3$ metallic and $^2/_3$ semi-conducting species, present as tightly-bound, hexagonally-packed 'ropes' or 'bundles' due to relatively strong,[8] attractive van der Waals (vdW) interactions (~500 meV nm^{-1}), and are, therefore, challenging to disperse or dissolve. The SWNT family will be outlined in this chapter with an overview of their geometries, properties, synthesis and processing.

I. 2. SINGLE-WALLED CARBON NANOTUBES

I. 2. 1. Properties and applications of SWNTs

SWNTs have impressive mechanical, chemical, optical and electrical properties that correlate to new phenomena and enable specific applications.[9, 10] SWNTs have very high specific surface area[11] (~1315 m^2 g^{-1}), and high aspect ratios.[5] High aspect ratios are particularly important for electrically conducting devices, allowing the formation of percolating networks at lower concentrations. SWNTs have already found application in high-strength composites and structural materials due to their impressive mechanical properties[12] (tensile strength ~52 GPa; Young's modulus ~1470 GPa) that far exceed conventional materials such as steel, for example (maximum tensile strength ~0.4 GPa; Young's modulus ~200 GPa). Excellent thermal properties[13, 14] (theoretical thermal conductivity ~6600 W mK^{-1}; thermal stability ~750°C (atmosphere)) mean SWNTs are also good candidates for thermal interface material applications.[15] At the nanoscale, electrical properties are most interesting; quantum confinement allows ballistic conduction through metallic SWNTs[16, 17] at useful path lengths (electrical conductivity ~1-3 x 10^6 S m^{-1}; maximum current density ~4 x 10^9 A cm^{-2}), suitable for transparent conductive film (TCF) applications, for example.

Today, the impact of carbon nanotubes is apparent in the automotive and aerospace industries following the industrial development of lightweight, high-strength nanocomposites, generally incorporating MWNTs that are produced on a significantly larger scale than SWNTs[18] (~1500 tons MWNTs produced in 2009). Emerging applications were recently reviewed,[10] including CNT-electrodes (organic light-emitting diodes (OLEDs), optically transparent devices, lithium ion batteries), supercapacitors, electronic components (contacts in organic transistors, CNT-based field-effect transistors (FETs)), catalyst supports (fuel cells, organic reactions), filtration and membrane devices, (bio)chemical sensors, and biomedical devices as well as further

mechanical applications (high strength materials, actuators). These applications have stimulated the interest of both industrial and academic institutions, for such novel technologies to become mainstream it is necessary to economically produce these materials on a large scale,[19] with other requirements depending on the application.

Unfortunately, many of these applications, especially electronic, have emerged extremely slowly due to challenges in uncontrolled SWNT synthesis. Ideally, well-defined samples containing specific SWNT diameter, helicity and length are required for electronic applications; until controlled synthesis is achievable, post-synthetic sorting can produce highly enriched samples of particular properties. Semi-conducting SWNTs (sc-SWNTs) are necessary in the fabrication of FET devices, electroluminescent and photovoltaic materials; metallic SWNTs (m-SWNTs) are essential for devices requiring unique electrical properties, such as nano-circuitry, transparent conductive coatings, and polymeric nanocomposites.[20] Hersam[21] recently outlined five necessary targets for an effective SWNT sorting strategy: "*i.* scalable: a sorting process should produce enough material to keep pace with anticipated increases in demand; *ii.* compatible: the process should be compatible with the wide range of SWNT lengths and diameters that are present in as-synthesised SWNT material; *iii.* non-destructive: the outstanding properties of SWNTs should not be degraded during sorting; *iv.* repeatable: it should be possible to repeat the sorting process to achieve improved purity levels; *v.* affordable: the process should enable economical incorporation into target applications."

Current post-synthetic sorting techniques rely heavily on laborious ultrasonication and high-speed centrifugation processes that can be destructive and difficult to reproduce on a larger scale; so far, only small-scale device studies have been possible. Due to issues with device design and fabrication, difficult solution-phase processing, and the intrinsic mixture of electronic character, a great deal of interest has shifted to the zero band-gap material graphene in recent years, due to its production from the low cost raw material, graphite. Much of the same work carried out on nanotubes is now being performed on single layer graphenes (SLGs); however, the properties of graphene vary as a function of its structural parameters, so many processing problems also exist.[3] While graphene-based devices tend to have similar performance compared to SWNT analogues, their processing is still poorly understood.[22]

The immediate challenge is to be able to disperse individualised SWNTs, process, functionalise, purify and sort SWNTs into their two electronic types in an economical, scalable

approach. With a robust methodology, it should also be possible to separate SWNTs by their helicity (discussed in the following sections), which would be highly advantageous to applications such as those previously mentioned.

I. 2. 2. The SWNT family

SWNT diameters range from ~0.4 nm up to ~5 nm (above ~5 nm, SWNTs begin to deflate at atmospheric pressure).[23, 24] This fixed diameter range restricts the family of SWNT molecules to *ca.* 2500 members with distinct helicity. The helicity of a SWNT is defined by its chiral angle, θ, and chiral vector, *(n,m)*. Each *(n,m)* pair defines a different way of rolling the graphene sheet to form a carbon nanotube. Three types of nanotube are defined: armchair ($n = m \neq 0$, $\theta = 30°$), zig-zag ($n \neq 0$, $m = 0$, $\theta = 0°$) and chiral (both left and right enantiomers) ($n \neq m \neq 0$, $0 \leq \theta \geq 30$) (Fig. I-3).
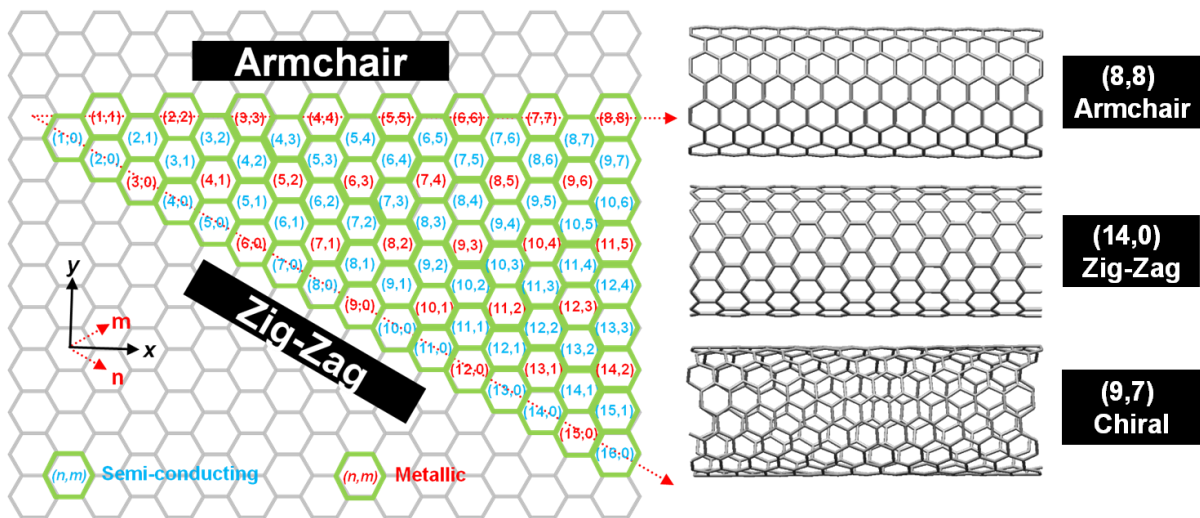
Fig. I-3 SWNT helicity map and examples of *(n,m)* chiral vectors that give rise to armchair, zig-zag and chiral nanotube structures with metallic or semi-conducting electronic character.

For a carbon nanotube defined by the index *(n,m)*, the diameter, *d*, and the chiral angle, θ, are given by Equation I-1 and 2, where *a* = 1.42√3 and 0 ≤ θ ≥ *30°*: [25]

Equation I-1 $$d = \frac{a\sqrt{m^2 + mn + n^2}}{\pi}$$

Equation I-2 $$\theta = \arctan\left(\frac{-\sqrt{3}m}{2n+m}\right)$$

SWNTs are more distinct at smaller diameter; upon increasing diameter there are more possible *(n,m)* species with less discrimination between their properties as confinement reduces, making SWNT characterisation challenging. However, double-, triple- and multi-walled carbon nanotubes may possess distinct characters when the outer diameter is relatively small. As an example, Kalbac *et al.* recently investigated DWNTs with different combinations of inner and outer shells (inner@outer: m@m, m@sc, sc@m, and sc@sc) with noticeable differences in charge transfer properties.[26]

I. 2. 3.   (Opto)electronic properties of SWNTs

The helicity of a SWNT determines its (opto)electronic properties; the three SWNTs highlighted in Fig. I-3 may have approximately the same tube diameter, however, their (opto)electronic properties are dramatically different. A SWNT is metallic if *n − m = 3q*, where *q* is an integer, while a SWNT is semi-conducting if *n − m ≠ 3q*; a ratio of 2:1 sc-/m-SWNTs is usually present in as-synthesised materials. Armchair SWNTs are metallic with a continuous electronic Density of States (DOS) near the Fermi level; in the case that the m-SWNT is chiral, a small pseudo-band gap (~50 meV) is present (semi-metallic).[27] The DOS of semi-conducting SWNTs show a significant band gap on the order of 500 meV that varies inversely with diameter (Fig. I-5). m-SWNTs (ε > 1000) have significantly higher dielectric constants than sc-SWNTs (ε < 10); larger diameter SWNTs also have larger dielectric constants than small ones.[28-30] Furthermore, the position of the Fermi level and, subsequently, the SWNT reduction and oxidation potentials, vary as a function of diameter that has many implications regarding the reactivities of SWNTs.[31] These redox potentials correlate with the LUMO and HOMO energies respectively, or the first Van Hove singularities (vHSs) in sc-SWNTs. These distinct differences will be explored in further detail in this section.

I. 2. 3. 1. Quantum confinement and band structure

Due to the nanometre dimensions coupled with the unique electronic band structure of a graphene sheet (from which the electronic structure of a SWNT can be derived),[32] the phenomenon of quantum confinement arises. Graphene is a zero band-gap semi-conductor whose electronic structure near the Fermi level consists of an occupied π band (valence) and an empty π^* band (conduction). These two bands meet at the Fermi level at the K points in the Brillouin zone,[33] where the π and π^* bands are degenerate by symmetry as shown in Fig. I-4.

The mixture of SWNT electronic character occurs due to differences in SWNT helicity; upon forming a nanotube, only a certain set of k states of the planar graphite sheet are allowed, based on a circumferential wave function. For a particular *(n,m)* nanotube, there are specific cutting lines that pass through the Brillouin zone based on these circumferential wave vectors. If the cutting lines pass through a K point of the Brillouin zone, the 1D bands have a zero-energy gap, and the nanotube is metallic. If the K point is not included, the nanotube is a semi-conductor with different sized energy gaps dependent on tube diameter.[27]
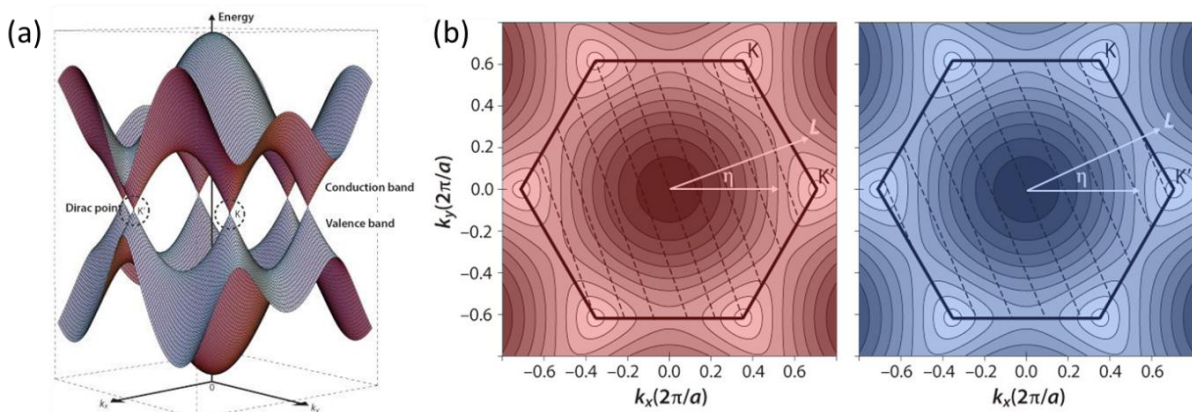
Fig. I-4 Schematic views of the graphene Brillouin zone. (a) 3D view showing the valence and conduction bands that touch at the K points at the Fermi level. (b) Equi-energy lines of the valence band in wave-vector space for m- and sc-SWNTs. The hexagon denotes the first Brillouin zone, L is the chiral vector and η is the chiral angle. Dashed lines denote allowed wave vectors when graphene is rolled into a cylinder to form a SWNT, and show the orientation perpendicular to L. The K and K' points lie on the dashed lines in metallic SWNTs (left), and lie away from the dashed lines in semi-conducting SWNTs (right). Modified from ref. 34.

I. 2. 3. 2. Electronic Density of States (DOS) and the Kataura plot

The electronic density of states (DOS) is an interpretation of the one-dimensional band structure of a SWNT. The "allowed" electronic states highlighted previously, are converted to a 'density' as the number of states per carbon atom per energy (eV). The DOS exhibits sharp peaks known as Van Hove singularities (vHSs).[32] These vHSs originate from the electronic wave functions around the circumference of the SWNT, therefore, the diameter of the SWNT controls the energy spacing between the corresponding vHSs.[35] vHSs are very important for determining many solid state properties of carbon nanotubes, such as the spectra observed by scanning tunnelling, optical absorption, photoluminescence and resonance Raman spectroscopies.[36] Optical transitions are "allowed" for light polarized along the SWNT axis (longitudinal), and occur between levels labelled E_{ii}, where i = 1,2,3,… numbering the valence and conduction sub-bands as shown in Fig. I-5. The energies E_{ii} are roughly inversely proportional to diameter, and were first plotted against the nanotube diameter, by Kataura.[37] E_{ij} transitions can be observed when light is polarized perpendicular to the SWNT axis (transverse), however, significant suppression of these transitions occurs due to the anisotropic geometry of SWNTs and their dielectric environment.[38]
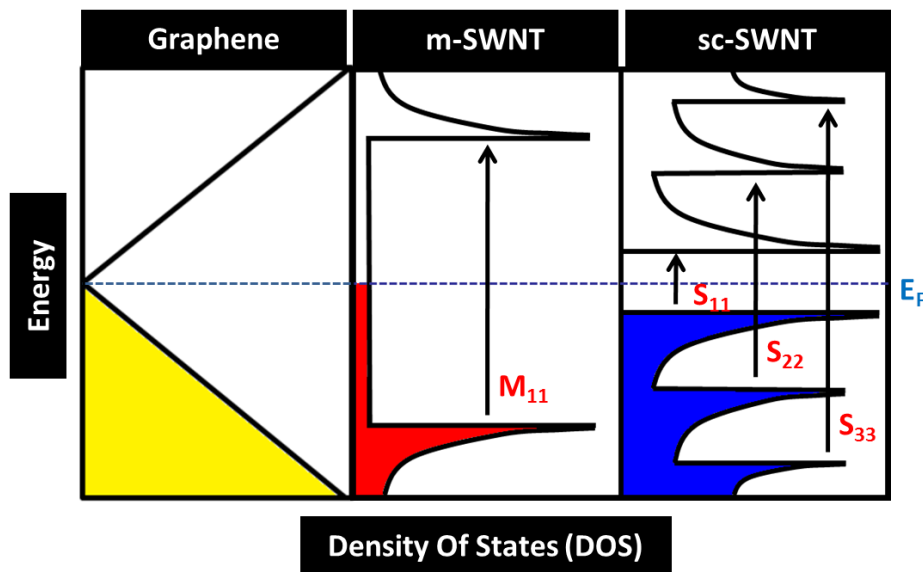
Fig. I-5 Schematic view of the electronic density of states (DOS) of graphene, m- and sc-SWNTs. The Fermi level (E_F) is highlighted by the dashed blue line. Electronic transitions that are allowed between the Van Hove singularities (vHSs) are represented by black arrows. M_{11} denotes the lowest energy transition for a metallic SWNT, S_{11} denotes the first energy transition for a semi-conducting SWNT.

Overall, SWNTs tend to have a low density of electronic states per unit energy around the Fermi level[39] (on the order of 0.01 eV per C atom for m-SWNTs). This low density causes the average energy spacings between adjacent states to be much larger than compared to common metals.[40] To reiterate, the electronic behaviour of SWNTs as determined by the *(n,m)* indices, $n - m = 3q$ tubes are metallic in character. Strictly, tube curvature effects give rise to so-called "trigonal warping,"[27] an effect that induces a pseudo-band gap for the case that q is non-zero ($n \neq m$). This gap (on the order of 50 meV) is very small compared to $k_B T$ at room temperature, so becomes negligible in practical circumstances. Armchair SWNTs ($n = m$) however, are always metallic, independent of curvature because of their symmetry. Typical band gap values for semiconducting SWNTs, S_{11}, are in the range of 0.3 to 0.8 eV for SWNTs with diameters of 3 to 1 nm respectively (inversely proportional to diameter).[40]

The Kataura plot[37] (Fig. I-6) of energy separation of the vHS transitions (E_{ii}) *vs.* nanotube diameter can be used in combination with experimental spectra to index SWNTs to their *(n,m)* type. The Kataura plot is the assignment of calculated transitions to experimentally determined S_{11}, S_{22} and M_{11} transitions based on resonant Raman spectra; variations of the plot have since been developed to account for different SWNT types[41] (Appendix VII. 3) and extended to higher energy transitions.[42]
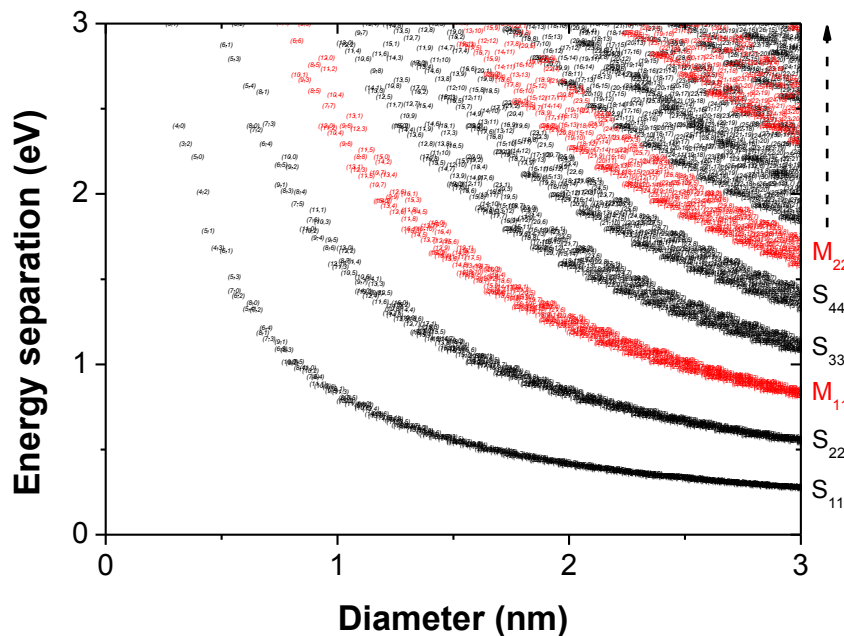
Fig. I-6 The Kataura plot showing the energies of several m- (red) and sc- (black) SWNT vHS transitions *vs.* tube diameter. Modified from ref. 43.

I. 2. 3. 3. SWNT work functions and Fermi levels

The work function is one of the most important physical quantities for nanotube applications, and is essential for understanding the contact properties between a metal electrode and a SWNT.[44] Defined[45] as "the energy with which electrons near the Fermi level are bound to the interior of the solid;" energies are quoted in electron volts (eV, the amount of kinetic energy gained by a single unbound electron when it accelerates through an electrostatic potential difference of one volt). The position of the Fermi level with respect to the vHSs can be tuned by doping *via* chemical or electrochemical methods. However, complications arise due to the presence of metallic and semi-conducting SWNTs, the variation in diameter and helicities and from tube-tube interactions in SWNT bundles or ropes.[46] However, according to Zhao *et al.*,[47] the work functions and electronic DOS at the Fermi level for metallic and semi-conducting bundles become indistinguishable upon alkali-metal intercalation. Electrochemical doping also has a similar effect on the Fermi level, it has been reported that electrochemical doping causes a change in the Fermi level proportional to the electrode potential[48] by a magnitude of ~0.4 to 0.7 eV V^{-1}. Studies by Okazaki *et al.*[49] estimated the absolute potential of the Fermi level of individual SWNTs from the potential dependence, which can be carefully related to any electrochemical system. Simple relations between ω_{RBM} (frequency of Radial Breathing Mode, see section II. 2. 1) and the work functions of metallic, Φ_M, and semi-conducting, Φ_S, tubes are given by:

Equation I-3 $$\Phi_M = 2.2 \times 10^{-2}\omega_{RBM} + 1.15$$

Equation I-4 $$\Phi_S = 1.2 \times 10^{-2}\omega_{RBM} + 1.59$$

The electrochemical potential measured with respect to a reference electrode can be related to the absolute potential relative to the vacuum level by Equation I-5, although there are many variations to this relation as discussed by Trasatti.[50] Reported potentials are observed to be dependent on temperature, solvent type (aqueous/non-aqueous), and different electrochemical setups that vary in terms of cleanliness and solvent purity, *etc.*

Equation I-5 $$V_{abs} \ (\textit{vs. } \text{vacuum level}) = V \ (\textit{vs. } \text{NHE}) + 4.44 \text{ V}$$

The establishment of how many vHSs are filled at a specific reducing potential would be a useful tool to have at one's disposal, unfortunately, the multiple electron affinities of individual SWNTs have not been studied. Average values of the electronic affinity and the first ionisation potential of semi-conducting SWNTs have been estimated by Kazaoui *et al.*[51] using spectroelectrochemical techniques as 4.8 eV and 5.4 eV, respectively; several others also present similar findings, later discussed in section I. 4. 2. However, upon filling the electronic DOS, electron affinities would be expected to change and introduce further complications.

Recent computational studies[52] based on density functional tight binding methodology have shown that carbon nanotubes filled with nanowires or clusters of 3d metals may have significantly altered structural, magnetic and electronic properties. The production of commercial HiPco SWNTs uses iron pentacarbonyl, $Fe(CO)_5$, which decomposes to give iron clusters that catalyse SWNT growth (section I. 3. 1). Clusters of as little as 8 metal atoms are theoretically enough to form pseudo-wires or encapsulated cluster structures inside these nanotubes. As a result, the Fe cluster DOS overlap both those of metallic and semi-conducting SWNTs at the Fermi level to distort these states. The major result of this study was that 3d metal M_n@CNT composites, whether of metallic or semi-conducting origin, had a metallic-like behaviour. This effect may have significant implications on this research, particularly with most types of SWNT containing metal catalyst nanoparticles.

I. 3. SWNT SYNTHESIS AND PROCESSING

From a chemist's viewpoint, single-walled carbon nanotubes (SWNTs) represent an entire family of molecules with distinct properties. In recent years, selective syntheses and post-synthetic separation strategies have been advanced, driven by the requirement for pure SWNTs displaying particular features. Separation methodologies for specific SWNT length, diameter and helicity have proven far more promising than selective syntheses; the differences in structure, especially size, strain, and symmetry, lead to variations in effective densities, electronic band structures, dielectric properties, spectroscopic features, and surface adsorption characteristics, which provide many potential methods for separation and characterisation.

I. 3. 1. Synthesis of SWNTs

Following the discovery of fullerenes *via* electric arc-discharge, small quantities of 'carbon filaments' (later to be known as carbon nanotubes) were observed to be grown by the same process, confirmed by Iijima in 1991.[53, 54] Since then, laser ablation, chemical vapour deposition (CVD) and many other techniques have been developed (Fig. I-7); However, 20 years on, each synthetic process still gives rise heterogeneous distributions of nanotube lengths, diameters and helicities, with defect concentration and the degree of contamination with metal catalyst, graphitic nanoparticles and amorphous carbons dependent on the manufacturing process. Although control of nanotube properties during growth is progressing, none of these synthetic techniques produce identical populations of SWNTs.[21]

Fig. I-7 Current methods used to synthesise carbon nanotubes. Reproduced from ref. 55.

Carbon nanotube syntheses have been extensively reviewed.[55] In recent years, high temperature arc discharge and laser ablation techniques have been replaced by low temperature CVD techniques (< 800°C). Catalytic chemical vapour depositions (CCVD) using thermal or plasma enhanced treatments are most frequently used, however, many other variations have been

developed to control certain SWNT properties. Water-assisted CVD, for example, is thought to prolong the metal catalyst lifetime and generate high-length forest-like SWNTs known as "Supergrowth" carbon nanotubes.[56]

Generally, raw commercial SWNT samples contain < 40 wt % nanotube material, while > 60 wt % is composed of carbonaceous debris and metal catalyst impurities; often, various grades are available following successive acid/gas-phase purifications. These processes are undesirable and may have a detrimental effect upon the overall SWNT (opto)electronic properties, although prices increase significantly as the overall nanotube content increases. Typical commercial starting materials for post-synthetic processing are HiPco and CoMoCAT SWNTs. The manufacture of HiPco SWNTs uses a high-pressure process developed by Nikolaev *et al.*[57] A small amount of $Fe(CO)_5$ is injected into a flow of hot carbon monoxide, subsequently, thermal decomposition of $Fe(CO)_5$ leads to the formation of gas-phase iron clusters, which act as nucleation sites for SWNT growth. The solid carbon shell of the nanotube is produced as a result of CO disproportionation *via* the Boudouard reaction $(CO + CO \rightarrow C_{(s)} + CO_2)$; gas-phase $Fe(CO)_5$ decomposes rapidly at $250^{\circ}C$, while the CO disproportionation occurs at a significant rate above $500^{\circ}C$. Generally, growth is performed between $800–1200^{\circ}C$; the highest yields and smallest diameter tubes were found to be produced at high pressure (10 atm) and temperature $(1200^{\circ}C)$. CoMoCAT SWNTs were first synthesised by the Resasco group[58, 59] using a silica support and a bimetallic catalyst (Co/Mo) prepared from cobalt nitrate and ammonium heptamolybdate precursors (molar ratio of 1:3), heated to $500°C$ in a flow of H_2 gas, and further heated to $750°C$ in flowing He. The process utilises a fluidised bed reactor under a flow of pure CO at 5 atm total pressure. Similar to the HiPco process, CO disproportionation produces the SWNTs; the SWNTs grown by this method remained mixed with the spent catalyst and also the silica support. To eliminate the silica from this mixture, the solid product is suspended in a stirred 20% HF solution for 3 h at $25°C$. From optical spectroscopy (Fig. I-8), CoMoCAT SWNTs are evidently of narrow *(n,m)*-distribution, with the *(6,5)* species dominant, whereas HiPco samples generally have a wider array of SWNT diameters and helicities.
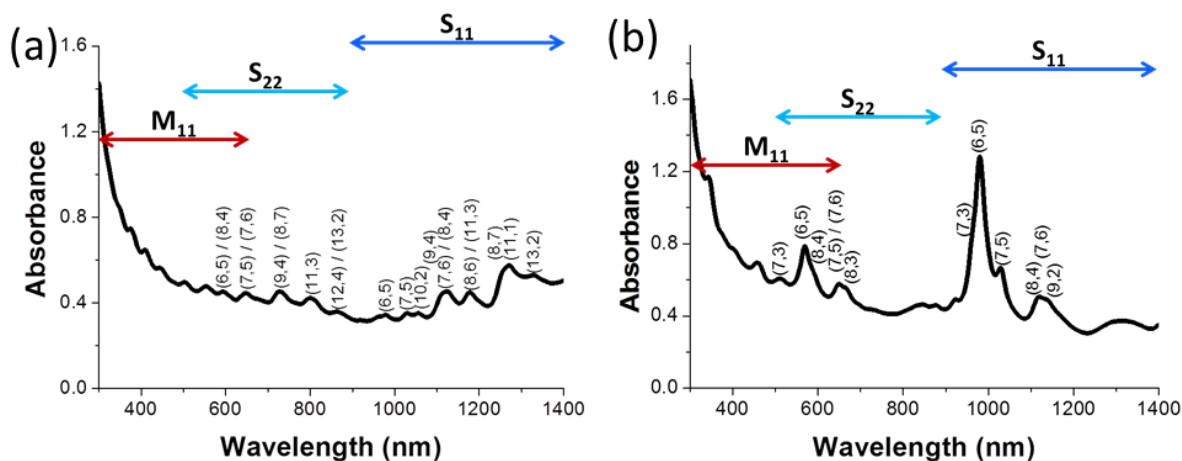
Fig. I-8 Typical SWNT UV-vis-nIR absorption spectra for (a) raw HiPco and (b) CoMoCAT SWNT dispersions. SWNTs were dispersed in 1 wt % sodium deoxycholate (DOC)/D_2O using ultrasonication (150 W, 30 min) and the remaining aggregates removed by ultracentrifugation (120000 g, 1 h).

Selective syntheses have progressed in recent years although the mechanisms are somewhat complex. The Hongjie Dai research group reported the selective synthesis of (~90%) sc-SWNTs using a low temperature (600°C) plasma enhanced chemical vapour deposition (PECVD) method.[60] Further computational studies[61] revealed a lower formation energy per-unit-length for sc-SWNTs with diameter ~1 nm, compared to m-SWNTs of the same diameter. This formation energy was found to be lower by ~0.15 eV per C-C bond length of 1.46 Å (or a stabilization energy of ~1.0 eV nm^{-1}), based on the atomic heats of formation. This energy is substantial ($k_B T$ ~0.08 eV at 600°C) and could be a driving force for the preferential growth of sc-SWNTs. The relationship also followed a $1/d^2$ dependence, subsequently, for samples with a low average SWNT diameter, the proportion of sc-SWNTs is likely to be higher. Similar experimental observations were also made by the Pfefferle group,[62] with SWNTs grown using Co:Mn (1:3) catalyst (thermal CO disproportionation). Proportions of sc-SWNTs were found to decrease with increased reaction temperature, attributed to the change in size and shape of the catalyst particles; Extended X-ray Absorption Fine Structure (EXAFS) spectroscopy revealed that the catalytic particles in samples synthesized at 600°C were, on average, 0.45 nm smaller than those in the samples reacted at 800°C.

The proportion of metallic SWNTs has been observed to dramatically change upon varying noble gas concentrations during thermal annealing of the catalyst in combination with oxidative

and reductive species.[63] The presence of H_2O in the catalyst annealing ambient supported by He, promoted the growth of m-SWNTs, whereas the same amount of H_2O supported by Ar ambient was more favourable for sc-SWNT growth. Differences in nanoparticle ripening and shape (faceted shape in the presence of He/H_2O *vs.* rounded shape in the presence of Ar/H_2O) were observed by *in situ* TEM studies. More recent reports have shown preferential growth of armchair (high chiral angle) SWNTs both theoretically[64] and experimentally.[65] While SWNT electronic structures are inherently linked to catalyst morphology, more extensive experimental evidence is required to understand the complex mechanisms at work.

I. 3. 2. Post-synthetic processing

Since as-synthesised SWNTs vary in terms of helicity, dimension, crystallinity, purity, impurity type, and degree of entanglement/bundling, it is important to select the appropriate starting material (CVD/arc discharge/laser ablation) before further processing or sorting. Defect type and concentration also vary with SWNT synthesis; CVD growth is particularly preferred since it is cheap, scalable, has a low reaction temperature, and allows controllable fabrication. Direct CVD growth on flat substrates is useful in creating isolated, low-defect density SWNTs; in contrast, SWNTs grown by laser ablation and arc-discharge are fabricated as bundles that require destructive post-synthetic treatments.[66] Commercial HiPco (high-pressure carbon monoxide) and CoMoCAT SWNTs are widely used starting materials for post-synthetic sorting, although purifications are usually performed.

I. 3. 2. 1. Purification, dispersion and individualisation

The purification of SWNTs is achieved by oxidation either in the gas phase (air, O_2, CO_2, H_2O vapour), or solution phase (HNO$_3$, H_2O_2, KMnO$_4$).[67] Commonly, combinations of treatments are used, often including HCl, surfactants and/or sonication. Recently, use of H_2O_2 in combination with HCl has proven very useful for SWNTs grown with iron catalyst due to the catalytic effect of iron on the decomposition of H_2O_2 to hydroxyl radicals that oxidise the SWNT ends, with relatively small loss of SWNT material.[68]

Subsequent dispersion of SWNTs is needed due to the blurring of the (opto)electronic properties in mixed bundles, or in the case of chemical modification, to avoid simply functionalising the outer surface of bundles, potentially even making further dispersion more

challenging. Some covalent modification reactions can intrinsically aid dispersion (*e.g.* Billups-Birch reduction[69]), in other cases, dispersion is carried out using sonication of either aqueous-surfactant[70] or organic solvent systems.[71] Surfactants vary in type (anionic, cationic, non-ionic or polymeric); typical loadings range from 0.5–2 wt %. Sonication may be carried out in a bath or using a cup-horn/microtip probe to debundle SWNTs, typically up to 1000 W for minutes to hours (for shortening). Isolation of the individual tubes is achieved through centrifugation at a relative centrifugal force (rcf) > 100000 *g* for several hours, in order to sediment the remaining heavy bundles and metal catalyst particles. Generally, aggressive sonication and repetitive centrifugation result in highly defective, chopped SWNTs; final yields are also very small.

I. 3. 2. 2. SWNT reactivity

Ideal SWNTs are relatively chemically inert, capped at both ends by hemi-fullerenes and have no surface functional moieties. In reality, one or both ends are likely to be open with oxygen-containing functionalities present at the opened ends and at defect sites on the side-walls as a result of SWNT synthesis,[9] sonication,[72] or purification processes. Generally, effective functionalisation requires aggressive reagents often involving initial acid oxidations, reductions, fluorinations, radical or ylide reactions of the nanotubes. The degree of functionalisation, commonly reported as a ratio of functional addends per SWNT carbon atom (following TGA or XPS characterisation), indicates the extent of how the (opto)electronic properties may be affected and the structural integrity of the functionalised SWNTs, but is also a useful tool if further modifications of the initial functionalities are to be performed. Often the degree of functionalisation is tuned to balance the selectivity for a particular SWNT characteristic, solubility, and the impact on (opto)electronic properties.

General mechanisms that govern the selective reactivity of SWNTs can be classified as either (1) SWNT size and diameter dependence, associated with strain and hybridisation effects or (2) a dependence on electronic effects such as electron density at the Fermi level, variable HOMO-LUMO energies, variable dielectric constant/polarisability, or tunable optical absorption (photochemistry). Combinations of steric and electronic features can also give rise to selective molecular adsorption, directly influenced by the degree of reactivity or SWNT dispersion.

In general, each covalent modification bears a rate-determining step; surface adsorption, electron transfer or the formation and stabilisation of sp^3 intermediates. The position at which

functionalisation occurs varies for different reactions; certainly the SWNT end-cap sites (if still present) are more reactive than the side-walls due to the high strains (Fig. I-9). The pyramidalisation angle for a trigonal sp^2 carbon atom is 0° compared to 19.47° for a tetrahedral sp^3 C atom. As an example, curvature and misalignment of the π-orbitals of the *(5,5)* SWNT generates a pyramidalisation angle of 6.0° at the side-wall; the hemifullerene end-cap is under significantly more curvature-induced strain, with a pyramidalisation angle of 11.6°, leading to higher reactivity.[73] In contrast, localised sp^3 defects have been proposed recently as the favoured sites for functionalisation following Billups-Birch reduction, leading to the formation of bands of functional moieties.[74]
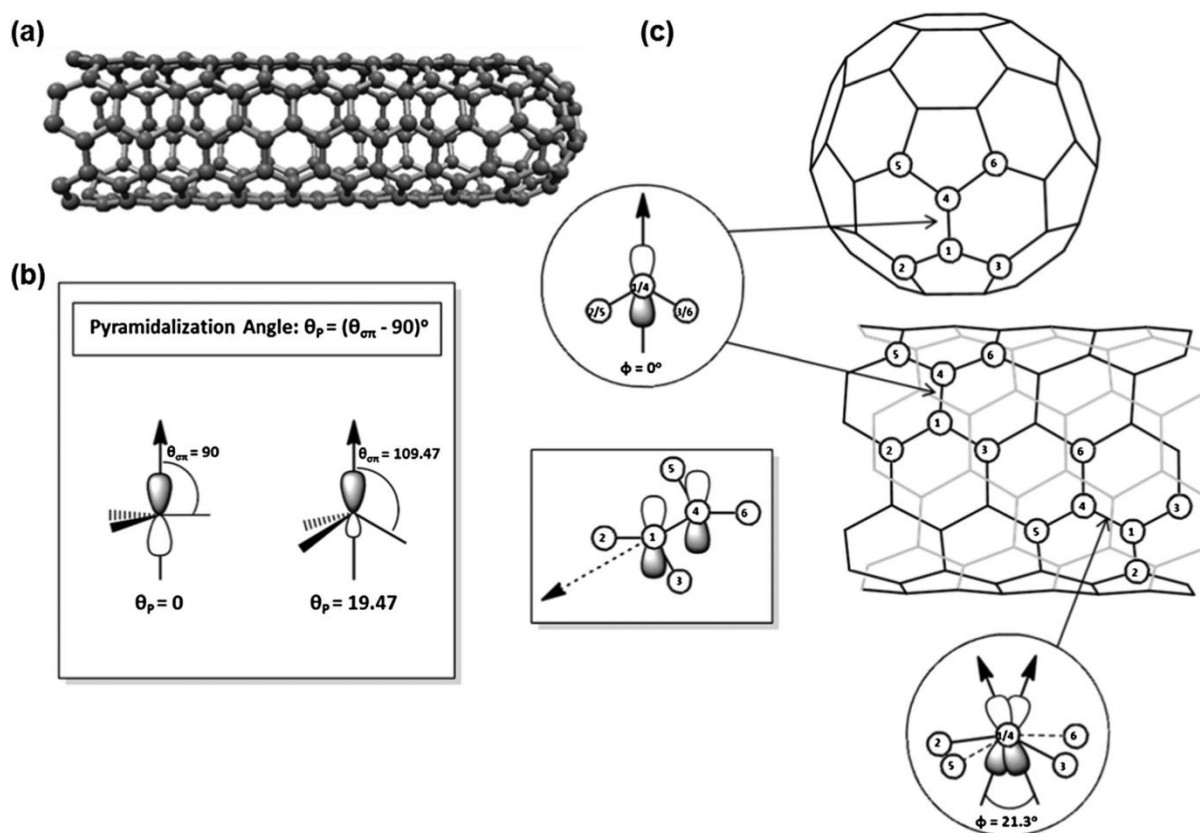
Fig. I-9 Strain as a mechanism for SWNT selectivity. Diagrams of (a) metallic *(5,5)* SWNT, (b) pyramidalisation angle (θ_P) (side-wall 6.0° *vs.* end-cap, 11.6°), and (c) the π-orbital misalignment angles (φ) along the C1–C4 in the *(5,5)* SWNT and its capping fullerene, C_{60}. Modified from ref. 73.

SWNT diameter selectivity is apparent in many covalent chemistries; generally, small diameter tubes are more reactive than larger diameter SWNTs, attributed to the degree of pyramidalisation

of the sp^2 C atoms, and/or curvature-induced strains that scale inversely with tube diameter.[73] Curvature effects are also apparent with SWNTs of different chiral angle. Bonds that are perpendicular to the tube axis, present in armchair SWNTs (high chiral angle, 30°) are under significant strain making these species more reactive than zig-zag SWNTs (low chiral angle, 0°) of the same diameter.[75]

Covalent functionalisation reactions that discriminate between electronic types are either based on the relative HOMO-LUMO positions of the reactant molecule and SWNT (Fig. I-10), or due to the electron density at the Fermi level (Fig. I-5). Metallic SWNTs have a finite electron density at the Fermi level, readily accessible for reaction, whereas semi-conducting SWNTs have no electron density at the Fermi level due to the presence of a large band gap. Band gap energy decreases proportional to increasing diameter, reactivities for different diameter sc-SWNTs are thus distinguishable. Whilst the Fermi level and HOMO-LUMO energies may also be a function of diameter,[31] metallic SWNTs tend to have greater initial electron affinity than semi-conducting species. This effect is exploited in selective diazonium functionalisation reactions in which the rate-determining step relies on the removal of an electron from the nanotube. Qualitatively, a higher dielectric constant will also allow a significantly higher concentration of dissociated charges on m-SWNTs, due to enhanced dielectric screening, increasing their reactivity following reductive process.

In terms of HOMO-LUMO energies, Joselevich[76] suggests semi-conducting SWNTs can be related to aromatic [4n + 2]annulenes, such as benzene, that are very stable with completely filled low-lying bonding orbitals and empty high-lying anti-bonding orbitals. This large HOMO-LUMO gap means that adding or extracting an electron or disturbing the conjugation has a relatively high energetic cost. Metallic SWNTs on the other hand, can be related to antiaromatic [4n]annulenes, such as cyclobutadiene, with a pair of half-filled, degenerate, non-bonding orbitals; electron addition or extraction is relatively favourable. In some cases, doping of the SWNTs such that the Fermi level shifts to give a higher electron density for semi-conducting SWNTs, will result in the increased reactivity of sc-SWNTs.[77]
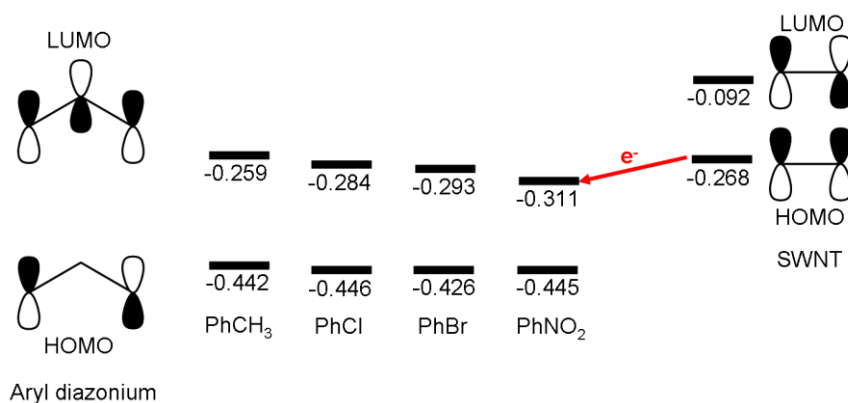
Fig. I-10 The reactions of para-substituted aryl diazonium salts with SWNTs are well-studied selective covalent modifications. Above are the relevant Frontier Molecular Orbitals of aryl diazoniums with varying R substituents (left), and a fragment of the *(5,5)*-armchair SWNT (right). The HOMO (SWNT) → LUMO (aryl diazonium) shown by the red arrow, is the favoured interaction, most notably for 4-nitrobenzene diazonium (-0.043 au). Modified from ref. 78.

A further possible mechanism, that so far has only been considered in (physical) dielectrophoretic separations[28] is the obvious difference in the dielectric constant of metallic and semi-conducting SWNTs ($\varepsilon > 1000$ and $\varepsilon < 10$ respectively).[28] Recently, new suggestions have emerged that metallic SWNTs should be preferentially reduced as they can withstand a higher charge density than semi-conducting tubes due to screening, and may explain why reactions utilising reducing agents such as alkali metals are favourable towards m-SWNTs. Other electronic differences are apparent in photochemical reactions, where reactions are accelerated for SWNT species for which the band gap energies (or other optical transitions) match the incident light.[79]

Selective adsorption of molecules on SWNT side-walls is a well-studied mechanism; that relate to both physical and covalent interactions. The selective non-covalent adsorptions of electron-rich aromatic molecules through π-π stacking interactions with the SWNT side-wall are also widely-used to distinguish metallic and semi-conducting SWNTs.[80] Non-selective reactions can be deliberately made selective by adding a group known to undergo selective adsorption (as illustrated by pyrene-substituted azomethine ylides).[81]

In general, the observation of multiple mechanisms working simultaneously is apparent throughout SWNT chemistry, giving rise to challenging characterisation in ascertaining the success of a selective reaction.

I. 3. 2. 3. SWNT sorting

There are many methods to sort SWNTs based on their distinct differences; physical techniques (density gradient ultracentrifugation, gel chromatography, dielectrophoresis), selective destructions (electronic breakdown, laser irradiation), covalent functionalisations, and selective non-covalent adsorptions have been reviewed previously.[21, 82-84] The first SWNT separation technique was reported by the IBM group in 2001;[85] Collins *et al.* demonstrated a simple method by removing the shells of MWNTs to convert them into either a m- or sc- SWNT. Also, with SWNT ropes, m-SWNTs were selectively eliminated *via* current-induced electrical breakdown, generating entire arrays of nanoscale field-effect transistors based solely on the fraction of sc-SWNTs.

To date, physical techniques have been the most widely used routes to SWNT sorting. AC dielectrophoresis allows the separation of metallic from semi-conducting SWNTs based on differences between the relative dielectric constants of the two species with respect to the solvent.[28] Mixed surfactant systems of sodium cholate (SC) and sodium dodecyl sulphate (SDS) offer preferential binding of semi-conducting SWNTs, therefore giving different densities for semi-conducting and metallic species;[86] density gradient ultracentrifugation (DGU) sediments these SWNTs into distinctive coloured bands of different characteristic types. Anion exchange chromatography of DNA-modified SWNT dispersions (involving π-π stacking interactions with the side-walls of carbon nanotubes) elutes metallic SWNTs preferentially, although fractions tend to be separated by nanotube length as well. Further investigations using DNA sequence motifs are selective for specific SWNT helicities, allowing the isolation of pure *(n,m)* species for the first time, albeit in small quantities.[87, 88] The Kataura group developed a gel column chromatographic technique initially showing diameter and electronic selectivity.[89] Recently, selectivity for highly pure single helicity sc-SWNTs using complex processes was observed.[90] m-SWNTs interacted poorly with the gel column eluting first, while semi-conducting species interacted to different extents dependent on their helicity (Fig. I-11). The major drawback to these separation techniques is the dependence on initial high-quality SWNT dispersions produced *via* ultrasonication which is destructive (especially towards the desirable electronic properties and tube lengths), and high-speed ultracentrifugation that can be difficult to reproduce on a larger scale. Generally, the yields of these physical processes are small, suited only to fundamental small-scale device studies.
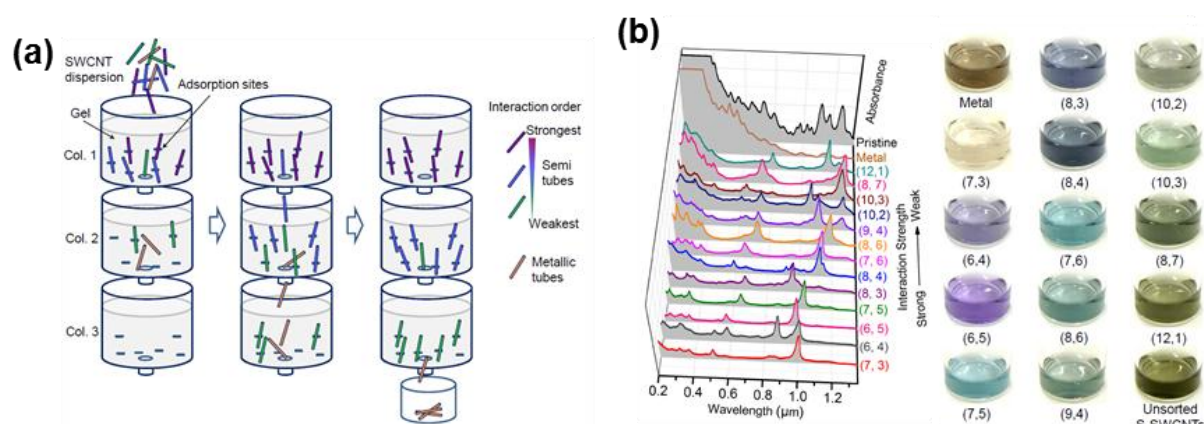
Fig. I-11 Single-surfactant multicolumn gel chromatography (SS-MUGEC) approach to separating SWNTs. (a) Schematic overview of the SS-MUGEC process. (b) Optical absorption spectra (left) and photographs (right) of 13 separated *(n,m)* semi-conducting species together with those of metallic and pristine HiPco mixtures. The spectra are ranked according to interaction strength between the *(n,m)* species and the gel. Reproduced from ref. 90.

Covalent modifications of SWNT side-walls are a useful complementary approach to sorting, and can be performed on a significantly larger scale. Enhanced solubility of carbon nanotubes, combined with the possibility for further derivatisations, allows the extraction of the reacted fraction from the remainder, based on solubility differences, or *via* secondary physical techniques. Functionalisation fundamentally alters the desired SWNT (opto)electronic properties, however, in some cases, the original electronic structure can be regenerated using thermal or chemical treatments, depending on the initial chemical reaction. Some chemistries may require the same level of intense sonication and centrifugation as physical sorting methodologies and should be avoided; other modifications, however, may need less intense sonication due to chemistries that stabilise or exfoliate SWNTs. Furthermore, centrifugation may be simplified by stronger solvent/non-solvent effects of functionalised SWNTs. In principle, the overall SWNT sorting process may be less destructive with milder dissolution steps (*e.g.* reductions) and low temperature annealing treatments.

The extensive chemistries that have been performed aid the understanding of the kinetics and reactivity differences of the full library of SWNT species. A wide range of covalent modifications have been reported to be selective, ranging from diazonium salt additions,[91-98] cycloadditions,[81, 99-107] silylations,[108, 109] gas-phase reactions,[75, 110-113] liquid-phase oxidations[77, 79, 114-120] and reductions,[121-125] recently reviewed by the author of this thesis.[84] So far, the greatest *(n,m)* discrimination in

reactivity has been shown using selective combustion of SWNTs in air,[75] although yields are very low (< 3 wt %); other reactions are likely to offer improvements in future.

Covalent chemistries offer a large toolkit for adapting SWNTs to a desired function. For high-yields, selective eliminations (oxidations and gas-phase reactions) and low-volume processes (sonication, centrifugation) should generally be avoided, although the SWNTs left behind can be highly enriched with specific properties. In contrast, reactions that intrinsically aid the dispersion of SWNTs (reductions) without the requirement for sonication and centrifugation, or exploit SWNTs that are grown as isolated networks, may prove most practical. In some cases, it is imperative that reactions are carried out under dry, inert conditions due to the increased reactivity of charged SWNT species (*e.g.* reductions). Other reactions may require highly corrosive reagents (liquid-phase oxidations), toxic precursors (carbenes) or highly reactive intermediates (radicals, ylides, carbenes, nitrenes), that are less attractive on an industrial scale.

For regeneration, intrinsically reversible reactions that avoid oxidations or high degrees of functionalisation are advantageous. Clean systems that avoid directly-bonded oxygen-containing moieties that are likely to evolve CO_2/CO are essential in providing high purity, low-defect SWNTs following thermolytic regeneration. It may also be important to avoid any side-groups that evolve these or other (*e.g.* H_2O) oxidative molecules which may *etc*h away the carbon framework of the underlying SWNT. Another interesting approach is to create addition structures that preserve sp^2 hybridisation (dichlorocarbene addition, Fig. I-12). For (opto)electronic studies, regeneration of the original properties is vital and should be confirmed using sensitive techniques such as PL spectroscopy (section II. 2. 3); for applications, device performance is the best guide. Where the objective is to utilise the "novel" properties of fundamentally modified SWNTs, the versatility and ease of grafting chemistry is of greatest importance. The degree of functionalisation must be adapted to the end-application, whether the goal is, for example, solubility, structural matrix compatibility, fluorescence, or catalytic activity. It may often be desirable to introduce higher molecular weight or branched species that maximise the required property with minimal modification of the SWNT framework.

Skewed   Orthogonal (closed)   Orthogonal (open)

Fig. I-12 Three possible configurations for a carbene group (CH$_2$) on a *(5,5)* armchair SWNT: skewed, orthogonal with an intact ("closed") side-wall bond, and orthogonal with a broken ("open") sidewall bond. The latter structure maintains the *sp^2* hybridisation of the two side-wall C atoms, reducing the effect of functionalisation on the electronic properties of the SWNT. Reproduced from ref. 126.

I. 3. 3. Milder processing of SWNTs

Mild dissolution processes that are the focus of this thesis, avoid the use of any sonication or centrifugation, critical for larger scale processing. Previously, mild dissolution has been achieved *via* chemical methods that produce charged SWNTs. Nanotube reductions have been performed in sodium napthalide/THF[127, 128] and using alkali metal/liquid ammonia based systems;[129] protonation[130] of SWNTs is generally performed using high strength 'superacids' such as chlorosulphuric acid. Chemical charging of SWNTs yields polyelectrolyte nanotube salts that spontaneously dissolve under the right conditions (balance between charge density, polyelectrolyte and counterion concentration) due to charge repulsion that is significantly large enough to overcome the attractive vdW surface interactions; examples of spontaneous dissolution of SWNTs and graphenes are shown in Table I-1. While the protonation route has not been observed to afford selectivity, the reduction route has shown promising results. In the Penicaud group,[131] recent investigations with a large range of stoichiometries K(THF)C$_x$ (x = 8-100) reported that larger diameter SWNTs are preferentially dissolved at low charge/carbon ratios. The increased solubility of larger SWNTs was hypothesised as a result of a smaller enthalpic contribution to the Gibbs free energy of mixing (ΔG_{mix}). In the Shaffer group,[129] reduction using sodium metal in liquid ammonia with different Na/C ratios showed preference for dissolving amorphous/defective carbons at low charge stoichiometries, followed

by metallic/large diameter species; it was hoped better discrimination could be achieved using novel electrochemical strategies outlined in this thesis.

Table I-1 Reported methods for the spontaneous dissolution of SWNTs and graphenes.

Material	Pre-Treatment (Purification/ Dispersion)	Reaction Details	C atoms per charge	Max. Solubility Reported	Reported Selectivity	Ref.
SWNTs						
AD/H	None	3 mM naphthalene, slight excess Li or Na, reflux; poured over SWNT soot (ca. 216 mg), stir, rt, overnight; reduced SWNT powder added to organic solvent	10–50	Arc: 4.2 mg/g sulpholane H: 0.4 mg/g DMSO	Large D [131]	[128]
H	Purified, finely ground with a mortar and pestle	0.3% wt. of SWNTs/superacid (chlorosulphonic, fuming sulphuric, or a combination of the two), stir, rt, 3 days	–	12.1 wt % in $CHCl_3$	–	[132, 133]
CoMo/ H/AD	20 mg SWNTs outgassed, 400°C, <10^{-6} mbar, 48 h	SWNTs:Na (varying ratios), 0.12 mol liquid NH_3; 20 mg SWNT^{n-}, 20 mL DMF	10 – 100	2 mg mL^{-1} 14% yield	M, Large D	[129]
Graphites						
Natural and expanded	None	Graphite powder/K metal (molar ratio C/K=8) in a sealed tube, 200 °C, vacuum, several days. 20 mg of KC_8/8 mL of anhydrous NMP, RT, stirring, 24 h. Centrifugation, 4000 rpm, 60 min	8	0.7 mg mL^{-1} 35% yield	–	[134]

Abbreviations: AD: arc discharge; H: HiPco; CoMo: CoMoCAT, rt: room temperature; M: metallic SWNT; SC: semi-conducting SWNT D: SWNT diameter

I. 3. 3. 1. Nanotube polyelectrolyte solutions

Charged nanotube systems can be modelled as rigid polyelectrolyte solutions defined by discrete charge densities, often reported as fractional charge (charge associated with one individual carbon atom) or the number of carbon atoms that share one charge (1 charge per n carbon atoms). As the concentration of polyelectrolyte increases, the electrostatic attraction between polyelectrolyte chains and counterions results in an increase of counterion concentration in the vicinity of the polyelectrolyte chain. In the case of nanotube polyelectrolytes, this behaviour is best described by the Oosawa–Manning (OM) two-state model,[135] whereby counterions in a polyelectrolyte solution are classified into two categories: counterions that are localised inside potential valleys along polymer backbones (state 1) and counterions that are able to freely move outside the region occupied by polyelectrolyte chains (state 2) as shown in Fig. I-13a. The OM counterion condensation parameter, γ_0, is given by $l_B n/L$, in which l_B is the Bjerrum length (the separation at which the electrostatic interaction between elementary charges is equal to the thermal energy), given by Equation I-6;[131] n/L is the linear density of charges in the absence of condensation.

Equation I-6 $$l_B = \frac{e^2}{4\pi\varepsilon_r\varepsilon_0 k_B T},$$

where e is the elementary charge, ε_r is the solvent dielectric constant, ε_0 is the permittivity of free space, k_B is the Boltzmann constant, and T is the temperature.

Free counterions are able to explore the solution volume, while the condensed counterions are localised within a small volume surrounding the polyelectrolyte backbone. The counterion condensation is a result of competition between the electrostatic attraction of a counterion to a polyelectrolyte chain and the loss of the translational entropy by counterions due to their localisation in the vicinity of the polyelectrolyte backbone. In a very dilute polyelectrolyte solution, the penalty for counterion condensation is very high and almost all counterions leave polyelectrolyte chains and stay 'free' in solution. However, as polyelectrolyte concentration increases, the entropic penalty for counterion localisation decreases, resulting in a gradual increase in the number of condensed counterions.[136]

The strength of electrostatic interactions between charged polyelectrolytes in solutions with finite salt concentrations decays exponentially with increasing distance between neighbouring polyelectrolytes. However, the charges still interact through the unscreened Coulomb potential at distances much smaller than the Debye screening length, $\varkappa^{-1}$ (Equation I-7):[136]

Equation I-7 $$\kappa^{-1} = \sqrt{\frac{\varepsilon_r\varepsilon_0 k_B T}{2N_A e^2 I}} = \frac{1}{\sqrt{8\pi l_B N_A I}},$$

where N_A is Avogadro's number and I is the ionic strength of the electrolyte (mol m^{-3}).

To stabilise nanotubides in solution, it is important to consider both the Debye screening length and the Bjerrum length; adjustments in salt concentration will have a significant impact on the dispersability, as will the nanotubide concentration as it increases over time. Overall, the dispersion of nanotubides occurs once the electrostatic repulsion energy overcomes the attractive van der Waals interaction energy, subsequent stabilisation of nanotubides is driven by the self-repulsion of back-bone charges (Fig. I-13b-c).
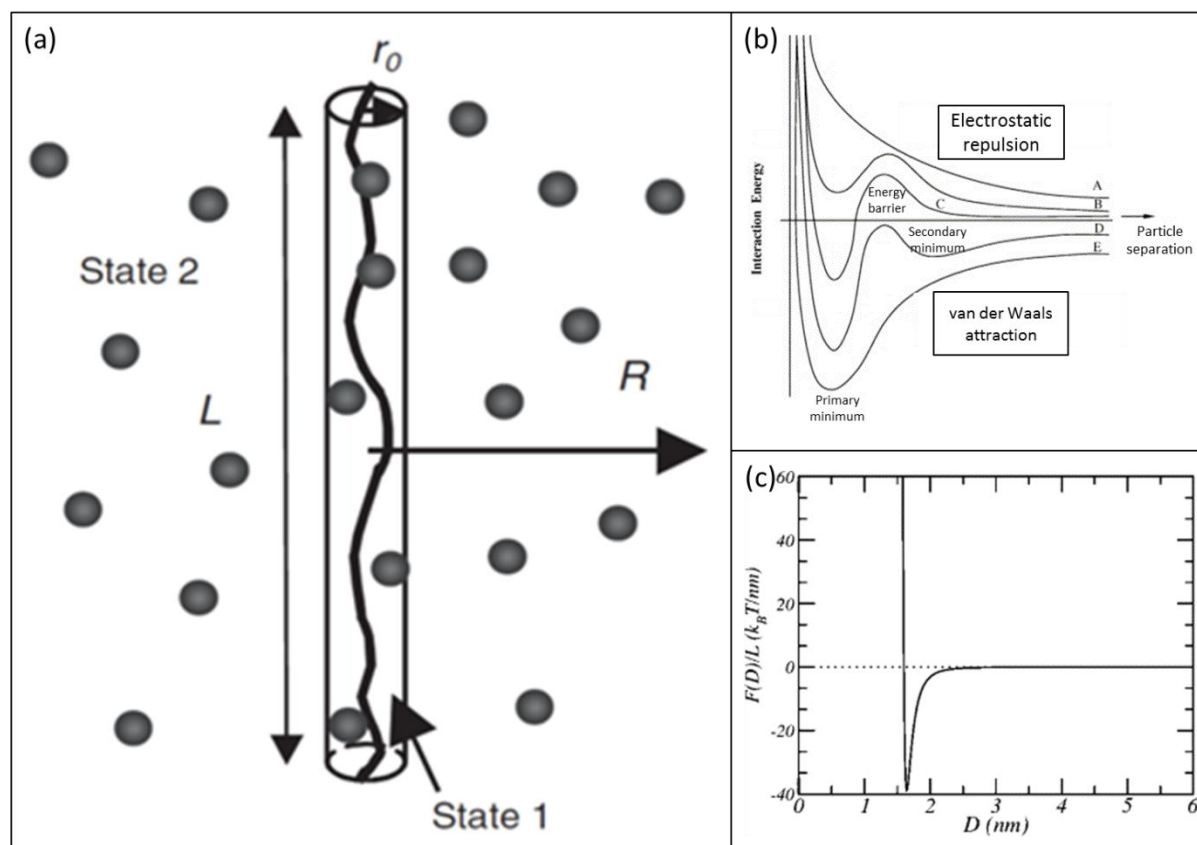
Fig. I-13 Electrostatic stabilisation of nanotubides. (a) Schematic sk*etc*h of a polyelectrolyte chain and the definition of different length scales for the Oosawa–Manning (OM) two-state model. L is the length of rodlike polyion and R the cell size (R ≪ L). Reproduced from ref. 136. (b) Schematic representation of total potential energy vs. inter-particle distance curve between two particles showing the effect of decreasing electrostatic repulsion: A = spontaneous dispersion of particles; B = no primary aggregation due to high energy barrier; C, D = weak secondary minimum aggregation; E = fast aggregation into primary minimum. Modified from ref. 137. (c) The specific interaction potential between two parallel SWNTs as a function of inter-tube distance. Reproduced from ref. 138.

I. 3. 3. 2. The chemistry of nanotubides

In recent years, the reduction of SWNTs has shown promise for large scale SWNT surface modifications. A wide variety of covalent functionalisations have been performed on these highly reactive nanotubide species, even offering ways to separate SWNTs based on specific properties. Reductive chemistries (Scheme I.1) of carbon nanotubes were established by the Haddon group using Birch reductions to hydrogenate SWNTs using lithium in ethylenediamine or liquid ammonia.[139] The enhanced solubility of reduced SWNTs avoids the use of sonication and centrifugation in creating the initial SWNT dispersion. Organometallic compounds have been used to generate negatively charged SWNT intermediates which can be used to produce new

functional groups (alkyl, aryl and carbonyl) or polymer chains on nanotube side-walls. Generally, reduction reactions favour metallic SWNTs, presumed as a consequence of their band structure and dielectric differences; the higher strains of small diameter SWNTs also offer increased reactivity.

The Hirsch group have pioneered several reductive strategies (Scheme I.1a-c). The nucleophilic addition of *tert*-butyllithium to the SWNT surface followed by re-oxidation using bubbling oxygen,[121] covalent additions of organolithium and organomagnesium compounds (*n*-butyllithium, *tert*-butyllithium, ethyllithium, *n*-hexyllithium, *n*-butylmagnesium chloride, *tert*-butylmagnesium chloride) to SWNTs,[122] and the covalent side-wall modification of SWNTs *via* reduction with sodium (Billups-Birch reaction) followed by alkylation with butyl iodide.[123] Generally, these reactions are all selective for m-SWNTs especially those with smaller diameters, with a relatively high degree of functionalisation due to the highly reactive nature of nanotube anions (~1 addend per 30 C atoms). The degree of functionalisation generally increases with the length of the alkyl chain, although, steric effects also play a key role (reactivity of *n*-butyl > *tert*-butyl), protonation gave the lowest degree of functionalisation. Organometallic addition reactions were further used for the formylation of SWNT surfaces following *n*-butyllithium addition, with a similar degree of functionalisation (~1 addend per 27 C atoms).[124]

Recent Billups-Birch modifications by Deng *et al.*, to generate alkylcarboxyl functionalised HiPco SWNTs, showed strong diameter dependence, in contrast to the previously reported electronic discrimination. Extraction by a competitive water–hexane partitioning method allowed the sequential separation of SWNTs with increasing diameter due to decreasing SWNT functionalisation and solubility. Recycling the reaction with ω-bromocarboxylic acids produced water soluble nanotubes at high concentrations (up to 3.38 mg mL^{-1}).[125] Further studies have revealed that the reaction takes place exclusively at sp^3 defect sites, confining the reaction to propagate in a tubular direction creating 'banded' SWNTs.[74]
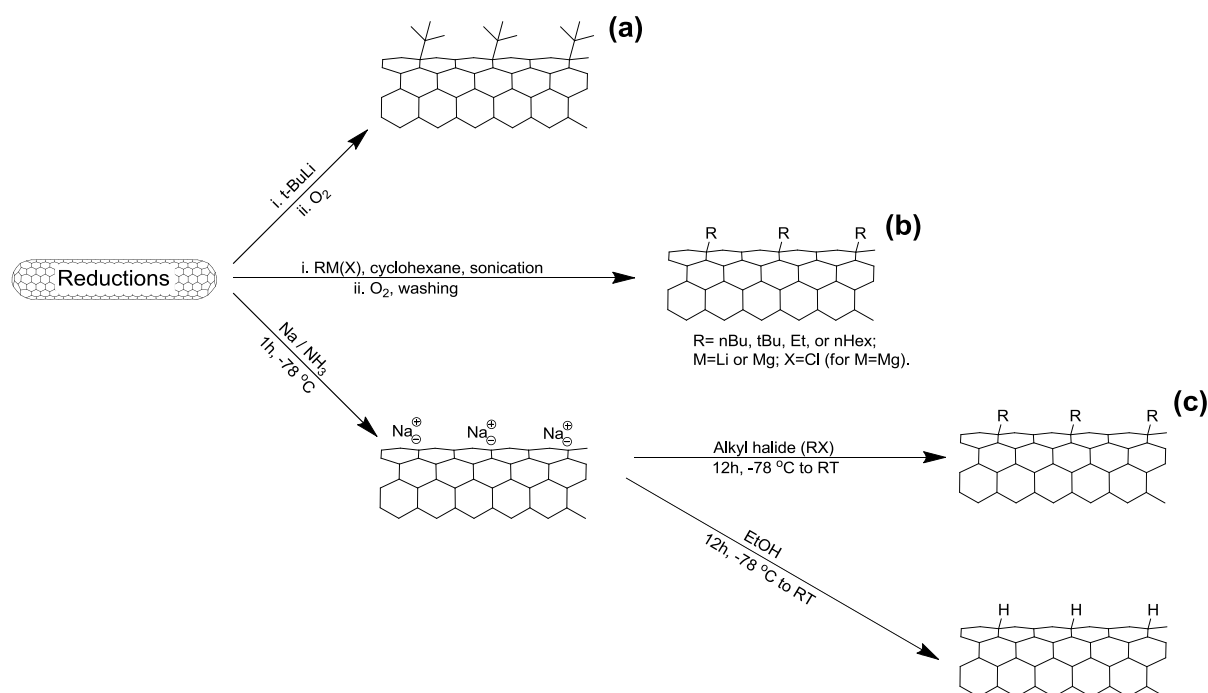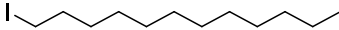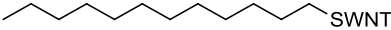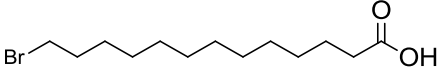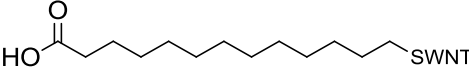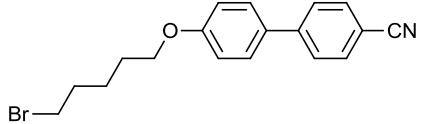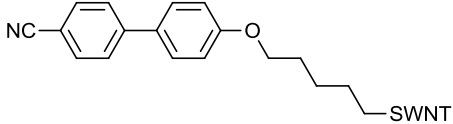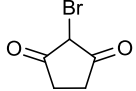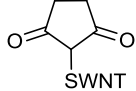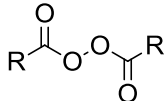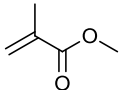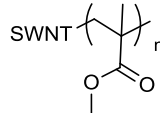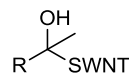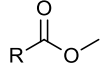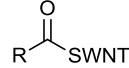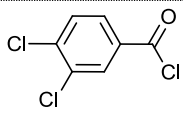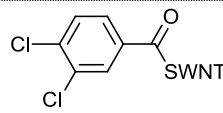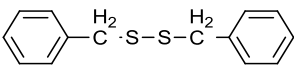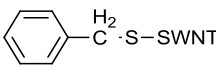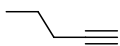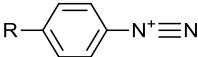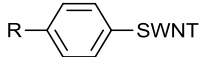
Scheme I.1 Selective SWNT reduction reactions. (a) *tert*-butyl addition using *tert*-butyllithium, (b) alkylation using organolithium and organomagnesium reagents, (c) alkylation of sodium reduced SWNTs.

A whole range of other reductive functionalisation reactions have also been explored using different methods of reducing the SWNTs prior to the addition of various electrophiles (Table I-2). Scheme I.2 outlines the generic route for the addition of R groups to reduced SWNT side-walls.
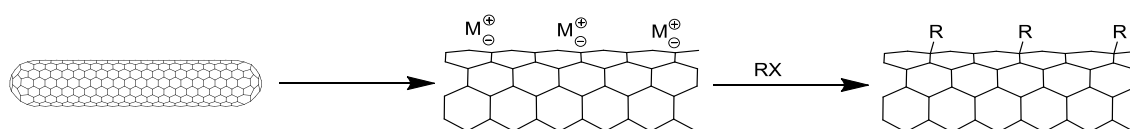
Scheme I.2 Generic route to nanotubide functionalisation.

Table I-2 Examples of reagents that react with nanotubide species.

Reagent	Grafting (See Scheme II-2)	Ref.
		69, 140
		141, 142
		141
		143
R–O–O–R	RO–SWNT	143
	H₃C–SWNT	144
	R–SWNT	145
		146
		147
		147
		147
O=C=O		148
		149
		150
		151

From Table I-2, it is clear that the functionalisation of nanotubide species is highly versatile in offering a wide array of functional moieties ranging from simple alkyl chains to oxygen-containing addends (ethers, ketones, epoxides, carboxylic acids) as well as polymers (*e.g.* PMMA). However, the reaction mechanisms that govern these additions are not clear; there is evidence to support single electron charge transfer radical based mechanisms, although electrophilic additions are also supported. Using GC-MS, the Billups group identified phenyl radicals that were generated *via* a single electron transfer (SET) mechanism following diphenyl sulphide reactions. The process also yielded a carbon-centred free radical and a mercaptide ion.[149] The Penicaud group recently proposed a free radical chain reaction mechanism[141] for the functionalisation of reduced SWNTs (Scheme I.3), based on the free radical mechanism of diazonium coupling to SWNTs.[98] While surface modifications are a key nanotubide application, the mechanistic pathways of nanotubide functionalisation are beyond the remit of this thesis, although an area of interest for future research.
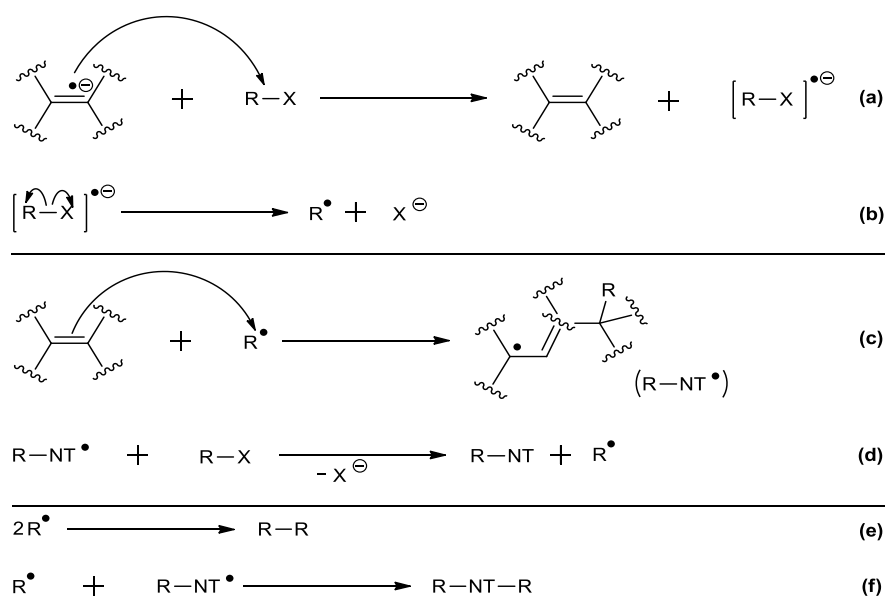
Scheme I.3 A proposed free radical mechanism for the functionalisation of nanotubides with alkyl halides (R-X). Steps (a) and (b) are initiation steps, (c) and (d) propagation, and (e) and (f) termination. Modified from ref. 141.

I. 3. 3. 3. Electrochemical dissolution, sorting and purification strategy

In the Shaffer group, Fogden[152] demonstrated the possibility of using non-aqueous electrochemistry to reduce SWNTs, generating spontaneously dissolved nanotubide

polyelectrolyte salts. Dissolved SWNTs were observed to be sorted by differences in size and/or electronic properties, although yields were typically small (< 15 wt %). Electrochemistry was performed on a Schlenk line to maintain low levels of water and oxygen, with the electrochemical cell consisting of a three-necked round bottom flask into which three electrodes could be inserted through suba-seals. The working electrode was a small piece of SWNT bucky paper (> 10 μm film thickness prepared by the lengthy ultrasonication of SWNT powders in dichlorobenzene (DCB) prior to filtration through a cellulose acetate membrane); a platinum wire was pierced through a hole in the bucky paper and partially submerged into the electrolyte (~0.01 M STPB/DMF). The counter and pseudo-reference electrodes were also Pt wires.

Upon the application of a fixed reducing potential to the SWNT anode, the spontaneous dissolution of SWNTs was observed without the application of sonication; however, in all experiments, the electrolytic solution was stirred. Using Raman spectroscopy, it was observed that metallic/large diameter SWNTs were in higher concentration in the dissolved fraction compared to the undissolved fraction and raw starting material, albeit, the dissolved fraction appeared highly defective.

These preliminary results provided the motivation for this thesis; the electrochemical dissolution and deposition of SWNTs as a method to purify and sort SWNTs will be explored. Unlike many other SWNT processing methods outlined in chapter II.3.2, electrochemical processing is simple, non-destructive, offers accurate potential control compared to other charging methods that typically use unpleasant reagents (liquid ammonia, superacids), and could be highly cost-effective as a continuous process in line with other industrial electrochemical processes.

I. 4. ELECTROCHEMISTRY OF NANOMATERIALS

I. 4. 1. Principles of electrochemistry

Electrochemistry is the study of systems in which reduction or oxidation reactions occur as a result of the movement of electrons between an external power source and ions in solution; this transfer of electrons is known as a redox reaction. Reduction occurs when a species gains an electron, oxidation is the loss of an electron. In a simple electrochemical system, for example a galvanic or voltaic cell,[153] two metal electrodes (*e.g.* zinc and copper) are submersed in an aqueous solution of their respective electrolytic salts ($ZnSO_4$ and $CuSO_4$). A salt bridge (glass tube filled

with a relatively inert electrolyte such as KCl or NaCl, plugged at either end with porous glass or a porous membrane that forms two half-cells), allows the flow of ions to maintain a balance in charge between the two chambers while keeping the contents of each separate to minimise contamination or undesirable reactions taking place. The movement of ions occurs across the two half-cells, while electrons are transported through the external circuit; the number of electrons transferred in both directions must be equal. The two half-cells combine to give the net electrochemical reaction. The standard reduction potential, E^0 (1 M ion concentration, 25°C, 1 atm), is a measure of the tendency of a chemical species to acquire electrons. Standard reduction potentials are measured relative to a reference electrode, typically, the standard hydrogen electrode where the standard reduction potential is arbitrarily set to 0 V. Each species has its own intrinsic reduction potential; the more positive the potential, the greater the affinity for electrons and, therefore, the greater the tendency to be reduced.

An electrode reaction refers to the net oxidation or reduction process that takes place at an electrode. This reaction may take place in a single electron transfer step, or as a succession of two or more steps. The substances that receive and lose electrons are called the electroactive species.[153] Electron transfer processes take place within a thin interfacial region at the electrode surface, involving the quantum-mechanical tunnelling of electrons between the electrode and the electroactive species. Electrode reactions are influenced by many factors, such as the applied potential, reactivity of the electroactive species, the nature of the electrode surface, and the structure of the electrode-solution interface.[154] The kinetics of an electrode reaction are not only controlled by the rate of electron transfer between the electrode and electroactive species in solution, but also by the transport of material to and from the electrode interface. Mass transport[154, 155] occurs *via* three mechanisms: diffusion (the spontaneous movement under the influence of a concentration gradient), convection (transport to the electrode by a gross physical movement, *e.g.* stirring, rotation or vibration of the electrode, or due to thermal or density gradients), or migration (movement of charged particles along an electrical field). The modelling of mass transport effects is somewhat complex and attempts are made to minimize the impact by careful design and control of the electrochemical experiment. Migration, for example, is reduced by incorporating a non-active background electrolyte that shields the reactant species from electrode charges, but also act as an ionic charge carrier. Convection can also be eliminated to a

certain extent by using an unstirred solution, although it is difficult to completely eliminate natural convection.

The electrical double layer[156] is the array of charged particles and/or oriented dipoles that exists at every material interface, whereby the charge on the electrode is counterbalanced by the nearby charges of ions in solution. A positively charged electrode thus attracts a layer of negative ions (and vice versa). The electrical double layer was first modelled by Helmholtz, then developed independently by Gouy and Chapman (Gouy-Chapman model) introducing a diffuse double layer. Stern's model introduced further factors such as diffusion/mixing in solution, the possibility of absorption on to the surface and the interaction between solvent dipole moments;[157] Grahame's[158] electrical double layer made up of several distinct layers is the most accurate model. The inner Helmholtz plane (IHP) contains solvent molecules and specifically adsorbed ions (which are not fully solvated); the outer Helmholtz plane (OHP) reflects the imaginary plane passing through the centre of solvated ions at their closest approach to the surface.[156] The solvated ions are attracted to the surface by long-range coulombic forces. The diffuse layer is a three-dimensional region of scattered ions, which extends from the OHP into the bulk solution. The concentration of ionic species at a given distance from the surface decays exponentially.[156] Due to the presence of the electrical double layer, charging or capacitive (non-Faradaic) current is always present in voltammetric measurements. A schematic view of the electrical double layer is shown in Fig. I-14. For a general overview of the electrical double layer, refer to Mark *et al.*[159] and references therein.
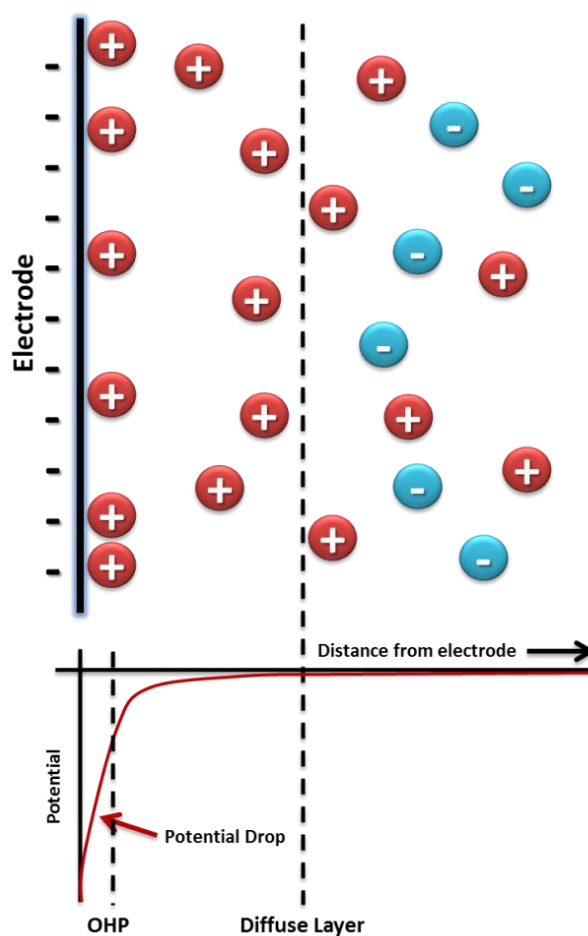
Fig. I-14 Schematic diagram of the electrical double layer showing the outer Helmholtz plane (OHP) and the diffuse layer. Modified from ref. 157.

For the study of specific reactions, three-electrode setups are commonly used, measuring only one half of an electrochemical cell. The electrode potential is controlled to raise or lower the energy of the Fermi level such that an electron transfer reaction can take place.[154] Three electrodes (working, reference, and counter) are immersed in the sample solution; the working electrode is the electrode at which the reaction of interest occurs. Generally, the reduction or oxidation of a substance at the surface of a working electrode is followed by the mass transport (diffusion, migration, convection) of new material to the electrode surface and the generation of a current (Faradaic current).[160] Throughout the experiment, the reference electrode provides a stable and reproducible potential (independent of the sample composition), against which the potential of the working electrode is compared.[156] The reference electrode provides a stable, reversible half-reaction with Nernstian behaviour, for example, Ag/AgCl (silver-silver chloride

electrode) or Hg/Hg_2Cl_2 (saturated calomel electrode, SCE).[160] The reference electrode should be as close as possible to the working electrode to minimise the ohmic potential drop (iR drop) due to solution resistance that may cause shifts in peak potential, peak separation or a decrease in the magnitude of the current. The counter electrode supplies the current to maintain the potential between the working and reference electrodes; an inert conducting material, such as platinum wire or graphite rod, is typically used as the counter electrode. Most voltammetric analysis is performed over a very short time frame, generating minimum concentrations of reduced or oxidised species. Therefore, the separation of counter electrode from the working electrode compartment is not normally required.[160] However, in cases where the experimental timeframe is significantly long, the build-up of contaminants is prevented by isolating the counter electrode behind a porous membrane.

A potentiostat is connected to the three-electrode setup (working, reference and counter electrodes), with the primary function of controlling the potential of the working electrode relative to the reference electrode, whilst measuring the current flowing between the working and counter electrodes during voltammetric analysis. For a simple schematic and explanation of several components of the potentiostat, the reader should refer to reference 161.

Voltammetric experiments performed during this research are outlined in the characterisation section II. 5.

I. 4. 2. Electrochemistry of carbon nanomaterials

The electrochemical intercalation of graphitic carbons have been extensively studied over the last 50 years due to their properties that include electrical conductance, the ability to accommodate ions or molecules between the lattice layers, and the ability to react *via* functional groups at their surfaces.[162] A vast array of electrochemical intercalation compounds either by cations (especially Li), anions or solvent molecules has developed; upon intercalation, the graphite interlayer/lattice spacing increases with guest ions penetrating the lattice layers following cathodic reduction/anodic oxidation of the carbon electrode. This process generates charges in the carbon host lattice as shown by:

Equation I-8 $C_n + M^+ + e^- \rightleftharpoons M^+C_n^-$ (Cathodic reduction)

Equation I-9 $C_n + X^- - e^- \rightleftharpoons C_n^+X^-$ (Anodic oxidation)
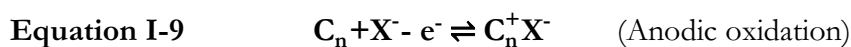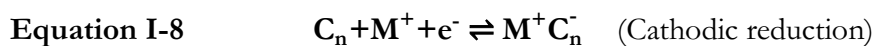
For intercalation, the carbon lattice must be capable of accepting the guest ions on both steric and electronic grounds. Typical M^+ species include alkali and alkaline earth metal ions, while X^- species include halides, perchlorates, tetrafluoro and hexafluoro anions, *etc.* Generally, ternary phases are produced that are generated from the acceptance of solvent molecules in the electrolyte into the carbon lattice[162] (*e.g.* $M^+(solv)_y C_n^-$ or $C_n^+(solv)_y X^-$); the degree of solvation determines either a two- or three-dimensional solvation phase (Fig. I-15).
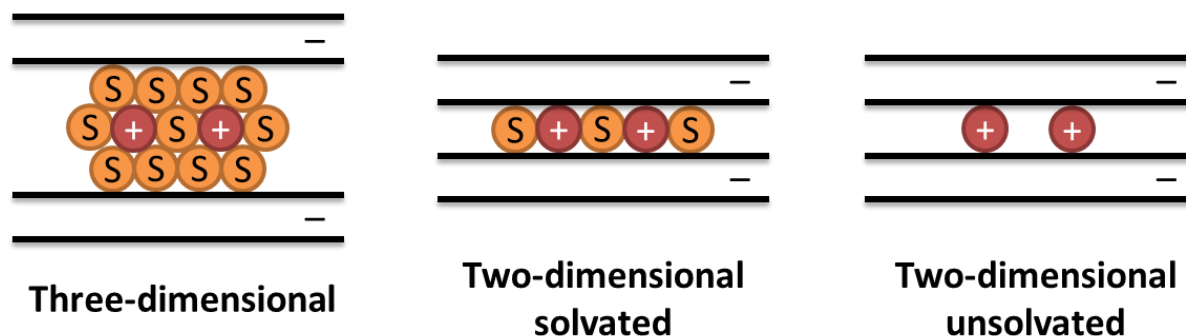
Fig. I-15 Schematic diagram of the solvation phase following cationic intercalation into the graphite lattice (S = solvent). Modified from ref. 162.

The electrochemistry of carbon nanomaterials has advanced considerably in recent years, following the discovery of fullerenes. Due to the interesting (opto)electronic properties of C_{60}, and its relatively high solubility in many polar aprotic solvents,[163] the electrochemistry of fullerenes is a vast subject area. Theory predicts three low-lying degenerate LUMOs in C_{60}, which leads to an exceptionally low reduction potential (Fig. I-16a). C_{60} has the ability to reversibly accept up to six electrons;[164] the chemistry of fullerene anions (fullerides) is extensively reviewed.[165] In polar aprotic electrolytic solvents, it is possible to generate C_{60}^{3-} at potentials close to -2 V (*vs.* Fc^+/Fc).[166] The hexanion, C_{60}^{6-}, is usually generated from alkali-metal saturation-doping to form $M_6 C_{60}$ where M = K, Rb, and Cs. However, a wider expansion of the available potential window to -3.3 V (*vs.* Fc/Fc^+) was reported,[167] accomplished by the use of a mixed solvent system (0.1 M $TBAPF_6$ in 15–20% acetonitrile in toluene) and low temperatures (-10 to +5°C), allowing the observation of C_{60}^{6-} (Fig. I-16b) and C_{70}^{6-}. The oxidation of C_{60} to C_{60}^+ is relatively difficult although the formation of even the extremely reactive C_{60}^{2+} and C_{60}^{3+} species have now been generated electrochemically in DCM with 0.05 M $TBAAsF_6$ as supporting electrolyte.[168]
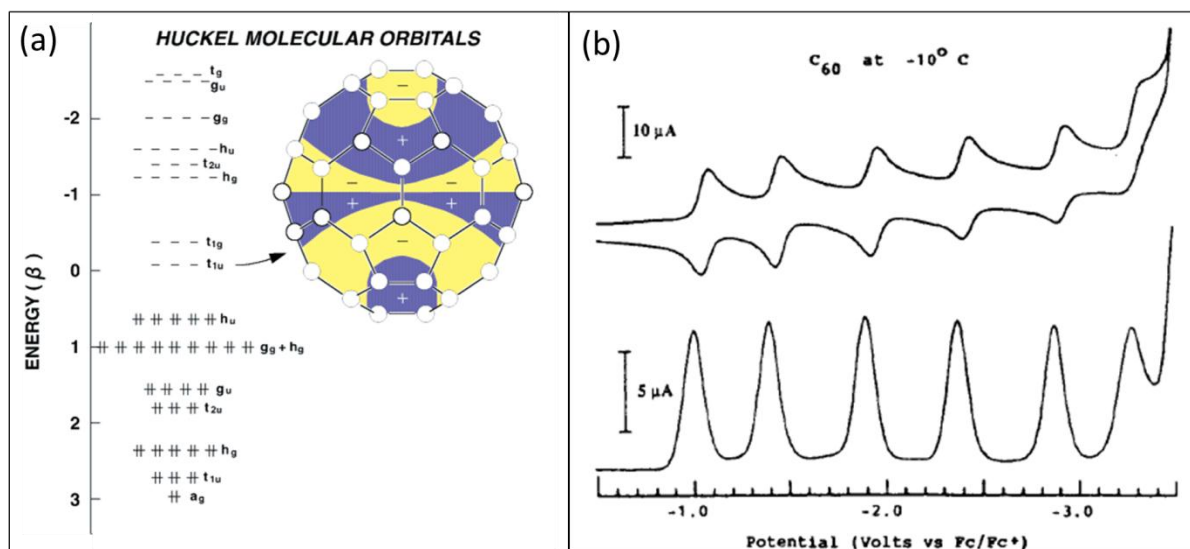
Fig. I-16 C_{60} molecular orbital levels and electrochemical behaviour. (a) Hückel energy levels of C_{60} together with one component of the triply degenerate t_{1u} set of molecular orbitals which become populated on alkali-metal doping. Modified from ref. 164. (b) Cathodic cyclic and differential pulse voltammograms of C_{60} in acetonitrile/toluene at -10 °C showing successive reversible reductions to C_{60}^{6-}. Reproduced from ref. 167.

The electrochemistry of carbon nanotubes is a relatively new, but rapidly advancing area; applications range from energy storage, sensing, actuators and nanoelectronics due to their high surface area and conductivity properties.[35] Carbon nanotubes have been studied with regards to developing such electrochemical devices as capacitors, batteries, sensors and microelectrodes; carbon nanotubes have also been synthesised[169] and covalently functionalised[151] using electrochemical processes.

(Spectro)electrochemistry of carbon nanotubes and electrochemistry at carbon nanotube electrodes have been reviewed extensively by Kavan and Dunsch[35, 170] and Dumitrescu *et al.*[171] respectively. Dumitrescu highlighted concerns regarding the electron transfer activity at carbon nanotube electrodes. In some cases, edge-plane-graphite-like open ends and defect sites are apparently responsible for electron transfer activity; in other cases, studies of well characterised SWNT electrodes, either as individual tubes or as two-dimensional networks, suggest sidewall activity dominates. The presence of surface impurities, including amorphous carbon and metal nanoparticles, oxygen-containing and charged surface functionalities (*e.g.* COOH) following SWNT purification, are likely to affect the behaviour of CNT-based electrodes; sidewall defects are also likely to play a significant role due to changes in the SWNT electronic DOS near the Fermi level, typically resulting in an increase in resistivity of the SWNT at these points. In order

to account for observed differences in electron transfer characteristics, comprehensive characterisation of SWNT electrode materials is essential, especially if purification processes are performed. In this thesis, in line with remarks made by Dumitrescu *et al.*, starting materials were fully characterised and used as-received without further purification or processing.

Other spectroelectrochemical reports[31, 172, 173] have focussed on correlating electrode potentials to key spectroscopic features for sc-SWNTs; the bleaching of characteristic vis-nIR or nIR PL signals associated with electronic transitions between vHSs, or corresponding resonant Raman features, have been used to derive energy levels relative to a chosen reference electrode. Despite different apparent trends in Fermi energy between these studies, in general, redox potentials depend on nanotube diameter, the first reduction (LUMO energy) and oxidation (HOMO energy) events occur more favourably for larger diameter tubes, consistent with the inverse relationship between band gap and tube diameter. The Fermi level was not observed to vary significantly with sc-SWNT diameter, and a similar (un)doping effect was observed for m-SWNTs in a vis-nIR study,[172] suggesting similar Fermi level energy positions. However, redox potentials were affected somewhat by the localised dielectric environment of the SWNT (surfactant or solvent effects).[31] In other studies, diameter/band-gap is reported to have a significant impact on the Fermi level, with an inverse relationship of redox potential to diameter.[49, 174] These differences may arise due to differences in sample type, morphology, local SWNT environment or differences in measurement technique. Generally, at constant diameter, m-SWNTs will have greater initial electron affinity than semi-conducting species; at smaller diameters, there are greater distinctions in SWNT Fermi level and redox behaviour. However, further studies are required in this area.
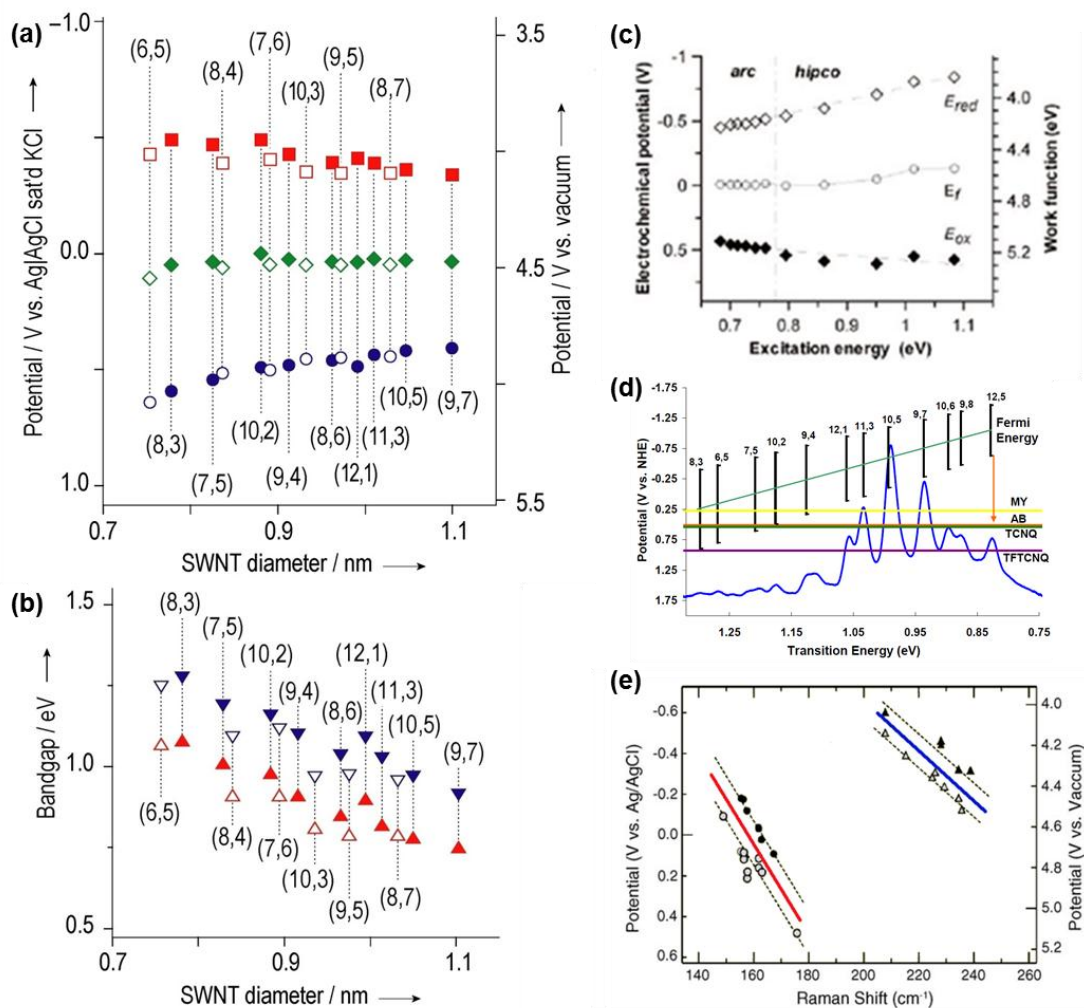
Fig. I-17 Collection of reported SWNT redox potentials determined by chemical or spectroelectrochemical methods. (a) Oxidation (blue circles), reduction (red squares), and Fermi level (green diamonds) potentials of fifteen isolated SWNTs as determined by spectroelectrochemical nIR PL experiments (b) Optical (inverted blue triangles) and the electrochemical (red triangles) band gaps of the isolated SWNTs. In (a) and (b), solid symbols represent mod 1 (2n + m, 3) = 1) and open symbols represent mod 2 (2n + m, 3) = 2), respectively. Reproduced from ref. 173. (c) Vis-nIR spectroelectrochemical data showing oxidation (solid diamonds) and reduction (open diamonds) standard potentials and Fermi levels (open circles) of semi-conducting SWNTs *vs*. SCE (left axis) or vacuum level (right axis), as a function of the excitation energy of the Van Hove optical transitions. Reproduced from ref. 172. (d) Plot of relative potential energies of the valence band, conduction band and Fermi levels of specific nanotube chiralities in relation to reduction potentials (determined by cyclic voltammetry) for the organic acceptor molecules used in the study. The nanotube fluorescence spectrum (785 nm excitation) is superimposed. The red arrow indicates the electron transfer from the SWNT to the acceptor. Reproduced from ref. 174. (e) Relation between observed ω_{RBM} and the work function (φ_0) for metallic (circles) and semi-conducting (triangles) SWNTs. Closed and open symbols correspond to results obtained at the cathodic and anodic scans, respectively. Modified from ref. 175.

Cyclic voltammetry of SWNT electrodes was first performed by Liu *et al*.[176] comparing the behaviour of SWNT films deposited on Pt or Au electrodes with those of C_{60} and C_{70}, which showed well defined redox events using 0.1 M $TBAPF_6$ in acetonitrile as electrolyte. SWNT CVs showed broad capacitive cycles with no observable features; variations in SWNT concentration and electrode temperature during deposition did not make a difference to the observed CVs proposed due to the heterogeneous distribution of SWNTs. Typically, the cyclic voltammetric response of SWNT electrodes are dominated by capacitive charging. In general, square loops are observed for ideal capacitors; SWNT electrodes reveal "butterfly" shaped voltammograms due to increased capacitance with increased reduction/oxidation potential away from the open circuit potential (OCP) (Fig. I-18a-b). This trend was previously observed for activated carbon electrodes[177] and assumed to be a consequence of the electronic structure of the electrode material. Developments in the cyclic voltammetry of SWNT electrodes over the last decade have witnessed various explanations of the characteristic "butterfly" shaped voltammograms. This feature has primarily been attributed to the increased contribution from semi-conducting SWNTs following electron/hole doping of the electronic DOS,[178] although it is apparent that the DOS of all SWNTs in the sample will blur the overall electronic structure of the electrode. Early reports suggested trace water may have a significant effect on the CV of SWNTs;[179] an increase in the Faradaic pseudocapacitance of surface oxides was attributed to the presence of trace water upon exposure of the polar aprotic electrolyte (0.2 M $LiClO_4$ in acetonitrile) to the atmosphere.

Recently, Al-zubaidi *et al*.[180] observed dumbbell shaped CV responses using a SWNT paper electrode consisting of highly crystalline, open-ended arc-discharge synthesised SWNTs (Meijo SO) at slow scan rates (5 mV s^{-1}) in 1.0 M triethylmethylammonium tetrafluoroborate ($TEMABF_4$) in propylene carbonate (PC) electrolytic solution. CVs revealed an area near the OCP where there is little or no electron density on the sc-SWNTs (band gap), and 'bulges' attributed to the (un)doping of the sc-SWNT electronic DOS corresponding to the first vHS of the *(17,3)* sc-SWNT that was the predominant species following electronic separation using DGU. CVs for m-SWNTs on the other hand showed square shaped cycles with no distinguishable features.

The research presented in this thesis investigates the cathodic reduction of carbon nanotube electrodes, at significantly greater reducing potentials than previous spectroelectrochemical reports with the use of non-aqueous electrolytes. Recently, non-aqueous electrochemistry was

performed on SWNT bucky paper electrodes to characterise these materials for electrochemical double layer capacitor applications.[178] An electrochemical dilatometer was used to study the swelling of the SWNT bucky paper upon ion intercalation; the setup is shown in Fig. I-18d. The shape of the SWNT CV was the typical "butterfly" shape (Fig. I-18a-b). One interesting feature is the observed swelling of the bucky paper electrode upon intercalation of anionic species at positive potentials (*vs.* a carbon pseudo reference electrode) when the electrolytic system was tetraethylammonium tetrafluoroborate (TEATFB) in acetonitrile. The dissolution of $SWNT^{n+}$ (nanotube cations) using similar electrolytes used to generate C_{60} cations is a possible avenue for future study.
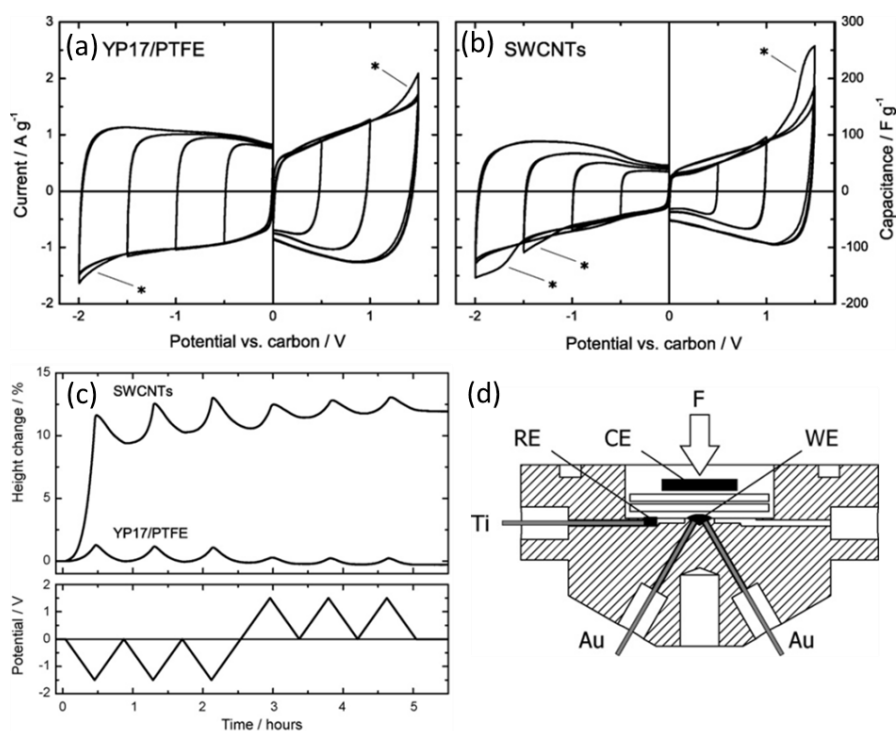
Fig. I-18 Electrochemical dilatometry of SWNT bucky paper electrodes for electrochemical double layer electrode applications. Half-cell CVs of (a) activated carbon (YP17) with 10 wt % PTFE and (b) SWNT bucky paper in 1 M TEATFB/acetonitrile at a scan rate of 10 mV s^{-1}. Asterisks mark the first cycles where shown. (c) Height change of SWNT bucky paper and YP17/PTFE (top) during a defined potential profile (*vs.* YP17/PTFE quasi-reference electrode) at a scan rate of 1 mV s^{-1} (bottom). (d) cross-section view of the electrochemical cell setup. Reproduced from ref. 178.

I. 5. SUMMARY

The versatility of SWNT structures provides many opportunities and challenges. Technological applications require the separation of m- and sc-SWNTs, at least; control over aspect ratio may also be important for specific applications. The requirements for sc-SWNTs are more demanding because applications will typically be sensitive to the band gap and to the presence of contaminating metals. *(n,m)* separation is the ultimate challenge; the distinctive chemistry of specific *(n,m)* species remains to be explored and is a further area for development as separation/selective synthesis strategies improve.

At present, due to the heterogeneity of SWNT samples, in terms of their inherent structures and impurities, post-synthetic separations are of great importance, in the long term, selective syntheses are likely to provide better defined materials. Physical methods at the very small scale are just beginning to highlight the future possibilities of single *(n,m)* SWNT types; the distinctive properties and reactivities of SWNTs will be increasingly considered in the future, reliant on their respective functionalisations.

Currently, the mechanisms that govern selectivity are still relatively poorly understood due to their complex nature, and the range of multiple effects that occur simultaneously. Further detailed mechanistic studies are needed, enabled in future by more homogeneous *(n,m)* starting materials, as well as computational/theoretical work. Progress is also limited by the difficulties of bulk characterisation of nanotube properties (Chapter II); consequently, the quantification of yield, selectivity and rate is limited. Further improvements in metrology would be highly beneficial.

In terms of its versatility, intrinsic dispersion mechanism, and the ability to regenerate the original electronic properties, reductions stand out as the most promising route towards SWNT modification and sorting; superacid protonations might play a similar role in the future. SWNT reductions are widely studied mechanisms, thus far utilizing chemical methods (*e.g.* sodium napthalide/THF, sodium/liquid ammonia). The electrochemistry of carbon nanotubes is steadily gathering interest, currently only the first redox potentials have been studied spectroelectrochemically. This thesis probes further reducing potentials in order to utilize the reductive dispersion mechanisms observed with chemical methods, with the additional advantage of stricter potential control accessible with electrochemistry.

The overall objective for electrochemical dissolution and deposition of SWNTs is in many ways analogous to other reported processes, most notably the industrial electrolytic refining of copper, and the electrochemical synthesis of telluride Zintl anions[181] *via* the cathodic dissolution of telluride electrodes that does not appear to have been studied further since reports more than a decade ago.

Electrorefining of copper approach to SWNT separation

Copper is electrorefined from impure copper anodes or extracted from leach/solvent solutions during an electrowinning process.[182] The electrorefining process involves two stages: Firstly, the copper is dissolved electrochemically from the impure anodes into an aqueous electrolyte containing $CuSO_4$ and H_2SO_4. Secondly, pure copper is selectively electroplated on a cathode without the anodic impurities. These anodic impurities which include gold and silver, are highly valuable, and are recovered as a sludge by-product which is further treated. Copper is oxidised to Cu^{2+} during the dissolution step, and reduced at the cathode. The electrochemical dissolution of SWNTs involves reductive dissolution of nanotubide anions (Chapter III) and oxidation of neutral SWNTs on the anode during the deposition step (Chapter IV). A simple overview of how the two processes compare is outlined in Table I-3.

Table I-3 The copper electrorefining process *vs.* electrochemical processing of SWNTs.

Step	Copper Electrorefining (115)	SWNT electrochemical processing
(a)	Copper is electrochemically dissolved from the anode into the electrolyte: $Cu_{anode} \rightarrow Cu^{2+} + 2e^- (E^o = -0.34\ V)$	Electrons are transported through the power supply and external circuit to the cathode
(b)	Electrons are transported through the external circuit to the cathode	SWNTs are electrochemically dissolved from the cathode into the electrolyte: $SWNT_{cathode} + ne^- \rightarrow SWNT^{n-}$
(c)	Cu^{2+} ions migrate to the cathode by convection and diffusion	$SWNT^{n-}$ ions migrate to the anode by convection and diffusion
(d)	Electrons and Cu^{2+} ions recombine at the cathode surface to form copper metal (without the anode impurities) $Cu^{2+} + 2e^- \rightarrow Cu_{cathode}$	The $SWNT^{n-}$ ions liberate their electrons at the anode and form a SWNT deposit $SWNT^{n-} \rightarrow SWNT_{anode} + ne^-$

Industrial electrorefining of copper involves using hundreds of large (1 m x 1 m), thin (0.04-0.05 m) anodes of impure copper and very thin stainless steel cathodes (3 mm) separated by approximately 0.05 m in a cell filled with the $CuSO_4$ electrolyte. The anodes are at a fixed

potential while the cathodes are at a fixed lower potential. These electrodes are spaced evenly along the cell to maintain a fixed current, ensuring all anodes dissolve at the same rate.[183]

Applying the same logic to a carbon nanotube separation strategy requires more extensive facilities, since the required experimental conditions are far more challenging (inert atmosphere, non-aqueous electrolytes, *etc*.); however, the electrochemical deposition of aluminium using non-aqueous electrolytes (*e.g.* toluene) is a highly industrialised process using electrolytes that are highly sensitive to water and other atmospheric species.[184]

Electrochemical synthesis of telluride Zintl anions

Zintl anions are heteropolyatomic species in the form of anionic clusters that are usually generated by the reduction of heavy main group *p* elements (metals or semi-metals) with alkali metals. Typically synthesised by high temperature fusion of the elements, Warren *et al.*[181] developed a novel electrochemical technique for the formation of telluride Zintl anions.
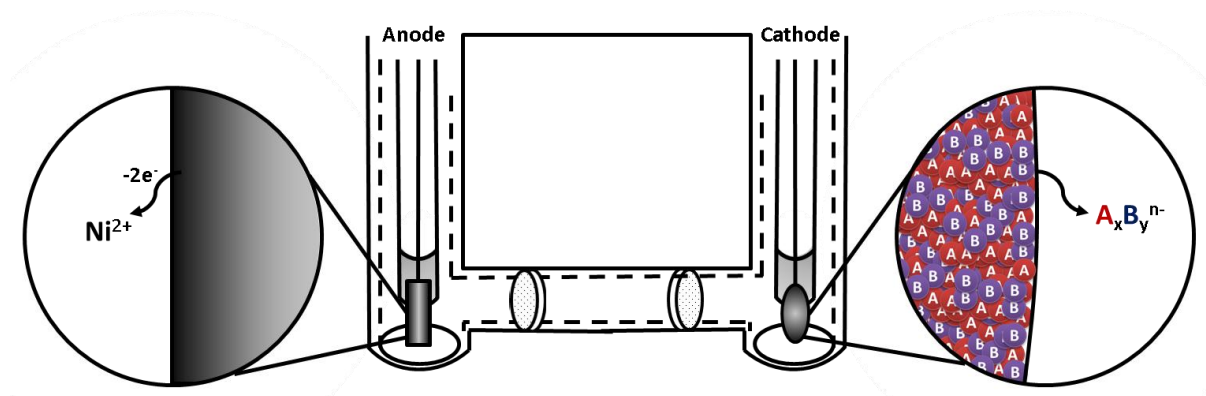
Fig. I-19 Experimental setup for the electrochemical dissolution of telluride zintl anions. Modified from ref. 181.

The electrochemical setup used a standard H-type cell (Fig. I-19) with three independent chambers; the two outer chambers housed the electrodes, the inner chamber served as liquid junction to help prevent cross-contamination of products from the anode and cathode chambers. The cell was sealed to ensure an inert atmosphere needed to preserve the anions that were generated and to keep out atmospheric oxygen that interfered with the process. The electrochemical cells were dried in an oven at 200°C overnight before use in order to remove any moisture that would also interfere with the cathodic dissolution process. All three chambers of the electrochemical cell were each filled with tetraalkylammonium (TAA) salts (dried overnight in an oven at 150°C to remove any moisture) in ethylenediamine solutions (purified by distillation

over CaH_2 and then multiple distillations over K_4Sn_9). The TAA salts served as the supporting electrolyte as well as being used as cations for the crystallisation process. The cathode electrodes were fabricated from the pure elements using the congruently melting binary telluride phase of a heavier main group element or post-transition metal (*e.g.* Au, Sb, As, In, Ga). The anode electrodes were simply pieces of nickel foil; the preference for the use of nickel (over platinum) as a sacrificial electrode was due to the formation of an insoluble purple by-product ($NiBr_2.x$(en) or $NiI_2.x$(en)) upon the reaction of Ni^{2+} with anions of the supporting electrolyte, preventing cross-contamination with the cathodic products.

Current applied to the cathode caused alloy AB to dissolve into a stream of intensely coloured anionic species, $A_xB_y^{n-}$. The stream originated from the cathode electrode and, as it was heavier than the electrolyte material, immediately sank to the bottom of the cathode chamber. As the concentration of anions generated in these streams increased in a concentrated supporting electrolyte of cations, crystals formed and deposited throughout the cathode chamber. The choice of supporting electrolyte greatly affected the products isolated, and by simply changing it, sometimes only by one carbon atom, made the difference between generating an isolated anion, a large anionic cluster, a one dimensional chain material, or no crystals at all.

All cells were loaded in a glove-box, tightly sealed and then brought out to be electrolysed on the benchtop; electrochemical reactions were performed at room temperature under the contained inert He atmospheres (< 1 ppm O_2) present within the chambers of the cells. Each electrochemical cell was connected to its own individual constant current power supply which was connected to the cathode and anode electrodes and set to run at the maximum current allowed. The current range was determined by the solubility of the tetraalkylammonium salts in the ethylenediamine, and was typically ~100 μA to 1 mA (with the maximum compliance voltage of the power supplies ~11 V). The majority of these reactions were performed over 2-5 days. Longer reaction times, in general, increased the chemical yields but were limited by the build-up of insulating layers on the cathode electrode, the physical loss of this electrode (disintegration), and the potential for cross-contamination from products generated in the anode chamber. However, longer reaction times did not increase the electrochemical yields; a continuation of the passage of current without any further dissolution of the electrode material meant current was spent on reducing the solvent, the electrolyte or other unrelated species.

Applying the lessons learnt in this study to the SWNT dissolution/deposition process, it is essential that all glassware, SWNTs and electrolytic salts are vacuum dried at high temperature for long periods to remove any moisture and oxygen. Also, the development of an electrochemical cell with separate compartments is necessary in order to minimize cross-contamination, although long reaction times may still present problems with current being spent on processes other than SWNT dissolution/deposition.

II. Characterisation Techniques

II. 1. Introduction

Characterisation is essential in identifying the properties and structural makeup of a material. Due to the complexity, unique properties, and small size of materials in the 'nano' domain, characterisation is challenging. Determination of the structural characteristics of as-synthesised SWNT materials is widely reviewed,[185] although quantification remains challenging.[186] Some methods (mainly spectroscopic) allow studies of bulk samples to give population statistics; the alternative characterisation of SWNTs individually is costly, tedious, but often most relevant to device application. These tube-by-tube techniques require considerable expertise but are the gold standard for identifying *(n,m)* species. Independently, any of the techniques outlined below are insufficient to convincingly identify SWNT helicity, rather, they should support each other in order to fully define sample characteristics.

Bulk characterisation methods, including optical spectroscopies, generally require simple sample preparation and are routinely performed in research laboratories. Other relevant bulk techniques include X-ray photoelectron spectroscopy (XPS), solid-state ^{13}C NMR, and electron paramagnetic resonance spectroscopy (EPR), but are less widely-used for SWNTs as they are technically demanding, difficult to interpret, less specific, and often require larger quantities of material. Selectivity using XPS is identified by changes in the valence band,[114] solid-state NMR distinguishes distinct signals for metallic and semi-conducting SWNTs,[187] while EPR has been shown to discriminate between electronic types following the selective surface adsorption of cobalt(II) porphyrin onto the SWNT side-walls.[188]

Direct tube-by-tube characterisation techniques include various microscopies that allow the direct imaging and identification of SWNT lengths, diameters, helicities, defects, purities *etc*. Aberration-corrected transmission electron microscopy[189] has been reported to determine *(n,m)* distributions and identify defects, voltage-contrast scanning electron microscopy (VC-SEM)[190] to image electronic conduction pathways through individual SWNT networks, and combined

atomic force microscopy (AFM)-Raman,[109] used to characterise isolated SWNTs. Scanning tunnelling microscopy and spectroscopy (STM/STS)[191] has been used to atomically resolve the electronic structure of SWNTs, identifying chiral angle, diameter, electronic DOS and band gap energies, selected-area electron diffraction (SAED)[192] can also be used to categorically identify SWNT helicity. Other commonly reported techniques are performance-based, monitoring changes in I-V characteristics of SWNT network, film or single-tube devices.[92-94] Tagging[91]/coating[74] reactions have also been be used to identify SWNT functional group positions, but could be further integrated with electron microscopies/diffraction to study the nature and locus of functionalisation, potentially combined with *in situ* assessment of local electronic properties. While individual SWNT characterisation is highly convincing, the major drawback is the technical difficulty and the effort needed to acquire statistically significant data. In addition, great care is still necessary to avoid any selectivity during sample preparation steps.

In this section, the main characterisation techniques employed in the course of this thesis will be discussed. A list of instrumentation and software used can be found in Appendix VII. 2. 2.

II. 2. OPTICAL SPECTROSCOPY

The most common approaches to ascertain the *(n,m)* distribution of a SWNT sample rely on bulk optical techniques, specifically Raman, UV-vis-nIR and photoluminescence (PL) spectroscopies. These optical techniques are widely recognised as key SWNT metrological tools; measurements are simple to perform, quick, can be carried out at ambient conditions, and are ultimately non-destructive and non-invasive.[193] However, many measurement issues can arise, as comprehensively detailed by the National Institute of Standards and Technology (NIST);[186] the potential selectivity of sample preparation steps, or the degradation of spectroscopic signals after functionalisation are particular issues, in the current context.

II. 2. 1. Raman spectroscopy

Raman spectroscopy is used to probe the structural characteristics of a molecule, using an incident laser that generates photo-excited electrons in virtual/forbidden energy states, which can nominally decay *via* different processes. These decay processes emit photons of varying energies and hence wavelengths dependent on the energy between excited and ground state energy levels. The electron can decay to a level higher, lower or to the same level as its original

state, producing three different classes of scattering process:[194] Rayleigh, when the photon is elastically scattered, Stokes, when a photon is lower in energy (longer wavelength); Anti-Stokes, when the photon is higher in energy (shorter wavelength); these events are represented in Fig. II-1. Approximately ~0.000001% is scattered at different wavelengths dependent on chemical structure (Stokes or Anti-Stokes Raman scattering).[195] The Raman spectrometer filters out the intense Rayleigh scattering, the resulting spectra is attributed to the red-shifted Stokes scattering, which is more intense than Anti-stokes scattering, since at room temperature the population state of a molecule is principally in its ground vibrational state.

Peaks in the Raman spectrum correspond to specific molecular bond vibrations for individual or groups of bonds *e.g.* C=C, C-C, N-O, C-H, polymer chain vibrations, benzene ring breathing *etc.*[195] For crystalline solids, *e.g.* SWNTs, the Raman spectrum correlates to phonons (collective vibrational modes). A Raman active vibration can be detected if the polarisability in a molecule changes during the normal vibration; these vibrations are defined by symmetry elements, instilled in a molecule by its point group symmetry. Laser types range from UV through to visible and near IR; laser choice is important for Raman spectroscopy, compromising between Raman scattering efficiency (scales with λ^{-4}), and the risks of fluorescence and sample damage/heating. In the case of SWNTs, multiple lasers are required due to resonance effects (Fig. II-4).
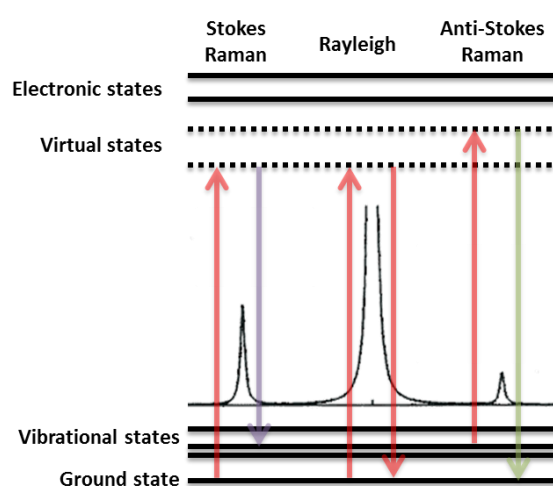
Fig. II-1 Schematic view of the different types of scattering observed in Raman spectroscopy (Stokes, Rayleigh and Anti-Stokes). The relative intensities of these transitions are shown; typical Raman spectrometers filter out the intense Rayleigh scattering peak allowing for either Stokes or Anti-Stokes Raman signals to be observed.

Raman spectroscopy can be used for a wide range of materials (inorganic, organic, biological) in various forms (solids, powders, liquids, gels, slurries and gases); information can be deduced regarding the composition of materials (characteristic Raman frequencies), stress/strain of a material (shift in peak frequency), crystal symmetry and orientation (polarisation of Raman peaks), quality of crystal (width of Raman peak), concentration of material (intensity of Raman peak). Specifically in terms of SWNT characterisation, Raman spectroscopy offers a wealth of information regarding the structure and properties of carbon nanotubes (see Dresselhaus *et al.*[196] and references therein) and can be carried out on both isolated and bundled nanotubes either in solution or solid phase. Typical SWNT Raman spectra (Fig. II-2) display a range of different features allowing semi-quantitative evaluation of nanotube purity, diameter, metallicity, crystallinity and most important the lattice vector, *(n,m)*. In cases where the laser excitation energy (E_{laser}) matches the vHS electronic state transitions in the DOS of specific *(n,m)* tubes, strong resonance Raman scattering is observed.
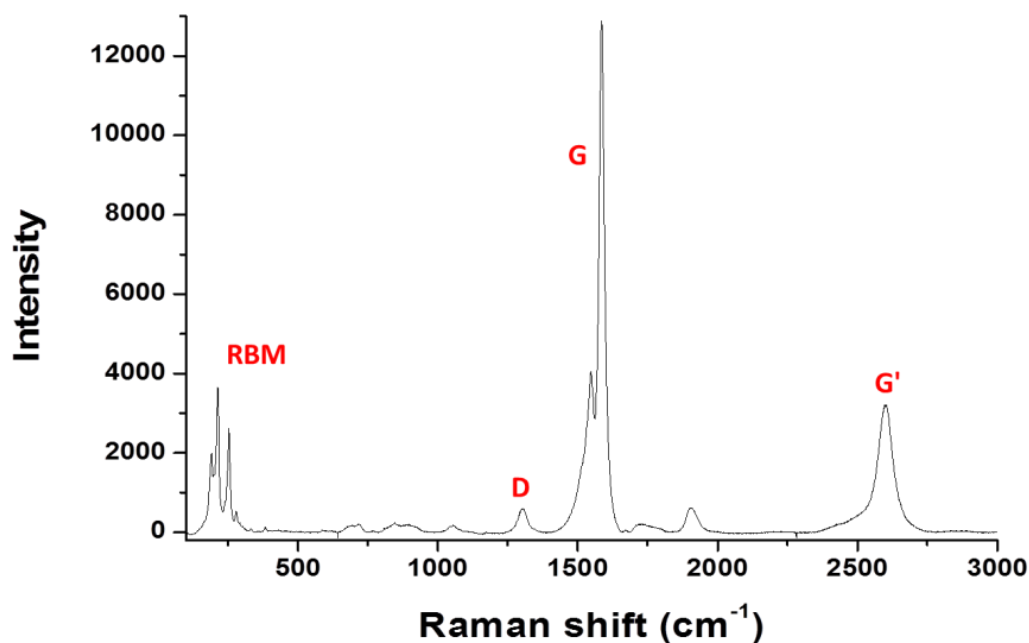
Fig. II-2 A typical SWNT Raman spectrum showing the dominant features. Here, raw HiPco SWNT powder is probed using E_{laser} = 1.96 eV (633 nm). The key characteristic SWNT peaks are highlighted, the radial breathing mode region (RBM) that relates to nanotube diameters, D and G peaks that relate to structural disorder and order, respectively, and the G' (also called 2D) peak that relates to sample crystallinity.

Radial breathing mode (RBM) peaks appear at low wavenumber $< \sim 500$ cm^{-1} and correspond to the concerted atomic vibration of the carbon atoms in the radial direction. RBMs can be used to determine nanotube diameters based on the simple equation:

Equation II-1 $\qquad \omega_{RBM} = (c_1/d_t) + c_2,$

where c_1 and c_2 are experimentally determined constants and d_t is the tube diameter. Typical values for c_1 and c_2 are 223.5 nm cm^{-1} and 12.5 cm^{-1} for HiPco SWNTs[197] and 218.7 nm cm^{-1} and 15.3 cm^{-1} for CoMoCAT SWNTs[198] respectively; Supergrowth[199] SWNTs were found to fit the relation $227/d_t$. The Kataura plot[37] of the allowed vHS transitions (E_{ii}) *vs.* nanotube diameter can be used in combination with experimental Raman spectra to index SWNT samples to the *(n,m)* types present, using multiple laser excitations (Fig. II-4a).[91] Where there is ambiguity over the dividing line between m-/sc-SWNT transitions or RBMs are broad and not fully resolved, it is helpful to use a combination of these plots to improve confidence in *(n,m)* indexing.

Due to the non-linearity of the resonance Raman scattering effect, several laser excitations are required; three laser excitations may be sufficient for characterising a mixture of SWNT helicities and diameters; full characterisation, however, requires many more lasers to identify all SWNTs present. A resonance Raman map[200] (Fig. II-4a) includes m-SWNTs unlike a PL excitation *vs.* emission (PLE) map, albeit quantification of SWNT species is less obvious. Heeg *et al.* recently explored the differences in quantification of *(n,m)* tube type by Raman and PL measurements of three specific SWNTs;[201] each *(n,m)* type has a particular Raman resonance profile that strongly influences apparent abundances. There is clear evidence that SWNT resonance profiles respond to their local environment, including chemical functionalisation specifically, due to electron transfer doping effects; for example, resonance peaks are reported to shift by as much as 7-8 cm^{-1} when oxygen atoms are directly bonded to the side-wall.[202] Furthermore, changes in sample morphology,[203] as a result of debundling and reaggregation, can alter the interband transitions of the SWNTs, moving various nanotubes into and out of resonance with the Raman excitation energy, leading to intensity variations (Fig. II-4c).
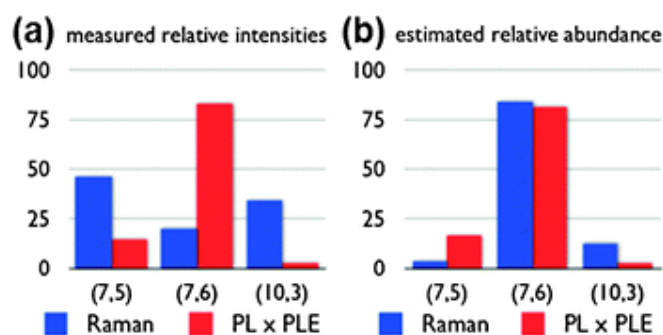
Fig. II-3 Quantitative comparison of the optical characterisation of three (n,m) species. (a) Relative signal intensities obtained by Raman (blue, scaling to full resonance included) and PL x PLE (PL intensity x PL excitation) (red) measurements. (b) Estimated abundance including corrections. Reproduced from ref. 201.

The G band is a tangential mode observed for all graphitic materials in the frequency range from 1520 to 1630 cm^{-1}, and is related to structural order. This feature contains multiple components; for SWNTs, there are well-established dependencies on both diameter and electronic type. Two intense peaks are observed that originate from the symmetry breaking of the tangential vibration when the graphene sheet is rolled, G^{+} and G^{-}.[196] The G^{-} peak can identify changes in electronic character; sc-SWNTs have a Lorentzian G^{-} lineshape, while m-SWNTs have a downshifted, broadened G^{-} lineshape based on a Breit-Wigner-Fano (BWF) form caused by coupling of the discrete phonons to an electronic continuum.[204] This effect is assumed to be proportional to the electronic DOS at the Fermi level, and exhibits a diameter dependent shift since smaller tube diameter (higher curvature) generates stronger phonon-plasmon coupling. The D band (~1350 cm^{-1}) (double resonance feature) is dispersive (shifts to higher frequency as the excitation energy increases) and is linked to the reduction in symmetry of the SWNTs as result of functionalisation or the presence of defects (structural disorder). The intensity or area of the D peak in relation to the G peak (I_D/I_G or A_D/A_G) is widely-used to assess the defect concentration or degree of subsequent chemical modification in SWNTs. However, at high degrees of functionalisation the I_D/I_G ratio remains constant, consistent with the loss of resonance enhancement due to functionalisation.[205] Another double resonance feature is the G' peak (~2700 cm^{-1}), again, sensitive to SWNT diameter and chirality; a single peak is observed for the majority of graphitic materials, however, for isolated SWNTs, the presence of a two-peak feature relates to the specific cutting lines (1D wave-vectors) of the Brillouin zone, discriminating differences in SWNT helicity.[196]

Raman spectrometers are generally calibrated using a strong scattering material such as silicon, however, in the future, well-defined SWNTs of one specific *(n,m)* type may be used as a good reference material. Due to SWNT sample heterogeneity, spectra should be collected at a sufficient number of independent locations to ensure reliable statistical significance. The effect of laser power should also be checked so as not to (potentially selectively) heat or burn the sample, skewing results (Fig. II-4b). Since, the environment and the degree of nanotube aggregation will have a varying influence on excitation window, excitation energy and degree of heating, it is necessary to prepare samples uniformly to allow comparisons. Typically, sample preparation[186] is simple, measurements can be taken of raw, dry SWNT powders, as a pellet, or dissolved into solution (see section II. 2. 2); it is also possible to measure the Raman spectra of isolated individual SWNTs.
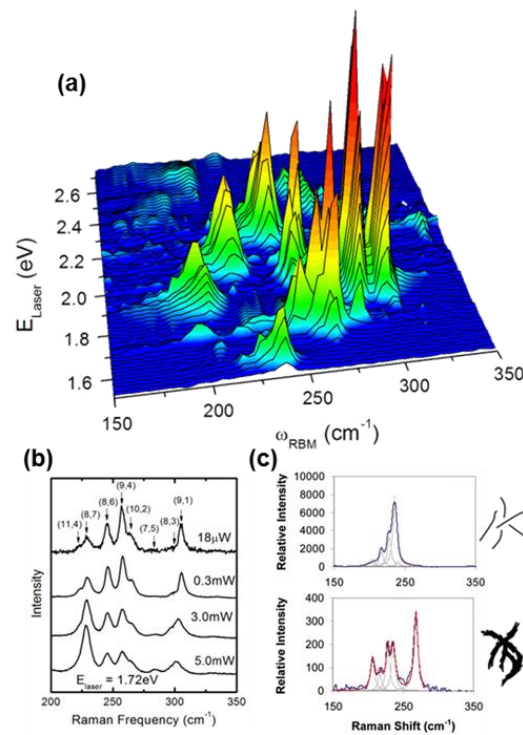
Fig. II-4 Raman spectroscopy of the Radial Breathing Mode region. (a) RBM Raman measurements of HiPco SWNTs dispersed in SDS aqueous solution, measured with 76 different laser lines. The non-resonance Raman spectrum from a CCl_4 solution is acquired after each RBM measurement for calibration of the spectral intensities and to check the frequency calibration. Reproduced from ref. 200. (b) The dependence of the RBM spectra for HiPco SWNTs in bundles on the laser excitation power for a fixed E_{laser} (1.72 eV). Reproduced from ref. 200. (c) The Raman spectra of HiPco SWNT samples with different morphologies (individual SWNTs *vs.* thick bundles) with E_{laser} = 785 nm. Modified from ref. 203.

II. 2. 2. UV-vis-nIR absorption spectroscopy

UV-vis-nIR spectroscopy probes the absorption and transmission radiation of a sample. When the energy of the incident light matches the energy of an electronic transition, the light is absorbed and a ground state electron is excited to a higher electronic energy level. Usually the conditions under which the sample is examined are chosen to minimise reflection, scattering and fluorescence processes.[206] The fraction of transmitted light (T) is given as a ratio of the incident (I_0) and transmitted radiation (I). The Beer-Lambert Law states that the concentration of a substance in solution is directly proportional to the absorbance of the solution (A). When monochromatic radiation passes through a homogeneous solution in a cell, the intensity of the emitted radiation depends upon the pathlength (l), the concentration of the solution (c), and its extinction coefficient (ε): [206]

Equation II-2 $\qquad\qquad A = \varepsilon c l$

The relationship between absorption and transmission ($T = I/I_0$) is given by:

Equation II-3 $\qquad\qquad A = log_{10}\left(\dfrac{I}{I_0}\right)$
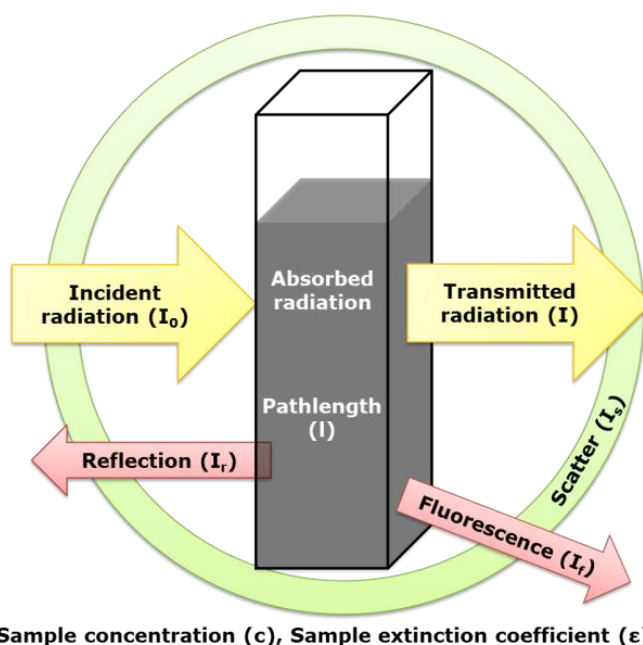
Fig. II-5 Schematic diagram showing the interaction of incident radiation with a sample medium during absorption spectroscopy. Modified from ref. 206.

The major source of scattering in absorption spectroscopy is Mie scattering, caused by the elastic scatter of particles that have a diameter similar to or larger than the wavelength of the incident light. The signal from Mie scattering is significantly stronger than Rayleigh scattering, therefore, a potential source of interference for SWNT samples, where the presence of large bundles, metallic and carbonaceous debris may be significant.

For SWNTs, UV-vis-nIR absorption spectroscopy measures the absorbance of light in the region of the interband electronic transitions of individualised SWNTs. In principle, optical absorption of SWNT suspensions in the UV-vis-nIR region carries information regarding every nanotube present in a sample, unlike other characterisation techniques that only probe specific nanotubes (Raman, PL, *etc.*). However, there are measurement issues again arising from selective sample preparation. In addition, absorption signals corresponding to the specific vHSs are diminished when the nanotubes are present as bundles or ropes, or excessively defective (possibly following covalent modification); signals are also bleached when there is a charge-transfer causing a Fermi level shift in the SWNTs.[170] Due to the fundamental peak width, *(n,m)* resolution is difficult, especially at larger tube diameters, for which more *(n,m)* types are available. However, in general, for typical diameter distributions, regions where the sc- (S_{ii}) and m- (M_{ii}) transitions take place can be identified. As an example, for HiPco SWNTs, the M_{11} transitions occur from approximately ~400-600 nm; the S_{11} and S_{22} transitions are observed at ~900-1600 nm and ~600-900 nm, respectively (Fig. II-6).
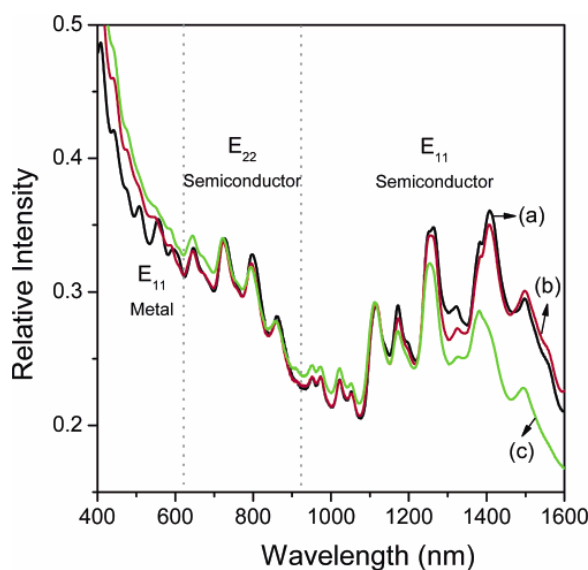
Fig. II-6 A typical SWNT UV-vis-nIR absorption spectra showing the M_{11}, S_{11} and S_{22} regions. These spectra are of SDS-suspended HiPco SWNTs after the addition of varying amounts of 4-hydroxybenzenediazonium salt: (a) control, (b) 0.245 mM, and (c) 0.344 mM. At 0.245 mM only metallic SWNTs are covalently functionalised whereas at excess concentrations (0.344 mM) large diameter (small band gap) semi-conducting SWNTs are also partially reacted. Reproduced from ref. 207.

SWNT samples can be thin films or solutions; thin film spectroscopy[186] is useful for SWNTs that are very difficult to disperse, especially long SWNTs or purified SWNTs after high temperature annealing in vacuum. Thin films may be created by drop-casting, spin-coating, spray-coating or using a draw-down bar. This approach, however, suffers from poor reproducibility of film thickness and difficulties in obtaining homogeneous non-scattering samples, more easily achieved in solution-phase following ultracentrifugation. SWNT solutions should be prepared at around 1 mg mL^{-1} starting concentrations in D_2O solutions containing 0.5–2 wt % surfactant. D_2O is used to measure the absorption spectra of SWNTs to avoid H_2O peaks which appear at 760 and 1000 nm; for D_2O, these peaks are red shifted.[208] Surfactant systems may be selective in themselves, leading to the misinterpretation of spectra; the best surfactants[70] for SWNT dissolution are generally ionic, sodium dodecylbenzene sulphonate (SDBS) is the current choice for well resolved spectral features. Nonionic surfactants (*e.g.* Pluronic, Triton-X, polyvinylpyrrolidone (PVP)[209]) improve with increased molecular weight due to the enhancement of steric stabilisation; an alternative may be to use an organic solvent system (*e.g.* DMF, NMP, CHP).[210] For high-quality dispersions, an ultrasonic processor with cup-horn or

tapered microtip is required to make the initial SWNT dispersion followed by ultracentrifugation with rcf > 100000 g, 1 h. Typically, 0.001–0.2 mg mL^{-1} SWNT concentrations are obtained following centrifugation, and scanned in a standard 10 mm path length quartz cuvette. These concentrations should give absorbance values ranging from 0.033–6.53, based on the average extinction coefficient 3264 ml mg^{-1} m^{-1} at 660 nm for HiPco SWNTs in NMP.[211] In principle, extinction coefficients are a function of SWNT type, though rather similar average values have been reported for a wide range of polydispersed systems.[212] Note that SWNTs have different degrees of dispersability depending on the original type and subsequent treatments; sample preparation methods may need to be adjusted and can be difficult to compare.

Typical UV-vis-nIR absorption spectra for the main types of SWNT used in this research are shown in Appendix VII. 3, for SWNTs dispersed in 1 wt % sodium deoxycholate (DOC) in D$_2$O subjected to probe sonication (150 W, 30 min) and ultracentrifugation (120000 g, 1 h).

II. 2. 3. Photoluminescence spectroscopy

Photoluminescence (PL) spectroscopy is widely-used to study SWNTs, although it is not possible to characterise m-SWNTs, since they do not fluoresce. Many spectral features that overlap in simple emission or absorption spectra are clearly separated in two-dimensional excitation-emission spectra allowing the direct *(n,m)* identification of the sc-SWNTs.[213] Excitation occurs between the conduction and valence bands of sc-SWNTs (S$_{ii}$), while the emission of S$_{11}$ fluorescence is detected. Similar to absorption spectroscopy, SWNT samples are usually prepared as thin films or in D$_2$O solutions containing 0.5–2 wt % surfactant; however, low SWNT concentrations are measured (< 0.020–0.025 mg mL^{-1}), in order to minimise fluorescence quenching from bundles and m-SWNTs. Similarly to UV-vis-nIR, ultracentrifugation is essential for these high-quality dispersions and choice of surfactant system is an important consideration. A PL contour map is obtained by measuring the emission intensity as a function of both excitation wavelength and emission wavelength.[213] A non-emissive region that lies between the regions of the S$_{22}$ and S$_{33}$ branches is due to the m-SWNTs in the sample. Again, the resolution measurement of large diameter *(n,m)* species is difficult as discussed in the previous section. However, the concentration of *(n,m)* species is obtained almost directly from the relative peak intensities since only minor adjustments are required due to the varying ratio of PL emission/excitation for each individual species.[201] PL spectroscopy is also highly sensitive to

defects and sites of covalent modification at nanotube sidewalls that cause fluorescence quenching as a result of the relatively long exciton diffusion length[214] in SWNTs (~90 nm).

PL spectra for the main types of SWNT used in this research are shown in Appendix VII. 3, for SWNTs dispersed in 1 wt % sodium deoxycholate (DOC) in D_2O subjected to probe sonication (150 W, 30 min) and ultracentrifugation (120000 g, 1 h).
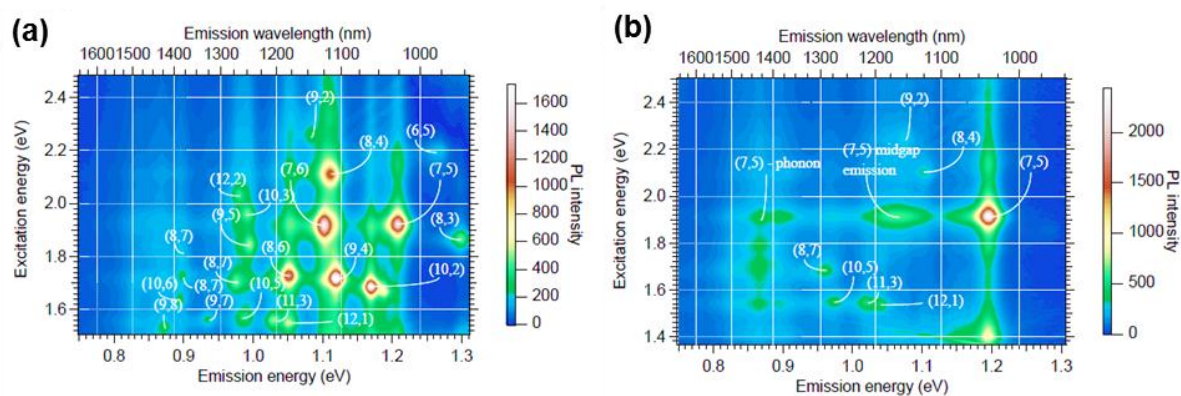
Fig. II-7 SWNT PL excitation *vs.* emission (PLE) contour maps. (a) purified HiPco SWNTs suspended by 1 wt % sodium cholate/D_2O and (b) the same suspension added to an equal part of H_2O_2 after 7 days. This PLE map represents a key *(n,m)* selective covalent modification of SWNTs. Many new phonon-assisted absorption and emission features are present in (b). Reproduced from ref. 120.

II. 3. MICROSCOPY

Several microscopy techniques are used to probe the characteristics of SWNT samples. Beyond simple optical microscopy, both electron and scanning probe microscopies are essential in understanding sample properties. Scanning electron and transmission electron microscopies (SEM/TEM) were used in this research, with atomic force microscopy (AFM) the only scanning probe microscopy (SPM) technique used in this research. TEM offers atomic resolution, and is able to probe the internal structures of carbon nanotubes; however, the resolution of SEM and AFM are significantly lower, consequently, these techniques allow the characterisation of SWNT length and surface morphology as shown in Fig. II-8.
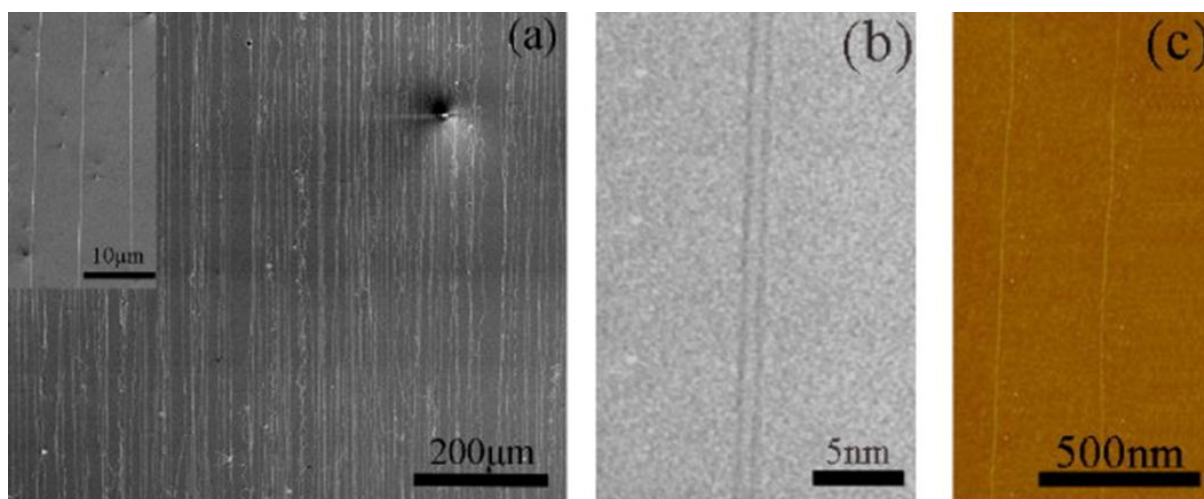
Fig. II-8 Microscopy characterisation of well-oriented SWNT arrays on SiO$_2$/Si wafer. (a) SEM image, (b) TEM image of individual nanotube in (a), (c) AFM image of nanotubes in (a). Reproduced from ref. 215.

II. 3. 1. Electron Microscopy

Electron microscopes were first developed to overcome the limited image resolution of optical microscopes. Most modern electron microscopes are aberration corrected, with Ångström resolution using TEM. Electrons interact with samples generating many signals allowing various methods of analysis (Fig. II-9).

Scanning electron microscopy (SEM) utilises a focused beam of high-energy electrons that is raster-scanned across a specimen surface to provide an indication of the surface morphology.[216] Electron beam interactions with the material cause a variety of signals including secondary electrons, backscattered electrons, X-rays, *etc.* which may be used to characterise a material with respect to specific properties (surface topography, composition, electrical conductivity).[217] SEM allows the imaging of SWNT ropes and bundles with typical resolution on the order of 2-5 nm, thus individual tubes cannot be distinguished from bundles.[218] As well as imaging, it is also possible to obtain energy dispersive X-ray (EDX) spectra, providing elemental analysis by detecting emitted X-rays of specific energies. For lighter elements such as carbon where electron density is low compared to heavy metals, an electron energy loss spectrometer (EELS) in line with a TEM instrument is more reliable. SEM samples need to be conductive for imaging (in order to dissipate the build-up of charge); sample holders are typically an aluminium stub, upon which SWNT powders can be firmly attached by adhesive carbon tabs or silver dag. SWNT dispersions can be drop casted on to polished aluminium stubs for subsequent analysis.

Transmission electron microscopy (TEM) requires a thin specimen that is illuminated with electrons. Normal imaging is caused by elastic scattered signals, while other scattering events include Bragg scattering, diffraction, refraction, and inelastic scattering, allow the observation of a diffraction pattern on the viewing screen, and detect X-ray or EELS spectra outside the optical column.[219] When imaging SWNTs, the most useful imaging mode is phase contrast/lattice imaging. Phase contrast arises due to a difference in phase of electron waves scattered through a thin specimen. A large or totally removed objective aperture should be used to allow a maximum number of diffracting beams into the image, which essentially interfere to form a lattice image; the image is very sensitive to small changes in thickness, orientation, and astigmatism of the objective lens.

For SWNT samples, holey carbon grids are typically used (amorphous carbon film on a copper mesh). Minimal concentration SWNT dispersions (< 0.0001 mg mL^{-1}) can either be drop-cast on to suspended grids (requiring high temperature vacuum oven treatments to remove typical amide solvents), or drop-cast on to grids placed on filter paper (to instantly remove the majority of solvent). Key issues with TEM include beam damage[220] of SWNT samples due to a low energy knock-on collision threshold (~86 keV), although carbon nanostructures are stable[221] for relatively long periods at typical operating voltages (~200 keV).
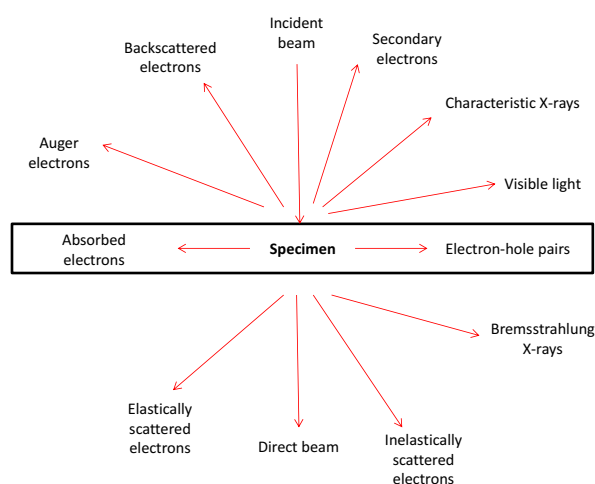
Fig. II-9 Electron microscopy beam-specimen interactions. Modified from ref. 219.

II. 3. 2. Atomic Force Microscopy

Scanning probe microscopy involves the interaction of a scanning probe with the surface of the object of interest. The atomic force microscope (AFM)[222] is used to image surface morphologies with resolution down to the nanometre level,[223] and can also measure the physical (electronic, magnetic), or chemical properties of a material.[224] The AFM probe is raster-scanned across the sample to form a map of the measured property.

AFM is useful in imaging isolated SWNTs, which may be prepared by processing bundles, and can be used to measure their diameter and length. Furthermore, samples can be imaged with relatively low cost and within a short time.[225] SWNT dispersions are deposited on cleaned silica (acid treated) or freshly-cleaved mica substrates. Minimal concentration SWNT dispersions (< 0.0001 mg mL^{-1}) can either be drop-cast, spin-coated, or spray-coated on to these substrates with subsequent vacuum drying for at least 24 hours to remove residual solvent. For SWNT samples, tapping mode AFM is used to obtain height information, a piezoelectric crystal oscillates the tip alternately so that it makes contact with the surface and is then removed, to avoid problems associated with friction, adhesion, electrostatic forces, and other difficulties associated with conventional AFM scanning methods.[226] Other advantages include the modification and patterning of silica surfaces (*e.g.* using 3-(aminopropyl)triethoxysilane[227]) to allow the selective deposition of SWNTs that strongly bind to the amine moieties. However, compared to TEM imaging, organic residues and impurities are observed to a higher extent with AFM, although high temperature vacuum annealing of silicon or mica surfaces is possible unlike for amorphous carbon TEM grids.

II. 4. THERMAL ANALYSIS

Thermogravimetric analysis (TGA) measures the rate of weight loss of a material as a function of temperature under a controlled atmosphere. For SWNTs, TGA is primarily used to examine their thermal stability at high temperatures (up to ~900°C), to measure the content of the components that make up the material (carbon : metal catalyst), and functional groups/coatings that may be present on the SWNT surface. The measurement is normally carried out in an oxidative atmosphere (air) or in an inert atmosphere such as nitrogen, helium or argon, with a linear temperature ramp. The maximum temperature is selected so that the specimen mass is stable at the end of the experiment, implying that all chemical reactions are completed; for

SWNTs, the end temperature is generally ~850°C, so that all of the carbon is burnt off leaving behind metal oxides. TGA provides the ash content (residual mass) and the oxidation temperature. The oxidation temperature has been defined in many ways, NIST recommend this temperature should be defined as the temperature of the maximum in the mass loss rate (dm/dT_{max}), as the onset may be very gradual (up to 100°C) due to the presence of carbonaceous debris that oxidise at lower temperatures than the SWNTs. Also, the mass loss due to carbon decomposition may be superimposed on the mass gain due to catalyst oxidation. A TGA curve showing these features for raw HiPco SWNTs is shown in Fig. II-10. Particular issues include rate dependencies due to different sample masses, gas flow rates and temperature ramps and material inhomogeneity. For consistent, comparable data, all parameters should be kept constant between samples and sample should be repeated at least three times to minimise the effect of sample inhomogeneity.
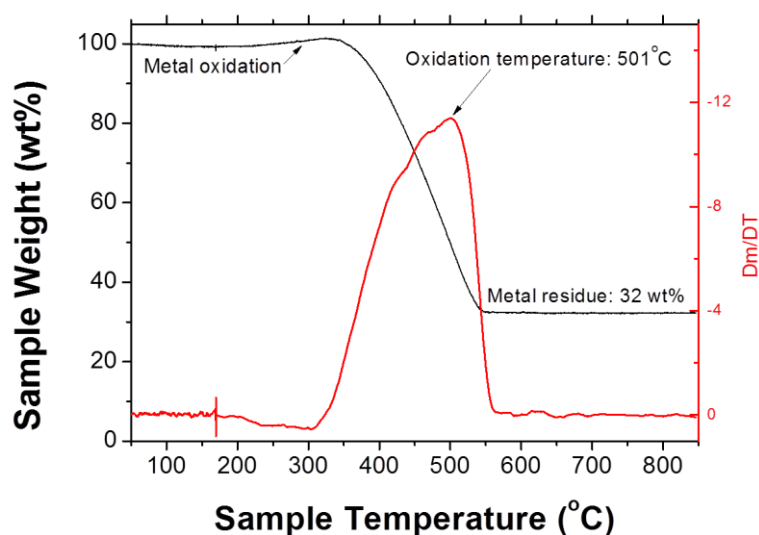
Fig. II-10 Thermogravimetric analysis (TGA) of raw HiPco SWNT powder (Batch R0488). Due to the fluffy nature of the raw powder, the sample was ground with an agate pestle and mortar beforehand and ~2 mg was used for the measurement. The sample was exposed to an oxidative atmosphere (air, 20 mL min^{-1}) and the temperature was ramped from 50°C to 100°C at 10°C min^{-1} then held isothermally at 100°C for 30 min to remove residual moisture; the temperature cycle was then ramped from 100°C to 850°C at 10°C min^{-1}. The oxidation temperature is 501°C as shown by the maximum on the differential curve. Slight weight gain is observed at low temperatures where the metal catalyst is oxidised. The ash content, composed of metal oxide, Fe_2O_3 in the HiPco case, comprises 32 wt % of the sample equating to 22 wt % Fe metal catalyst in the starting material.

II. 5. ELECTROANALYTICAL METHODS
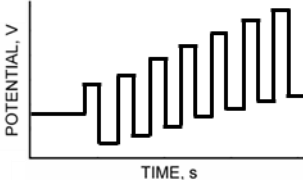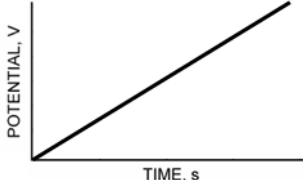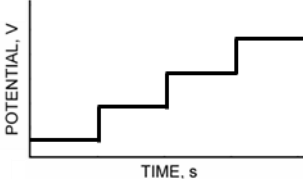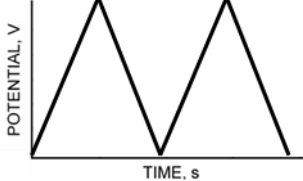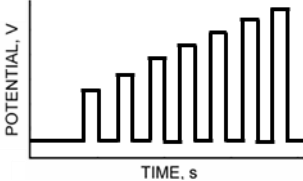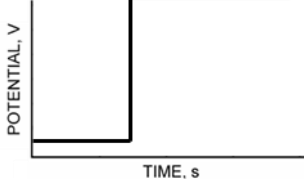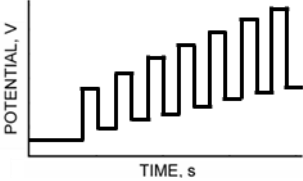
Electroanalytical methods relate the measurement of electrical quantities (current, potential, or charge) with chemical parameters (reduction, oxidation, HOMO/LUMO energies, *etc*.).[156] As discussed in section I. 4. 1, electrochemical processes take place at the electrode-solution interface, with several types of electroanalytical methods available to quantify these chemical properties. The main branches of electroanalysis are potentiometry (measure potential between two electrodes), coulometry (measure charge over time as an electroactive species is converted from one oxidation state to another under current or potential control), and voltammetry (current measured as a function of voltage). A family tree of electroanalytical techniques[228, 229] has been developed to attempt to simplify the broad array of methodologies as shown in Fig. II-11.
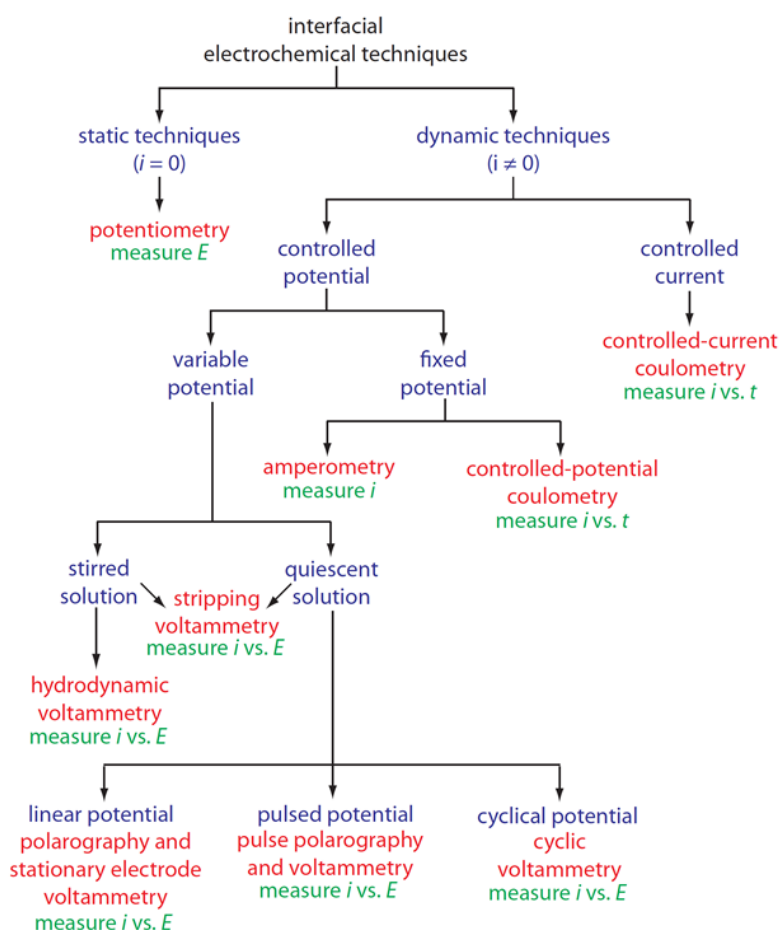
Fig. II-11 Family tree of selected electroanalytical techniques. The specific techniques (red), experimental conditions (blue), and the analytical signals (green) are highlighted. Reproduced from ref. 229.

In this research, controlled-potential electroanalytical methods were used, where the electrode potential is varied or fixed in order to drive an electron transfer reaction. The measured current reflects the rate at which electrons move across the electrode-solution interface. Typical methods include chronoamperometry (measure current as a function of time at a fixed voltage), cyclic or pulsed (normal-pulse, differential-pulse, square-wave, staircase) voltammetry. The potential waveforms of some of these methods are summarised in Table II-1. The predominantly used electroanalytical methods in this research are cyclic voltammetry (CV) for the study of nanomaterial redox behaviour, and chronoamperometry experiments for nanomaterial dissolution and deposition; these methodologies will be discussed in this section.

Table II-1 Electroanalytical methods and their potential waveforms.

Electroanalytical Method	Potential Waveform	Electroanalytical Method	Potential Waveform
DC potential chronoamperometry		Square-wave voltammetry (SWV)	
Linear sweep voltammetry (LSV)		Staircase voltammetry (SCV)	
Cyclic voltammetry (CV)		Normal-pulse voltammetry (NPV)	
Potential step voltammetry (PSV)		Differential-pulse voltammetry (DPV)	

II. 5. 1. Cyclic voltammetry

In order to observe possible SWNT redox events, cyclic voltammetry (CV) was used to measure the current as a function of the sweeping voltage of the working electrode. CV is used to probe redox reactions by scanning the voltage in one direction and then performing the reverse cycle. CV is carried out at a stationary electrode (typically an inert material *e.g.* platinum, gold, glassy

carbon, in this research, the SWNT electrode plays an active role) with a defined scan rate, v (mV s^{-1}). Reversible, quasi-reversible and irreversible processes show distinct features as shown in Table II-2 and Fig. II-12 below.
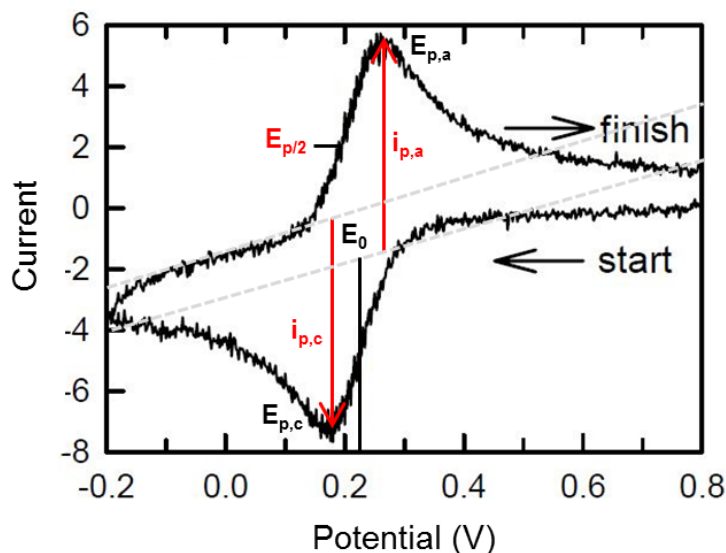
Fig. II-12 Typical reversible (Nernstian) cyclic voltammetric response showing anodic and cathodic peak potentials (E$_{pa}$ and E$_{pc}$, respectively), peak currents (i$_{pa}$ and i$_{pc}$). Modified from ref. 230.

Table II-2 Characteristics of reversible, quasi-reversible and irreversible cyclic voltammograms.

Reversible	Quasi-reversible	Irreversible
$\Delta E_p = \dfrac{59\ mV}{n}$	$\Delta E_p = f(v)$	E_p moved by $\dfrac{30\ mV}{\sqrt{\alpha n}}$, when v is tenfold
$E_p - E_{p/2} = \dfrac{56.5\ mV}{n}$	-	$E_p - E_{p/2} = \dfrac{47.7\ mV}{\alpha n}$
$E_0 = 0.5(E_{pa} + E_{pc})$	$E_0 = 0.5(E_{pa} + E_{pc})$, $0.3 < \alpha < 0.7$	-
$I_{pa} \propto \sqrt{v}$	-	-
$\dfrac{I_{pc}}{I_{pa}} = 1$ for all v	$\dfrac{I_{pc}}{I_{pa}} = 1$ for all v	No reverse peak

Abbreviations: v (scan rate) = dE/dt, in mV s^{-1}, n: number of electrons per reaction step, α: transfer number (usually 0.5)
Table reproduced from ref.231

The Nernst equation is given by:

Equation II-4 $$E_{red} = E_{red}^0 - \frac{RT}{nF} ln \frac{\alpha_{Red}}{\alpha_{Ox}},$$

where E_{red} is the half-cell reduction potential at the temperature of interest, E^0_{red} is the standard half-cell reduction potential, n is the number of electrons per mole of iodine, F is the Faraday constant (96485 C mol^{-1}), and α_{Red} and α_{Ox} is the chemical activity of the reductant and oxidant, respectively. The peak current for a reversible couple (at 25°C), is given by the Randles-Sevcik equation:

Equation II-5 $$i_p = (2.687 \times 10^5) n^{\frac{3}{2}} v^{\frac{1}{2}} D^{\frac{1}{2}} AC,$$

where n is the number of electrons transferred/molecule, A is the electrode surface area (cm^2), C is the concentration (mol cm^{-3}), and D is the analyte diffusion coefficient (cm^2 s^{-1}). Irreversible processes occur as a result of slow electron transfer or secondary reactions of the reduced/oxidised species; redox peaks are often diminished in size and widely separated. Totally irreversible systems are characterised by a shift of the peak potential with scan rate.

The capacitor like behaviour of carbon nanotubes results in a large non-Faradaic cyclic voltammetric response. However, due to the possible redox events that can occur with the (un)filling of the electronic DOS, the observance of related broad features for a heterogeneous SWNT electrode, and more distinct signals from *(n,m)* enriched electrodes was hypothesised. These features are explored in section III. 3.
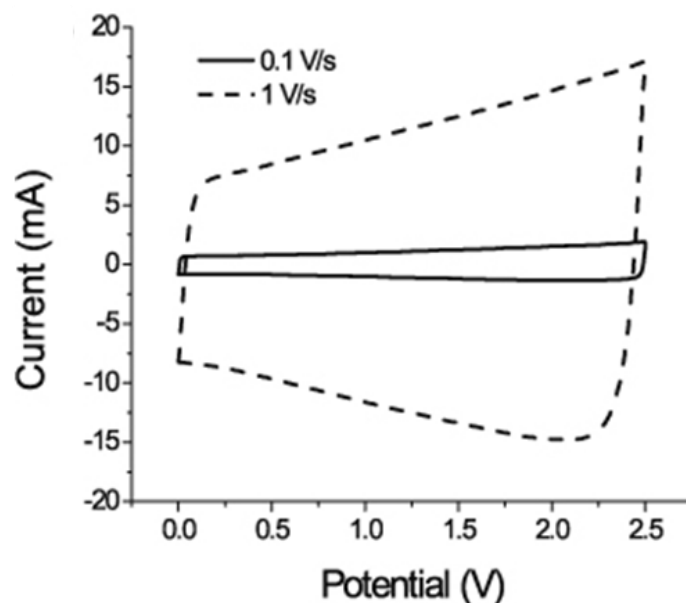
Fig. II-13 Cyclic voltammogram of vertically aligned SWNTs measured in 1 M tetraethylammonium tetrafluoroborate (TEABF$_4$)/propylene carbonate (PC), showing capacitive behaviour. Reproduced from ref. 232.

II. 5. 2. DC potential chronoamperometry/coulometry

Chronoamperometry is the study of current as a function of time, typically from a square-wave voltage signal. The potential step initiates an instantaneous current as a result of a reduction or oxidation reaction and drops as the electrolysis proceeds. Generally, chronoamperometry is used to measure the diffusion coefficients of electroactive species.[228] In the case of SWNT electrodes, the electrode is active (undergoing intercalation, followed by cathodic dissolution). Experiments are performed by fixing the working electrode at a highly reducing potential and observing the current as a function of time over a period of several days. A typical current-time plot (chronoamperogram) is shown in Fig. II-14. Integration of the chronoamperogram (Equation II-6) gives the total charge passed, hence the number of electrons transferred to the SWNTs throughout the process can be determined.

Equation II-6 $$Q = \int_0^t i(t).dt$$
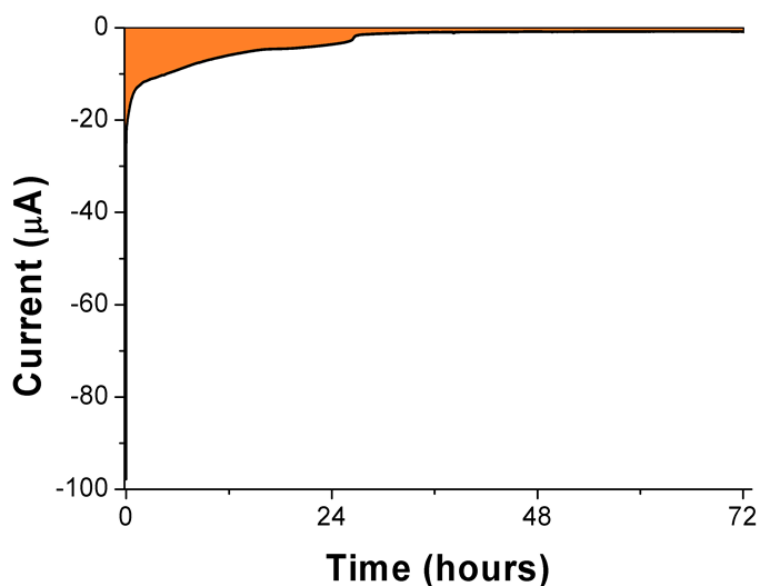
Fig. II-14 Typical current-time plot (chronoamperogram) for a SWNT electrode during electrochemical processing. Here, raw HiPco SWNTs are held at a fixed potential of -2.3 V *vs.* Ag/Ag⁺ for 72 h. The integration of the chronoamperogram (area shaded orange) gives the total charge passed during the reaction. One counter-argument could imply that charge may also be spent on other electrolytic processes (*e.g.* electrolyte degradation, residual moisture/O_2 reduction, *etc.*).

Due to the reactive nature of charged carbons, all electrochemistry was performed using dry, air-free solutions to minimise competing reactions. Non-aqueous electrochemistry utilizes the significantly wider potential stability window compared to aqueous electrolytes (see section III. 2. 4. 3); however, the presence of residual water will cause current to be expended in breaking down water to H_2 and O_2. Amide solvents that are typically used in this research are very difficult to dry due to hydrogen bond formation with water molecules. Karl Fischer coulometric titrations[233] were used to measure the water content of solvents used. The Karl Fischer titration cell used was a diaphragm-less type, consisting of an anode solution containing iodide, methanol, imidazole/diethanolamine (base, RN), and sulphur dioxide. Platinum electrodes (anode and cathode) conduct current through the cell; iodide is electrochemically oxidised to iodine, subsequently reacting with the water in the sample. The end-point of the reaction is reached when all the water present has been reacted with I_2 (consumed in a 1:1 ratio); it is essential that the test samples do not contain species that are likely to cause side reactions with any of the above reagents. The overall Karl Fischer reaction proceeds as follows:[233]

Equation II-7 $CH_3OH + SO_2 + RN \rightarrow [RNH]^+CH_3SO_3^-$

$[RNH]^+CH_3SO_3^- + H_2O + I_2 + 2RN \rightarrow [RNH]^+CH_3SO_4^- + 2[RNH]^+I^-$
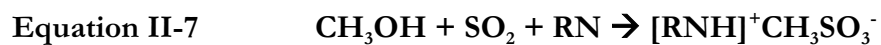
The mass of reacted iodine is given by a rearrangement of Faraday's Law:

Equation II-8 $Q = nFN_A \rightarrow m = \frac{M \times Q}{n \times F}$,

where m is the mass of reacted iodine (g), M is the molar mass of iodine (g mol^{-1}), Q is the measured charge (C), n is the number of electrons per mole of iodine, and F is the Faraday constant (96485 C mol^{-1}).

III. ELECTROCHEMICAL DISSOLUTION OF SWNTs

III. 1. INTRODUCTION

This chapter is primarily focused on the experimental development of the reductive electrochemical dissolution process for SWNTs, investigating various areas of improvement. The key starting area was the implementation of a non-aqueous reference electrode to identify the true electrochemical stability of the electrolytic solutions, followed by a series of fundamental developments to the electrochemical cell glassware, electrode types and electrolytic systems, explored in this chapter.

III. 2. EXPERIMENTAL CONSIDERATIONS AND DEVELOPMENTS

III. 2. 1. SWNT compatibility

Processing and sorting strategies should be compatible with a wide range of SWNTs synthesised by different methods; for future scalability, it is important that the separation of commercial SWNT materials is possible. For these reasons, the main SWNT types used in this research were commercially available products that are ubiquitous among the worldwide research community, specifically HiPco and CoMoCAT SWNTs. Significantly longer ARC-grown and water-assisted CVD "Supergrowth" SWNTs were also used on the basis that these SWNTs are difficult to disperse individually using common processing methods (sonication, centrifugation). However, these SWNTs typically have larger diameters that make their characterisation more challenging.

SWNT materials are obtained in powder form, varying from "fluffy" raw powders to densified powders following acid purification, and vary in SWNT content from < 40% to > 90%; the rest is made up of a large proportion of metal catalyst (most of which remains trapped inside the SWNTs), amorphous and graphitic nanoparticles. Manufacturers tend to offer

different grades of SWNT material; HiPco SWNTs for example, are supplied in three grades (Raw, Purified and Super Purified) that contain increasingly lower metal contents following successive acid or thermal oxidative treatments. Such treatments are not ideal for SWNT sorting processes due to tube shortening and detrimental effects on (opto)electronic properties. Consequently, the majority of SWNTs used in this research were used as-received with no further purification treatments. Table III-1 shows a list of all SWNT types used throughout this research, compiling data obtained from the manufacturer's datasheets as well as in-house experimental data using TGA, optical spectroscopy, and microscopy; further optical spectroscopic characterisation can be found in Appendix VII. 3.

Table III-1 Summary of the SWNTs used in this research.

SWNT type	Batch	Grade	Synthetic process	Manufacturer purification	Metal Catalyst	Metal content (wt %)	Diameter (nm)	Length (µm)	I_G/I_D [c]	
									1.96 eV	2.33 eV
HiPco	R0488	R	CVD	–	Fe	22 [a]	0.8 – 1.2 [b]	0.1 – 1 [b]	9.7	6.6
HiPco	R0550	R	CVD	–	Fe	17 [a]	0.8 – 1.2 [b]	0.1 – 1 [b]	13.1	7.6
HiPco	P0261	P	CVD	Acid purification	Fe	13 [b]	0.8 – 1.2 [b]	0.1 – 1 [b]	11.9	8.9
CoMoCAT	SG0002	R	CVD	Unknown	Co/Mo	10 [a]	0.7 – 0.9 [b]	0.1 – 1 [b]	6.9	6.9
CoMoCAT 65	SG0033	R	CVD	Unknown	Co/Mo	11 [a]	0.7 – 0.9 [b]	0.1 – 1 [b]	7.1	6.9
Carbon Solutions	AP183	R	ARC	–	Ni/Y	23 [a]	~1.4 [b]	0.1 – 1 [b]	7.1	30.6
Hanwha	A-091230 -2	R	ARC	–	Fe	20 [b]	1.3-1.7 [b]	1 – 10 [b]	10.5	36.3
Meijo	SO	P	ARC	Acid purification	Ni/Y	5 [a]	~1.4 [b]	1 – 5 [b]	21.7	51.8
SG	STD2	R	Water-assisted CVD	–	Fe	~0 [a]	1.0 – 4.5 [c,d]	10 – 250 [d]	2.8	3.5

Abbreviations: SG: Supergrowth R: Raw; P Purified; CVD: Chemical Vapour Deposition; ARC: Electric-ARC discharge; [a] from TGA data; [b] from manufacturer's datasheet; [c] from optical spectroscopy (Raman, UV-vis-nIR, PL); [d] from microscopy characterisation (AFM/SEM/TEM).

As-received HiPco and CoMoCAT SWNTs were predominantly used for dissolution as it was possible to observe a mixture of metallic and semi-conducting SWNTs of both small and large diameters with Raman spectroscopy using a combination of 1.96 eV and 2.33 eV laser excitations. For other SWNT types (ARC, SG), problems are introduced due to their larger SWNT diameters; there are several possible *(n,m)* SWNTs with the same diameter, resulting in broad vHS transitions in UV-vis-nIR spectra. Indexing SWNT helicities for these samples is challenging; PL spectroscopy is also hindered, as the detector range does not allow the measurement of large diameter SWNTs (> 1.4 nm), and Raman spectra are difficult to interpret

due to the possible overlap of RBMs with the notch filter (in place to block the intense Rayleigh scattering signal).

III. 2. 2. Cell type

For general electrolytic processes, the initial consideration is the type of electrochemical cell that is used. Initially, a 25 mL three-necked round bottom flask was used, a simple, readily available setup. Subsequent custom-designs were made by Adams & Chittenden Scientific Glass (Berkeley, CA, USA) or by an in-house glassblower, designed for further scalability, multiple electrode insertion or the ability for spectroelectrochemical experiments (Fig. III-1). The most commonly used electrochemical cells were (c) – small volume cell and (d) – large volume cell. Electrochemical cell (c) was used for the majority of cyclic voltammetry and chronoamperometric dissolution/deposition experiments, (d) was used predominantly to test the scalability of the process.
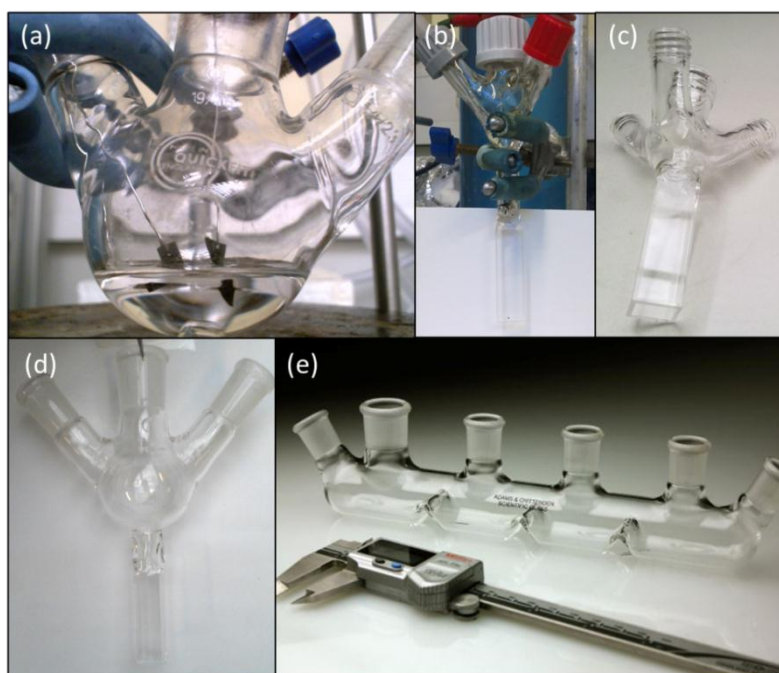
Fig. III-1 Electrochemical cells used during the research. (a) 25 mL three-necked round bottom flask, (b) 3 mL volume cell with four necks and 1 mm path length quartz cuvette attachment (suffered from poor diffusion in cuvette, was expensive to make and very fragile), (c) 7 mL volume cell with four necks and 10 mm pyrex cuvette attachment, (d) 30 mL volume cell (10 mm pyrex cuvette welded to three-necked round bottom flask), (e) 90 mL four compartment cell with 6 necks for multiple electrode insertion offering the potential for simultaneous electrodepositions at different potentials.

The design of the electrochemical cells with a welded cuvette was developed to allow for *in situ* spectroelectrochemistry of the dissolved species. However, at significant reducing potentials the SWNTs become heavily doped such that the transitions between the first and second Van Hove singularities are fully occupied for small diameter SWNTs (~1 nm) as shown schematically in Fig. III-2; for larger diameter SWNTs, the third and fourth vHS transitions are also likely to be doped. However, the design was still well suited to visual observations and measurements of nanotubide concentration.
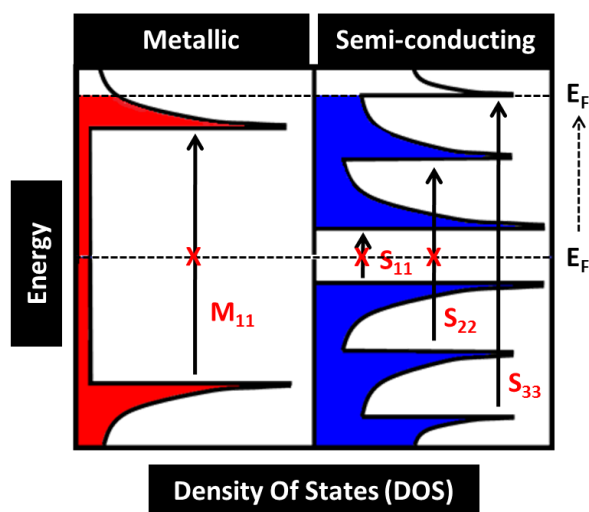
Fig. III-2 Schematic view of the SWNT band structure upon electrochemical charging. Electron doping causes the filling of at least the first metallic (M_{11}) and semi-conducting (S_{11}) vHS transitions, and potentially more depending on the potential shift in Fermi energy (E_F); subsequently, optical spectroscopic characterisation of nanotubides does not reveal these distinct features.

The presence of high energy electrons makes optical characterisations difficult as allowed transitions are only possible for M_{22} or S_{33} vHS that are overlapped by the absorption of air (< 200 nm), and the maximum absorption of non-aqueous solvents used in the process at ~200-300 nm in UV-vis-nIR spectra (*e.g.* DMF, λ_{max} = 270 nm), or simply outside of the detector range. Consequently, *in situ* spectroelectrochemistry revealed featureless UV-vis-nIR spectra, albeit with a rising baseline due to the increased likelihood of scattering events as nanotubide concentrations increase. Nanotubides with electrons in high energy states are highly reactive, increasing the likelihood of SWNT functionalisations; exposure to ambient conditions leads to

either the quenching of these charges to generate neutral SWNT species, or functionalised SWNTs due to reactions of the high energy electrons with atmospheric H_2O, O_2 or CO_2.

III. 2. 3. Electrodes

For general cyclic voltammetry experiments, noble metal electrodes such as platinum or gold are well suited as both working and counter electrodes due to their high electrochemical stability. Carbon electrode materials (refer to Aurbach[234] and references therein) are also commonplace, in the form of glassy carbon, graphitic, disordered and amorphous carbons, fullerenes and diamonds. Carbon nanotube and graphene electrodes are relatively new electrode materials, although their electrode properties are similar to other carbonaceous materials. According to Aurbach,[234] the presence of redox active surface functional groups on carbonaceous electrodes will affect the voltammetric response of the electrochemical system being studied. These electrodes also undergo intercalation/insertion processes with solution species (solvent/ions); usually, smaller cations produce a more pronounced response upon intercalation. Non-graphitic, disordered carbons can undergo both intercalation and adsorption-like processes. Analogous to noble metal electrodes at excessive reduction/oxidation potentials, carbon electrode surface reactions may also occur with solvents, salt ions or other contaminants, in some cases covering them with passivating surface films.[234]

III. 2. 3. 1. Active working electrodes

General electrochemistry is performed at inert electrodes, where a reaction takes place at the electrode surface and the reactants and products are continually depleted/generated depending on the experimental parameters. In this research, nanomaterial working electrodes are active, undergoing intercalation and dissolving into the electrolytic solution.

The electrochemistry of SWNTs has previously been carried out either at a "supported thin layer of nanotubes, a supported single isolated tube, a free-standing bucky paper or even a free-standing single tube."[35] In the previous work, Fogden[152] looked only at thick SWNT films (10-100 μm thickness) known as bucky papers. Bucky papers were produced by dispersing HiPco or CoMoCAT powders in 1,2-dichlorobenzene (DCB) *via* prolonged probe sonication, followed by filtering the suspension through 0.2 μm cellulose acetate membranes. Although the method worked very well for HiPco SWNTs, the CoMoCAT SWNTs were very poorly dispersed, and

were used in the electrochemical cell whilst still attached to the filter membrane; the quality of the paper led to very little dispersion into the electrolyte. The obvious drawback to this procedure was the requirement for ultrasonication, well-known to functionalise (especially in chlorinated solvents), induce defects, and chop the SWNTs.[72, 235]

Preliminary experiments for this thesis were also carried out using the same procedure, substituting DCB for NMP, due to the increased solubility of SWNTs in amide solvents.[71, 236] Better dispersions of the CoMoCAT SWNTs were found using NMP albeit with long periods of ultrasonication. The maximum concentration obtained was ~0.1 mg mL^{-1} (~30 mg in 300 mL NMP) using a Branson Sonifier S-150D at 5 W power output for 1 h. A small piece of bucky paper (~10 mm x 5 mm) was suspended from a platinum wire, connected through a hole pierced in the bucky paper. Although the use of bucky papers had some practical benefits (easy to accurately weigh using TGA balance, uniform thickness and density), often the bucky papers tore quite easily upon the threading of the platinum wire, or fell apart in the electrochemical cell during dissolution (swelling of bucky paper electrodes following intercalation, exfoliation and debundling often led to the loss of cohesive integrity). The addition of a platinum clip (folded platinum foil) improved the contact and hence conductivity of the electrode, however, the structural integrity of bucky paper electrodes throughout the electrochemical dissolution process was still poor. Other drawbacks included difficulties in dispersing different types of SWNTs at sufficient concentrations, without having to process large volumes of organic solvents.

A novel strategy was to perform electrochemistry directly using the as-received SWNT powder; initially using a platinum cup electrode. Whilst results were promising, the significant swelling of SWNT powders caused some undissolved material to overflow the platinum cup and sink to the bottom of the electrochemical cell, contaminating the dissolved fraction. To overcome this issue, a new configuration was designed that allowed the raw powder to be placed at the bottom of the electrochemical cell in contact with a piece of platinum foil in the form of a plunger-type electrode. This approach simplified the process somewhat, allowing SWNTs to be dried under vacuum prior to experiments, and maximised yields by having no loss of SWNT material during the swelling process. Photographs of these electrode configurations are shown in Fig. III-3. For the active powder electrodes, the majority of SWNTs were used as-received. Some powders (*e.g.* raw HiPco) are fluffy and difficult to handle; these were ground using a mortar and pestle for ~5 minutes to form a densified powder. For bucky paper experiments, only the

SWNTs were submersed in the electrolyte due to concerns with electrode reactions occurring at the platinum wire, however, with powder-based experiments, the platinum foil had to be completely submerged in the electrolyte; no effect on the dissolution process was observed.
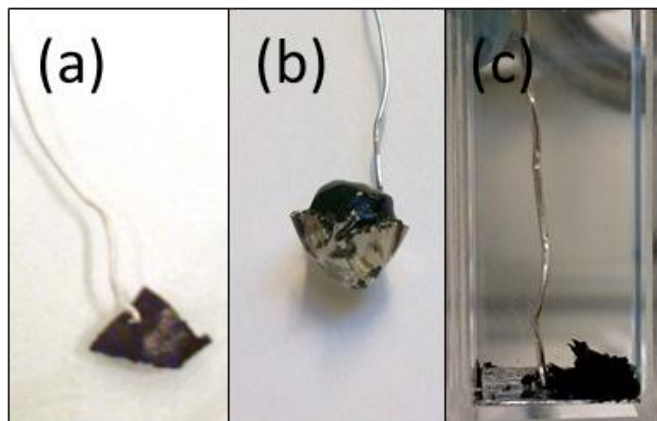
Fig. III-3 SWNT electrode types used during the research. (a) SWNT bucky paper connected to a platinum wire, (b) platinum cup electrode holding SWNT powder, and (c) platinum plunger-type electrode in contact with SWNT powder. The need for ultrasonication to form a bucky paper was avoided by the use of raw SWNT powders in (b) and (c), however, the loss of SWNTs from the platinum cup electrode following the swelling of the SWNT powder during the dissolution process favoured the plunger-type electrode where SWNTs sit at the bottom of the cell. The platinum wire thicknesses are 0.5 mm in each case.

III. 2. 3. 2. Reference electrodes

Most non-aqueous electrochemistry is performed using the $Ag/AgNO_3$ (Ag/Ag^+) redox couple as a reference electrode. This electrode consisted of a silver wire immersed in a filling solution of 0.01 M $AgNO_3$, 0.1 M TBAP in acetonitrile, and was calibrated against the ferrocene/ferricinium (Fc/Fc^+) redox couple. The location of the reference electrode is also very important in this context; for the small volume cells, it can be positioned very close to the working and counter electrodes, in the larger volume cells, the distance between electrodes is significant, and may introduce a significant iR drop. The non-aqueous reference electrode had an electrode potential of ~-0.1 *vs.* Fc/Fc^+ and therefore ~+0.3 V *vs.* NHE (normal hydrogen electrode).[237] *Note: All potentials in this thesis are quoted vs. Ag/Ag$^+$ unless stated.*

III. 2. 3. 3. Counter electrodes

Aside from the potential problems discussed above, carbon nanotubes, either in powder, bucky paper or other form, have a significantly large surface area which presents problems with the required compliance voltage (maximum voltage output of the counter electrode). Counter electrodes are required to swing to extreme potentials to maintain the working-reference electrode potential, typically minimised by having a large surface area *vs.* the working electrode. At such potentials the reduction or oxidation of solvent or supporting electrolyte ions is likely. These reactions introduce various other impurities into the system, which may interfere with nanotubide dissolution as a consequence, either by radical functionalisation or competing redox reactions. Therefore, the counter electrode was separated from the working electrode compartment by placing a platinum wire in a glass tube sealed with a porous Vycor® frit. This frit is chemically inert and prevents the inter-diffusion of the electrolytes in either compartment while providing only a modest resistance to the ionic current, allowing the electrochemical reaction to take place unaffected. With the protected counter electrode, the compliance voltage requirements can be significantly high (±20 V), especially with a working electrode with a very high surface area as discussed above. The compliance voltage issue can be facilitated by increasing the background electrolyte concentration, however, for the stabilisation of SWNT polyelectrolytes, low salt concentrations are critical. The problem was overcome by having a high electrolyte concentration in the counter electrode chamber (~1-2 M electrolytic salt/solvent), ensuring the salt and solvent combination was the same as that being used in the working electrode chamber to prevent any cross-mixing of solvents.

III. 2. 4. Electrolytic systems for electrochemical processing
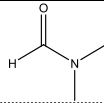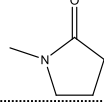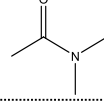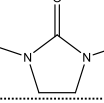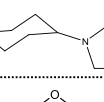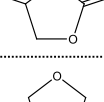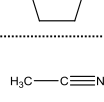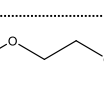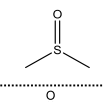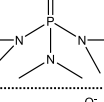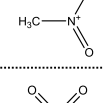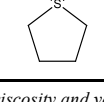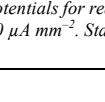
III. 2. 4. 1. Solvents

The ideal solvent for the electrochemical separation of SWNTs would be one which offers a good solubility for nanotubide ions ($SWNT^n$), whilst also having a large potential window, good conductivity, and few impurities. The useful potential range is not only dependent on the solvent, but often limited by the electrode material, supporting electrolyte and temperature. Non-aqueous solvents with high dielectric constants are preferable, because salt dissociation occurs more readily; the solvent should also be readily available, anhydrous, and high purity. The most applicable solvents for the reductive electrochemical processing of SWNTs are listed in Table

III-2. Amide solvents are typically preferred solvents for SWNTs,[210] and were predominantly used in the electrochemical process, especially DMF due to the ability to purchase the anhydrous grade at high purity and low moisture content (< 30 ppm) at relatively low cost.

Other non-amide solvents were tested to investigate the versatility of SWNT dissolution; sulpholane and DMSO are reported to successfully solvate nanotubide species.[128] In the future, it may be possible to observe oxidative dissolution in solvents such as acetonitrile or nitromethane that are highly stable to oxidation. These solvents also have relatively low boiling points that would facilitate sample preparation for analysis and device manufacture.

Table III-2 Physical properties of selected polar aprotic solvents.

Solvent (Acronym)	Structure	Density (g/cm³)	Dielectric constant (ε)	Liquid range (°C)	Viscosity (cP)	Vapour Pressure (kPa)	Potential window (V)	Na⁺/Na electrode potential (V)
N,N-Dimethylformamide (DMF)		0.95 @ 23°C	36.7 @ 25°C	-61 to 153	0.81 @ 25°C	0.49 @ 25°C	-3.0 to +2.0	-2.81
N-Methylpyrrolidone (NMP)		1.03 @ 20°C	32.2 @ 25°C	-24 to 202	1.67 @ 25°C	0.05 @ 25°C	-3.2 to +1.8	-2.87
N,N-Dimethylacetamide (DMA)		0.94 @ 25°C	37.8 @ 25°C	-20 to 165	0.93 @ 25°C	0.17 @ 25°C	–	-2.84
Dimethylethyleneurea [238] (DMEU)		1.05 @ 25°C	37.6 @ 25°C	8 to 220	1.94 @ 25°C	0.50 @ 78°C [239]	–	–
Cyclohexylpyrrolidone (CHP) [240]		1.03 @ 25°C	7 @ 25°C	12 to 304	11.5 @ 25°C	0.05 @ 25°C	–	–
Propylene Carbonate (PC)		1.20 @ 25°C	66.1 @ 20°C	-55 to 242	2.53 @ 25°C	0.16 @ 55°C	-2.9 to +3.4	-2.56
Tetrahydrofuran (THF)		0.89 @ 20°C	7.5 @ 22°C	-108 to 66	0.46 @ 25°C	21.6 @ 20°C	-3.2 to +1.9	–
Acetonitrile (AN)	$H_3C-C\equiv N$	0.78 @ 20°C	36.6 @ 20°C	-45 to 82	0.36 @ 20°C	9.6 @ 20°C	-2.5 to +3.7	-2.56
1,2-Dimethoxyethane (DME)		0.86 @ 25°C	7.3 @ 23.5°C	-58 to 82	0.46 @ 25°C	9.27 @ 25°C	-3.1 to +2.3	–
Dimethylsulphoxide (DMSO)		1.10 @ 25°C	46.6	19 to 189	1.99 @ 25°C	0.08 @ 25°C	-3.1 to +1.6	-2.85
Hexamethyl-phosphoramide (HMPA) [241]		1.03 @ 20°C	30 @ 20°C	7 to 235	3.5 @ 60°C	0.01 @ 30°C	-3.2 to +1.0	–
Nitromethane (NM)		1.14 @ 20°C	35.8 @ 30°C	-29 to 101	0.61 @ 25°C	3.7 @ 20°C	-2.3 to +4.1	-2.45
Sulpholane (TMS)		1.26 @ 30°C	43.3 @ 30°C	28 to 287	10.29 @ 30°C	0.0008	-3.4 to +3.2	-2.75

Note: density, liquid range, viscosity and vapour pressure data from ref. 242 unless stated. All dielectric constants from ref. 243 unless stated. Potential windows taken from ref. 244; potentials for reduction and oxidation of solvents based on a common potential scale (vs. Fc⁺/Fc), obtained by voltammetry at a smooth Pt electrode at 10 μA mm⁻². Standard potentials of Na⁺/Na electrodes in various solvents also from ref. 244, (V vs. SHE in water, 25°C).
– denotes an unknown value.

III. 2. 4. 2. Electrolytic salts

Supporting electrolytes are present in electrochemical solutions to increase the conductivity of the solution, helping diminish the magnitude of the electric field across the bulk electrolytic solution (migration).[245] Generally, high salt concentrations are required in non-aqueous solutions due to the lower conductivity of these solutions compared to aqueous systems.

Typical electrolytic salts with wide electrochemical potential windows comprise cations such as alkali-metals (Li^+, Na^+, K^+) or tetraalkylammoniums (NH_4^+ [ammonium], TMA^+ [tetramethylammonium], TEA^+ [ethyl], TBA^+ [butyl]) and anions such as halides (Cl^-, Br^-, I^-), perchlorates (ClO_4^-), boron/phosphorus tetrafluorides (BF_4^-, PF_4^-), tetraphenylborates (BPh_4^-), *etc*. In general electrochemical experiments, electrolyte concentrations of at least 0.1 M are used;[246] however, to create stable charged-colloidal suspensions of SWNTs, process optimizations led to the discovery that lower salt concentrations were required (~1 mM) in order to avoid flocculation (discussed in section III. 3. 2). Electrolytic salts, although anhydrous when purchased, are difficult to keep dry. Salts were dried by prolonged heating/vacuum treatment and then stored in a dessicator/glove box. Also, some salts may contain unwanted impurities; PF_4^-/BF_4^- for example, may be contaminated by HF that attacks glass, undesirable for the present setup.[234]

III. 2. 4. 3. Removal of water/oxygen and other impurities

Aqueous electrochemistry is not effective for SWNT dissolution since SWNTs are insoluble in water, and the stable potential window is narrow[234] due to cathodic ($H^+ + e^- \rightleftharpoons \frac{1}{2}H_2$) and anodic ($\frac{1}{2}O_2 + 2H^+ + 2e^- \rightleftharpoons H_2O$) limiting reactions that are separated by ~1.3 V.

The electrochemical window of many non-aqueous systems is much wider than that of water, however, these systems can be highly sensitive due to the presence of redox active species such as H_2O, O_2, CO_2, and in some cases N_2 (reactive towards Li metal,[247] typical glove boxes for Lithium handling are argon filled). The presence of water and oxygen is a major contributor to competing reactions or SWNT functionalisations, due to the preferential reduction and oxidation of these species.

For the majority of this research, electrochemistry was performed on a Schlenk line. The main sources of water contamination originate from the electrolytic salts (can be very hygroscopic), SWNT powders (in the form of both adsorbed moisture and oxygen-containing surface

functional groups) and wet glassware. Therefore, before any electrochemical experiment, all glassware was oven dried at ~150°C overnight and further dried under vacuum (connected to Schlenk apparatus) at ~250°C using a heat gun for 30 minutes. Further to these procedures, the as-received anhydrous solvents stored in a solvent cabinet would have been susceptible to the slow leakage of air and moisture over time following the piercing of their septa during cannula or syringe techniques that were used to transfer solvent to the electrochemical cell (~25-50 ppm leakage H_2O per week).[248] For this reason, fresh solvent was regularly purchased (~2-3 months). Dissolved oxygen was removed by bubbling an inert gas (N_2) through the non-aqueous solvent; during all experiments, a positive pressure of N_2 was maintained in the cell to minimise oxygen/water entry. Other impurities such as silicon grease, used to create vacuum tight seals, were problematic during electrode entry and long experiment times that generated yellow coloured solutions upon their electrochemical decomposition; silicon grease was avoided altogether with the use of a screw-threaded electrochemical cell.

Towards the latter part of this research, all electrochemistry was performed inside a nitrogen-filled glove box, with levels of H_2O and O_2 maintained < 1 ppm. Glassware and nanomaterial powders were also vacuum dried on a Schlenk line, sealed and transferred to the glove box before use. Electrolytic solutions were prepared and further dried over molecular sieves (3 Å) for at least 72 hours before use; the storage of all electrodes, electrolytic salts and solvents inside the glove box environment avoided any moisture uptake.

The presence of water has been observed previously to lead to the formation of blister-like structures[249] in HOPG basal planes due to the following side reactions:

Equation III-1 $\quad\quad\quad \mathbf{C_x + 2H_2O \rightarrow C_xO_2H_y + (4\text{-}\mathit{y})H^+ + (4\text{-}\mathit{y})e^-}$ (x = 8-12, y = 1-2)

Equation III-2 $\quad\quad\quad \mathbf{C + 2H_2O \rightarrow CO_2 + 4H^+ + 4e^-}$

Equation III-3 $\quad\quad\quad \mathbf{2\mathit{H}_2O \rightarrow O_2 + 4H^+ + 4e^-}$
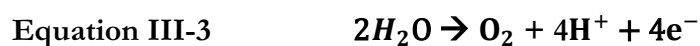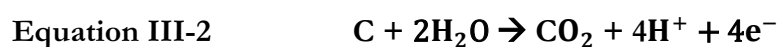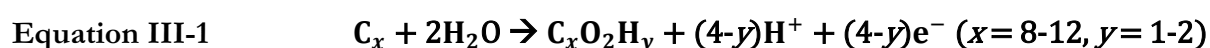
Following intercalation of the electrolyte and water into the HOPG basal plane, blisters form as a result of electrolytic gas evolution at sub-surface active sites, with accompanying electrolytic formation of graphite oxide. The side reactions of water on reduced graphite electrodes should result in similar blister formation. In view of the experimental setup with a separated anode (counter electrode), the reduction of water (Equation III-4) at the working electrode (nanotubide

species) is counter-balanced by the oxidation of OH$^-$ (Equation III-5) at the counter electrode, leaving protonation of nanotubide species as the major route of possible functionalisation.

Equation III-4   **Cathode (reduction): $2\ H_2O_{(l)} + 2e^- \rightarrow H_{2(g)} + 2\ OH^-_{(aq)}$**

Equation III-5   **Anode (oxidation): $4\ OH^-_{(aq)} \rightarrow O_{2(g)} + 2\ H_2O_{(l)} + 4\ e^-$**
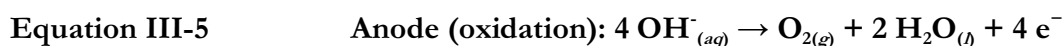
Electrochemical experiments performed on a Schlenk line are intrinsically difficult to keep dry due to the entry of air/moisture upon inserting electrodes and possible leaks *via* electrode threads through rubber septa over the experimental timeframe. Manipulations inside the glove box gave markedly different results; it was presumed there are competing mechanisms between charging and functionalisation. The water content of non-aqueous electrolytes in different atmospheres has been reported recently,[250] comparing electrochemistry of a sealed system in the presence or absence of an inert atmosphere, with experiments performed in external atmospheres of varying relative humidity (Fig. III-4).
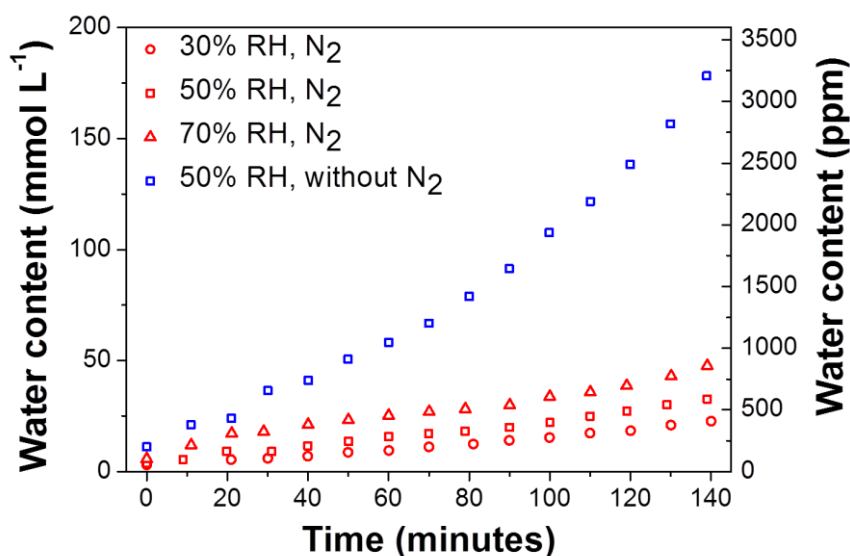
Fig. III-4 DMF moisture uptake in different atmospheres. This plot shows how DMF water content (measured by KF titrations) changes over time when pre-dried DMF (containing 0.2 M Bu$_4$NPF$_6$) was stored in an electrochemical cell under an N$_2$ atmosphere at a fixed flow of 100 cm^3 min^{-1} with an outside atmosphere at different relative humidity values (30%, 50%, and 70%) at 22 ± 2°C (red), and stored in an electrochemical cell with an outside atmosphere at 50% relative humidity at 22 ± 2°C in the absence of an internal N$_2$ atmosphere (blue). Data taken from ref. 250 using Quintessa Graph Grabber.

DMF moisture uptake in an N_2 atmosphere represents experiments on a Schlenk line, the increasing trend is somewhat alarming, since this would suggest that water is always present in the electrochemical cell during the electrochemical dissolution of SWNTs, contributing to competing reactions or SWNT functionalisations. The experimental timeframe for the electrochemical dissolution of SWNTs is significantly longer than the 140 minutes shown here (typically 24 to 120 hours); fitting a linear trend to the data at 30% RH would give a water content of ~200 mmol L^{-1} after 24 hours (~3600 ppm).

With the availability of a glove box towards the latter stages of this project, it became possible to store all solvents and electrolytic salts in an atmosphere of < 1 ppm water and oxygen; the capacity to subsequently maintain the dryness of all electrolytes and perform further drying with the aid of molecular sieves displayed markedly enhanced yields of dissolution and changes to SWNT selectivity compared to previous experiments performed with the Schlenk line. Following these results, Karl Fischer analysis of as-received DMF batches revealed ~8 ppm water content, with no uptake of water in the glove box environment. Electrolytic salt addition increases the water content by a small amount (~3 ppm) for the typical 1 mM concentration (used for dissolution experiments), however, pre-drying electrolytic solutions with 3 Å molecular sieves for 72 hours before use significantly reduced water content to ~5 ppm. The 0.1 M $NaClO_4$ / DMF solution (used for CV experiments) required a period of at least 7 days or multiple drying stages to achieve lower moisture content. The importance of drying glassware is apparent when only vacuum purging sample vials in the glove box antechamber, the water content rises to ~20-30 ppm due to adsorbed surface moisture on glassware.
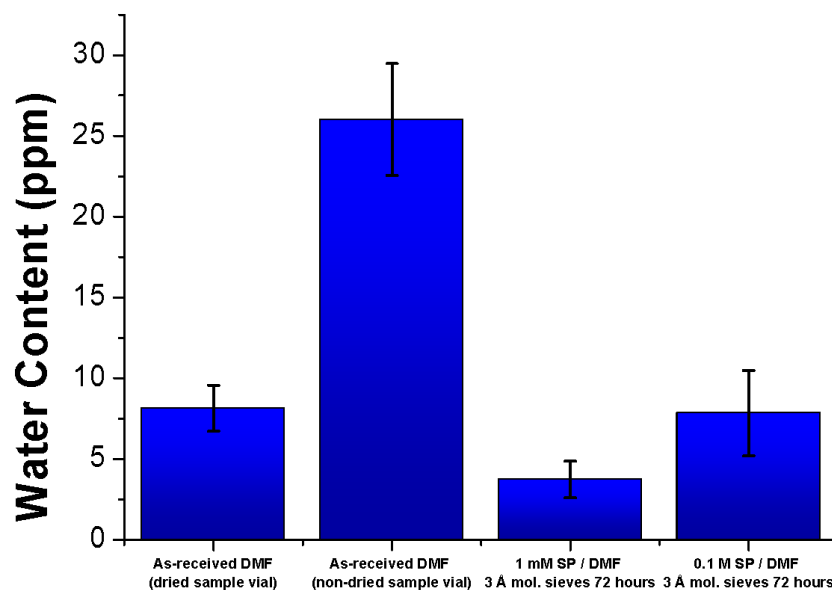
Fig. III-5 Karl Fischer measurements of anhydrous DMF and electrolyte solutions. From left to right: As-received DMF in a dried sample vial (flame dried; vacuum dried in glove box antechamber); as-received DMF in a non-dried sample vial (only vacuum purged in glove box antechamber); anhydrous DMF containing 1 mM sodium perchlorate ($NaClO_4$) dried using molecular sieves; anhydrous DMF containing 0.1 M $NaClO_4$ dried using molecular sieves. Error bars indicate the standard deviation of three sample measurements.

III. 2. 4. 4. Cyclic voltammetry of suitable electrolytes

Previously, Fogden used sodium tetraphenylborate (STPB) as the electrolytic salt in tandem with anhydrous DMF as non-aqueous solvent. Other electrolyte systems were explored in this research to fully examine the cyclic voltammetric behaviour of the SWNT electrodes and also to find suitable electrolytes for producing stable nanotubide dispersions. Electrolytic salts included sodium perchlorate, lithium perchlorate and tetrabutylammonium perchlorate/tetraphenylborate. Typically, electrolyte degradation limits are given as the potential at which the current reaches > 1 mA cm^{-2}. However, due to significantly long reaction times required for dissolution a more rigorous condition was enforced, defining degradation as the point at which the minimal current was no longer constant.

Initial Schlenk line electrochemistry of STPB and TBAP/DMF electrolytic solutions with no SWNTs present showed significantly wide potential windows, stable to ~-2.5 V (*vs.* Ag/Ag$^+$) on the reduction cycle. Beyond these potentials, alkali metal cations are reduced to the alkali metal and plate on to the working electrode; tetrabutylammonium cation reduction generates radical species that decompose immediately to form tributylamine and a butyl radical[234] that is likely to

functionalise the nanotube species. Perchlorate anions were generally preferred to tetraphenylborate due to their higher oxidative stability and provided a stable oxidation window to ~+0.5 V (*vs.* Ag/Ag$^+$) compared to ~+0.25 V (*vs.* Ag/Ag$^+$) for tetraphenylborate.

III. 2. 5. Experimental procedure development

Fogden observed the spontaneous dissolution of SWNT bucky paper electrodes following electrochemical reduction in ~0.01 M STPB/DMF at -2.5 V *vs.* Pt wire pseudo-reference electrode.[152] The proposed mechanism stated that sodium cations intercalate the SWNT bundles generating charged SWNT species, overcoming the relatively strong vdW intertube surface interactions. Tetraphenylborate was chosen as the electrolyte counterion due to the hypothetical ability to stabilise the dispersed SWNTs *via* π-π stacking of the phenyl substituents to the SWNT framework. The electrochemical cell was connected to a Schlenk line to maintain an inert atmosphere throughout experiments, as well as the drying of glassware, STPB electrolytic salt, and the use of cannula techniques to introduce anhydrous DMF to the cell. A slight positive pressure of nitrogen (BOC, standard grade, 99.9% purity) was used in order to prevent oxygen and moisture entry upon inserting/removing electrodes.

Throughout this research, the basic electrochemical procedure has changed significantly; developments included different SWNT electrode types, electrochemical cell geometries, the introduction of a non-aqueous reference electrode, the removal of stirring from the electrochemical process so that electrochemistry was diffusion controlled, and separation of the counter electrode from the working electrode compartment. Also, higher-purity nitrogen gas was used (BOC, zero grade, 99.998% purity), due to concerns with the presence of low level moisture in the standard-grade cylinders. The most significant adaptation to the electrochemical procedure was the transfer of experiments from Schlenk line to glove box. In this section, the experimental results will be discussed as a comparison between the results obtained using both methodologies, followed by a discussion of the mechanisms of the process in each system. The electrochemical setups in different electrochemical cells are shown in Fig. III-6.
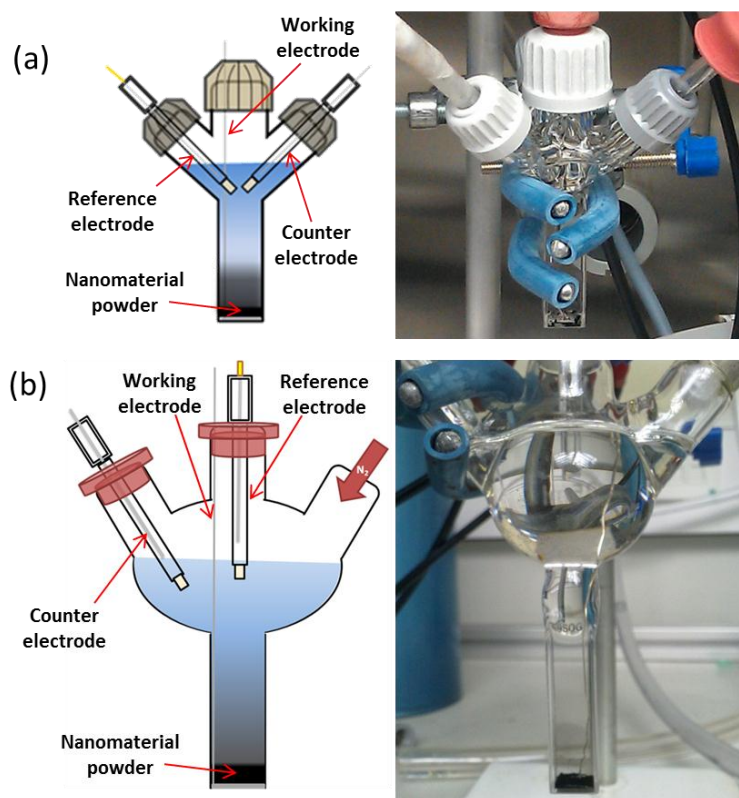
Fig. III-6 Schematic diagrams and photographs of the typical electrochemical setups. (a) Small volume cell used for cyclic voltammetry and dissolution experiments. (b) Large volume cell used for scalability testing.

Optimised experimental procedure

Electrochemical cells were cleaned with ethanol and oven dried (150°C) overnight. SWNT powders were ground using an agate mortar and pestle (if necessary) inside a HEPA-filtered cabinet, weighed, and placed at the bottom of the electrochemical cell; some powders also required de-staticisation prior to handling. The platinum plunger (working electrode) and platinum wire counter electrode were sonicated (bath) in ethanol for approximately 5 min. If any debris remained on the electrodes, the Pt wires were soaked in concentrated nitric acid, neutralised and washed with ethanol again; the electrodes were then dried at 250°C using a heat gun. Working and counter electrodes were threaded through suba-seals; the working electrode was inserted into the electrochemical cell and gently pushed down on to the SWNT powder using wide-tipped tweezers to prevent bending of the Pt wire. The electrochemical cell inlets were sealed with screw-caps/ground glass stoppers. For one inlet, a tap fitting was attached and closed. The tap fitting was connected to a Schlenk line and the electrochemical cell evacuated by carefully opening the tap (some SWNT powders can be sucked into the Schlenk line upon

evacuation, prevented by placing a small piece of glass wool securely in between the tap and the Schlenk tubing). The electrochemical cell containing the SWNT powder was dried *in vacuo* at ~250°C using a heat gun for 30 min and at room temperature for at least 12 h. The tap was closed and the setup transferred to the glove box antechamber. Once inside the glove box, the tap fitting was removed and pre-prepared electrolytic solution added (dried over 3 Å molecular sieves, > 72 h). Following several initial attempts at activating molecular sieves, an effective method was established: 500 g molecular sieves (3 Å) were heated (microwave, 3 min), vacuum dried on a Schlenk line with further heating (400°C, 1 h), and left under vacuum at room temperature for 24 h before transfer to the glove box for storage. Reference and counter electrodes were inserted into the electrochemical cell. During all experiments, the electrochemical cell remained sealed. Finally, electrodes were connected to the potentiostat *via* a glove box feed-through; all wires were clamped in place to prevent any short-circuiting.

Reference and counter electrode preparation

Fritted glass chambers were prepared for reference and protected counter electrodes. A glass tube was cleaned with ethanol and oven dried (150°C) overnight. A small piece of PTFE heat-shrink tubing and porous Vycor glass frit was attached to the narrow end of a glass tube and heated to ~250°C; excess tubing was removed with a scalpel blade. Before using electrodes for the first time it was important to let them stand in their electrolytic solution for at least 24 hours, and were stored in their constituent filling solution when not in use (reference electrode, 0.1 M TBAP, 0.01 M $AgNO_3$; counter electrodes, ~1-2 M electrolytic salt/solvent (depending on salt solubility) to match working electrode compartment). Vycor frits tend to become blocked with nanotube material following several experiments, the ends were gently cut with a scalpel blade to provide a fresh surface.

III. 3. RESULTS

III. 3. 1. Cyclic voltammetry of SWNT electrodes

Cyclic voltammetry (CV) was used to examine the possible redox activity of SWNT electrodes. Several electrolytic salts were tested as discussed in section III. 2. 4. 4. Due to the promising dissolution of nanotubides generated using chemical strategies in DMF, this solvent was primarily used, although others were investigated later. For CV experiments, a 0.1 M electrolyte

concentration was discovered to overcome an inherently large hysteresis present in voltammograms at the typical electrolyte concentrations used for dissolution (1 mM); slow scan rates (< 1 mV s^{-1}) were also required due to the high surface area of the SWNT electrode[251] (> 400-1000 m^2 g^{-1}) and slow movement and intercalation of ions through the dense SWNT network.

Fig. III-7 shows the cyclic voltammetric behaviour of SWNT electrodes in both Schlenk line and glove box environments. Large capacitive charging signals were observed for all SWNTs in a range of different electrolytes during cyclic voltammetry (CV) experiments. Increasing capacitance at more reducing potentials has previously been attributed to sequential electron doping of the semi-conducting SWNTs[252-254] as discussed in section I. 4. 2. It is important to note that at such slow scan rates (< 1 mV s^{-1}), reductive debundling and dissolution is followed by reaggregation (rebundling) on the reverse cycle.

During Schlenk line electrochemical experiments, raw HiPco SWNT electrode CVs revealed the presence of a small pseudo-redox cycle centred at -1.0 V. According to Kavan *et al.* trace water may have a significant effect on the CV of SWNTs;[179] an increase in the faradaic pseudocapacitance of surface oxides was attributed to the presence of trace water upon exposure of a polar aprotic electrolyte (0.2 M LiClO$_4$ in acetonitrile) to the atmosphere. In aqueous media, the charging of surface oxides on SWNTs was found to be pH dependent, schematically represented by Equation III-6:

Equation III-6 $\qquad$ **=C=O + H$^+$ + e$^-$ ⇌ =COH**
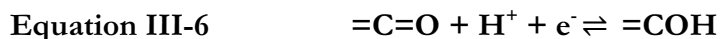
From Fig. III-7c, the presence of trace water is apparent in voltammograms at levels as low as 50-100 ppm. It was expected that the decomposition of water to gaseous H$_2$ may result in the complete removal of moisture, however, trace water and its decomposition products are not removed following 10 cycles, indicating these species are always present in SWNT electrochemical processes.

Compared to CVs performed inside the glove box, the presence of the broad pseudo-redox feature was observed for HiPco SWNTs but not at all for Supergrowth (SG) SWNTs; this feature may correlate to oxygen-containing functional groups on the SWNT surface, defect concentration and amorphous carbon content, all of which are significantly higher in the HiPco SWNT samples compared to SG SWNTs.
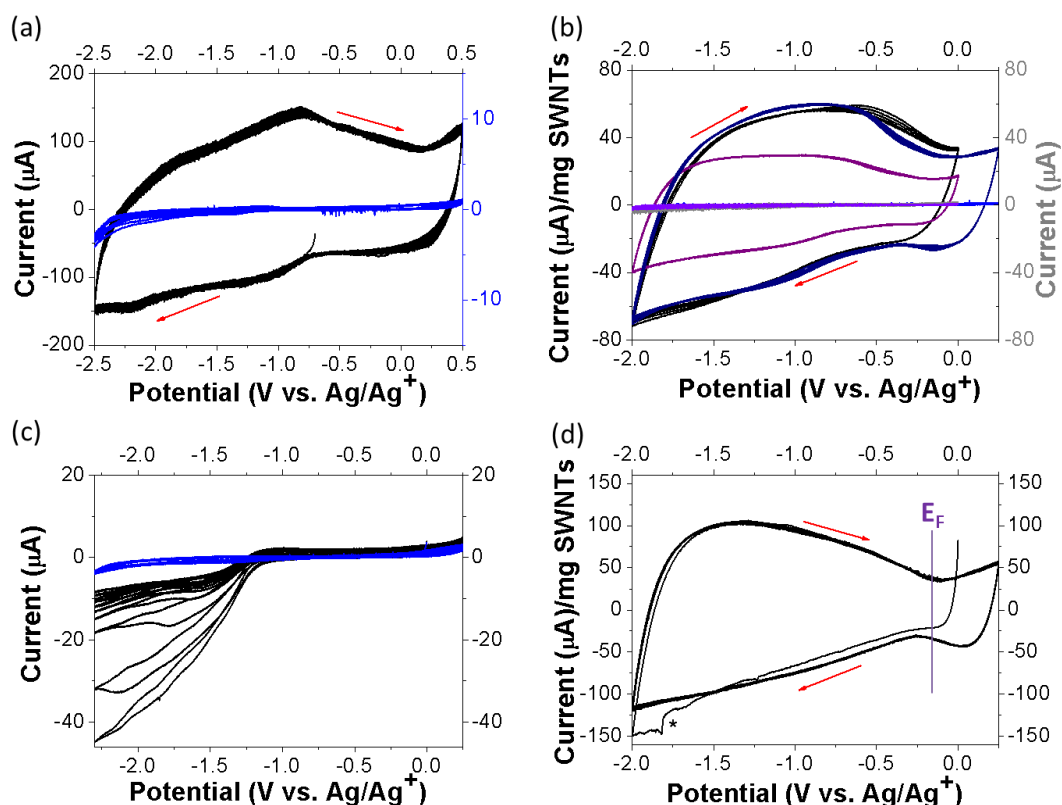
Fig. III-7 Cyclic voltammetry (CV) experiments performed on the Schlenk line and in the glove box. (a) Schlenk line CV of HiPco bucky paper in 0.1 M TBAP/DMF, 30 cycles, 10 mV s^{-1}. A control CV (blue line) was carried out under the same conditions (refer to scale on right y-axis). (b) Glove box CV of a raw HiPco SWNT powder electrode in 0.1 M STPB/DMF at scan rates 1 mV s^{-1} (black) and 0.5 mV s^{-1} (purple), and a raw HiPco SWNT powder electrode in 0.1 M TBAP/DMF at a scan rate of 1 mV s^{-1} (navy). The grey, violet and blue CVs are the respective control of a Pt wire and plate working electrode with no SWNTs present. (c) Glove box CV of Pt wire working electrode in 0.1 M TBAP/DMF electrolytes containing ~50-100 ppm moisture (black) and ~10 ppm (dried with 3 Å molecular sieves, 72 h) (blue) respectively, 10 cycles, 1 mV s^{-1}. (d) Glove box CV of a Supergrowth SWNT powder electrode in 0.1 M NaClO$_4$/DMF at a scan rate of 1 mV s^{-1}, 5 cycles (black). * indicates the first cycle, where swelling of the SWNT electrode takes place; the approximate position of the Fermi level is shown by the purple line.

The charging of SWNTs of defined chiralities was first observed for Meijo SWNTs very recently,[180] whereby specific vHS features (*(17,3)* S$_{11}$ – HOMO/LUMO energies) were observed using CV; metallic SWNTs on the other hand showed purely capacitive behavior. The CV experiments presented here for Meijo and CoMoCAT SWNTs (Fig. III-8), also reveal the appearance of multiple broad features below ~-0.25 V, which can be attributed to the

un(doping) of the large number of distinct *(n,m)* species that are present. Meijo SWNTs have well defined diameters and have high proportions of the *(17,3)* sc-SWNT according to ref. 180, whilst CoMoCAT SWNTs are predominantly *(6,5)* species. Both SWNT electrodes gave distinct voltammograms, with a broad region of low capacitance near 0.0 V, giving a resulting dumbbell shape at positive and negative voltages in line with the band gaps of the sc-SWNTs present in these samples as shown in Fig. III-8. The observation of further broad features at increasing reduction potentials relates to the filling of the first few vHS of the electronic DOS; the first derivative of these cycles also further highlight these features (Fig. III-8b), and intersect at a point that appears to correspond to the electrode Fermi level.

The Fermi level of the Meijo SO electrode is positioned at ~-0.050 V *vs.* Ag/Ag$^+$, which is significantly different to that previously reported (~-0.4 V *vs.* Ag/Ag$^+$), suggesting major influence from the different solvent, electrolytic salt and scan rates used (1 M TEMABF$_4$ in PC, 5-100 mV s^{-1}). For the CoMoCAT65 electrode, the locus of the Fermi level is at ~+0.007 V *vs.* Ag/Ag$^+$ (~+0.3007 V *vs.* NHE). The energy of the first oxidation event for the *(6,5)* species is positioned at ~+0.551 V *vs.* Ag/Ag$^+$ (~+0.851 V *vs.* NHE), in excellent agreement with previously reported oxidation potentials using chemical doping (~+0.8 V *vs.* NHE).[255]
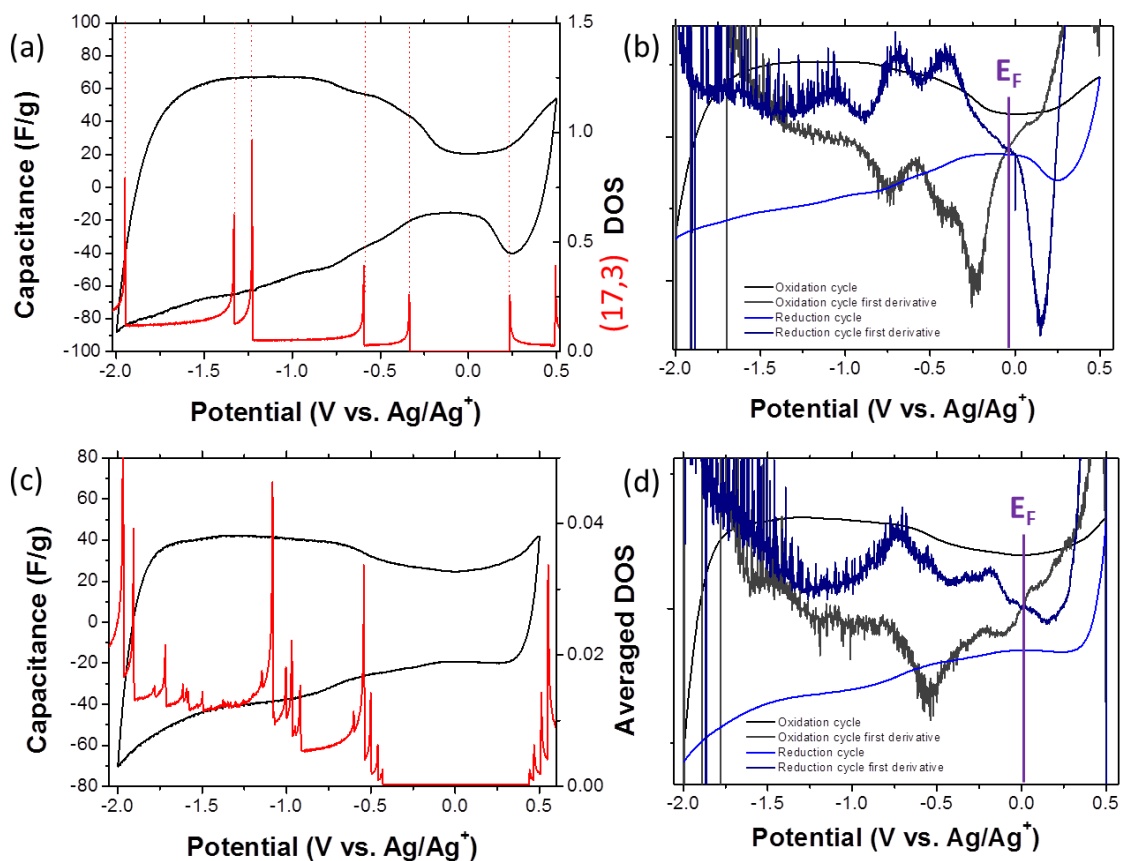
Fig. III-8 CVs of SWNT electrodes showing broad features related to their electronic DOS. (a) 0.5 mV s^{-1} scan of a Meijo SO SWNT electrode in 0.1 M NaClO$_4$/DMF, with the *(17,3)* DOS overlapped. This SWNT type is reported[180] to be the most abundant species in the Meijo SO sample. (b) First derivative of the reduction and oxidation cycles in (a). The potential at which the derivative curves overlap is assumed to be the Fermi level, E$_F$, ~-0.050 V. (c) 0.5 mV s^{-1} scan of a CoMoCAT65 SWNT electrode in 0.1 M NaClO$_4$/DMF, with the averaged DOS for all species present in the sample overlapped. Each sc-SWNT species is weighted towards their total abundance from PL and m-SWNTs from ref. 256. (d) First derivative of the reduction and oxidation cycles in (c) giving E$_F$ ~+0.007 V. In both (a) and (c), the DOS of the SWNT are adjusted to the measured E$_F$ from the derivative plots. DOS data from ref. 257.

III. 3. 2. Chronoamperometric dissolution

Dissolution of SWNTs was not observed when bucky paper or powder electrodes were left to sit in DMF based electrolytes for several days; at fixed reducing potentials of at least -1.6 V (*vs.* Ag/Ag$^+$), the charge density is high enough and the electrolyte concentration low enough, that an electrostatically-stabilised colloid forms. Significant swelling of the SWNT electrode is followed by black coloured trails leaving the electrode after a short period of time (Fig. III-9a-b), without stirring, heating or sonication. During this process, SWNTs are charged and reduced to

nanotubide species that spontaneously debundle and dissolve into the electrolyte driven by electrostatic repulsion.

Fogden's previous investigations showed remarkable preference for the dissolution of large diameter metallic SWNTs, unfortunately, dispersions were not stable under the inert atmosphere provided by the Schlenk line. Also, yields were relatively small over a 3–24 h timeframe, and the electrode potentials were relative to a platinum wire pseudo-reference electrode, susceptible to drifting over time. Further dissolution experiments were performed in order to reproduce the selective dissolution, understand the mechanisms that led to the observed selectivity, and discover how discrimination could be further enhanced. Experiments were performed at different potentials, electrolyte concentrations, electrode configurations (bucky paper/powder) and longer reaction times to identify optimal conditions for the electrochemical dissolution process.

Once the electrolyte degradation window was determined for the DMF-based electrolytes with the non-aqueous reference electrode ($\sim$-2.5 V *vs.* Ag/Ag$^+$), it was possible to fine tune the process. A reducing potential of -2.3 V gave the most significant yields without degrading the electrolyte; at reducing potentials greater than -2.5 V, the electrolyte generated a yellow colour, indicating decomposition. The potentials required for nanotubide dissolution did not vary with the specific electrolytic (salt or solvent) system used. Other than DMF, a range of electrochemically-stable solvents, including propylene carbonate (PC), gave similar results (Table III-3), although their respective nanotubide concentrations were not measured. In DMF, nanotubide dissolution was not observed when electrolyte concentrations were > 0.1 M, highlighting the formation of charge-stabilised colloidal systems that become destabilised at high counterion concentrations due to the contraction of the Debye screening length.[258] The typical electrolyte concentration of 1 mM correlates to a Debye length of $\sim$6.7 nm in DMF[259] (ε = 36.7, 298 K). For HiPco SWNTs (average length $\sim$340 nm), this Debye length would allow a maximum concentration of $\sim$9.25 mg mL^{-1} based on several assumptions (*i.* linear packing, *ii.* $\sim$100 C atoms nm^{-1} SWNT length if d $\sim$1 nm). Electrochemical dispersions kept inside a glove box were stable for more than 6 months (Fig. III-9c). Upon exposure to air, precipitation was observed within seconds for alkali-metal based electrolytes (Fig. III-9d). Dispersions in tetrabutylammonium based electrolytes were stable for up to 5 days, likely, due to additional steric stabilisation of the bulky *n*-butyl chains of the TBA$^+$ ions.
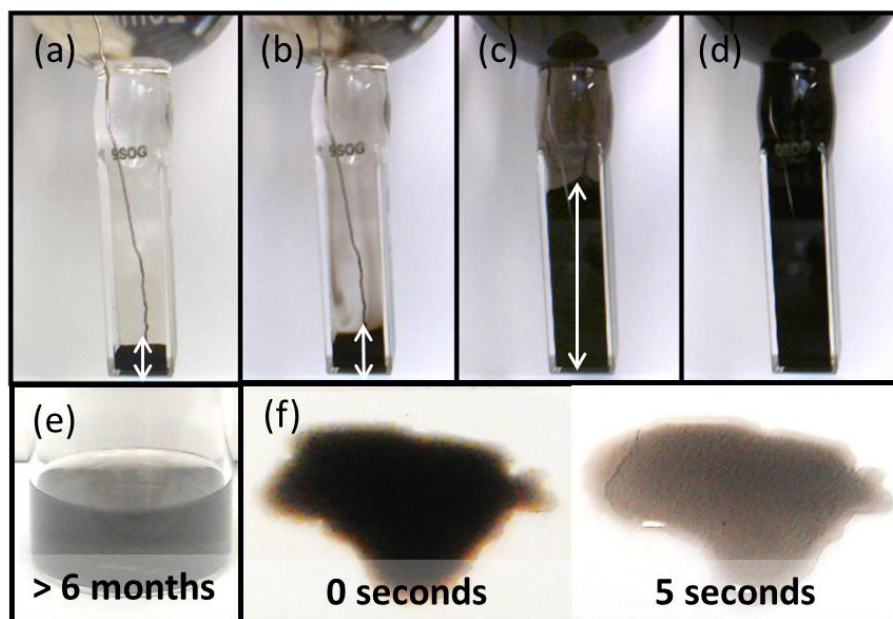
Fig. III-9 Overview of the electrochemical dissolution process. (a-d) Electrochemical dissolution of raw HiPco SWNT powder starting material in 1 mM TBAP in DMF at -2.3 V *vs.* Ag/Ag⁺ over 5 days. The white arrows indicate the significant degree of swelling of the SWNT powder bed. (e) Under inert conditions the electrochemical dispersions were stable for several months; (f) upon exposure to air, the dispersions in alkali-metal based electrolytes were only stable for ≤ 5 seconds due to rapid charge-quenching/functionalisation and subsequent reagglomeration.

Table III-3 Solvents for the electrochemical dissolution of nanotubide.

Solvent	Reported solubility of neutral SWNTs in solvent (mg mL⁻¹) [210]	Electrochemical dissolution of SWNT^{n-}	
CHP	3.5	✓	
NMP	0.116	✓	
DMEU	0.083	✓	
DMA	0.041	✓	
DMF	0.023	✓	(> 1.5 mg mL⁻¹)
PC	-	✓	
DMSO	-	✓	
THF	-	✗	
AN	-	✗	
DME	-	✗	

- not reported, or reported to be low; ✓ spontaneous dissolution; ✗ no dissolution observed
Note *The observed solubility of nanotubide in DMSO has previously been attributed to the decomposition of DMSO in the presence of nanotubide.*[144]

Electrochemical dissolution of SWNTs performed on both the Schlenk line and in the glove box gave markedly different yields of dissolution (Schlenk line: ~5-15 wt %; glove box: up to 100 wt %) that inherently led to differences in the nature of the dissolved material. In this section, the two strategies will be discussed separately, to highlight key issues surrounding the subject.

III. 3. 2. 1. Schlenk line dissolution experiments

Following the electrochemical dissolution procedure, DMF dispersions were exposed to the ambient atmosphere. Quenching/functionalisation caused SWNT agglomeration within a short space of time (hours to days depending on the electrolyte used); upon redispersion of these agglomerated SWNTs in 1 wt % surfactant (typically SC, DOC, SDBS, or SDS) in D_2O using ultrasonication (150 W, 30 min), featureless spectra were always observed. The lack of any absorption and PL spectra meant that Raman spectroscopy was the principal bulk characterisation tool available to identify any changes in metallic/semi-conducting content, or changes in SWNT diameter distribution.

Initial dissolutions using the Schlenk line typically showed dissolved fractions containing increased proportions of large diameter metallic species for both HiPco and CoMoCAT starting materials concurrent with Fogden's results, with the added benefit of improved dispersion stability using TBAP/DMF electrolyte. In combination with "metallic enriched" fractions, Raman spectra also showed a significant enhancement of the D peak, signifying a large increase in SWNT defects or functionalisation, or the presence of other amorphous/sp^3 carbons at higher concentrations relative to SWNT species. Initial hypotheses were that smaller impurities would be intrinsically less entangled and able to freely diffuse away from the SWNT electrode. Raman spectroscopy of small fractions collected at different time stages (Fig. III-10) allowed the study of changes in RBMs and the contribution from defects, impurities, or functionalisations. For both HiPco and CoMoCAT SWNT materials, initial fractions contained low concentrations of SWNTs, with little evidence of any RBMs and a significant enhancement of the D peak. Over time, RBMs intensified, inverse to the D peak that decreased over time although never reaching the same level as the starting material. Consequently, undissolved materials typically had a lower D peak contribution than the starting material, in accordance with purification.
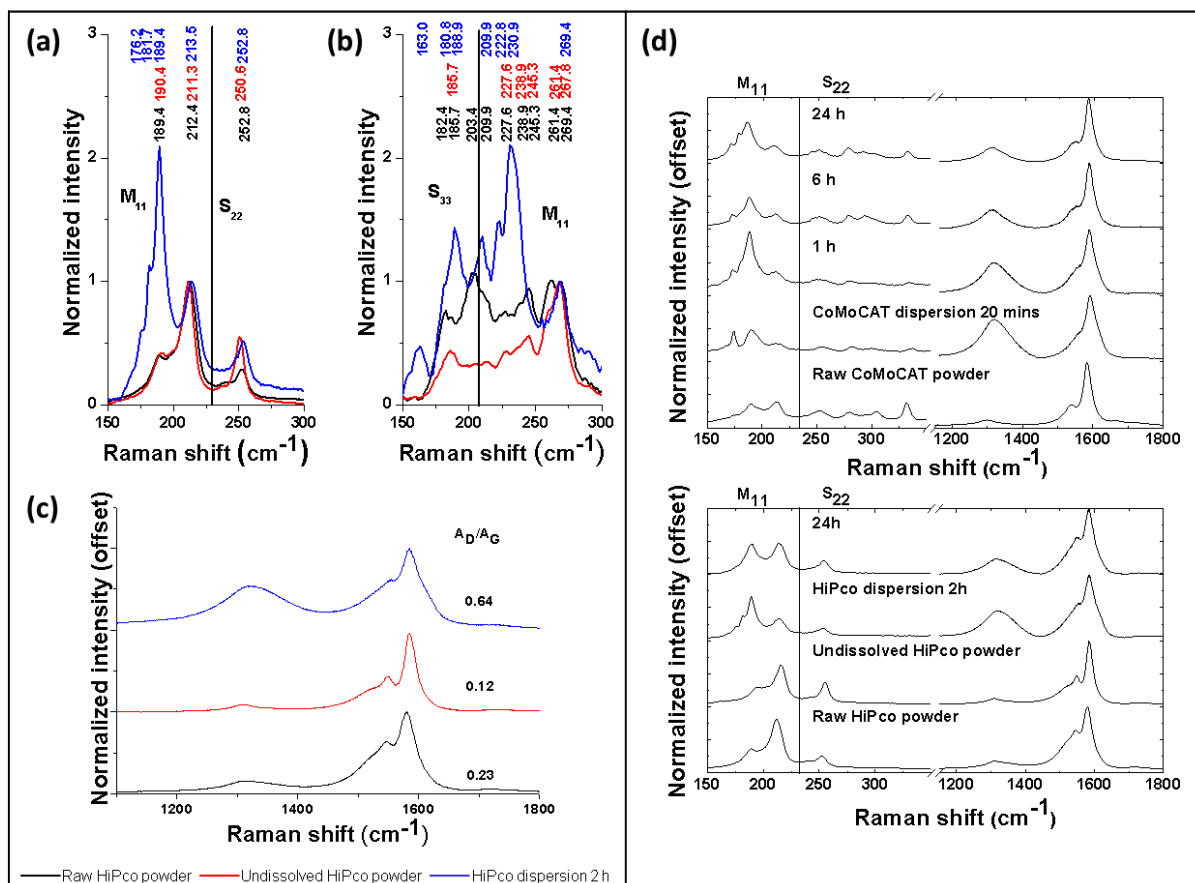
Fig. III-10 Raman spectroscopy of electrochemically dissolved SWNT fractions. (a) Raman analysis of raw, undissolved and electrochemically dissolved (-2.3 V *vs.* Ag/Ag$^+$) HiPco SWNTs using E_{laser} = 1.96 eV. Each spectrum is an average of 5 scans at different positions. Intensities are normalized to the RBM at ~212 cm^{-1}. RBM intensities were fitted to Lorentzian curves for analysis of m-SWNT : sc-SWNT content. Divisions between the M$_{11}$ and S$_{22}$ regions are highlighted. (b) Raman analysis of raw, undissolved and electrochemically dissolved (-2.3 V *vs.* Ag/Ag$^+$) HiPco SWNTs using E_{laser} = 2.33 eV. Each spectrum is an average of 5 scans at different positions. Intensities are normalized to the RBM at ~269 cm^{-1}. Divisions between the S$_{33}$ and M$_{11}$ regions are highlighted. (c) A$_D$/A$_G$ analysis of the raw, undissolved and electrochemically dissolved HiPco SWNTs using E_{laser} = 1.96 eV. (d) Raman analysis of CoMoCAT and HiPco electrochemical dispersions over 24 hours (-2.3 V *vs.* Ag/Ag$^+$) with E_{laser} = 1.96 eV. Each spectrum is an average of 5 scans at different positions. Intensities are normalized to the G peak in each case. CoMoCAT RBM intensities are multiplied by 3 for clarity.

Table III-4 RBM analysis of raw, undissolved and electrochemically dissolved HiPco SWNTs as plotted in Fig. III-10a-b.

Raw HiPco ω_{RBM} (cm^{-1})	Undissolved HiPco ω_{RBM} (cm^{-1})	HiPco dispersion after 2 hours ω_{RBM} (cm^{-1})	Diameter (nm)	(n,m) assignment	Transition
			E = 1.96 eV		
-	-	176.2	1.37	(10,10)	M$_{11}$
-	-	181.7	1.32	(15,3)	M$_{11}$
189.4	190.4	189.4	1.26	(12,6)	M$_{11}$
212.4	211.3	213.5	1.12	(11,5)	M$_{11}$
252.8	250.6	252.8	0.94	(10,3)	S$_{22}$
			E = 2.33 eV		
-	-	163.0	1.49	(17,3)	S$_{33}$
182.4	-	180.8	1.32	(13,6)	S$_{33}$
185.7	185.7	-	1.29	(14,4)	S$_{33}$
-	-	188.9	1.27	(16,0)	S$_{33}$
203.4	-	-	1.17	(13,3)	S$_{33}$
209.9	-	209.9	1.13	(11,5)	M$_{11}$
-	-	222.8	1.06	(13,1)	M$_{11}$
227.6	227.6	230.9	1.04	(9,6)	M$_{11}$
238.9	238.9	-	0.99	(10,4)	M$_{11}$
245.3	245.3	-	0.96	(7,7)/(11,2)	M$_{11}$
261.4	261.4	-	0.90	(8,5)	M$_{11}$
269.4	267.8	269.4	0.87	(9,3)	M$_{11}$

The defect concentration in the dissolved material (Fig. III-10c) (as indicated by an increased peak area ratio A_D/A_G), was greater than that in the raw material, whilst that in the undissolved material was correspondingly lower, suggesting a separation on the basis of purity. The effect is strong, offering a factor of two improvement in A_D/A_G ratio for the undissolved material after 24 hours. Observations over a period of 24 hours for both CoMoCAT and HiPco SWNT dispersions showed a declining defect content in the dissolved fraction over time (Fig. III-10d). The result rules out ongoing functionalisation as a primary dissolution mechanism, instead suggesting that impurities such as amorphous carbons, graphitic (metal-containing) nanoparticles and short/defective SWNTs are reduced preferentially and/or diffuse away from the working electrode more rapidly; subsequently, purer SWNT material dissolves progressively. These purification trends were confirmed with TGA (Fig. III-11) and AFM (Fig. III-13a) analysis. Following sequential dissolutions, the dispersions contained significantly lower amounts of amorphous, graphitic and metal catalyst debris; after electrochemical treatment, both HiPco and CoMoCAT powders showed an increased peak combustion temperature and lower residual

metal content in the undissolved fraction. This removal of amorphous carbons and other impurities provides a new purification route for raw SWNT powders, an alternative to more conventional, but destructive, liquid and gas-phase oxidation or plasma treatments.[67] However, a significant reduction in metal content was not observed due to significant amounts of metal that remains trapped within the nanotubes during this mild process (no end chopping).

According to resonant Raman mapping of HiPco SWNTs[200] (Fig. II-4a), a total of 45 distinct *(n,m)* SWNT species were observed. Only ~40-50% of these species resonate with the 1.96 eV laser while ~20-30% resonate with the 2.33 eV laser, with some species common to both excitations. Resonant Raman mapping of CoMoCAT SWNTs[256] highlighted 25 *(n,m)* species, ~45% resonate with the 1.96 eV laser whilst ~45% resonate with the 2.33 eV laser, although the significant proportion of *(6,5)* species means the majority of resonant SWNTs make up a very small fraction of the sample (< 10%). Debundling effects may further reduce these proportions as resonance profiles narrow, as well as possible RBM frequency shifts with functionalisation.[202, 203] Furthermore, with only five spectra recorded for each sample at random locations, material inhomogeneity may induce statistical errors; as a result, the measurement of RBM intensities using two laser excitations is not sufficient to give concrete evidence of a selective dissolution process, although it can give an overview of trends in electronic type and tube diameter.[203] m-/sc-SWNT content, for example, was calculated semi-quantitatively by measuring the integral area of both the M_{11} and S_{22} regions using Lorentzian fitted peaks of the RBMs; whilst not an absolute measure, these values are useful for relative comparisons. Peaks were then indexed to specific *(n,m)*-SWNT types using a Kataura plot.[37] Fig. III-10a-b indicate significant m-SWNT enrichment of raw HiPco SWNTs with both laser excitations; most notably with 1.96 eV excitation, the relative m-SWNT region signal intensity more than doubled in the material dispersed after 2 hours, with a large intensification of the *(12,6)* metallic signal (189.4 cm^{-1}). Results also highlighted a preference for dissolving larger diameter m-SWNTs with the appearance of peaks at 176.2 cm^{-1} *(10,10)* and 181.7 cm^{-1} *(15,3)*. With 2.33 eV excitation, there was significant enrichment of the *(9,6)* m-SWNT (230.9 cm^{-1}), but also some large diameter sc-SWNTs, *(17,3)*, *(13,6)*, and *(16,0)* [163.0 cm^{-1}, 180.0 cm^{-1}, and 188.9 cm^{-1} , respectively]. Importantly, the undissolved HiPco powder, after the electrochemical process, showed a complementary increase in sc- and small diameter m-SWNTs with both excitations, providing confirmation of a genuine selective dissolution process.

The SWNT selectivity of the dissolution process also evolves with time. Early fractions showed the enrichment of larger diameter m-SWNTs; after longer periods of time, smaller diameter m-SWNTs also dissolved, followed by larger diameter sc-SWNTs. The gradual shift to dissolving sc-SWNTs is expected to occur as m-SWNTs are depleted from the powder bed. For example, for CoMoCAT dispersions (Fig. III-10d), an increase of the M_{11} region from a relative measure of 51% m-SWNTs in the as-received material, to 79% after 1 hour was observed. After 24 hours, with the depletion of the initial metallic species, there was an increase in dissolution of sc-SWNTs as shown by an enhancement of peaks in the S_{22} region, lowering the apparent m-SWNT content to 68%. Similarly, the enrichment to 87% m-SWNTs observed in HiPco after 2 hours (Figure 3b), falls to 79% after 24 hours. Observations of m-SWNT enrichment are supported by changes in the G peak lineshape. Made up of two components: G^- (~1550-1570 cm^{-1}) and G^+ (~1590 cm^{-1}), the lineshape of the G^- peak becomes broad and asymmetric with increasing m-SWNT content moving away from a characteristic Lorentzian for sc-SWNTs to a Breit–Wigner–Fano (BWF) lineshape for m-SWNTs.[260] This broadening occurs as expected for early dissolved fractions with more m-SWNT content (Fig. III-10c), becoming sharper as more sc-SWNTs are dispersed over time.

Identifying the mechanism of this observed selectivity is far from simple; the most obvious argument may be the dielectric differences leading to the preferential charging of metallic SWNTs that can screen the electric field. On the other hand, we may be witnessing a selective functionalisation of the nanotubide species with electrolyte species or trace water. Whilst, in principle, there is a possibility for nanotubide to react as a nucleophile with DMF to produce formyl moieties on the SWNT surface,[124, 261] such a reaction can be ruled out in the present case for a number of reasons. Firstly, vacuum annealing of the m-SWNT enriched fractions at various temperatures (350, 450, 550°C), a process known to regenerate RBMs suppressed by covalent functionalisation,[205] does not alter the measured spectra. Secondly, the electrostatic (anionic) rather than steric (functionalised) stabilisation of the dispersed SWNTs was confirmed by the sensitivity to high electrolyte concentrations and air exposure. Thirdly, the dissolution phenomenon was observed in a wide range of solvents and electrolytes, including those without obvious reactive pathways. Lastly, the evolution of the D peak, demonstrates a purification effect inconsistent with ongoing functionalisation chemistry, although functionalisation from moisture cannot be completely ruled out since the effect of functionalisation may be weaker than the

purification effect. Also, vacuum/heat treatment of these SWNTs may not result in annealing, but may leave behind further defect sites following the generation of oxidative species as discussed in section I. 3. 2. 3.

Sample	Degradation Onset Temperature (^{o}C)	Metal Catalyst (Oxide) Remaining (wt%)
Raw HiPco	340	32.3
Undissolved HiPco	350	29.8
Raw CoMoCAT65	425	15.9
Undissolved CoMoCAT65	445	11.0
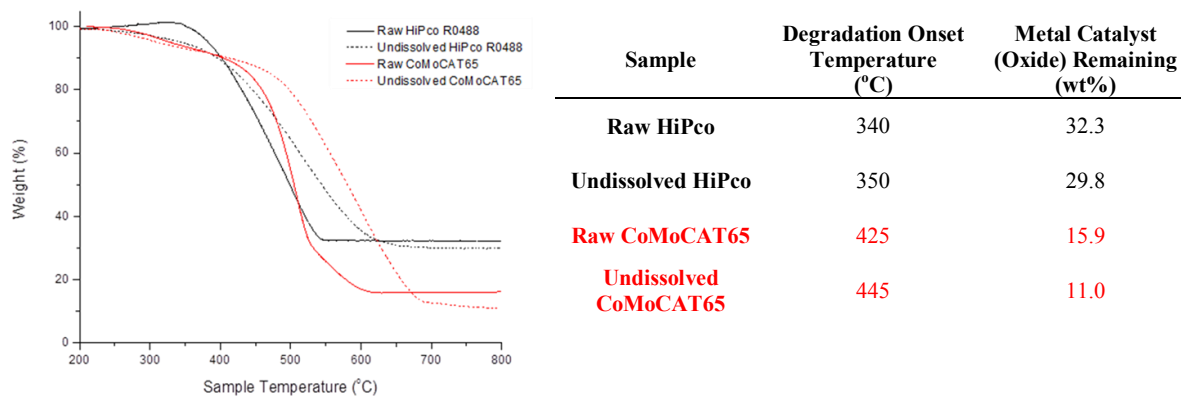
Fig. III-11 TGA of SWNT powders before and after electrochemical purification. Here, only partial dissolution was achieved (~5 wt % yield). The reduction in metal content after the dissolution process is expected to result from the direct dissolution of free metal, or graphitic-coated metal catalyst particles. Metal catalyst particles present inside the SWNTs are not removed due to the milder procedure that does not induce end chopping observed with sonication and acid oxidation treatments.

TEM (Fig. III-12) and AFM (Fig. III-13) were used to visualize the extent of SWNT individualisation throughout the electrochemical dissolution process. Electrochemical dispersions produced on the Schlenk line mostly exhibited small bundles of SWNTs in the presence of significantly large amounts of amorphous/graphitic/metallic debris. This aggregation of SWNTs was presumed to be a consequence of neutralisation/functionalisation and subsequent rebundling during sample preparation in atmospheric conditions. The large amount of impurities was likely to be higher due to the low process yields and their preference for dissolution. Whilst the electrochemical dissolution does not shorten SWNTs, evidence of cutting following heat treatment was observed using AFM (Fig. III-13a), likely to be a consequence of the presence of hydroxide species generated following exposure of electrochemically dissolved fractions to ambient conditions. Following these observations, heat treatments were avoided and further washing steps were introduced (soaking AFM samples in water or ethanol for 24 h).
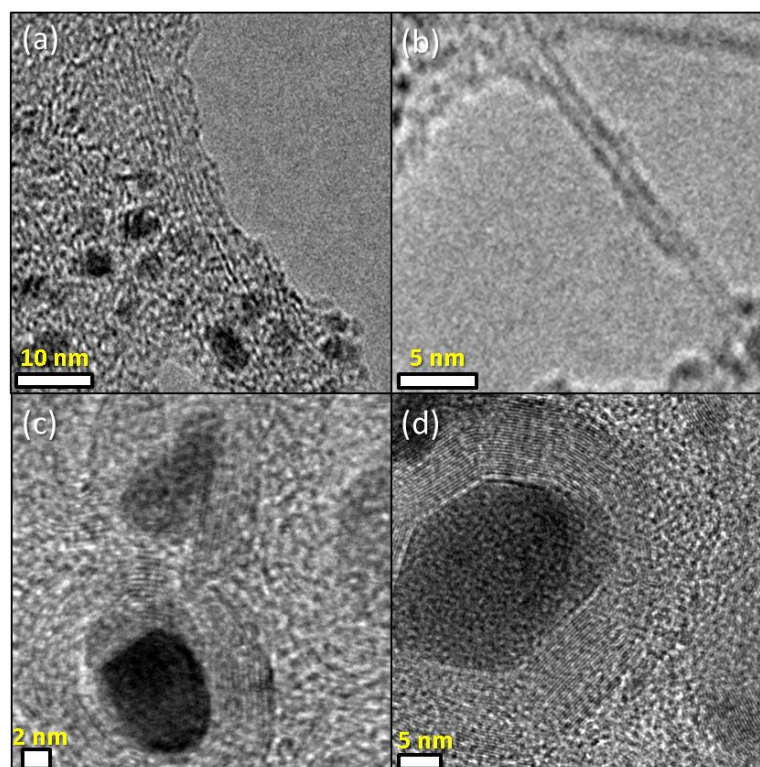
Fig. III-12 TEM images of electrochemical dispersions performed on the Schlenk line. (a) and (b) Raw HiPco SWNT dispersion predominantly showing large bundled SWNTs with a significant number of iron catalyst impurities. (c) and (d) Large graphitic and metal catalyst impurities in the form of nano-onions observed in CoMoCAT electrochemical dispersions; no SWNTs were observed.
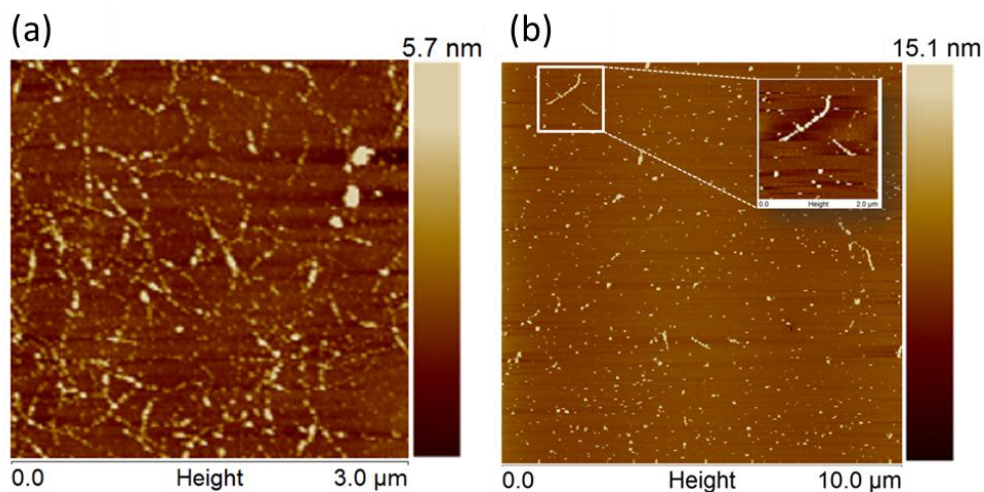
Fig. III-13 AFM images of electrochemically dissolved SWNTs performed on the Schlenk line. (a) Height micrograph of a raw HiPco electrochemical dispersion in 1 mM TBAP/DMF at -2.3 V *vs.* Ag/Ag$^+$ following five sequential dissolution steps, showing significantly fewer impurities than (b) the height micrograph of a typical raw HiPco electrochemical dispersion showing the presence of individual SWNTs along with many other amorphous carbons, graphitic and metal catalyst impurities that are preferentially dissolved during the process.

III. 3. 2. 2. Glove box dissolution experiments

Upon transferring all experiments to a glove box, significantly larger yields were immediately observed, and therefore greater nanotubide concentrations were achievable. For raw HiPco SWNTs, using the Schlenk line, yields were observed to reach only ~5 wt %. The same SWNTs were later dissolved using the glove box and 100 wt % dissolution was repeatedly observed, importantly, with the preservation of (opto)electronic properties as evidenced by UV-vis-nIR and PL spectra following exposure to the ambient atmosphere (refer to section III. 4. 2). Furthermore, reverting back to sodium based electrolytes that were not able to stabilise nanotubide polyelectrolytes using the Schlenk line, it was possible to generate nanotubides that were stable for more than 6 months in an inert atmosphere (Fig. III-9c).

Between -1.6 to -2.0 V (*vs.* Ag/Ag$^+$), overall dissolution was small (~5-20 wt %); at increasing potentials up to -2.3 V (*vs.* Ag/Ag$^+$), 100 wt % dissolution could be achieved. Using raw HiPco SWNTs, concentrations of at least 1.5 mg mL^{-1} in DMF were achieved as determined by mass measurements, similar to other reductive chemical approaches.[129] Overall, the relative proportion of high-quality SWNTs in solution should be considerably higher following electrochemical dissolution due to the higher process yields. Compared to the electron potentials provided by chemical methods (naphthalide[262] in THF: ~-2.7 V *vs.* NHE; solvated electrons[263] in liquid ammonia: -1.9 V *vs.* NHE), electrochemical potentials for dissolution are similar (~-2.0 V *vs.* NHE), yet yields are significantly higher (only ~14 wt % using Na/NH$_3$ followed by dissolution in DMF[129]). However, the reduction potentials required for SWNT dissolution are significantly larger than for spectroelectrochemical phenomena[172, 173] due to the need for a high charge density, before dissolution. Despite practical issues with the current embodiment (discussed further below), these relatively concentrated nanotubide solutions are noteworthy considering there is no requirement for ultrasonication; previously reported concentrations of neutral SWNTs in DMF are typically orders of magnitude lower.[210]

Overall, the electrochemical dissolution of SWNTs required ~1 charge/20–40 C atoms for HiPco SWNTs, and ~1 charge/20-35 C atoms for CoMoCAT SWNTs (as observed by dissolution experiments in which a 100 wt % yield was obtained, assuming a 100% electrochemical yield, Fig. III-14a), in reasonable agreement with Penicaud[128] and Fogden,[129] who reported the reduction of SWNTs required 1 charge/10-50 C atoms, and 1 charge/10 C atoms, respectively. The resulting chronoamperograms correlate to the continual filling of the SWNT

DOS with the driving force of the applied voltage, as opposed to increasing current over time due to redox reactions. The observation of two distinct plateaus in the HiPco chronoamperograms was presumed to correlate to two key processes: *i.* the SWNT powder swelling process following intercalation and exfoliation, and *ii.* the diffusion of nanotubides away from the working electrode. These features were further demonstrated for CoMoCAT SWNTs but not for other longer and typically larger diameter SWNT type electrodes, for which the swelling process is significantly slower. These distinct plateaus were also not present in CoMoCAT chronoamperograms upon the introduction of water in later experiments (Fig. **III-20**), the swelling process is notably slowed by competing reduction reactions. For HiPco SWNT reductive dissolution at different loadings, prior to the point at which current starts to plateau for a second time, the charge per carbon ratio reaches ~1 charge/40 C atoms in both cases (Fig. III-14b), relating to the charge density at which the SWNT electrode no longer expands.
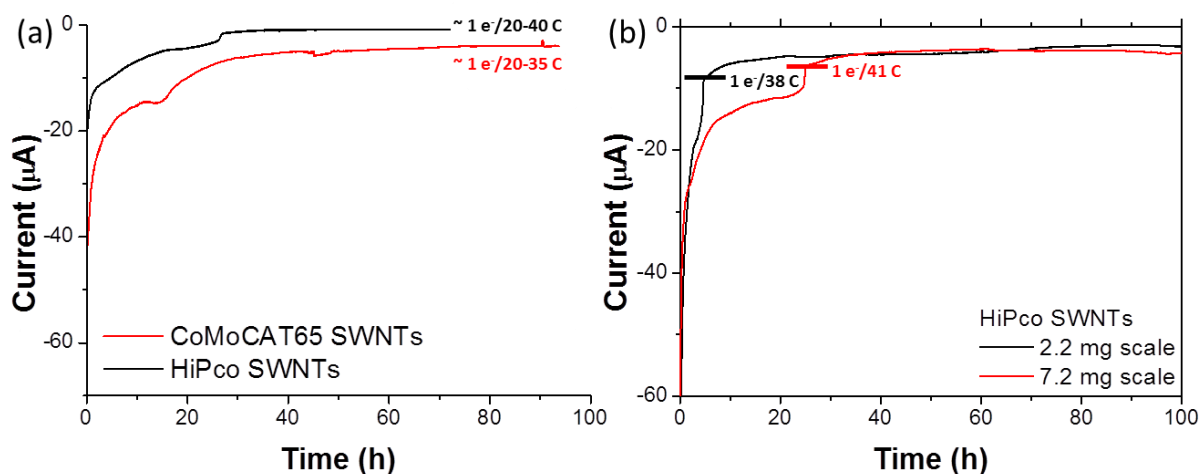
Fig. III-14 SWNT chronoamperograms during the reductive dissolution process. (a) HiPco and CoMoCAT SWNT electrodes giving a 100 wt % yield of dissolution. (b) The chronoamperograms for HiPco SWNTs at different powder loadings. At the point at which current starts to plateau for a second time, the charge per carbon ratio reaches ~1 charge/40 C atoms in both cases.

TEM micrographs of electrochemical dispersions produced in the glove box (Fig. III-15) showed significant numbers of individualised SWNTs with few small bundles; the possibility to drop-cast dispersions on to TEM grids under inert conditions avoided any potential reaggregation, and higher process yields led to better quality SWNTs observed in dissolved

fractions. The dissolution of all SWNTs consequently gives a non-selective process, although a more useful one in terms of process scalability. To attempt to recapture selectivity, sequential dissolutions were performed at gradually increased potentials (-1.6 V to -2.3 V). Fig. III-16a-b show the Raman spectra from all fractions including undissolved HiPco material.
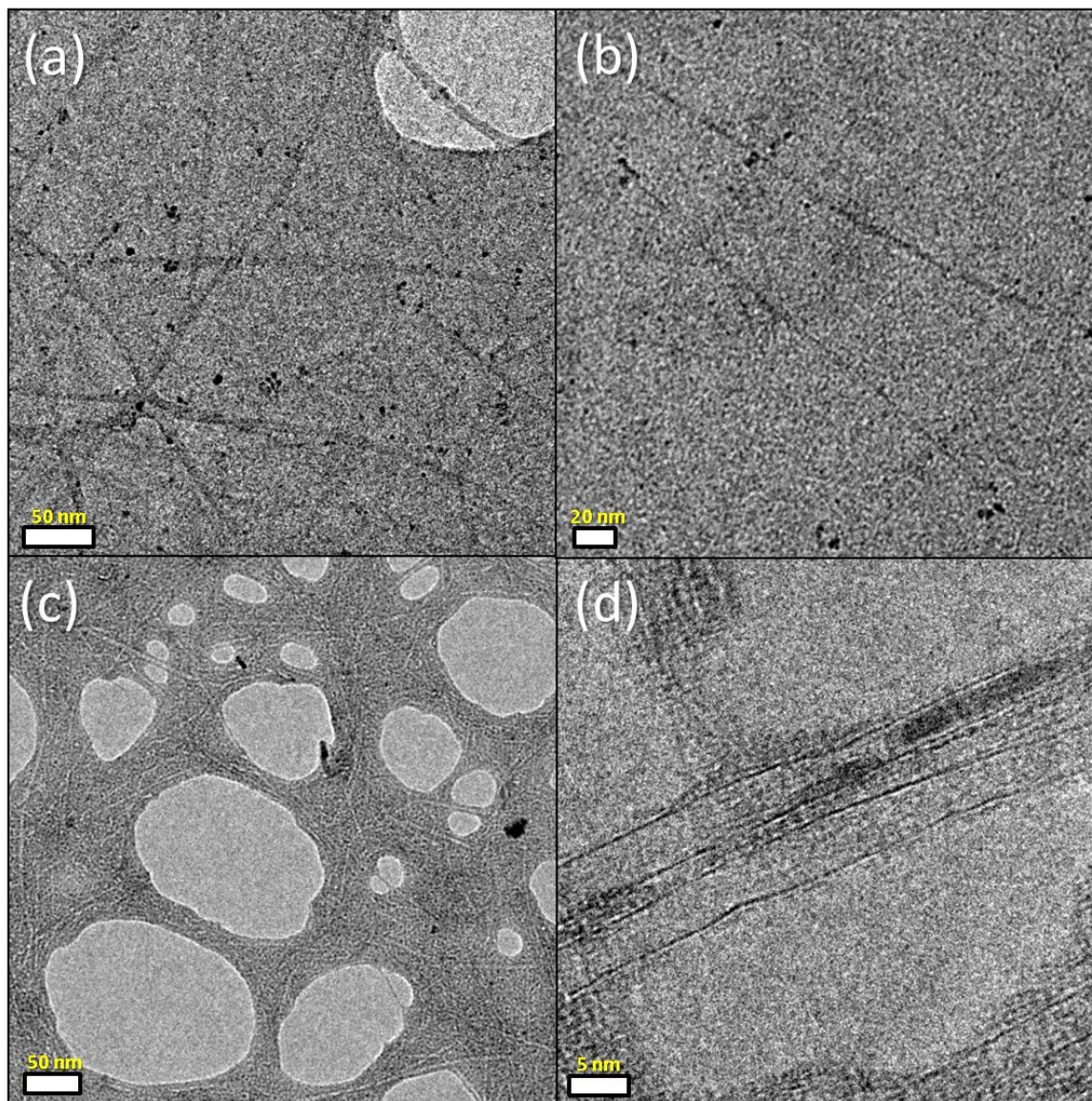
Fig. III-15 TEM images of electrochemical dispersions performed in the glove box. (a)-(b) Raw HiPco SWNT dispersions showing highly individualised SWNTs. (c) SG SWNT dispersions showing a region of individualised SWNTs. (d) A high magnification view of two parallel SG SWNTs. with significantly large diameter (~4-5 nm); there is also evidence to suggest a small proportion are double-walled carbon nanotubes (DWNTs).
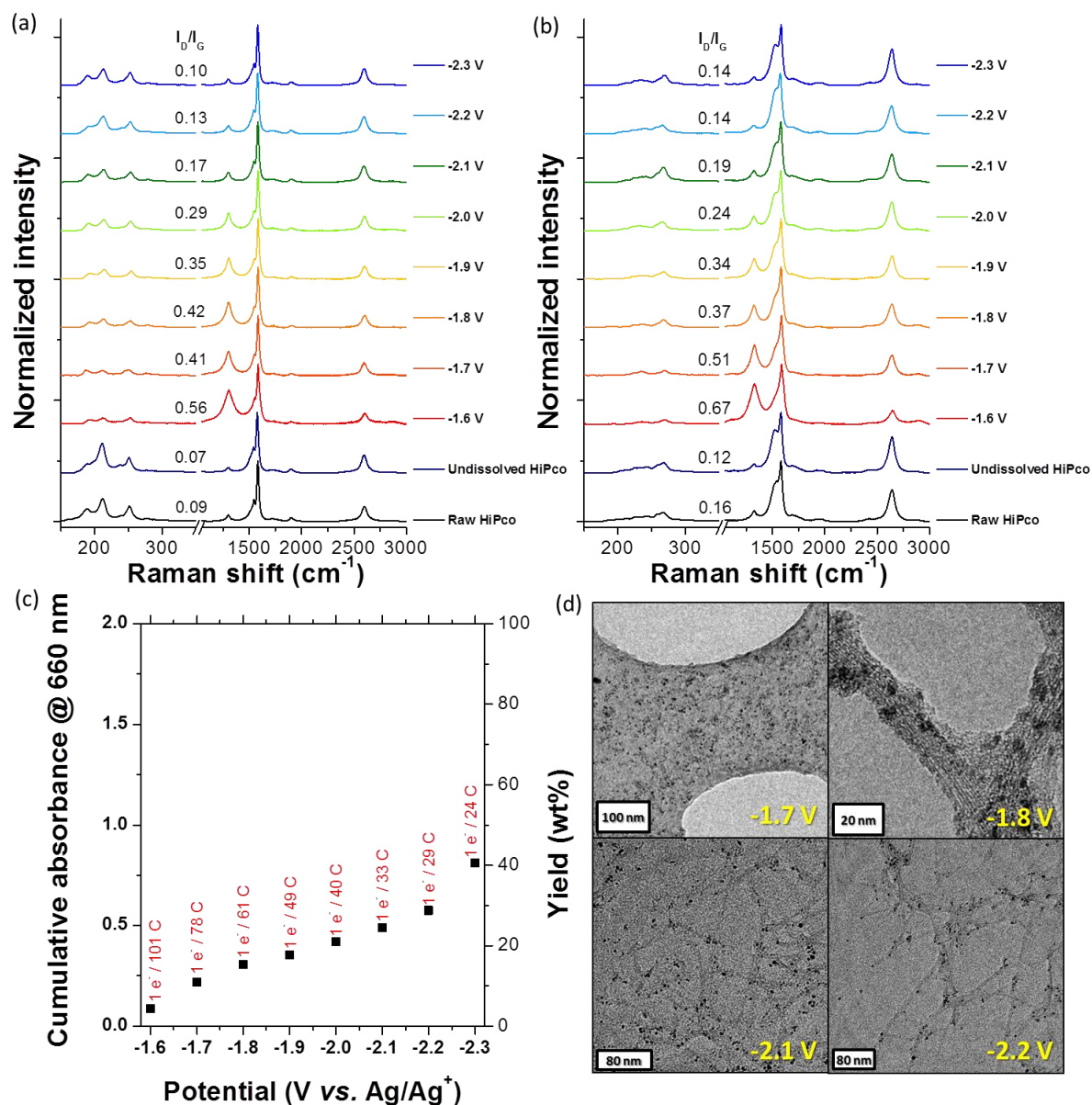
Fig. III-16 Fractional dissolutions of raw HiPco SWNT powder in 1 mM STPB/DMF electrolyte at increasing reduction potentials (V *vs.* Ag/Ag$^+$). Following each step the majority of the nanotubide dispersion was removed and fresh electrolyte (containing ~5-10 ppm water) added. (a)-(b), Raman analysis of the raw, undissolved and electrochemically dissolved HiPco fractions using E_{laser} = 1.96 eV and 2.33 eV, respectively. Each spectrum is an average of 5 scans at different positions. Intensities are normalized to the G peak. The enhancement of the D peak at mild reducing potentials is followed by a subsequent decrease with stronger reducing potentials in line with TEM observations. (c) The process yield following each fractional dissolution step. Labels show the charge per number of carbon atoms at each potential. (d) TEM images of selected nanotubide fractions showing the preferential dissolution of metallic and carbonaceous debris (-1.6 to -2.0 V) followed by the progressive dissolution of purer SWNT material (> -2.0 V).

The reason for this incomplete dissolution (only ~40 wt % dissolution at 1 charge/24 C atoms, Fig. III-16c) stems from the addition of fresh electrolyte after each fraction taken. The moisture content of the fresh electrolyte (~5-10 ppm) may introduce competing reduction reactions, charge quenching of the SWNTs, or SWNT functionalisations. An interesting observation was the flocculation of a small amount of dispersed SWNTs as fresh electrolyte was added, that would suggest direct quenching as opposed to functionalisation.

Unfortunately, the previously observed selective dissolution of large diameter m-SWNTs was not observed; the RBM features are almost identical to the starting material, potentially highlighting selective functionalisation of small diameter sc-SWNTs by protons (generated from the reduction of water) during the process performed on the Schlenk line. The role of water is investigated in section III. 4. 1. 1. Nevertheless, the same purification trend as observed for the Schlenk line experiments prevails here; the defect concentration in the fractions dissolved at less reducing potentials was significantly greater than that in the raw material (as indicated by an increased peak intensity ratio, I_D/I_G). The defect concentration in the undissolved material was lower, as observed using the Schlenk line. Again, impurities such as amorphous carbons, graphitic (metal-containing) nanoparticles and short/defective SWNTs are reduced preferentially. The mechanism is not primarily diffusion based since electrochemical dissolution at mild potentials does not lead to the progressive dissolution of purer SWNTs; these species require significantly increased charge densities, available at greater reducing potentials. TEM of different fractions confirmed the purification trend (Fig. III-16d); at increasingly more reducing potentials, fractions contained significantly lower amounts of amorphous, graphitic and metal catalyst debris.

With larger yields and separated fractions, the SWNTs dissolved at more reducing potentials bear a similar, if not lower defect concentration than the starting material, whilst the undissolved material is also significantly purer. A useful strategy would be to run the process at -2.0 V to dissolve the majority of impurities (~20 wt %), followed by a dissolution of the purer material at -2.3 V, so as not to introduce significant amounts of water.

III. 3. 2. 3. Compatibility and scaling

Various commercial SWNT powders were tested to examine whether the electrochemical processing of SWNTs was compatible with different SWNT synthetic methods. Commercial

SWNTs are predominantly synthesized by CVD and ARC methods; due to the high cost of production of the laser ablation process, these SWNTs are only produced on very small scales at research level and are subsequently very difficult and expensive to purchase. For these reasons, laser ablation synthesized SWNTs were not investigated in this research. Fig. III-17 shows a selection of SWNTs that were successfully electrochemically dissolved.

Different SWNTs gave different yields, typically dependent on SWNT length, although raw SWNTs generally dissolved better than those that had undergone pre-purification by the manufacturer (worse quality, more amorphous material *vs.* altered (opto)electronic properties, increased packing density, hydrogen bonding between inter-surface functional groups, *etc.*). Consequently, the maximum yield from a given SWNT sample will depend on physical parameters such as nanotube length, entanglement, and density, as well as electronic effects including chirality, and connectivity. Since amorphous carbon and particulates dissolve preferentially, they can increase the apparent yield. Raw HiPco SWNTs, typically 300-700 nm length, showed the highest yields (100 wt % when performed in the glove box); CoMoCAT SWNTs also repeatedly gave 90-100 wt % yields. Hanwha SWNTs (ARC), typically 1-10 μm, swelled significantly at reducing potentials but only minimal dissolution was observed; these SWNTs were tested only once using the Schlenk line, repeating in the glove box should provide significantly higher yields. Meijo SWNTs (ARC), typically 1-5 μm length, showed promising dissolution with yields up to ~10 wt % when performed in the glove box, whereas SG SWNTs with lengths up to 250 μm, showed no dissolution on the Schlenk line, although significantly higher yields (< 10 wt %) were achieved when performed in the glove box.

The electrochemical cell geometry plays a key role in the overall process yield – the present design is optimised for *in situ* spectroscopy but suffers slow diffusion. In cases where long SWNT materials are used, SWNTs may still remain entangled in the powder bed limiting the yield, since the reptation time (τ_{rep}) scales with L^3 (where L is SWNT length).[264] Bulk processing would benefit from thin electrodes and possibly gentle agitation. Assuming that electrical percolation within the dispersed SWNTs is avoided due to electrostatic repulsion, the ultimate concentration limit should be defined by the type of complex phase diagram identified for protonated SWNTs in superacid.[133, 265] Higher fractional charge (~1 charge/12 C atoms), if attained without disconnection, should offer the opportunity to form nematic phases.

Fig. III-17 Photographs of the electrochemical dissolution of various commercial SWNTs synthesised *via* different processes. All SWNTs were dissolved at -2.3 V *vs.* Ag/Ag⁺ for different lengths of time. (a) Raw HiPco SWNTs, (b) Hanwha SWNTs (ARC), (c) Meijo SWNTs (ARC), and (d) SG SWNTs (water-assisted CVD).

Efforts to scale the process to dissolve at least milligram quantities were performed with raw HiPco SWNTs. These experiments were performed on the Schlenk line (prior to glove box experiments), using UV-vis-nIR spectroscopy to spectroelectrochemically observe changes in SWNT concentration over time. The extinction coefficient[211] for HiPco SWNTs in NMP (3624 mL mg^{-1} m^{-1} @ 660 nm) was used to determine the concentration of nanotubide dispersions at different scales over time, as well as confirming the yield by mass measurements. The small scale experiment (5 mg) showed a plateau in the nanotubide absorbance after about 24 hours. This effect was not observed for the large scale experiment (50 mg) even after 120 hours. The rate of dissolution is approximately the same in both cases (~0.01 mg SWNTs per hour), although the dissolution kinetics are significantly offset due to the increased level of charging with increased scale. Fig. III-18 shows the experimental setup with a plot of nanotubide solution absorbance over time; after the initiation period (discussed in the following section) the

concentration of dissolved SWNTs increases with time, eventually reaching a plateau that defines a process yield. On increasing the initial loading of SWNTs, the absolute mass dissolved increases. The yield of dissolved HiPco reaches saturation after 2 days with an initial loading of 5.4 mg with a fractional charge of 1 charge/28 C atoms (Fig. III-19b); for larger loadings the kinetics were considerably slower. For the largest loading (50.6 mg), the fractional charge per carbon atom loaded was 1 charge/43 C atoms after 5 days. Saturation occurred after 10 days with an almost identical fractional charge per C atom loaded (1 charge/29 C atoms) as the 5.4 mg scale. The yield of dissolved material at this loading exceeded the milligram scale (1.7 mg, 3.4 wt % yield). At intermediate loadings, the process yield was not reached after 5 days due to the slower kinetics, inherently linked to the depth of the electrode powder bed; upon swelling (Table III-5) it is likely that electrode connectivity is impaired. Furthermore, the lack of any agitation through stirring limits diffusion of the nanotubide species away from the powder bed.

Unfortunately, spectroelectrochemistry inside a glove box required a miniaturised spectrometer, therefore, these experiments could not be repeated. On the other hand, similar mechanisms are at work in the glove box process, especially with regard to the swelling of the powder bed, increased initiation times with larger loadings, and slower kinetics, *etc.*
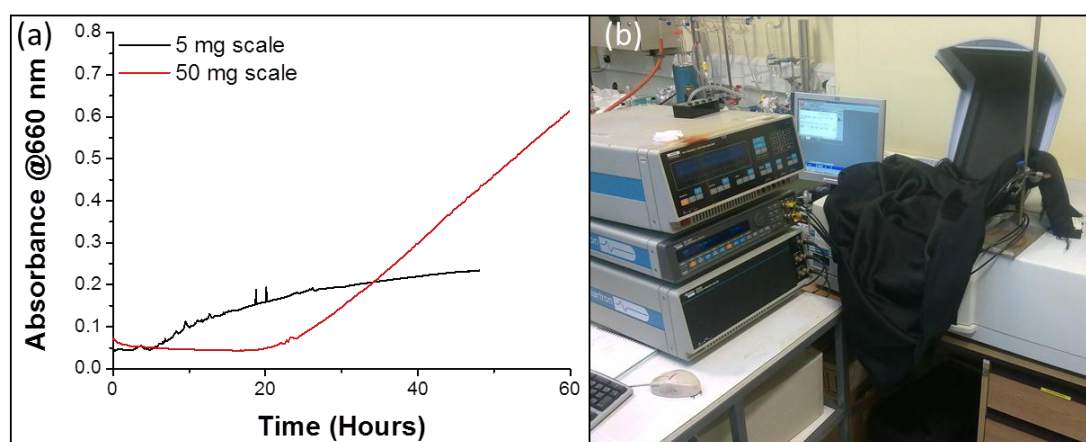
Fig. III-18 UV-vis-nIR spectroelectrochemical analysis during the reductive dissolution process. (a) The absorbance of of raw HiPco nanotubide dispersions at 660 nm over time with different initial loadings. (b) The experimental setup showing the potentiostat connected to the electrochemical cell placed inside a UV-vis-nIR spectrometer (covered with black material to block outside light).

Table III-5 Tabulated data for spectroelectrochemical measurements.

SWNT loading ± 0.05mg	SWNT^{n-} dissolved ± 0.005 mg	Initiation time ± 0.25 hours	Charge before initiation/SWNT loading Coulombs mg^{-1}	Initial powder bed height (H$_i$) ± 0.1 mm	Final powder bed height (H$_f$) ± 0.1 mm	Swelling factor H$_f$/H$_i$
5.4	0.19	0.5	0.033	1.4	9.5	6.8
11.9	0.34	3	0.034	3.1	16.4	5.3
20.3	0.49	7	0.034	4.6	20.3	4.4
50.6 Fraction 1	1.10	18	0.030	9.4	24.7	2.6
50.6 Fraction 2	0.60 (1.70)	n/a	n/a	n/a	33.8	3.6
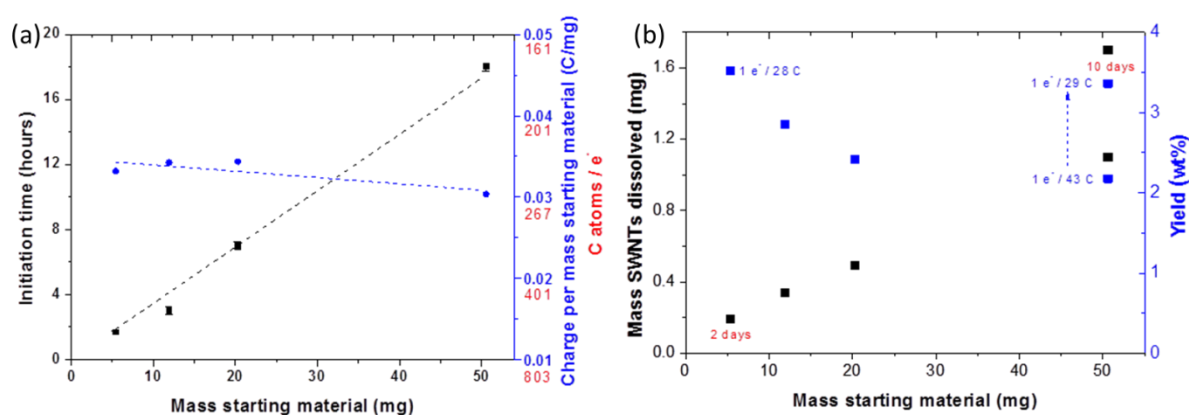
Fig. III-19 Scalability of the dissolution process. (a) The initiation time (squares) and the charge required (circles) and (b) the yield of dissolution for raw HiPco SWNTs with increasing amounts of starting material (-2.3 V *vs.* Ag/Ag$^+$, 1 mM TBAP/DMF electrolyte). The dissolution processes were performed for 5 days unless stated.

III. 4. ELECTROCHEMICAL MECHANISMS

III. 4. 1. Mechanisms for dissolution

The nanotubide dissolution process is driven by the intercalation of the background electrolyte and solvent into the SWNT powder electrode to balance the electronic charge introduced at reducing potentials. During these processes, which correlate with capacitive charging of the SWNT network (Fig. III-19a), the powder swells significantly (Fig. III-9b); as electrostatic interactions overcome the intertube vdW forces, the SWNT network exfoliates and debundles. Diffusion of the charged species away from the electrode generates a charged polyelectrolyte

nanotubide solution. However, the SWNT working electrode gradually forms a bulky, swollen, gel-like network. Electrochemical double-layer charging has been demonstrated in electromechanical actuators, with actuation caused by expansion due to charging.[266] In the present case, the charge density is high enough and the electrolyte concentration low enough, that an electrostatically-stabilised colloid forms. The spontaneous nature of the dissolution confirms that the process is thermodynamically-favoured, with a lower enthalpy of dissolution than for a neutral SWNT system.[134] Amide solvents are typically preferred solvents for SWNTs,[210] but the success of electrolyte systems based on other solvents such as PC, highlights the importance of electrochemical charging. As well as this primarily electrostatic mechanism, condensation of TBA^+ counterions, when used, may provide additional steric stabilisation. It is also anticipated that nanotubide dissolution may extend to a wide range of solvents including other cyclic carbonates, lactones and sulpholanes, provided that they are sufficiently dry.

The initiation time (defined as the first observation of black trails diffusing away from the SWNT powder electrode) varied between SWNT batch and manufacturer, but was linked to charging of the entire powder. The charge passed before first observed dissolution (Fig. III-19a) was consistently ~0.03 C mg^{-1} SWNT, independent of starting mass, (1 charge/270 C atoms) for raw HiPco powder; this charging threshold varies between SWNT batch and material (*e.g.* CoMoCAT ~0.08 C mg^{-1}). For the HiPco powder used, accumulation of charge equates to a gravimetric capacitance of 13 F g^{-1}. Compared to the capacitance of highly pure HiPco SWNTs in 1 M $LiClO_4$/PC electrolyte (45 F g^{-1}),[267] our value is relatively low due to low electrolyte concentration and a significantly higher fraction of amorphous carbon bound bundles in the raw powder. In addition, the larger size of TBA^+ ions compared to Li^+ inherently produces a lower gravimetric capacitance.

Overall, the electrochemical dissolution of SWNTs required ~1 charge/20-40 C atoms, in reasonable agreement with others.[128, 129] The negative charges are either delocalised or shielded by the condensation of counterions, as determined by the Bjerrum length.[268] Packing charge more densely than this critical threshold offers no additional advantage for dissolution, as the counterions remain condensed on the nanotubes, screening the electrostatic repulsion. The observed selectivity for m-SWNTs over sc-SWNTs and the enhancement of large diameter species during Schlenk line experiments was hypothesised to be implicitly related to the dielectric properties and electronic band structure of the nanotubes. Classic estimations of Bjerrum length

often consider only the dielectric constant of the solvent, ignoring any contribution of the polyelectrolyte molecule itself. In the current context, the dielectric contribution of the nanotubes is significant. m-SWNTs ($\varepsilon > 1000$) have higher dielectric constants than sc-SWNTs ($\varepsilon < 10$);[29, 83] larger diameter SWNTs have larger dielectric constant than small ones.[30] Qualitatively, a higher dielectric constant will reduce the Bjerrum length allowing a significantly higher concentration of dissociated charges on m-SWNTs, due to enhanced dielectric screening, and a greater tendency to dissolve. However, other factors may also contribute; intrinsically, different nanotubes have characteristic electron affinities, and thus charge will be partitioned heterogeneously when in contact. Whilst the Fermi level may be a function of diameter,[31] m-SWNTs tend to have greater initial electron affinity than sc-SWNTs. In the present case, however, there is sufficient charge available to saturate at least the first few vHS, and the distinction between the multiple electron affinities of the various nanotube types is less obvious. The initial stages of the electrode swelling and exfoliation process may, nevertheless, be affected. An alternative theory surrounding observations of preferential reductive dissolution of large diameter SWNTs at low charge:carbon ratios is based on thermodynamic principles;[131] smaller diameter SWNTs have a higher specific surface area than their larger counterparts, introducing a high enthalpic penalty that leads to a higher ΔG_{mix}. However, the absence of selectivity at even the mildest reduction potentials using the glove box process suggests other factors are at work; the role of water, for example, could have a significant impact on the dissolution process.

III. 4. 1. 1. The role of water

The differences in the character of the dissolved fraction between electrochemical dissolution experiments on the Schlenk line and in the glove box suggest that water may play a significant role in determining both the yield and selectivity of the dissolution process. During the electrochemical reduction process there are several possible simultaneous competing mechanisms, *i.* the reduction and dissolution of SWNTs, *ii.* the functionalisation of SWNTs by H_2 surface reactions (protonation) generated from the water reduction, *iii.* charge quenching from water/oxygen.

The observation of metallic/large diameter enrichment in dissolved fractions during the reductive dissolution using the Schlenk line suggests water may react with the small diameter SWNTs. The controlled addition of water to the electrochemical dissolution process was

performed in an attempt to reproduce the level of moisture common in the Schlenk line setup. Water was therefore introduced to the glove box dissolved fractions after successful dissolution, or prior to the charging process. For these experiments, molecular sieve dried DMF or 1 mM $NaClO_4$/DMF was removed from the glove box in a Schlenk tube, 1000 ppm water added, and then freeze-thawed to remove any dissolved gas molecules in the transfer process, before returning to the glove box. Different standards were then made by diluting these stock solutions with dry DMF or 1 mM $NaClO_4$/DMF to make a 100 ppm solution.

Addition of water to dry electrolytes

Electrochemistry was performed in dry and wet electrolytes containing the same amount of CoMoCAT powder (~7 mg) at -2.3 V *vs.* Ag/Ag^+ over almost 4 days. Chronoamperograms (Fig. III-20a) of the dry and 100 ppm processes show the characteristic two plateaus in current, related to the filling of the SWNT DOS as discussed previously. The 1000 ppm chronoamperogram showed no prominent features. It was observed that the powder bed swelled much slower and to a higher level for the 1000 ppm reaction, due to competing water electrolysis that caused slower charging of the SWNTs, and perhaps charge quenching (Fig. III-20b); the overall current used to drive these reactions increased with the addition of water, although only slightly for the 100 ppm reaction; the addition of 1000 ppm showed a significant increase in the overall charge passed. Having achieved a 100 wt % yield of dissolution for the dry system, the introduction of water led to a noticeable reduction in yield, although still much higher than Schlenk line dissolutions (~80 wt % at 100 ppm, ~60 wt % at 1000 ppm), suggesting competing electrolysis is dominant compared to the initially hypothesised functionalisation. This result also confirms that the moisture level is continually increasing in the Schlenk line experiments, whereas it is consumed to a large extent in the glove box experiments; consequently, the same reaction conditions could not be replicated. Due to the significantly high yields, selectivity was not observed using Raman spectroscopy.
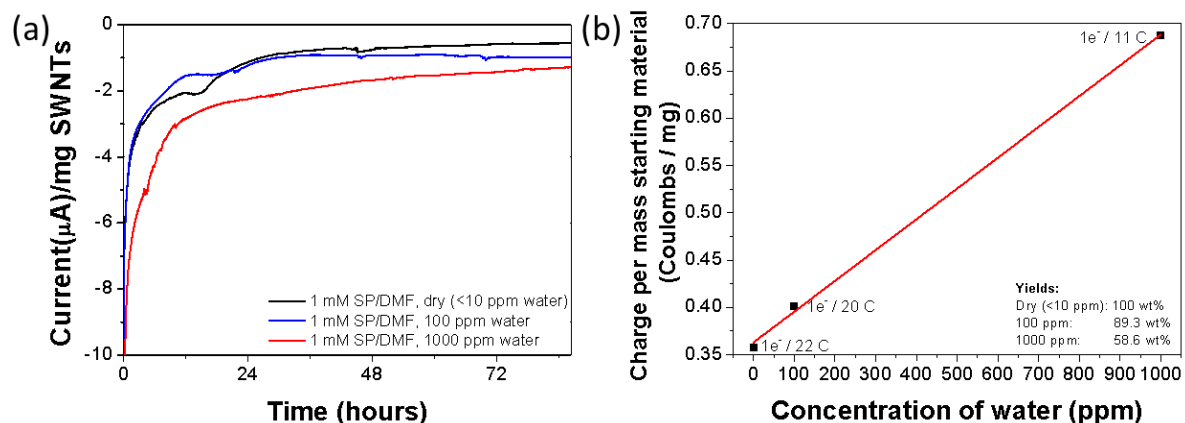
Fig. III-20 The effect of added water content on the reductive electrochemical dissolution of SWNTs. (a) Chronoamperogram of raw HiPco dissolution in the presence of varying water concentration. (b) Overall charge passed per mass starting material with increased water concentration. The yield is lower with increased water content, although still significantly higher than previous Schlenk line experiments, suggesting that water is electrolysed and not continually replaced.

Addition of water to dry dissolved fractions

0.5 mL 1000 ppm and 100 ppm water in DMF solutions were added to 0.5 mL fractions containing dissolved HiPco SWNTs from the fractional dissolution process (section III. 3. 2. 2), generating 50 ppm and 500 ppm solutions. After 24 hours, these fractions had completely flocculated, indicating charge quenching/functionalisation. Changes in Raman spectra were very subtle (Fig. III-21a-b); only with the addition of 500 ppm water were slight differences observed, the 50 ppm spectra were unchanged. With both laser excitations, there was a slight decrease in the relative intensities of small diameter species, suggesting a selective functionalisation. However, in combination with results for the wet electrolytes, the level of moisture in Schlenk line experiments may be significantly higher (~3600 ppm) giving the appearance of a more selective dissolution process.
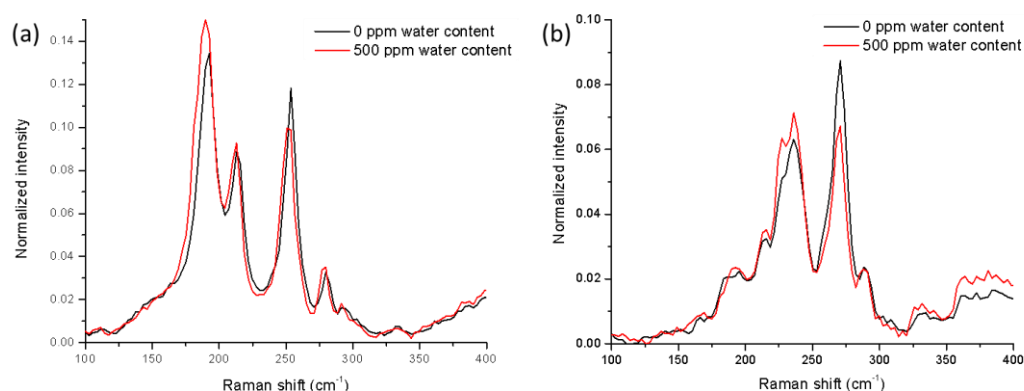
Fig. III-21 Raman analysis following the addition of water to electrochemically dissolved SWNTs. Raman spectra for HiPco fractions in dry electrolyte and following 500 ppm water addition using (a) E_{laser} = 1.96 eV and (b) E_{laser} = 2.33 eV. Each spectrum is an average of 5 scans at different positions. Intensities are normalized to the G peak.

It is difficult to completely determine the role of water in the electrochemical dissolution process. However, at a best guess, it is obvious that water plays a large part in influencing both the nature of the dissolved species and the experimental yield. Using the Schlenk line, the continual introduction of atmospheric moisture over the long experimental timeframe (as discussed in section III. 2. 4. 3) could cause the electrode potential to become fixed at the water reduction potential (~-1.2 to -1.6 V) where only defective materials, short SWNTs that are large diameter and metallic in character are able to dissolve. It is assumed that this selectivity is observable over longer periods of time due to significantly slower kinetics caused by competing water electrolysis. From previous reports[74] SWNTs may become functionalised primarily at defect sites; over time, the dissolved material has a decreasing degree of functionalisation since these materials are longer and less defective. The remaining undissolved fractions comprise less defective SWNTs that are less susceptible to functionalisation, leading to significantly low yields due to an insufficient charge density, or due to solubility issues.

In the glove box, it is reasonable to suggest that the lower water content may be removed in the form of H_2 gas following electrolysis at the Pt wire electrode surface. Indeed, slight functionalisation of the initial dissolved nanotubide fraction may occur, but is soon followed by less defective charged SWNT species once the water content has been suppressed. High yields are therefore achievable, even when significant amounts of water are present (~60 wt % yield

with 1000 ppm water), since electrolysis of water appears to dominate functionalisation/charge quenching processes. Table III-6 summarises the comparison of mechanisms involved in the Schlenk line and glove box processes.

Table III-6 Comparison of Schlenk line and glove box dissolution processes.

	Schlenk Line	Glove Box
Moisture content? Ratio if 5 mg SWNTs in 7 mL electrolyte	Brand new DMF: ~10-20 ppm (~1 mM in DMF) ~1 H_2O/100 C atoms Significant leakage of moisture/air (continuously over experimental timeframe), significant degree of functionalisation or charge quenching	Molecular sieve dried electrolytes: ~3-5 ppm (~0.25 mM in DMF) ~1 H_2O/400 C atoms Minimal functionalisation/charge quenching
Depletion of water?	Water never depleted due to continual leakage	Water depleted to a very low level
Charging vs. Functionalisation?	Defective materials preferentially charged but will be functionalised primarily at defect sites by water	
Degree of swelling?	Swelling more significant in Schlenk line process due to slowed kinetics (competing electrolysis of SWNTs *vs.* water, or charge/discharge processes)	
Character of dissolved fraction?	Material that dissolves first has lower reduction potential (small graphitic impurities), defective or short SWNTs (high mobility, less entanglement), Metallic, large diameter selectivity in early fractions	Material that dissolves first has lower reduction potential (small graphitic impurities), defective or short SWNTs (high mobility, less entanglement). No selectivity over time
Undissolved material?	Undissolved material is less defective and therefore less susceptible to functionalisation	Long entangled SWNTs left undissolved, very low defect concentration and very stable toward functionalisation
Yield?	Very low (~5%) Current goes into reducing water *vs.* charging SWNTs	Significantly higher (up to 100%), entanglement/diffusion/potential limited
Quenching (air)?	Further functionalisation of the charged/already functionalised dissolved fraction Very low degree of functionalisation of undissolved material	Functionalisation/charge quenching of the dissolved fraction
TBA or sodium electrolytes?	TBA dispersions stable due to steric stabilization . The large the amount of water present increases the likelihood of formation of NaOH which rapidly flocculates SWNTs	Both TBA and Na electrolytes produce stable nanotubide dispersions
Possible functional groups/side-reactions?	$TBA^+ + e^- \rightarrow Bu\bullet + (Bu)_3N\bullet$	Butyl radical addition to SWNTs
	$Na^+C_n^- + H_2O \rightarrow NaOH + H^+C_n^-$	Protonation of SWNTs
	$2H_2O + 2e^- \rightarrow H_2 + 2OH^-$	Formation of H_2 gas / hydroxide
	$O_2 + ne^- \rightarrow O_2^{n-}$ (n =1 or 2)	Formation of superoxide / peroxide
	$O_2 + 4e^- \rightarrow 2O^{2-}$	Formation of oxides

III. 4. 2. Mechanisms for charge quenching/functionalisation

Following the electrochemical dissolution process, it is important to regenerate the original electronic properties of the SWNTs so that future applications are feasible. Therefore, it is extremely important to remove this charge on the nanotubide species without causing unnecessary functionalisations. There is much debate over reported literature that suggests exposing nanotubides to air will result in charge quenching by O_2 to form neutral species.[269] However, exposure of nanotubides in liquid-phase dispersion or as a dried powder to atmosphere is likely to result in very different products due to the many different interacting species. The most likely reactive candidates are O_2, H_2O and CO_2; O_2 is reported to result in the complete quenching of charge *via* the formation of alkali metal superoxide,[134] H_2O is likely to result in the protonation of SWNTs along with alkali metal/tetraalkylammonium (TAA) hydr(oxides). CO_2, however, will generate carbonate surface moieties that maintain their association with electrolyte cations; subsequent exposure of these moieties to the atmosphere will generate carboxylic acid groups along with alkali metal/TAA hydr(oxides).[148]

In order to mimic the removal of charge from nanotubide dispersions in DMF, Karl Fischer analysis of the water uptake of ~4 mL (volume typical of dissolved fraction) as-received anhydrous DMF containing ~25 ppm water content (~1 mM) exposed to a relative humidity of 23% revealed rapid water uptake to ~1400 ppm (~80 mM) within 1 hour (Fig. III-22). The rate of water uptake depends on many factors including the humidity, solution volume, shape and size of vial; recent reports show the uptake of water in an open electrochemical cell containing 0.2 M $TBAPF_6$ in DMF to be ~2500 ppm (~140 mM) after 2 hours (@ 50% relative humidity).[250] Oxygen uptake in DMF saturates at ~152 ppm (~4.5 mM) with bubbling O_2 gas for 1 hour;[270] this value corresponds to a rate of O_2 uptake of ~2-3 ppm per minute. However, the stronger oxidising power of oxygen may result in the rapid quenching of nanotubide dispersions in DMF as opposed to functionalisation by H_2O.

Table III-7 Maximum O_2 solubility and rate of moisture uptake of selected polar aprotic solvents.

Solvent	Max O_2 solubility (mM) (*ppm*)	Moisture content analysis			
		t = 0 (mM) (*ppm*)	Rate of uptake (mM min⁻¹) (*ppm min⁻¹*)	Relative Humidity (% RH)	Temperature (°C)
DMF	4.5 ± 0.3 (*~152*)	~1.40 (*~27*)	~1.28 (*~24*)	23	21
THF	8.16 (*~294*)	~0.11 (*~2*)	~0.79 (*~16*)	36	21
AN	8.1 ± 0.6 (*~330*)	~0.14 (*~3*)	~0.87 (*~20*)	36	21
DMSO*	2.1 (*~61*)	~30.0 (*491*)	~0.15 (*~2*)	30	22
DMF*	See above	~3.0 (*~57*)	~0.14 (*~3*)	30	22
AN*	See above	~0.7 (*~16*)	~0.07 (*1.6*)	30	22

Max. O_2 solubilities from ref. 270, 271 or 272. Rate of H_2O uptake measurements performed by Miss. Charlene Lawton using Karl Fischer analysis; 4 mL fractions in open top 30 mL volume vials were exposed to fume hood make-up air.
* Indicates Karl Fischer measurements reported in ref. 250, after exposing 25 mL solutions to an atmosphere containing 30% RH; solvents also contain 0.2 M $TBAPF_6$ supporting electrolyte.
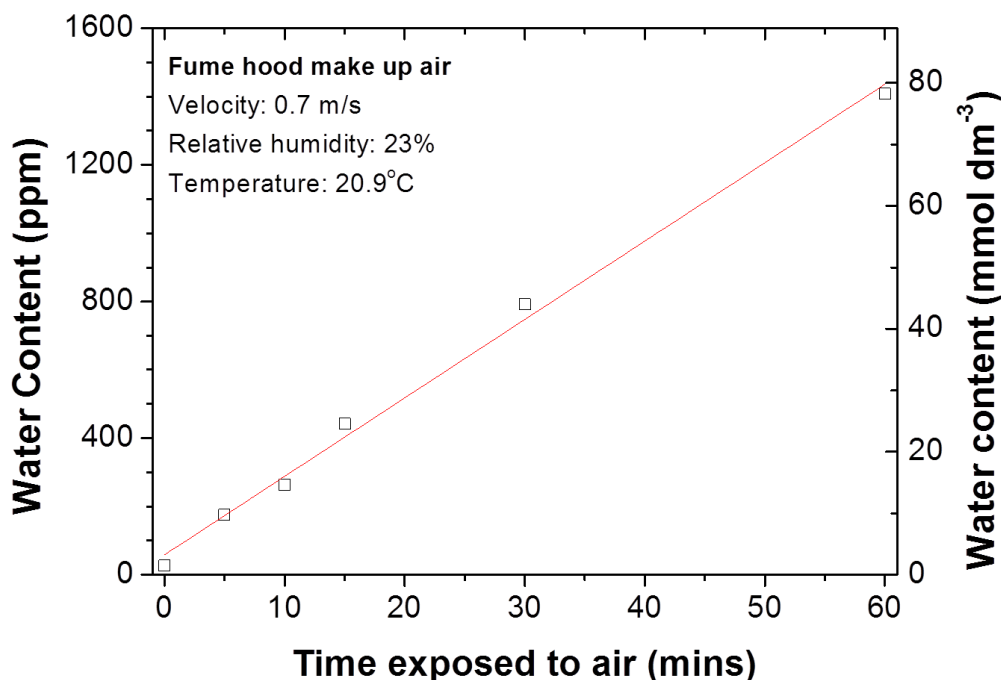
Fig. III-22 Karl Fischer analysis of DMF moisture uptake upon exposure to the ambient atmosphere. Here, 4 mL DMF fractions in open top 30 mL volume vials were exposed to fume hood make-up air for 60 minutes as shown in Table III-7.

Removing the solvent from nanotubide dispersions before removal to the ambient atmosphere is likely to increase the rate at which O_2 can quench the charge with minimal functionalisation from water; indeed, little change was observed in the D peak in Raman spectra indicating no surface modification. UV-vis-nIR and PL spectra are significantly more sensitive to

defects and functional groups due to the modification of the SWNT band structure and relatively long exciton diffusion length. Throughout the majority of this research, a lack of UV-vis-nIR and PL data for dissolved SWNT fractions was an indication of possible functionalisations or the large abundance of highly defective material that quench photonic processes. Only upon increasing the yields to 100 wt % for raw HiPco SWNTs and drying the dispersions in the glove box (without heating) before exposure to air were vHS signals observed in UV-vis-nIR and PL spectra (Fig. III-23), indicating minimal functionalisation.
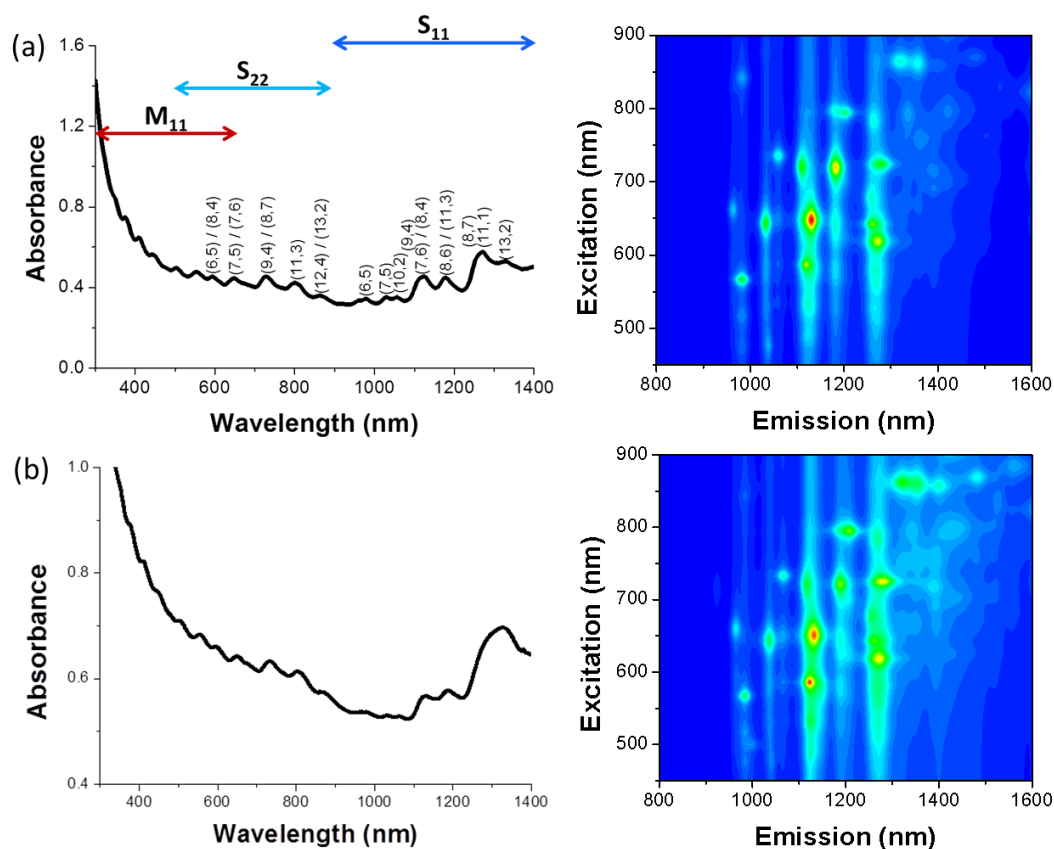
Fig. III-23 UV-vis-nIR and PL spectra of raw HiPco SWNTs before and after electrochemical treatment. (a) UV-vis-nIR and PL spectra for raw HiPco dispersion in 1 wt % DOC/D_2O using ultrasonication (150 W, 30 min) followed by ultracentrifugation (120000 g, 1 h). (b) UV-vis-nIR and PL spectra for raw HiPco SWNTs dissolved electrochemically in 1 mM NaClO$_4$/DMF at -2.3 V vs. Ag/Ag$^+$ for 3 days (100 wt % yield). The dispersion was subsequently dried in the glove box (without heating) before exposure to air, washed with DMF to remove the electrolytic salt and redispersed in 1 wt % DOC/D_2O using ultrasonication (150 W, 30 s) but no ultracentrifugation. Both sets of spectra are almost identical, showing that the SWNTs have not undergone significant functionalisation if any, upon exposure of the dried sample to air.

Further evidence for charge quenching and SWNT individualisation was achieved with thin film UV-vis-nIR spectroscopy of raw HiPco electrochemical dispersions. Dispersions produced in the glove box were drop-casted on to borosilicate glass microscope slides and left to dry without heating; resulting films were of high quality with no visible aggregates. One microscope slide was exposed to ambient conditions, while another was exposed to a pure O_2 atmosphere. The resulting UV-vis-nIR spectra (Fig. III-24) with well-defined vHS transitions suggest minimal functionalisation in both cases.
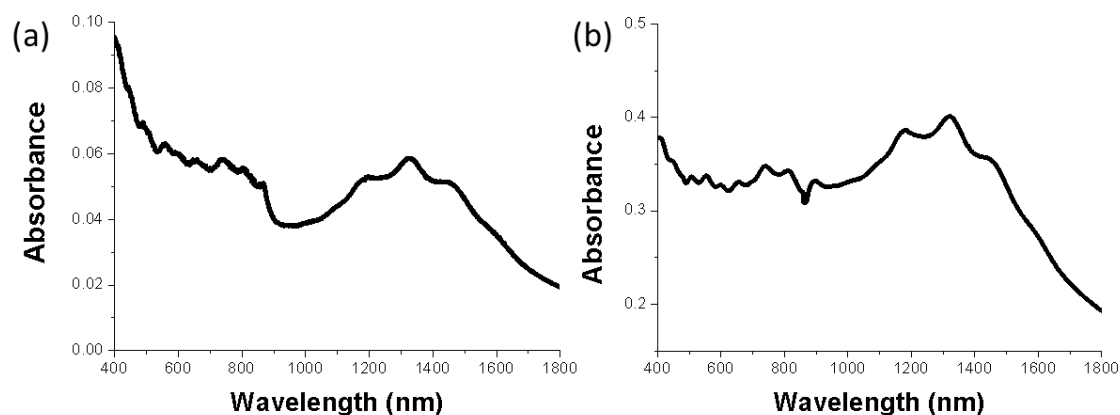
Fig. III-24 Thin film UV-vis-nIR absorption spectroscopy of electrochemically dissolved HiPco SWNTs. (a) Dried film exposed to ambient conditions, (b) dried film exposed to pure O_2 atmosphere. In both cases there is a large background contribution from the borosilicate glass; further sample was dried and redispersed in 1 wt % DOC/D_2O as shown in Fig. III-23.

III. 5. PRELIMINARY APPLICATIONS

III. 5. 1. SWNT functionalisations

Applications of reduced SWNT species benefit from the intrinsic dispersion mechanism without the use of ultrasonication that often leads to tube shortening and irreversible effects on (opto)electronic properties. The highly reactive nature of these species can also be a significant advantage if SWNT functionalisation is the end-goal; specific functional groups can be tailored to the application (increased solubility of SWNTs in different solvents, better matrix-adhesion in composites, *etc.*) and have been reviewed extensively.[273] The functionalisation of nanotubide species generated following electrochemical dissolution was performed with 1-iodododecane (IDD). Initial attempts showed inconclusive modification by TGA analysis in an oxidative

atmosphere. It later emerged following the development of an inert TGA methodology (60 mL min^{-1} N$_2$ flow rate with 90 minute purge time), that the grafted IDD was removed at a temperature close to the CoMoCAT decomposition temperature in air ($\sim$400-500°C), indicating the grafting is undetectable using oxidative TGA.

1 mL IDD was degassed (freeze-thawed, 5 cycles) and dried (3 Å molecular sieves, 48 h) prior to addition to 3 mL spontaneously dissolved CoMoCAT SWNTs ($\sim$1 mg mL^{-1}; $\sim$1 charge/20 C atoms) in DMF and stirred for 24 h. Subsequent filtration on to a 0.1 μm PTFE membrane was followed by washing with chloroform and water to remove any ungrafted IDD and the NaI by-product. The functionalised SWNT product had a gel-like feel and appearance (Fig. III-25c-e) that collapsed following washing and drying (Fig. III-25f); initial thoughts were that the dodecyl functionalities would cause extreme entanglement of the SWNTs, so it was decided that further soaking of the product in chloroform would be essential to remove excess IDD. After soaking for 72 h, the chloroform was exchanged for water, and soaked further. After drying, the product was similar in appearance to pieces of bucky paper and its weight was similar to the amount of CoMoCAT starting material used (2.6 mg). Unfortunately, solubility testing in different solvents (hexane, THF, toluene) revealed similar dispersability to the raw CoMoCAT powder.

From TGA analysis, the overall grafting constitutes $\sim$18.4 wt % material (Fig. III-25a, red curve); due to the presence of $\sim$5.1 wt % metal catalyst in the as-received material, this grafting gives a degree of functionalisation of $\sim$1 dodecyl per 58 C atoms, presenting a 34% yield for the amount of charge on the CoMoCAT SWNTs ($\sim$1 charge/20 C atoms). This yield is usually reported to be low, attributed to steric effects that limit functionalisation. Also, since it has been reported that reductive functionalisations occur predominantly at defect sites,[74] perhaps only the carbonaceous debris and short defective SWNTs that are preferentially dissolved in the electrochemical process are functionalised by IDD. This argument is also supported by most of the literature, in which pre-purifications (liquid- or gas-phase oxidations) are always performed prior to reductive functionalisations to remove impurities and metal catalyst particles; the use of sonication is also used to increase degrees of functionalisation. These aggressive treatments intrinsically create significantly more defect sites for reductive functionalisation to occur.

Raman spectroscopy (Fig. III-25b) was also used to confirm successful surface modification, revealing a slight increase in D peak intensity following functionalisation; the successful removal

of dodecyl groups following TGA treatment in an N_2 atmosphere was highlighted by the return of the D peak to that of the as-received material.
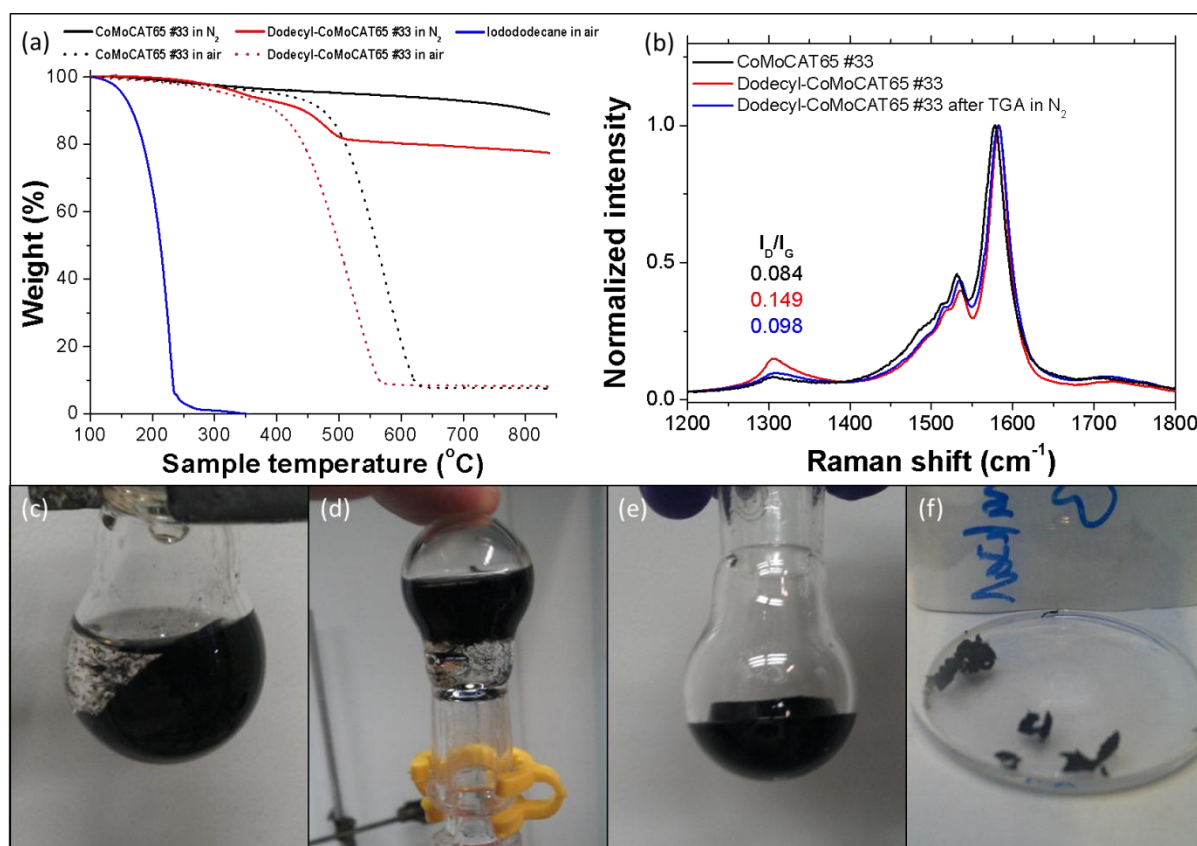
Fig. III-25 Functionalisation of electrochemically dissolved CoMoCAT SWNTs with 1-iodododecane (IDD). (a) TGA curves showing the decomposition of as-received CoMoCAT SWNTs in oxidative and inert atmospheres, CoMoCAT SWNTs following reaction with IDD in an oxidative and inert atmosphere, and pure IDD. (b) Raman analysis of raw CoMoCAT SWNTs, after IDD functionalisation and after TGA in an inert atmosphere using $E_{laser} = 1.96$ eV. Each spectrum is an average of 5 scans at different positions. Intensities are normalized to the G peak. (c)-(e) Photographs showing the gel-like product following reaction with IDD. (f) Photograph showing the product following several washing steps (membrane filtration, soaking) to remove unreacted IDD and NaI.

III. 5. 2. Device fabrication

The use of spontaneously dissolved SWNTs for device fabrication has significant advantages over current devices manufactured following liquid-phase exfoliation *via* sonication and ultracentrifugation. As part of an industrial collaboration (Linde Nanomaterials, CA, USA) on the spontaneous dissolution of nanotubides in DMF following Na^+/liquid ammonia reduction, the development of transparent conducting film (TCF) devices led to subsequent testing using HiPco SWNTs dissolved using the electrochemical reduction mechanism (Fig. III-26). TCFs were produced at Linde using a spin-coating deposition process on glass disks in a nitrogen-filled glove box. After five layers of spin-coating were performed, a soft bake, clean dry air oxidation (overnight), and two post-washing cycles were carried out to remove the solvent, quench the charge and wash away electrolytic salts respectively.
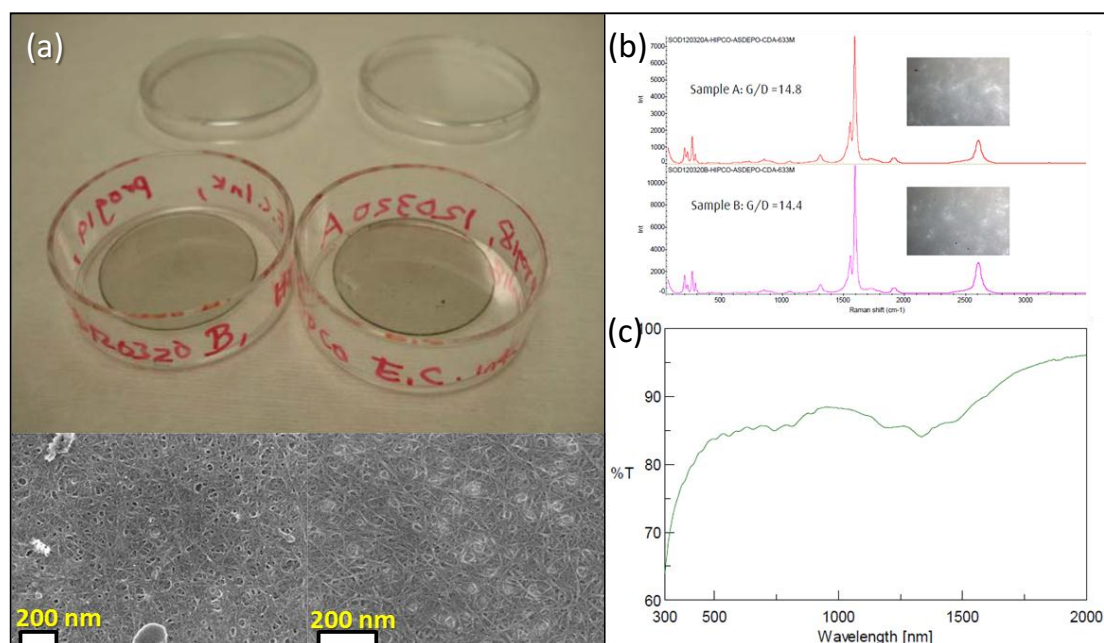
Fig. III-26 TCFs produced using electrochemically dissolved HiPco SWNTs. (a) Photographs of two TCFs produced. SEM images of these films are shown below. (b) Raman spectra of the as deposited TCFs following clean dry air oxidation showing very similar RBM features and I_G/I_D ratios. Inset images show optical microscope images of the films. (c) UV-vis-nIR transmission spectra of an as-deposited TCF (sample A), the distinct vHS are apparent.

The best TCF performance was obtained following acid washing, a process previously reported to dope TCFs,[274] giving a sheet resistance of ~1 kΩ sq^{-1} with 85% transparency @ 550 nm in both samples. SEM images of as-deposited films also showed highly uniform samples

with very similar Raman spectra. From a previous TCF study in the literature, typical plots of sheet resistance *vs.* transparency showed modest results for HiPco TCFs (Fig. III-27), produced by spray-coating aqueous dispersions (0.3 mg ml^{-1} SWNT concentration in 3 mg mL^{-1} SDS/H$_2$O; bath sonication, 400 W for 10 h; centrifugation, 10000 *g*, 10 min) on to PET substrates.[275] Material qualities such as purity, bundle length and diameter, defects, metallicity, and the degree of dispersion of SWNTs are the most important factors that influence TCF performance.[276] The TCF performance of electrochemically dissolved HiPco SWNTs (1 kΩ sq^{-1} at 85% T @ 550 nm), was slightly better than previously reported, primarily due to the benefit of significantly milder processing involved (avoiding sonication), but also may suggest improvements on the degree of dispersion. Furthermore, modest performance was observed without any purification of the SWNTs; removal of initial fractions containing defective SWNTs may result in additional TCF conductivity. However, further studies are required to discover the optimum oxidation and washing procedures.
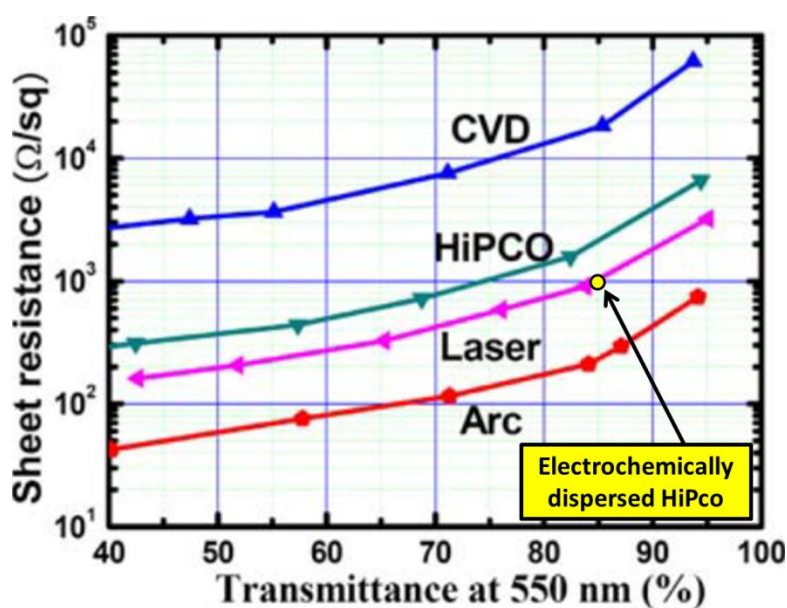
Fig. III-27 Characteristic curves of sheet resistance–transmittance of TCFs fabricated using various SWNTs. Each curve contains several data points from TCFs with different number of sprays of SWNT solution dispersed in deionised water with SDS. More sprays were applied to TCFs with data points in the left of the figure with low transmittance. Transmittance at 550 nm was selected for comparison. The comparison for electrochemically dispersed HiPco SWNTs is shown by the yellow circle. Modified from ref. 275.

III. 6. SUMMARY

In this chapter, an electrochemical dissolution process for single-walled carbon nanotubes that under specific conditions can generate solutions of relatively high concentrations (> 1.5 mg mL^{-1}) has been demonstrated. Through process development, the dissolution yields were increased from < 5 wt % to 100 wt %, no longer limited due to the presence of moisture that provided competing electrolysis reactions. This significant enhancement of yield makes the electrochemical dissolution route very attractive for larger scale processing, especially since the process is non-destructive towards SWNT structures, allows purification of later fractions or undissolved material, and most importantly retains SWNT (opto)electronic properties. Also, the avoidance of unpleasant reagents (pure alkali metals, liquid ammonia, and superacids), aggressive oxidative purification, sonication and lengthy ultracentrifugation make this process an ideal replacement to conventional strategies.

In terms of the nature of the dissolved material, the hypothesised preferential dissolution of large diameter, metallic SWNTs based on dielectric differences was observed, however, this result appeared to be misleading. The move to performing electrochemical dissolutions in a glove box resulted in significantly dryer electrolytes ($\sim$5-10 ppm), leading to less selectivity as larger quantities of SWNTs dissolved more rapidly. The hypothesis may still hold if it is the case that metallic SWNTs dissolve in the initial fraction with large amounts of defective and metallic debris that prevent their characterisation using traditional methods (UV-vis-nIR). However, the presence of water clearly plays a significant role, slowing the rate of SWNT dissolution and providing possible surface functionalisations, accentuating the selectivity of the process, albeit at a very low yield.

Quenching of the nanotubide dispersions is also another area where selective functionalisations are possible, avoiding such reactions is challenging since atmospheric O_2, CO_2 and H_2O behave very differently. The exposure of nanotubide dispersions in DMF to air is likely to generate protonated SWNTs through functionalisation with H_2O rather than O_2 due to the rapid rate of uptake of H_2O ($\sim$24 ppm per minute) in DMF compared to O_2 (2-3 ppm per minute). The exposure of dried nanotubide dispersions to air is likely to result in charge quenching by O_2 (followed by the generation of alkali metal superoxide), although the level of humidity may be sufficient that some degree of functionalisation also occurs. CO_2 exposure to nanotubide dispersions/powders is likely to from carbonate moieties on the SWNT surface that

remain negatively charged until exposed to moisture or oxygen. A more suitable approach to the quenching of nanotubide dispersions is to perform electrochemical depositions (Chapter IV) in order to obtain SWNT deposits at controlled potentials.

Since the redox potentials of SWNTs are well known,[273] in principle, given the prominent features in CV data (Fig. III-8), selective dissolution of SWNTs of specific diameter, helicity or electronic type should be possible. However, the effects of multiple charging are as yet unknown; dielectric effects, for example, may play a key role in defining the dissolution of specific SWNTs. Ultimately, entanglement effects may prevent the selective dissolution of SWNTs; further experimental and thoretical work is required. Alternatively, the selectivity of electrochemical depositions should be enhanced as the nanotubide species are individually dispersed and their redox potentials should be more distinct. Also, this process would be more attractive as the same electrochemical cell can be used, and a multitude of different electrodes (metallic, transparent, flexible) can be used depending on the end-application of the deposited SWNTs.

Aside from the dissolution process, nanotubide functionalisations have been investigated using a standard alkylation route to demonstrate the reactivity of electrochemically dissolved SWNTs. The development of TCF devices based on electrochemically dissolved SWNTs without the need for typical sonication and ultracentrifugation has also been demonstrated. However, the correct selection of starting material and washing procedures are essential for such devices, improving the dissolution of long, high purity SWNTs should provide significantly improved TCF performance.

Finally, the cyclic voltammetric behaviour of SWNT electrodes has been demonstrated to follow the structure of the electronic DOS. CoMoCAT SWNTs and well-defined, highly crystalline Meijo SWNTs revealed distinct features that are attributed to the filling of the sc-SWNT DOS; further work is required to realize the same observations for m-SWNTs, if possible. SWNT electrodes appear to have an extremely high sensitivity to the presence of trace water and the potential for these peaks to overlap with those of the vHS is apparent. On the other hand, this sensitivity may be advantageous, as CV could become a highly useful tool in characterising small changes in SWNT sample behaviour, such as identifying an increase in surface oxides following purification and functionalisation, or an increase in surface area (accessible inner channels) following tube end-chopping essential for hierarchical assemblies (*e.g.* peapods[277]). In the future, CV could become a useful bulk characterisation tool for measuring the

changes in the content of m- *vs.* sc-SWNTs following selective growth or post-synthetic sorting procedures, and could be adapted for use in parallel with spectroscopic techniques for the enhancement of understanding SWNT sample character.

IV. ELECTROCHEMICAL DEPOSITION OF SWNTS

IV. 1. INTRODUCTION

Following the electrochemical dissolution of SWNTs the next stage was to explore the possibility for electrochemical deposition with the purpose of processing SWNT constructs, successfully charge quench nanotubide species, and obtain additional evidence for selectivity towards specific SWNT properties. It was hypothesised that the highly individualised SWNTs following the dissolution process would be more discrete following disentanglement. Consequently, it should be possible to electrochemically deposit different SWNT types at different electrode potentials, ideally, forming dense, uniform coatings. Previously, carbon nanotube deposition has been performed dielectrophoretically[28] at excessive ac voltages (10 V, 10 MHz) to separate metallic from semi-conducting SWNTs. Mild electrochemical processing offers much stricter control over the deposition potential and should ultimately allow for the selective deposition of material that is spontaneously dissolved in the first stage of the process. Using the same electrochemical cells as used for the dissolution process, the aim was to demonstrate dissolution and deposition of SWNT material in the same system for ease of processing.

IV. 2. EXPERIMENTAL CONSIDERATIONS AND DEVELOPMENTS

Many electrochemical deposition techniques are an art form, perfected over the last few centuries since the pioneering work of Luigi Brugnatelli[278] in 1805. There are now many industrial processes (see copper purification process, section I. 5) involving the reduction of metal ions from aqueous, organic, and fused-salt electrolytes.[279] The electrodeposition of aluminium in toluene electrolytes under an inert atmosphere is a key example of non-aqueous electrodeposition that has since been developed on an industrial scale.[184] The application to

nanoparticle anions requiring similar experimental conditions for electrodeposition could thus be developed on a significantly large scale.

Experimental considerations include the shape and material of the electrode for deposition, concentration of nanotubide anions and supporting electrolyte ions, the use of additives, potential for deposition or peak current density, and fixed potentio/galvanostatic or pulsed electrochemical deposition techniques. Due to a significant number of variables, pulsed waveforms were not studied but may be a useful avenue for further development.

IV. 2. 1. Electrodeposition parameters

The crystal grain structure of an electrodeposit is dependent on the relative rates of nucleation and growth.[280] High nucleation rates give rise to a larger number of grains; combined with a low growth rate, a fine grain structure is expected. These processes are intrinsically linked to mass transport and charge-transfer control. In the present study, nucleation should be favoured by low nanotubide concentrations and high overpotentials, whilst growth will be favoured by high nanotubide concentrations and low overpotentials. In general, multiple parameters, including nanotubide ion concentration, additives, current density, temperature, agitation, and polarization, may all have a significant effect on deposit structure. Fig. IV-1 shows how a typical metal electrodeposit structure varies with an increase in specific parameters; the same principles are thought to govern SWNTs, although randomly oriented packing is expected. In order to create a dense, fine grain structured deposit, it is essential that low metal ion concentrations are used with low temperatures and minimal agitation. The increase in addition agents[281] (organic/inorganic compounds and surfactants), current density and polarization will also be beneficial to good quality deposition.
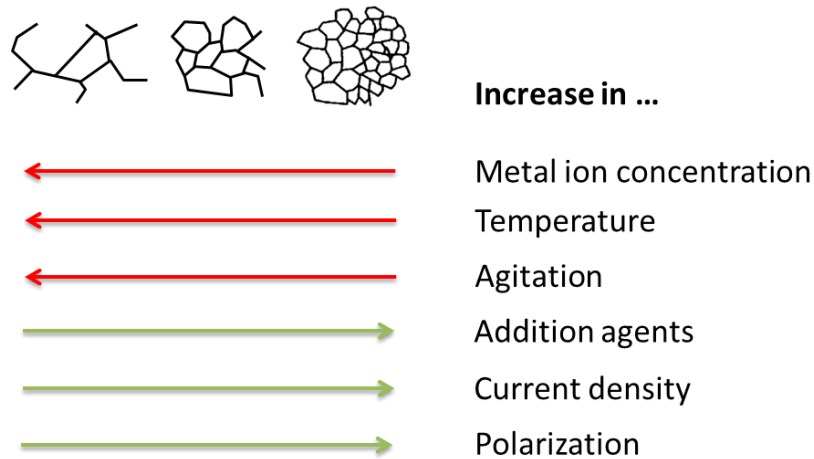
Fig. IV-1 The change in metal electrodeposit structure with varying parameters. The schematic structures represent deposit grain boundaries of decreasing grain size from left to right. Modified from ref. 280.

Diffusion was hypothesised to be the predominant mass transport mechanism during the SWNT electrochemical dissolution process, and would be expected to define the rate of electrodeposition. The translational and rotational diffusion coefficients of a rigid rod, D_{trans} and D_{rot}, respectively, are given by the equations:[282]

Equation IV-1
$$D_{trans} = \frac{k_B T}{6\pi\eta_s} \frac{2\ln\left(\frac{L}{d}\right) - \gamma_\parallel - \gamma_\perp}{L},$$

where k_B is the Boltzmann constant, T is the sample temperature, η_s is the solution viscosity, $\gamma_\perp$ and $\gamma_\parallel$ are end-correction coefficients, d is the effective rod diameter, and L is the rod length;

Equation IV-2
$$D_{rot} = \frac{3k_B T}{\pi\eta_s} \frac{\ln\left(\frac{L}{d}\right) - \gamma_r}{L^3},$$

where γ_r is a length-dependent end-correction coefficient.

Near-infrared fluorescence videomicroscopy was previously used to simultaneously study the translational and rotational diffusion of individual sc-SWNTs (raw HiPco) in 1 wt % SDBS/H_2O. SWNT lengths ranged from ~130−6000 nm, with diameter of the surfactant-wrapped SWNTs assumed to be 5 ± 2 nm. Translational diffusion coefficients ranged from ~1−6 μm^2 s^{-1}. Nanotubes of length ~500 nm are predicted to rotationally diffuse in water by an average of nearly 20° ms^{-1}, consequently, resolving the rotational motions of these shorter

species is difficult. The diffusion coefficients of $C_{60}{}^{n-}$ in 0.1 M TBAP in various aprotic solvents (with the exception of THF) decrease with increasing n, due to the increasing Stokes radius;[166] However, one would not expect this trend to follow for SWNTs, since the aspect ratio will not change significantly.

The observed timeframe of the dissolution process was significantly faster than these diffusion coefficients would suggest, implying the rate of diffusion is enhanced by electrostatic repulsion. Furthermore, the translational diffusion may be perturbed by the electric-field gradient present, especially with a low supporting electrolyte concentration. Nevertheless, in view of the apparently slow diffusion rates of nanotubide species, high nucleation and low growth rates should present themselves during the electrodeposition process, giving a fine grain structured deposit. However, the selective deposition of SWNT species may take an extremely long time to reach completion, especially with slow charge-transfer processes observed during the reductive dissolution process; to accelerate the process, slight agitation *via* stirring was later introduced.

IV. 2. 2. Electrodes for deposition

Several electrodes were tested for electrodepositions, including highly oriented pyrolytic graphite (HOPG), graphite foil, stainless steel foil, platinum wire and ITO coated glass. HOPG and graphite foils were generally brittle; visualization of SWNT deposition was also difficult due to the black/grey colour of these electrodes. Stainless steel has a narrow electrochemical stability and showed little or no deposition; platinum wire on the other hand, showed promising deposition, but SWNT material was weakly bound and frequently dropped off the electrode back into the electrolyte upon removal from the electrochemical cell.

In terms of the quality of the deposition and ease of subsequent characterisation, ITO was preferred; Raman spectroscopy, thin-film UV-vis-nIR and PL, AFM and SEM characterisation methods could be carried out directly on the electrode itself without any damage to the sample. ITO electrodes could be cut to size, washed easily, and were more robust than other materials. In terms of the electrochemical stability of ITO, previous experiments[283] in aqueous solutions containing 0.1-1 M NaOH (Fig. IV-2) revealed the reduction of Sn(IV) oxide to Sn(II) or Sn under cathodic polarization at -1.5 V (*vs.* SCE). As a consequence, the light throughput in the visible region decreased from about 90% to 12%, as well as significant increase in surface

roughness observed by SEM (granular/bubble structures on the ITO surface combined with intergranular corrosion).
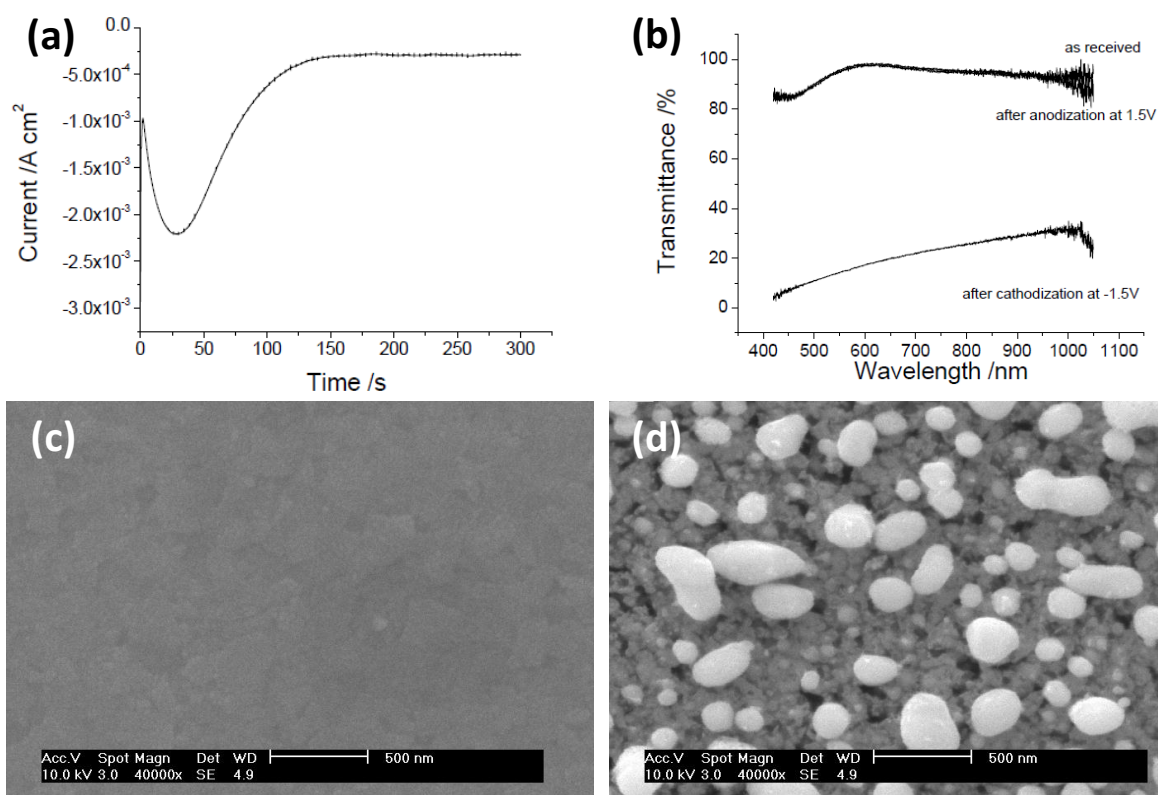
Fig. IV-2 ITO electrodes in aqueous 0.1 M NaOH electrolyte under anodic and cathodic polarization. (a) Cathodic polarization of ITO electrode at -1.5 V (*vs.* SCE) for 300 s. (b) Optical transmission of ITO electrodes before and after anodic/cathodic polarization. (c) SEM image of an as-received ITO electrode. (d) SEM image of an ITO electrode after cathodic polarization (-1.5V *vs.* SCE). No differences were observed following anodic polarizations. Modified from ref. 283.

Performing the same experiments in the DMF-based electrolytes used for electrochemical dissolution experiments allowed us to compare stability, and confirm whether ITO was a useful electrode material for nanotubide oxidations (Fig. IV-3). ITO showed excellent stability over the range -2.0 to +0.5 V *vs.* Ag/Ag$^+$ in 0.1 M NaClO$_4$/DMF (~-1.95 V to +0.55 *vs.* SCE), and showed no evidence of Sn(IV) reduction following UV-vis-nIR spectroscopy or SEM.
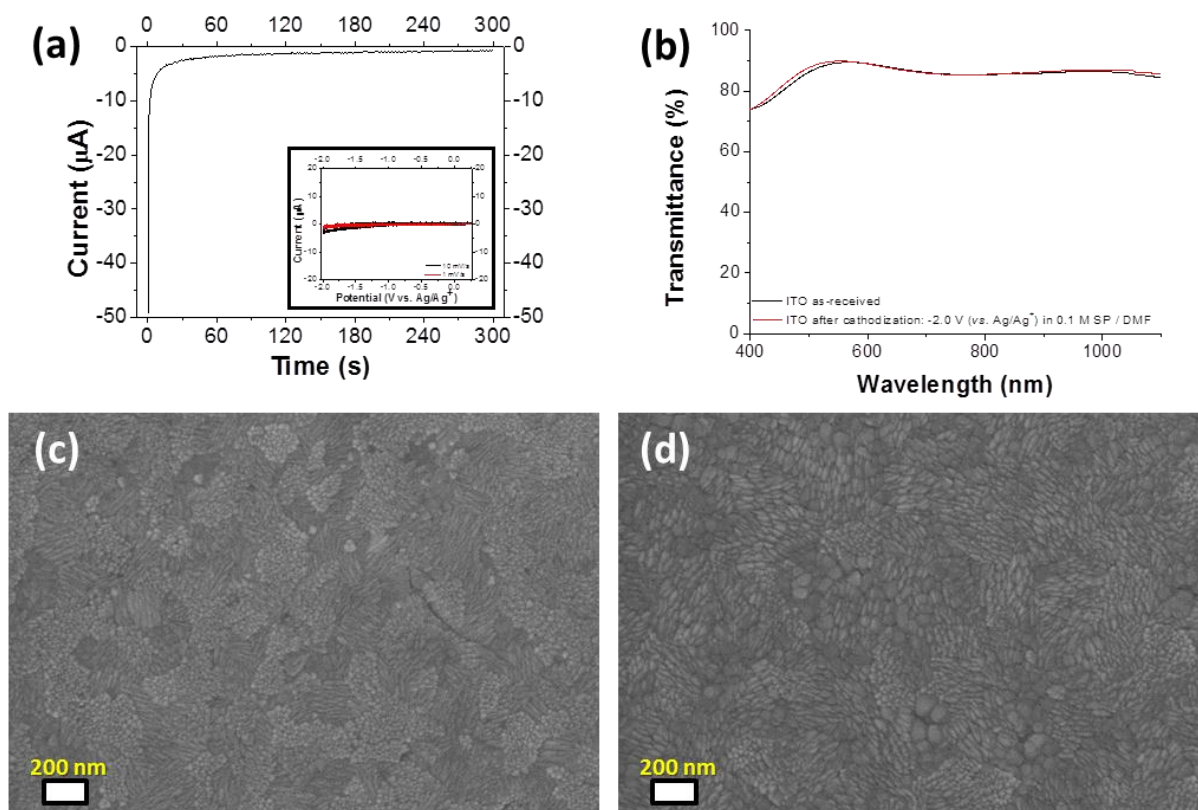
Fig. IV-3 ITO electrodes in 0.1 M NaClO$_4$/DMF electrolyte under cathodic polarization. (a) Cathodic polarization of ITO electrode at -2.0 V (*vs.* Ag/Ag$^+$) for 300 s. The inset shows a cyclic voltammetric scan over the range 0.25 V to -2.0 V (*vs.* Ag/Ag$^+$). (b) Optical transmission of ITO electrodes before and after cathodic polarization. (c) SEM image of an as-received ITO electrode. (d) SEM image of an ITO electrode after cathodic polarization (-2.0 V *vs.* Ag/Ag$^+$). No differences were observed following cathodic polarization suggesting high stability of ITO electrodes in DMF-based electrolyte.

IV. 2. 3. SWNT deposit characterisation

The amount of material deposited was generally small, so the use of non-destructive analytical techniques was important. Proof of concept studies were performed using platinum wire electrodes, which required the removal of SWNTs from the electrode by gentle sonication (bath). While characterisation of the SWNT properties is simple, characterising the morphology and quality of the deposition *via* this route was impossible since the deposit structure was no longer intact. Other advantages to using ITO are the potential for creating patterned electrodes that would allow the fabrication of devices. The disadvantages to using ITO glass electrodes are the high cost and limited supply of indium, the fragility and lack of flexibility of ITO layers; however, at this stage the main focus was towards small-scale device studies.

Microscopic characterisation of SWNT-ITO electrodes was impeded somewhat by the inherent surface roughness of ITO (large grain boundaries visible in AFM (Fig. IV-6)), although individual SWNTs could still be observed using AFM, and SEM could scan the overall surface morphology. Optical spectroscopies also highlighted ITO absorption, fluorescence, and Raman scattering signals. Raman characterisation of SWNT deposits was not an issue due to the strong resonance Raman scattering of SWNTs (required minor baseline correction).

IV. 2. 4. Experimental procedure development

The electrodeposition method was studied in parallel to the dissolution process, and has also undergone several developments including changes in electrochemical potential and electrode type, whilst also benefiting greatly from the dryer environment provided by the glove box. Initially, the electrochemical dissolution/deposition process did not incorporate a protected counter electrode, instead, the counter electrode was a means for the nanotubide species to deposit simultaneously. Using bucky paper working electrodes and Pt wire reference and counter electrodes, poor quality electrodeposits were observed. Typically, SWNTs would aggregate around the counter electrode, non-bound. The switch to powder based electrodes resulted in very thick, firm deposition to the Pt wire counter electrode, although still very brittle.

In this electrode layout, due to the unknown but likely extreme potentials of the counter electrode (see section III. 2. 3. 3), this deposition route was not favoured due to a lack of deposition potential control and a multitude of possible SWNT functionalisations. The development of the dissolution system with protected counter electrode meant depositions were not possible, and had to be carried out in a second process whereby the working electrode had to be changed for another electrode for subsequent deposition. This separation of the two processes allowed for more accurate electrode potential control, but could still be carried out in a continuous process if desired.

The results presented in this chapter are from experiments performed in the glove box environment due to concerns over the possible functionalisations and low dissolution yields during the Schlenk line reductive dissolution process that might have obscured any mechanisms for SWNT selectivity. These electrodeposition experiments and subsequent characterisation were performed in collaboration with Miss. Charlene Lawton during a supervised MSci project. The

optimised setup for electrodepositions is shown in Fig. IV-4; stirring (300 rpm) as a route to overcome the slow diffusion of nanotubides was introduced during process developments.
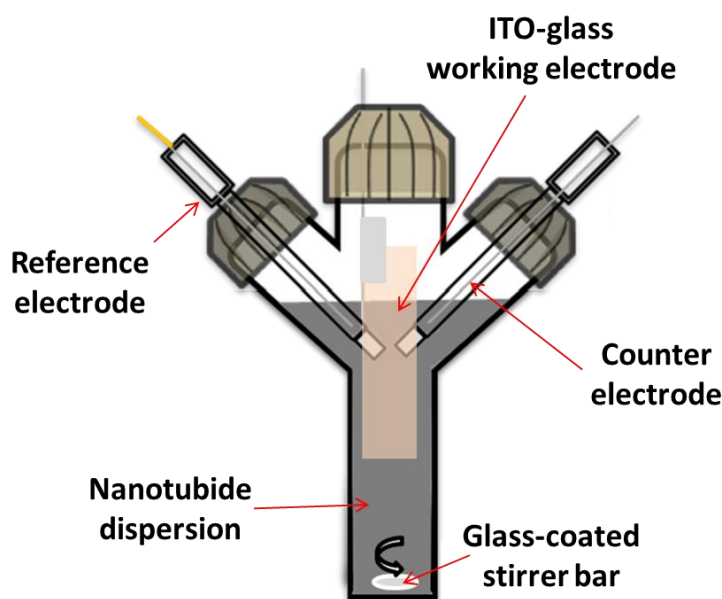
Fig. IV-4 Schematic diagram of the optimised electrodeposition setup showing the introduction of ITO-glass working electrode and glass-coated stirrer bar. SWNTs were initially dissolved using the reductive dissolution process outlined in chapter III. ITO-glass electrodes were cut to size (8 mm x 50 mm) and were held in place by a crocodile clip attached to a silver wire. The ITO electrode was only partly submerged in the nanotubide dispersion due to possible electrochemical corrosion of the stainless steel crocodile clip.

IV. 3. RESULTS

IV. 3. 1. Chronoamperometric deposition

Once all the SWNTs are solubilised as individual ions, selective electrodeposition at well-defined electrode potentials holds more promise for a scalable route to separation of distinct SWNTs than the dissolution step. Electrodeposition experiments were performed on both HiPco and CoMoCAT SWNTs since these materials showed effective reductive dissolution. CoMoCAT SWNTs stand out due to their notably defined CV characteristics (Fig. III-8b); apparent selectivity for these SWNTs should be more obvious. As for the dissolution process, electrodepositions were performed at constant potential; for the electrodeposition experiments

outlined in this section, an ITO-glass working electrode (anode) was inserted to replace the platinum plate electrode used for reductive dissolution of an SWNT cathode.

IV. 3. 1. 1. Electrodeposition proof of concept

In the following experiments, SWNTs were electrochemically dissolved using the methods outlined in chapter III. Electrodeposition of these nanotubide dispersions was either performed in the same electrochemical cell, or transferred to an identical cell using a syringe.

Initial tests were performed with HiPco SWNTs, dissolved in 1 mM STPB/DMF at -2.3 V to reductively dissolve all SWNTs. Preliminary electrodepositions were performed using an oxidation potential of +0.5 V. Whilst electrodeposition looked promising from Fig. IV-5, the deposition was very patchy and non-uniform. Deposition was only observed on the ITO side, suggesting dip-coating these electrodes into dispersion does not result in coating. Unfortunately, the majority of the remaining SWNTs in dispersion were no longer stable and flocculated from solution.

CoMoCAT SWNTs were then tested following complete dissolution at -2.3 V, 120 h. Electrodepositions were performed using a milder oxidation potential of -0.5 V. Observations of slight deposition but flocculation of the remainder of the dispersion indicated that the oxidation potential was still too severe. Raman spectra showed an identical makeup to that of the starting material, indicating all types of species present were deposited. It was decided that further experiments would require significantly milder oxidation potentials, to achieve better quality and potentially selective deposition.

Fig. IV-5 Photograph showing electrodeposition of HiPco SWNTs on an ITO electrode at +0.5 V, 24 h. Deposition is highly aggregated due to the extreme change in oxidation potential.

IV. 3. 1. 2. HiPco electrodeposition

Depositions at less extreme potentials were performed from -2.2 V to -0.6 V, at +0.2-0.4 V incremental potentials for 24 hours each, to identify whether selectivity could be performed during the deposition stage, and also to outline the potential where the dispersion will begin to flocculate. At each change in electrode potential, a fresh piece of ITO-glass was inserted. Washing in dry DMF was performed to remove excess non-deposited material as well as electrolytic salts, before exposing to atmosphere.

HiPco SWNTs (0.5-1 mg) were dissolved in 1 mM STPB/DMF (7 mL) at -2.3 V, 120 h, followed by their electrodeposition. HiPco SWNTs were observed to deposit at potentials more oxidising than -2.0 V, however, SWNT rebundling occurred at a potential of ~-1.2 V. The yield of deposition was low with the majority of remaining SWNTs agglomerated; the geometry of the current electrochemical cell and the slow diffusion of long SWNTs limited the deposits obtained to low thickness (~97% transmittance @ 550 nm). Deposition of the SWNTs on ITO electrodes was patchy, although there were large areas that showed high uniformity (Fig. IV-7). Of the electrode potentials studied, electrodeposits at -2.0 V and -1.4 V gave distinct RBM differences to the starting nanotubide dispersion (Fig. IV-8); deposits at -1.8 V and -1.6 V showed no change to the nanotubide dispersion.
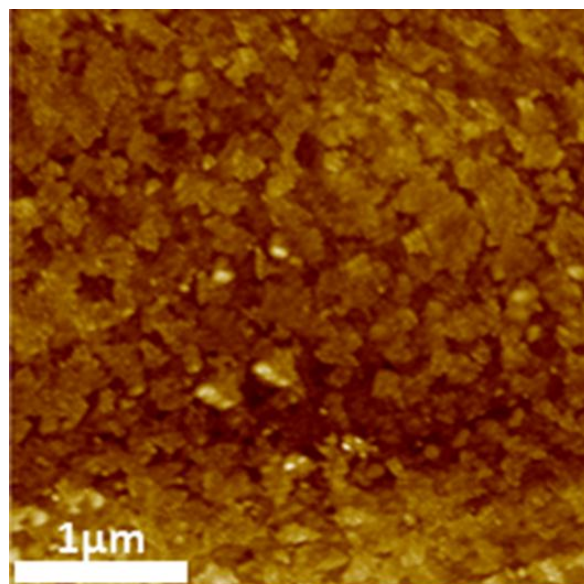
Fig. IV-6 AFM micrographs showing the surface of ITO coated glass electrodes. The ITO-glass has a rough surface with clearly defined grain boundaries (~350 nm sized grains).
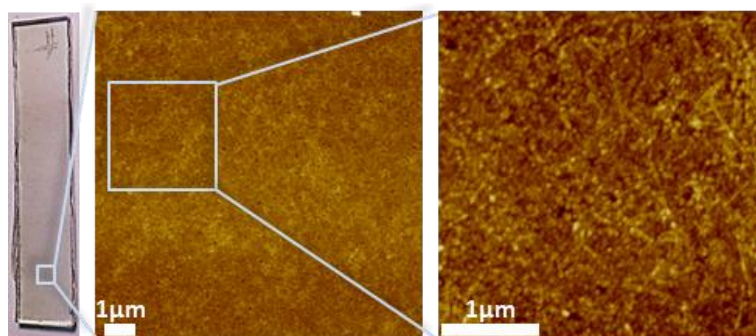
Fig. IV-7 Electrochemically deposited film of HiPco SWNTs on an ITO-glass electrode at -1.4 V, 24 h. Photograph (left) and AFM height micrographs (right) showing relatively large area, highly uniform SWNT network deposition.
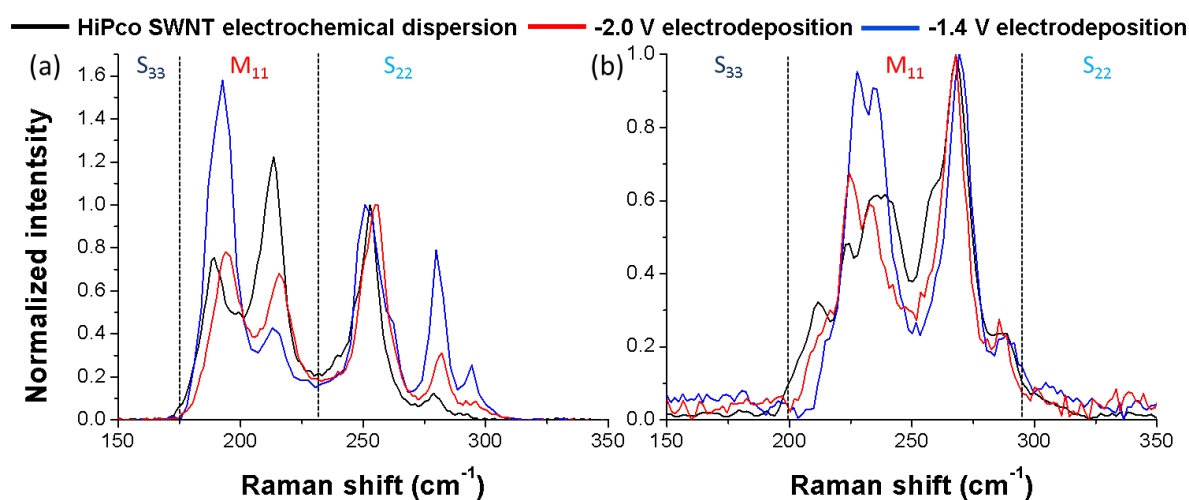
Fig. IV-8 Raman analysis of HiPco electrodeposits on ITO-glass electrodes at different electrode potentials using (a) E_{laser} = 1.96 eV, and (b) E_{laser} = 2.33 eV. Each spectrum is an average of 5 scans at different positions. Intensities are normalized to the 212 cm^{-1} RBM peak in (a), and to the 268 cm^{-1} RBM peak in (b).

Raman spectra using 1.96 eV laser excitation revealed striking features, especially for the -1.4 V deposited fraction. Here, the significant increase of the RBM at ~188 cm^{-1} *(12,6)* suggests preferential deposition of large diameter metallic species at more oxidising potentials. This enhancement is corroborated by spectra at 2.33 eV laser excitation, where the significant increase of RBM peaks at ~227 *(9,6)* and 234 cm^{-1} *(10,4)* are apparent. One other interesting observation using 1.96 eV excitaton is the relative increase in small diameter semi-conducting SWNTs at increasing oxidation potentials, which is peculiar since these species should have a significantly larger band gap than their larger diameter counterparts. One explanation could be the fact that these SWNTs are less stable in solution and are subsequently very easily deposited.

Another prominent feature is the lack of electrodeposition of the *(11,5)* species (~212 cm^{-1}), that gives a strong resonance in the dissolved fraction; the limited deposition of this species in further deposition experiments is also apparent as shown below.

Due to the apparent selectivity highlighted for HiPco SWNTs in these experiments, electrodepositions were repeated at even smaller voltage increments to see if further distinction over SWNT properties could be achieved. Potentials over the range -2.0 to -1.0 V were applied at +0.1 V increments for an extended period of 48 hours each to increase deposition yields, in view of the large amount of remaining material from the previous experiments. Typical SEM images of the deposited fractions are shown in Fig. IV-9. Again, deposition yields were low, however, Raman spectra (Fig. IV-10) highlighted prominent trends.
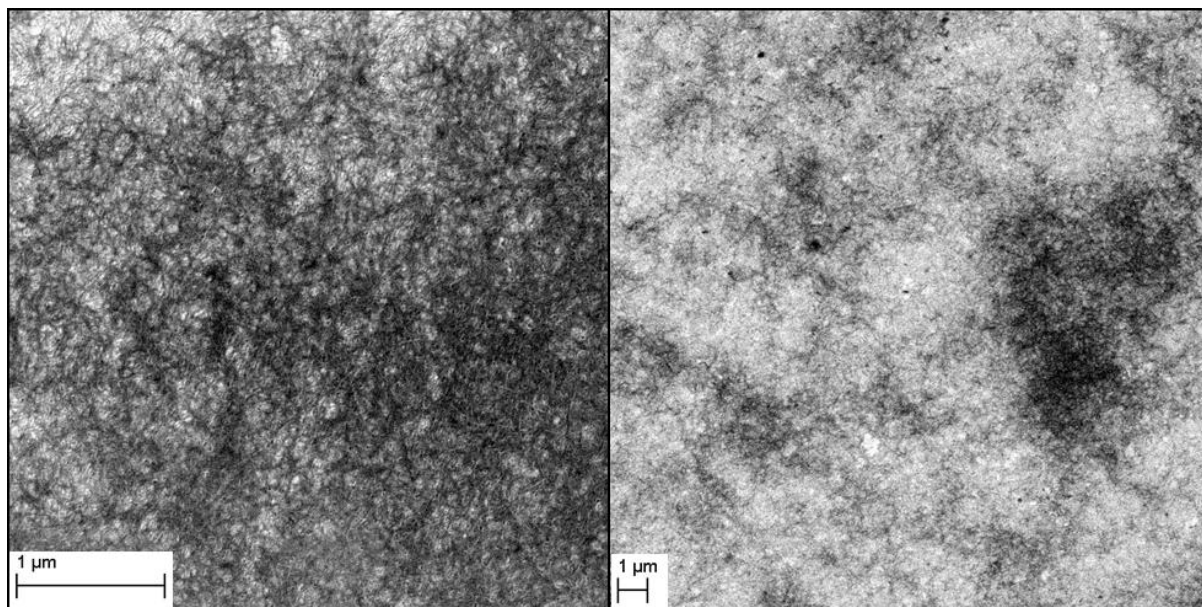
Fig. IV-9 SEM images of a HiPco electrodeposit on ITO-glass at -1.5 V, 24 h at different magnifications. Overall, deposition is patchy with the formation of relatively uniform large area SWNT networks.
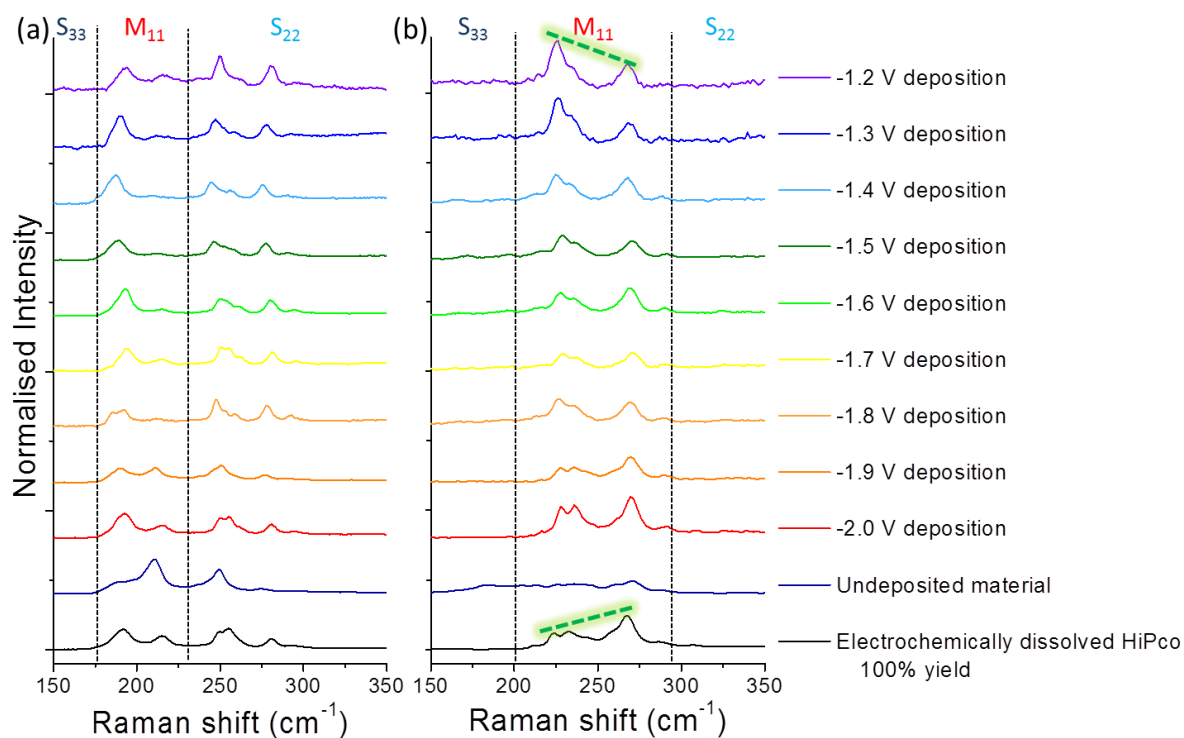
Fig. IV-10 Raman spectroscopy of HiPco electrodeposits on ITO-glass electrodes at +0.1 V increments using (a) E_{laser} = 1.96 eV, and (b) E_{laser} = 2.33 eV. Each spectrum is an average of 5 scans at different positions. Intensities are normalized to the G peak in each case and offset for clarification. Dashed green lines are added to indicate the trend in changing RBMs.

In these experiments, using 1.96 eV excitation, large diameter metallic species enrichment was not observed, although the poor deposition of the *(11,5)* was supported by its significant enhancement in the undeposited material, along with medium diameter semi-conducting species. Using 2.33 eV laser excitation, a definite trend of improved deposition of large diameter metallic SWNTs at increasingly oxidising potentials is apparent, especially in the -1.3 and -1.2 V fractions, where the RBM peaks at ~227 (9,6) and 234 cm^{-1} (10,4) dominate. Compared to earlier data (Fig. IV-8), this experiment showed less distinct changes in RBM data in line with incrementally smaller changes in electrochemical potential. It may be the case that different species have a wide deposition potential and therefore deposit over a wide range of potentials. One alternative issue could be the introduction of trace water with each electrode (surface adsorbed moisture on glass) that causes slight charge quenching leading to the observed flocculation.

IV. 3. 1. 3. CoMoCAT electrodeposition

Following the promising selectivity observed with the electrodeposition of HiPco SWNTs above, the deposition of CoMoCAT SWNTs was investigated at +0.1 V incremental potential control to identify possible preference for specific SWNT properties.

CoMoCAT SWNTs (7 mg) were dissolved in 1 mM $NaClO_4$/DMF (mL) at -2.3 $vs.$ Ag/Ag$^+$ for 120 h, to give ~100 wt % dissolved yield. The CoMoCAT dispersion was diluted from 1 mg mL^{-1} to 0.14 mg mL^{-1} to attempt to improve deposition quality. Electrodeposition onto ITO-glass electrodes was performed over the range -2.0 to -1.5 V (at which point the SWNTs flocculate) in +0.1 V increments for 48 hours at each stage. SEM showed that depositions were collected at all potentials, but appeared similar to those achieved using HiPco SWNTs (Fig. IV-11).
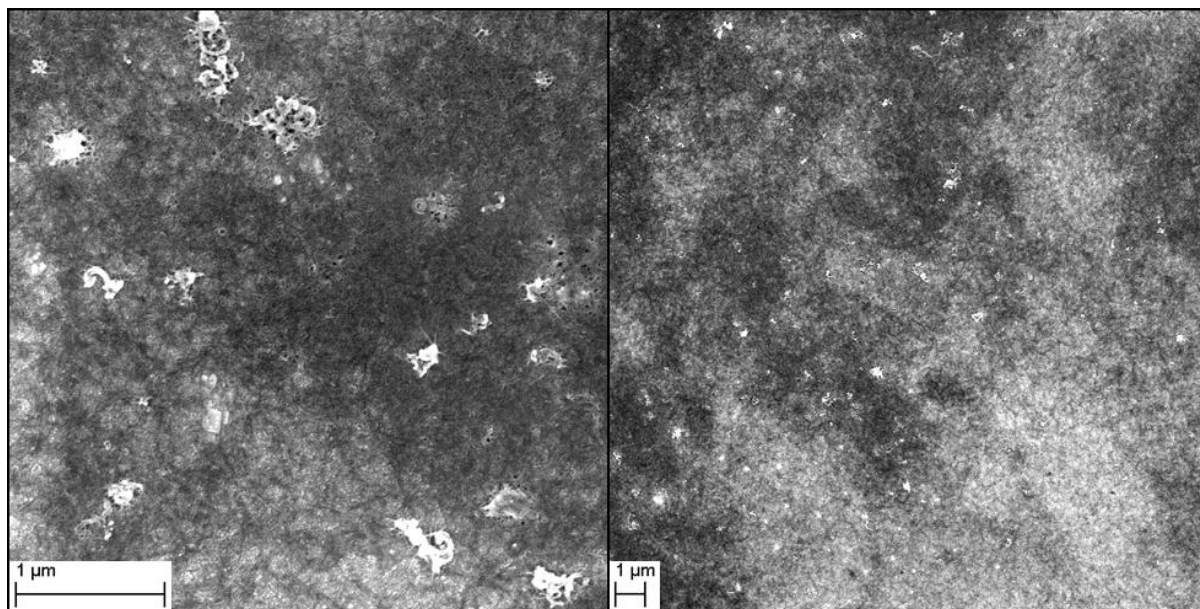
Fig. IV-11 SEM images of a CoMoCAT electrodeposit on ITO-glass at -1.5 V, 48 h at different magnifications.
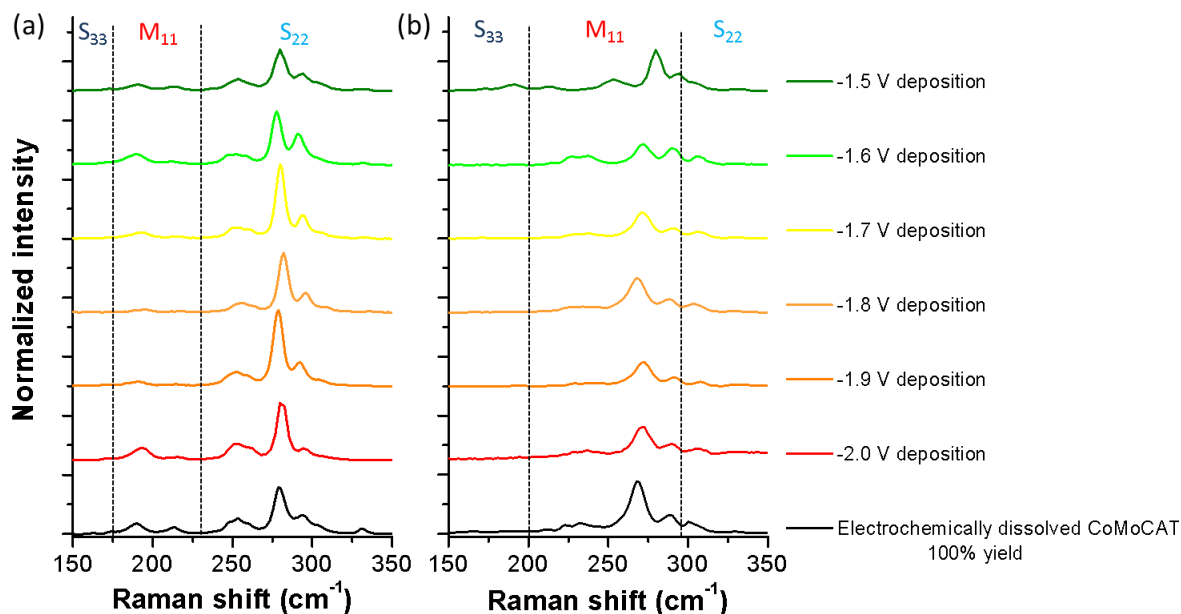
Fig. IV-12 Raman spectroscopy of CoMoCAT electrodeposits on ITO-glass electrodes at +0.1 V increments using (a) E_{laser} = 1.96 eV, and (b) E_{laser} = 2.33 eV. Each spectrum is an average of 5 scans at different positions. Intensities are normalized to the G peak in each case and offset for clarification.

Unfortunately, Raman spectra (Fig. IV-12) showed little evidence for preferential deposition; the significantly higher proportion of semi-conducting SWNTs in CoMoCAT samples meant changes in metallic species were less pronounced with 1.96 eV excitation. Using 2.33 eV excitation, there was slight relative enhancement of larger diameter metallic RBMs at -1.6 V and -1.5 V with the appearance of RBMs below 250 cm^{-1}. However, overall SWNT proportions remained relatively unchanged throughout.

IV. 4. DEPOSITION MECHANISMS

IV. 4. 1. Mechanisms for selective deposition

From the electrodeposition experiments presented here, weak diameter selectivity was achieved for HiPco SWNTs. The fact that this trend was not observed for CoMoCAT SWNTs suggests choice of starting material is important for sorting processes. CoMoCAT SWNTs manifest a very narrow diameter distribution that subsequently makes a diameter selective process inherently more difficult. During HiPco electrodeposition, it is presumed that selectivity was enhanced by reducing the effects of SWNT diffusion with the introduction of stirring, allowing

SWNTs of the same *(n,m)* type to deposit regardless of other factors such as length that slows diffusion.
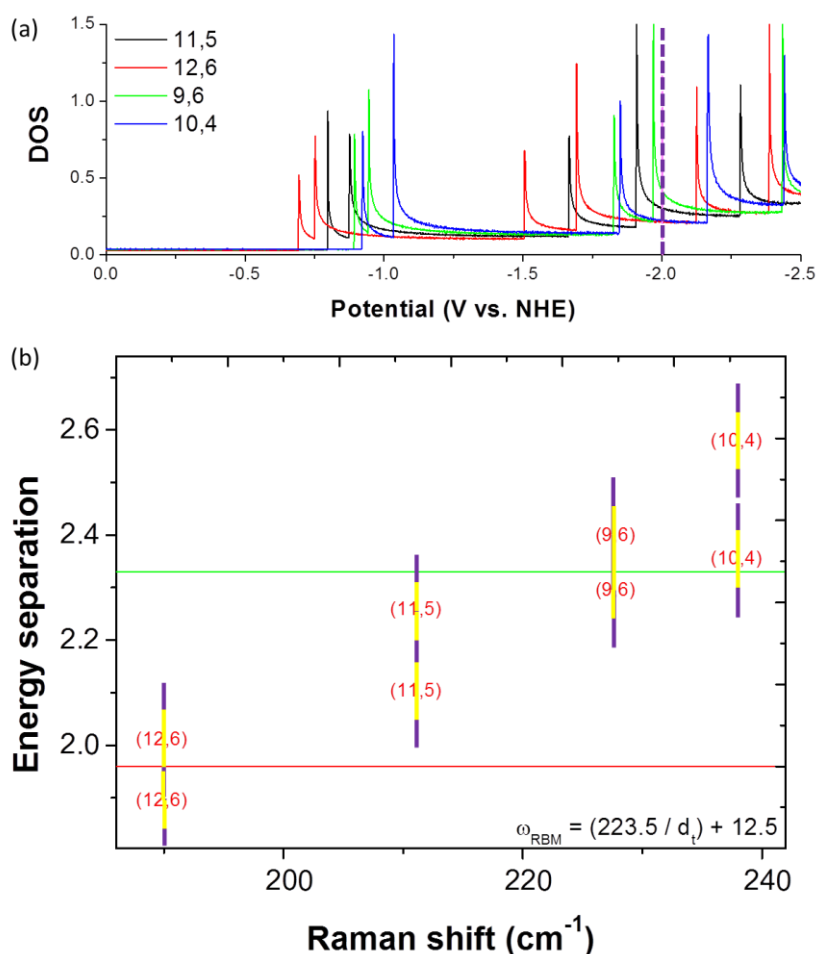
Fig. IV-13 DOS and excitation energies for selected metallic HiPco SWNTs. (a) Comparison of the DOS of (11,5), (12,6), (9,6) and (10,4) species. The dashed purple line at ~-2.0 V *vs.* NHE is the potential applied during electrochemical dissolution (-2.3 V *vs.* Ag/Ag$^+$). There are no distinguishable differences that would suggest poor deposition of the (11,5) SWNT. (b) M$_{11}$ transitions for the (11,5), (12,6), (9,6) and (10,4) species with respect to the 1.96 and 2.33 eV laser excitation energies (red and green lines, respectively). Purple vertical lines represent resonance profile width in bundled form,[200] yellow vertical lines represent profile width following debundling. The *(11,5)* falls out of resonance with debundling unlike the other m-SWNTs.

In general, reduction and subsequent oxidation should occur at more positive potentials for larger diameter SWNTs due to increased dielectric constants[28] and smaller band gaps (semi-conducting species). Studying the electronic DOS profiles for metallic HiPco SWNTs, it is

difficult to determine the mechanism of selective enrichment of the *(12,6)*, *(9,6)* and *(10,4)*, compared to the *(11,5)* tube that does not appear to deposit effectively (Fig. IV-13a). On the other hand, the effect of debundling that narrows the Raman resonance profile of these SWNTs could play a role. Technically, the *(11,5)* SWNT does not resonate with either laser used in the analysis; bundling effects in the starting material (drop-casted nanotubide dispersion) may give rise to a wider resonance profile. On the other hand, the *(12,6)* tube strongly resonates with the 1.96 eV laser, while the *(9,6)* and *(10,4)* species strongly resonate with the 2.33 eV laser (Fig. IV-13b). Further clarification is required with other spectroscopic techniques.

IV. 4. 2. Deposition morphology

Previous reports using AFM-CITS (Current Imaging Tunnelling Spectroscopy) show the electrical conductivity over the ITO surface is localised to the large crystal grains. Across single grains conductivity is relatively homogeneous, at the grain boundaries, however, relatively poor conductivity was highlighted by dark areas on the AFM-CITS image (Fig. IV-14).[284]
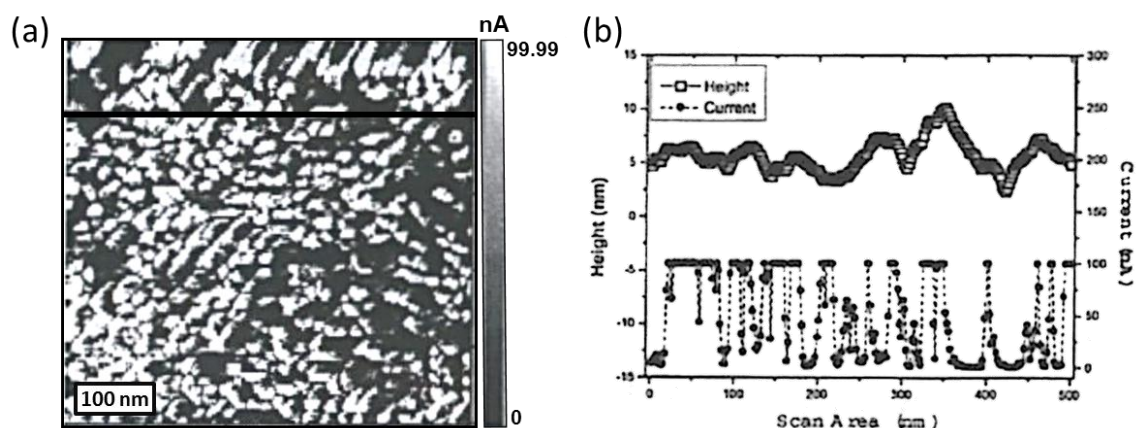
Fig. IV-14 AFM-Current Imaging Tunneling Spectroscopy (CITS) study of ITO films. (a) CITS image, (b) absolute height and tunnelling current of the line profile in (a). Modified from ref. 284.

Nucleation and growth of SWNT electrodeposits on ITO-glass electrodes is likely to be governed by the overall heterogeneity of the ITO electrode conductivity, seeded at multiple locations on these large crystal grains across the entire electrode surface. It is therefore not surprising that the resulting deposition is rather patchy in areas. To improve the surface morphology, more homogeneous deposition is likely to be achieved only by metallic electrodes where the electrical conductivity is significantly higher and homogenous.

IV. 4. 3. Mechanisms for charge quenching

An important consideration explored during the dissolution process was the potential for unwanted selective functionalisations. Following the electrodeposition process, SWNTs may still maintain a certain extent of charge; SWNTs deposited at -2.0 V, for example, have high energy electrons that still have the potential to react with water following exposure to the atmosphere. Following all electrodeposition experiments, significant washing with dry DMF was performed to remove loosely bound undeposited SWNTs, electrolytic salts. More recently, a separate electrochemical setup was introduced, containing 1 mM $NaClO_4$/DMF, whereby the potential of the SWNT-ITO electrode was swept from the electrodeposition potential to +0.19 V (open circuit potential (OCP) of the raw powder electrode before electrochemical dissolution) at a scan rate of 1 mV s^{-1} to discharge/deintercalate the SWNTs. However, following this process, the OCP immediately returned to the electrodeposition potential indicating an insufficient discharge again indicative of slow charge-transfer. This process is still in development, but could easily be improved by increasing the supporting electrolyte concentration (in the separate setup) to at least 0.1 M as used for CV experiments, or using more conductive metallic electrodes.

IV. 5. SUMMARY

Unlike the electrochemichemical dissolution process outlined in chapter III, electrodeposition has shown more promise for a scalable route to the separation of SWNTs by diameter or electronic character, vital for many applications such as thin conductive films (TCFs), nanoelectronic components, *etc*. Weak diameter selectivity dependence was observed during HiPco electrodeposition experiments, presumed to benefit due to the individualisation of nanotubide ions; entanglement effects may prevent the selective dissolution of SWNTs. There is still some way to go in fully defining SWNT selectivity and achieving high levels of enrichment of specific SWNTs; in doing so, further theoretical and experimental work is required to fully understand the mechanisms that give rise to selectivity following multiple charging events. Further areas of interest include the study of pulsed potentials to limit the deposition of unwanted SWNTs that may become entangled in the thick deposited networks, and different electrodes that are more conductive than ITO, including thin film metallic electrodes. Once selectivity is improved, subsequent cyclic voltammetric studies of the SWNT deposits could be used to confirm changes in sample character.

Unfortunately due to the very thin level of deposition, it has not been possible to observe vHS signals using UV-vis-nIR absorption or PL spectroscopy. In order to correlate selective deposition based on diameter, electronic character or helicity, it is necessary to increase the yield of deposition. Thicker films with more uniform morphologies of individualised SWNTs could be improved with cell redesign, finer potential control and the introduction of additives such as levelling agents and brighteners to enhance deposition quality. The type of brighteners widely used for traditional metal electrodeposition (organic/inorganic compounds and surfactants)[281] will need to be redesigned for the electrodeposition of nanotube anions.

V. Extension to other nanoparticle anions

V. 1. Introduction

Following the electrochemical dissolution of SWNTs it was hypothesised that the dissolution of many other nanoparticle anions should be possible without having to subject raw materials to ultrasonication and centrifugation. Primary candidates were other carbon nanomaterials, specifically multi-walled carbon nanotubes (MWNTs), with the objective of improving dispersability in composite matrices, and graphites, to develop a scalable approach to the production of single layer graphenes (SLGs). Initially, commercial and in-house grown MWNTs, fullerene (C_{60}), activated carbons, and graphite nanofibres were tested. Adapting the electrochemical dissolution process to other carbonaceous materials is relatively straightforward since these materials have relatively similar solubilities in the same non-aqueous solvents in their neutral forms; therefore, a dramatic change in electrolytic salt and solvent system would not be expected.

The possibility of extending the process to other non-carbonaceous materials was also a key objective, with the potential for the fundamental devlopment and study of nanoparticle anions; noble metal nanoparticles (*e.g.* silver) and layered transition metal dichalcogenides (MX_2, M_2X_3) were chosen as ideal candidates representing a scope of nanoparticles. For the dissolution of these systems, different solvents were investigated due to intrinsic solubility differences, as well as different electrolytes that offered varying degrees of intercalation.

The experimental procedures and setups were as used previously for the electrochemical dissolution of SWNTs (section III. 2. 5).

V. 2. RESULTS

V. 2. 1. Multi-walled carbon nanotubes

The obvious extension of the electrochemical dissolution process was initially applied to multi-walled carbon nanotubes (MWNTs). In terms of the electronic properties of MWNTs, the electronic DOS are a combination of all concentric tubes; the presence of both metallic and semi-conducting tubes within a MWNT structure will lead to an overall metallic character; therefore, the preferential dissolution of MWNTs with specific properties is likely to be governed by purity, diameter, and length effects. The obvious difference between SWNTs and MWNTs are the significantly larger mass of MWNTs due to the large diameters and greater number of walls, therefore, increased number of C atoms per unit length. Typical commercial CVD MWNTs (Nanocyl NC7000)[285] have ~6000 C atoms nm^{-1} based on their average diameter, 9.5 nm, and number of walls, ~6. In-house CVD MWNTs (average diameter 60-80 nm, ~30 walls) have > 200000 C atoms nm^{-1}; consequently, the dissolution process was expected to suffer from even slower diffusion of charged MWNTs compared to SWNTs (~100 C atoms nm^{-1}). On the other hand, the initial intercalation, exfoliation and repulsion stage is likely to proceed much faster since the surface area contact between neighbouring MWNTs is significantly smaller than SWNTs, thus, intertube vdW interactions are somewhat weaker.

Preliminary experiments were performed using the Schlenk line; chronoamperograms revealed purely capacitive behaviour as observed with SWNTs (related to electron doping of the electronic DOS). Commercial Nanocyl MWNTs showed slight dissolution, although diffusion of the charged species was slow, coupled with entanglement, leading to the MWNTs diffusing only within a few millimetres of the powder bed (Fig. V-1). Over time, MWNTs flocculated potentially as a result of water content (charge quenching/functionalisation). Subsequent experiments incorporated the agitation of the powder bed to aid the slow diffusion process, performed manually once per day by pausing the dissolution process and gently moving the platinum plunger electrode vertically before resuming. With added agitation, the electrochemical dissolution proceeded as normal, although yields were significantly lower than observed for SWNTs; entanglement effects may still dominate.
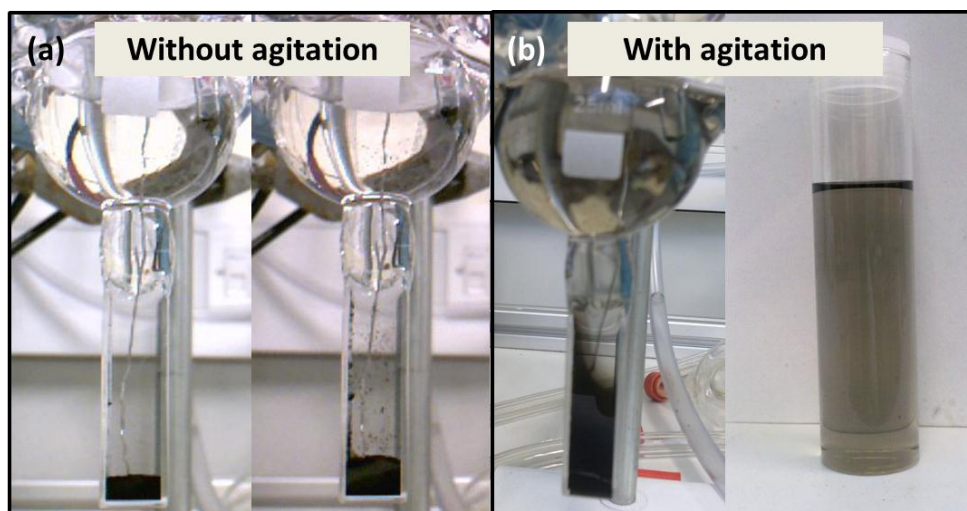
Fig. V-1 The effect of agitation on the electrochemical dissolution of Nanocyl MWNTs. (a) without agitation, flocculation occurs above the MWNT electrode powder bed, (b) following agitation ('plunger' movement of the platinum electrode) the quality of the nanotubide dispersion was significantly improved.

In-house grown injection CVD MWNTs (IH-MWNTs) were also investigated inside the glove box (Fig. V-2); IH-MWNTs showed increased dispersability (~20 x) using the electrochemical dissolution process (Fig. V-3) compared to mild bath sonication of the neutral species (previously performed by Dr. Robert Menzel)[286] with a yield of 5.4 wt %. Raman spectroscopy showed an increase in D peak contribution for the dissolved species, again implying amorphous and defective materials are dissolved preferentially, while TEM and SEM showed highly individualised MWNTs (Fig. V-2b-e) with the dissolution of relatively long species (> 10 μm).
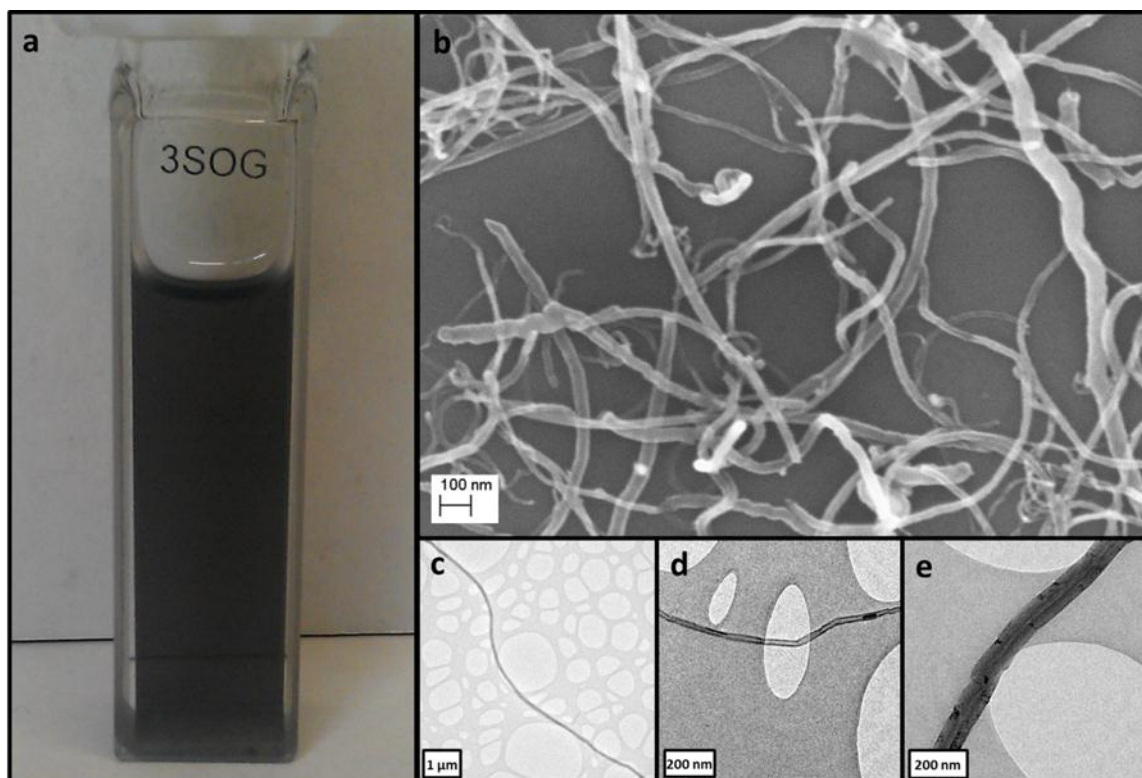
Fig. V-2 Electrochemical dissolution of IH-MWNTs in 1 mM STPB/DMF at -2.3 V *vs.* Ag/Ag$^+$ for 72 h. (a) Photograph, (b) SEM image and (c)-(e) TEM images showing IH-MWNTs following electrochemical dissolution.

In-house CVD MWNTs		Raman spectra (E_{laser} = 2.33 eV)
Concentration of MWNTs in DMF (mg mL^{-1}) (electrochemical dissolution *vs.* sonication bath)	~0.02 ~0.001	
Pristine MWNT A_D/A_G Ratio	0.29 ± 0.02	
Undissolved MWNTs A_D/A_G Ratio	0.33 ± 0.02	
Electrochemically dissolved MWNTs A_D/A_G Ratio	0.48 ± 0.02	
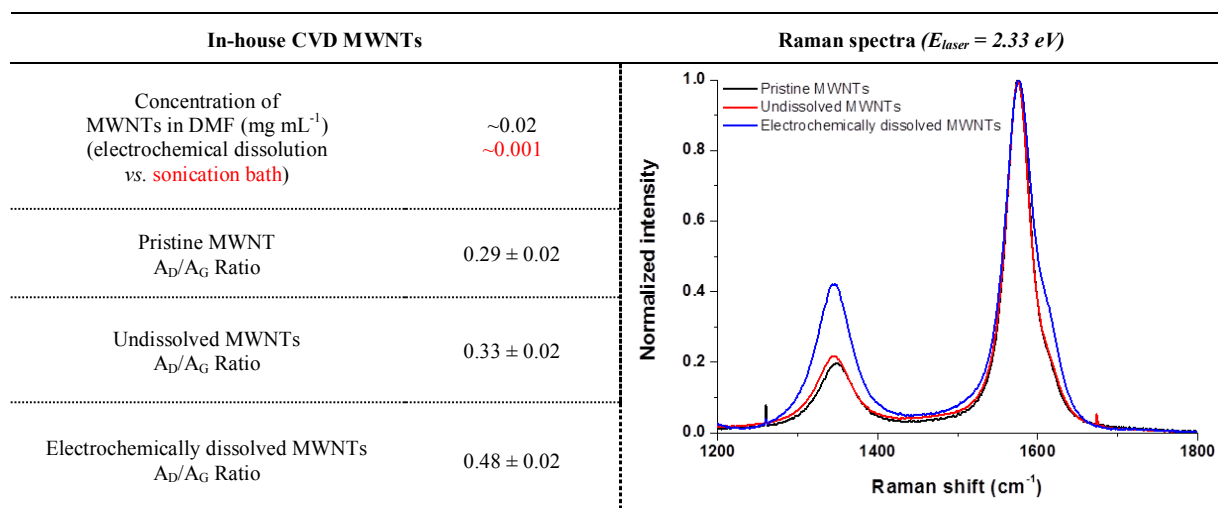
Fig. V-3 UV-vis-nIR and Raman spectroscopy of electrochemically dissolved IH-MWNTs. *Note*: the extinction coefficient for commercial Arkema MWNTs (3510 mL mg^{-1} m^{-1} @ 800 nm) was used to calculate MWNT concentrations.[287]

V. 2. 2. Graphene

Graphene's unique properties and potential applications have also been hampered by similar issues as witnessed with SWNT synthesis and processing in recent years. However, graphite is a fraction of the cost (~$6000 per tonne for the highest purity)[288] compared to SWNT powders. Choosing the appropriate type of graphite for the electrochemical dissolution process is challenging, as the shape and size of the graphene formed is likely to define the potential application. Carbon nanofibre platelet, CNF-PL (FutureCarbon GmbH, Bayreuth, Germany) electrodes were predominantly used since these structures were recently dissolved following a reductive chemical approach.[289] CNF-PL comprise several micrometre long fibres consisting of stacked 100-200 nm width graphite layers with a staggered surface structure (Fig. V-4a). Key advantages to using this material are the highly uniform size of platelets following exfoliation, and the absence of dislocations that tend to trap intercalant layers in natural and synthetic graphites.[290]

The intercalation of sodium ions into graphites is known to be significantly poorer than lithium or potassium ions, only generating NaC_{64} species in the vapour phase, but is a comparable intercalant in the solution phase.[291] Therefore, the same electrolyte systems as used for SWNTs could be trialled. KC_{8-24} graphite intercalation compounds (GICs) produced *via* K/liquid NH_3 reduction of CNF-PL showed poor dissolution in DMF, as observed during experiments performed by Mr. Patrick Cullen at UCL; however, potassium GICs did show spontaneous dissolution in THF and NMP albeit with markedly low yields. Significantly improved yields were observed with mild bath sonication (10 min), although not ideal for the present experiments. Slight adaptations were made to the experimental procedure following initial failings using 1 mM TBAP or STPB/DMF electrolytes. 1 mM potassium perchlorate (KP) in DMF was subsequently tested due to the limited solubility of KP in THF, and slight greying of the solution was observed following gentle agitation of the powder bed. Microscopy showed little evidence of the exfoliation of single layer graphenes, but some few layer flakes were observed (Fig. V-4b-c).
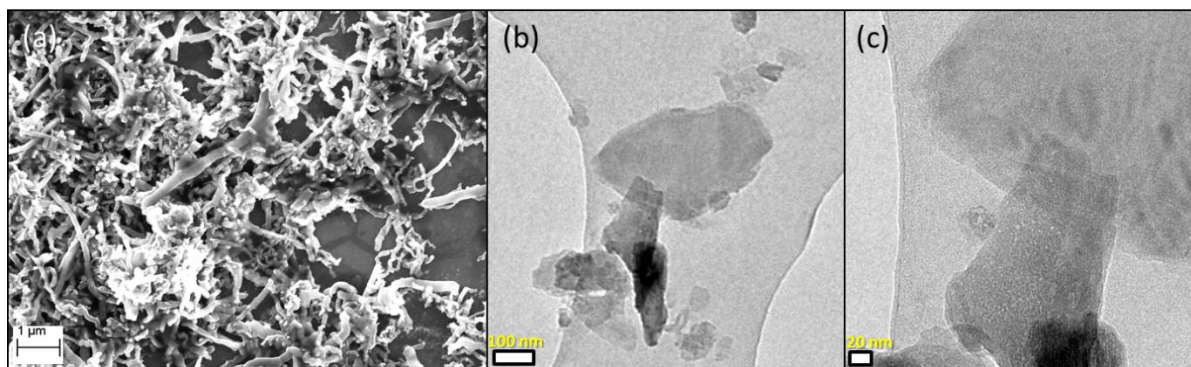
Fig. V-4 CNF-PL before and after electrochemical processing. (a) Raw CNF-PL mildly sonicated (bath) in THF. (b)-(c) Reductive dissolution of CNF-PL in 1 mM KP/DMF at -2.3 V *vs.* Ag/Ag$^+$, 120 h. The formation of small graphitic flakes is apparent, although these were only found in one location.

Attempts were then made to dissolve CNF-PL and natural flake graphite electrodes using a 1 mM lithium perchlorate (LiClO$_4$)/NMP based electrolyte. Although lithium does not expand the graphite lattice upon intercalation in dry systems, in the liquid-phase (THF as solvent), it is reported that lithium coordinates to up to four solvent molecules during intercalation, compared to just two for potassium.[291] NMP should be a better solvent for graphene due to a further increase in the inter-layer spacing as shown in Fig. V-5.
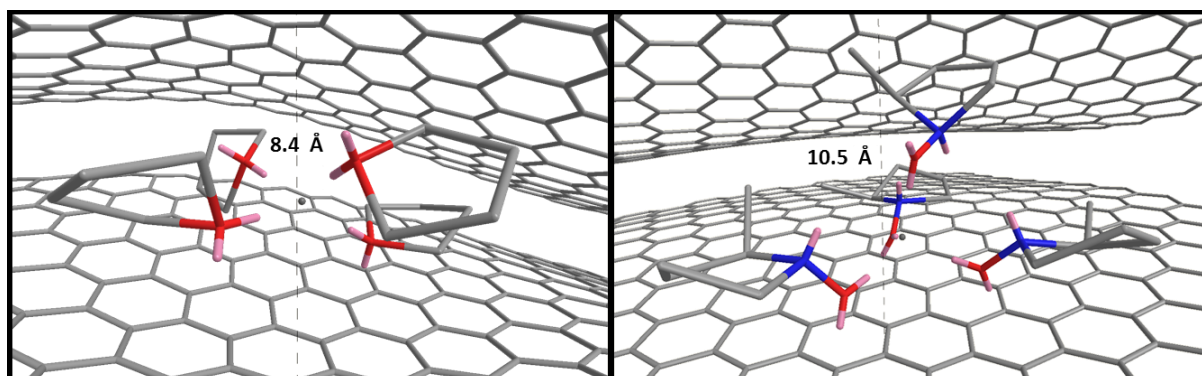
Fig. V-5 Simulation of lithium-solvent intercalation into the graphite lattice. (a) Lithium is encapsulated by four THF molecules giving an increase in layer spacing from ~3.4 to ~8.4 Å, changing THF to NMP should increase this layer spacing even further as shown in (b). In these models, simple MM2 energy minimizations were performed using ChemBio3D Ultra software to mimic previous XRD studies,[291] in which Li-THF intercalation increased the graphite layer spacing to 9.1 Å. The layer spacings reported in this figure are likely to be underestimated. This simplified model was used to determine the relative change in graphite layer spacing with varying solvent but is not a comprehensive study.

Constant potential charging of CNF-PL electrodes (-2.3 V *vs.* Ag/Ag$^+$, 1 mM LiClO$_4$/NMP, 3 days) generated no apparent swelling as typically observed with SWNT electrodes upon intercalation, however, stirring of the charged powder after 3 days led to the instant formation of a black dispersion. Stirring was continued overnight, and the dispersion left to settle. After 24 h, only some CNF-PL particles had precipitated, after 7 days, however, the dispersion had no visible colour indicating that the majority of the dispersion had settled out of solution. Typically, graphene solutions following chemical reductions are reported to have very low concentrations[292] (< 100 µg mL^{-1}), consequently, TEM samples were prepared using the dispersions following sedimentation to identify whether or not graphene was dissolved in solution. The observation of small platelet aggregates confirmed minimal exfoliation, but a promising step towards the isolation of SLGs.

A natural flake graphite electrode was then charged (-2.3 V *vs.* Ag/Ag+, 1 mM LiClO$_4$/NMP, 3 days) analogous to the CNF-PL electrode. No swelling was observed during the experiment, further stirring also showed a lack of any noticeable dissolution. However, TEM of the apparently clear solution revealed small quantities of micrometre sized few layer graphenes (Fig. V-7).
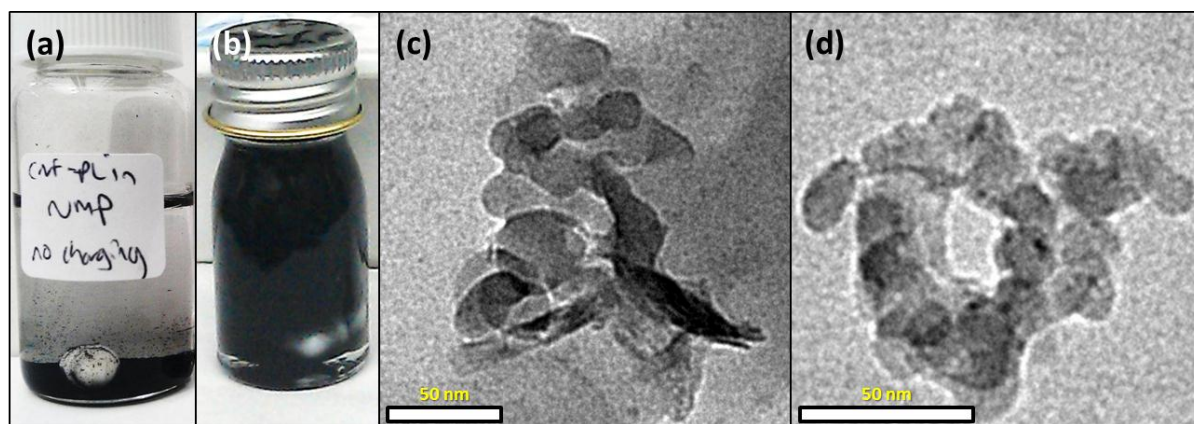
Fig. V-6 Electrochemical charging of a CNF-PL electrode in 1 mM LiClO$_4$/NMP at -2.3 V *vs.* Ag/Ag$^+$, 72 h. (a) Stirring of the neutral CNF-PL in NMP results in no dissolution. (b) Stirring of charged CNF-PL results in immediate dispersion that settles over a period of 7 days. (c)-(d) TEM images of the CNF-PL dispersion showing small agglomerated platelets.
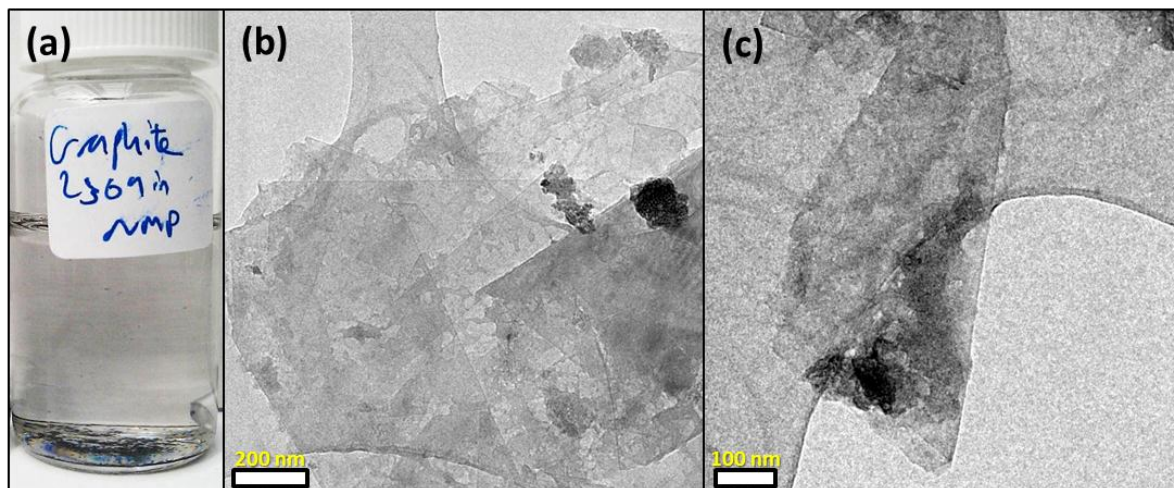
Fig. V-7 Electrochemical charging of a natural flake graphite powder electrode in 1 mM LiClO$_4$/NMP at -2.3 V *vs.* Ag/Ag$^+$, 72 h. (a) Stirring of the charged powder results in a slight grey solution, that quickly sediments within 24 hours. (b)-(c) TEM images of the grey dispersion showing exfoliated graphite with some evidence of few layer graphenes.

Comparing the chronoamperograms for the above reductive charging processes (Fig. V-8), after 72 hours the charge/carbon ratio reaches 1 charge/66 C atoms for the CNF-PL electrode, but only 1 charge/562 C atoms for the natural flake graphite electrode. This dramatic difference indicated very poor intercalation of the natural flake graphite electrode, perhaps as a result of the significantly larger dimension graphitic layers.
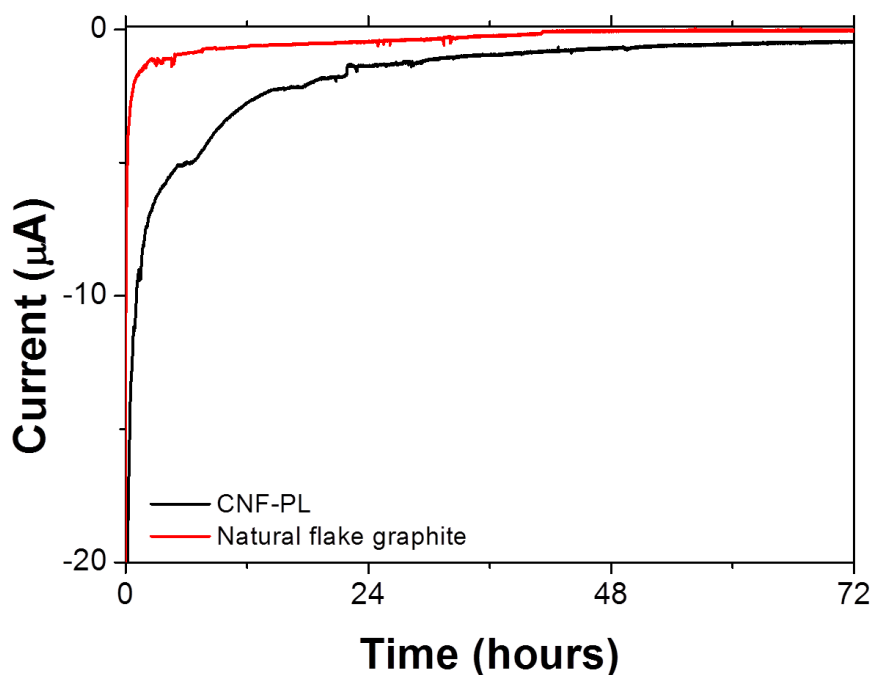
Fig. V-8 Chronoamperograms during the reductive charging of different graphitic electrodes in 1 mM $LiClO_4$/NMP at -2.3 V *vs.* Ag/Ag⁺, 72 h.

As an alternative to the difficult exfoliation and dissolution of single layer graphenes, we investigated the possible electrochemical reductive dissolution of graphene oxide (GO). Exfoliation should be inherently easier due to the significantly larger interlayer spacing[293] going from graphite (0.34 nm) to GO (~0.7 nm). Graphene oxide is known to be reduced electrochemically to form graphene, known as electrochemically reduced graphene oxide (ERGO), and has been achieved previously under constant potential control.[294] Attempts were made to dissolve commercial GO (NanoInnova Technologies, Madrid, Spain) and convert these layers to graphene in a one-pot process. Unfortunately, spontaneous dissolution did not occur, although small aggregates were generated above the powder bed. These observations may result from the significant degree of reductive reactions of the surface oxygen-containing functionalities that may generate a whole set of unknown side-reactions including the possible cross-linking of the graphite layers that would make dissolution impossible. Subsequent Raman spectroscopy showed slight improvement in I_D/I_G ratios suggesting partial reduction, but with minimal dissolution, the GO route is rather impractical.

Further studies should focus on the CNF-PL material as this has been successfully isolated as single layer graphenes following reduction with potassium/liquid NH_3 and subsequent

dissolution in NMP, albeit with mild sonication,[289] and showed improved electrochemical intercalation compared to natural flake graphite electrodes. Alternative solvents should also be investigated, especially propylene carbonate (PC), that is avoided in graphite electrode lithium ion batteries due to problematic exfoliation of the graphite layers,[295] a desirable end result in this research.

V. 2. 3. Fullerene

The dissolution of C_{60} in non-aqueous solvents is not a problem, high solubilities are found in 1-chloronapthalene[296] (51 mg mL^{-1}), although C_{60} is only sparingly soluble in DMF. Generally C_{60} forms clusters in solution[297] unless charged; subsequently, the electrochemical dissolution process was performed on a C_{60} powder anode using 1 mM TBAP/DMF as electrolyte. Traditional C_{60} electrochemistry is performed in the solution phase (section I. 4. 2), here, the solid state electrochemistry is probed, reported previously using a constant current approach.[298]

In the absence of sonication/agitation, C_{60} remained at the bottom of the electrochemical cell. At a constant potential of -2.3 V (*vs.* Ag/Ag$^+$), C_{60} was observed to dissolve in the electrolyte within 5 minutes, generating a mixture of different colours (Fig. V-9a-c) over 24 hours; these colours are a result of the formation of different fulleride anions (C_{60}, purple; C_{60}^-, dark red-purple; C_{60}^{2-}, red-orange; C_{60}^{3-}, dark red-brown).[299] Chronoamperograms (Fig. V-9d) showed a significant increase in current as a result of these redox events (not purely capacitive charging as observed for graphitic materials) until ~1 charge/2 C_{60} molecules was reached (~12 h); complete dissolution was achieved at a ratio of 1 charge/C_{60} molecule with concentrations of ~4 mg mL^{-1} after 24 h. This concentration is already greater than the solubility of neutral C_{60} in toluene (3 mg mL^{-1}), and could potentially be further increased with larger loadings.
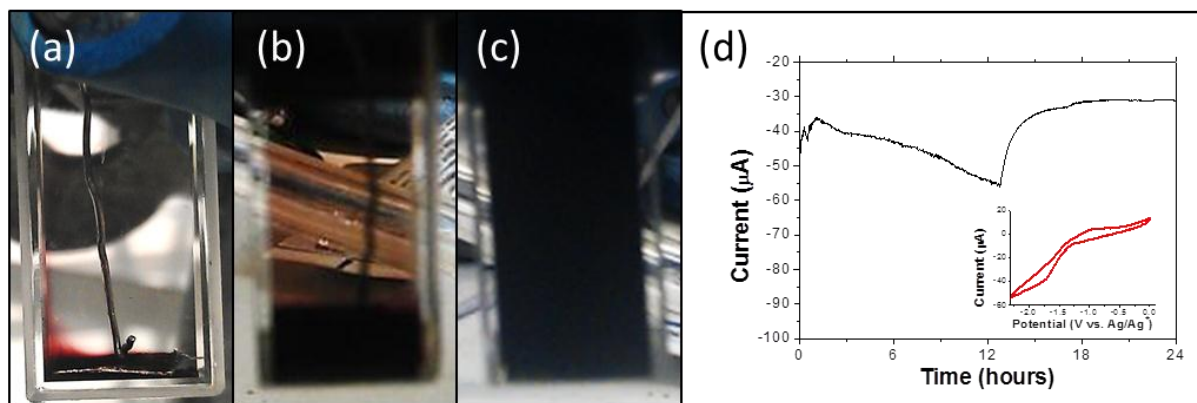
Fig. V-9 Photographs showing the spontaneous dissolution of fullerene anions. Here, 27 mg fullerene powder was dissolved in 1 mM TBAP/DMF at a potentiostatic voltage of -2.3 V *vs.* Ag/Ag^+ after (a) 5 min showing a dark red trail of C_{60}^- species, (b) 30 min showing an orange-yellow dispersion, (c) 24 h showing a very dark-brown dispersion (C_{60}^{3-}, or a mixture of C_{60} anions) after all of the powder had dissolved. (d) Chronoamperogram during the reductive dissolution process, inset: CV of the C_{60} powder electrode in 1 mM TBAP/DMF at a scan rate of 100 mV s^{-1}.

V. 2. 4. Activated carbon

Activated carbons are porous materials with very high surface area. Vulcan XC72R (Cabot Corporation, Billerica, MA, USA) used in this research, is used in applications ranging from power storage (batteries and fuel cells), conductive paper, conductive liquid dispersions and as catalyst supports;[300] TEM images reveal agglomerates containing nanoparticles of approx. 20-60 nm. The dissolution of activated carbons often requires mild sonication in the desired solvent; using the electrochemical process, Vulcan XC72R showed excellent dissolution in DMF based electrolytes without the aid of ultrasonication (Fig. V-10). A 100 wt % yield was obtained at a ratio of ~1 charge/91 C atoms, effectively representing defective materials that dissolve preferentially in SWNT/MWNT dissolution experiments. A concentration of ~0.34 mg mL^{-1} was measured by the dried mass of a 5 mL fraction. Measurements of the UV-vis-nIR absorption of a series of dilutions of the initial electrochemical dispersion gave an extinction coefficient of 3696 mL mg^{-1} m^{-1} @ 660 nm, on the order of SWNTs (HiPco SWNTs in NMP, 3264 mL mg^{-1} m^{-1} @ 660 nm) and other carbonaceous materials.[212]
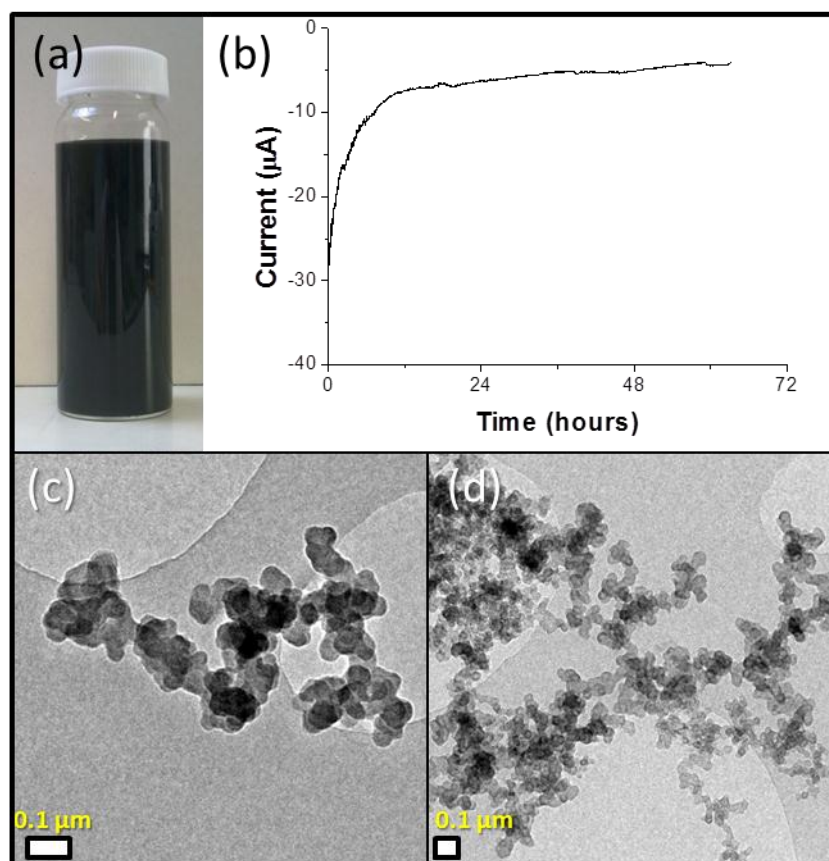
Fig. V-10 Electrochemical dissolution of activated carbon nanoparticles (Vulcan XC72R) in 1 mM TBAP/DMF under potentiostatic voltage of -2.3 V *vs.* Ag/Ag$^+$ for ~72 h. (a) photograph showing the dispersion after electrochemical dissolution with a concentration of 0.34 mg mL^{-1}. (b) Chronoamperogram during the reductive dissolution process. (c)-(d) TEM images showing the activated carbon nanoparticles following electrochemical dissolution.

V. 2. 5. Metal nanoparticles

The starting material for investigating metal nanoparticle reductive dissolution was challenging due to limited data from manufacturers. Having been unsuccessful in obtaining pure iron nanoparticle powders (nanopowders), it was decided that iron oxide (Fe$_3$O$_4$) nanopowder may be useful since its ability to undergo alkali metal intercalation has been applied to lithium-ion batteries.[301] Using cyclic voltammetry (Fig. V-11), the reversible redox reaction between Fe$_3$O$_4$ and Fe(0) was clearly observed as previously reported,[301] however, no spontaneous dissolution was observed following constant potential reduction at -2.3 V, 48 h.
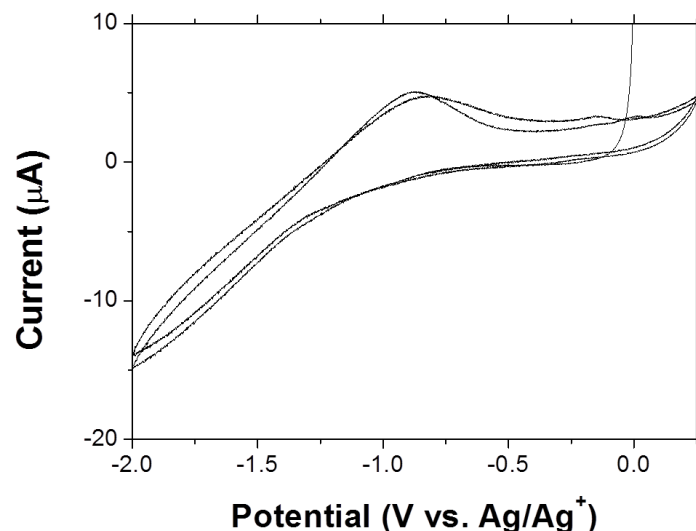
Fig. V-11 Cyclic voltammetric response of an Fe_3O_4 nanopowder based electrode in 1 mM STPB/DMF at 1 mV s^{-1}, 2 cycles.

Silver nanopowder (< 100 nm particle size) was obtained and showed no solubility in electrolytic systems. However, these particles were successfully dissolved at very low yields (< 2 wt %) in 1 mM TBAP/acetonitrile (AN) under constant potential control (-2.3 V *vs.* Ag/Ag$^+$, 120 h). Dissolution was not possible in DMF, the increased polarity of AN was thought to be responsible for enhanced Ag solubility. TEM showed the successful dissolution of individualised Ag nanoparticles at higher charge densities of ~1 charge/3 Ag atoms, with the majority consisting of very small (< 5 nm) particles as a result of their higher rate of diffusion than larger particles. This observation may also outline changes in electronic properties with nanoparticle size, offering a potential route to the size-based separation of metal nanoclusters/nanoparticles; smaller nanoparticles will have increased confinement (quantized electronic states) compared to larger nanoparticles that will resemble the bulk electronic properties of the metal.[302] The yellow colour of the dispersion may be indicative of the Ag nanoparticle surface plasmons, but the presence of organic materials that could coat the nanoparticles cannot yet be ruled out (information not disclosed by manufacturer).
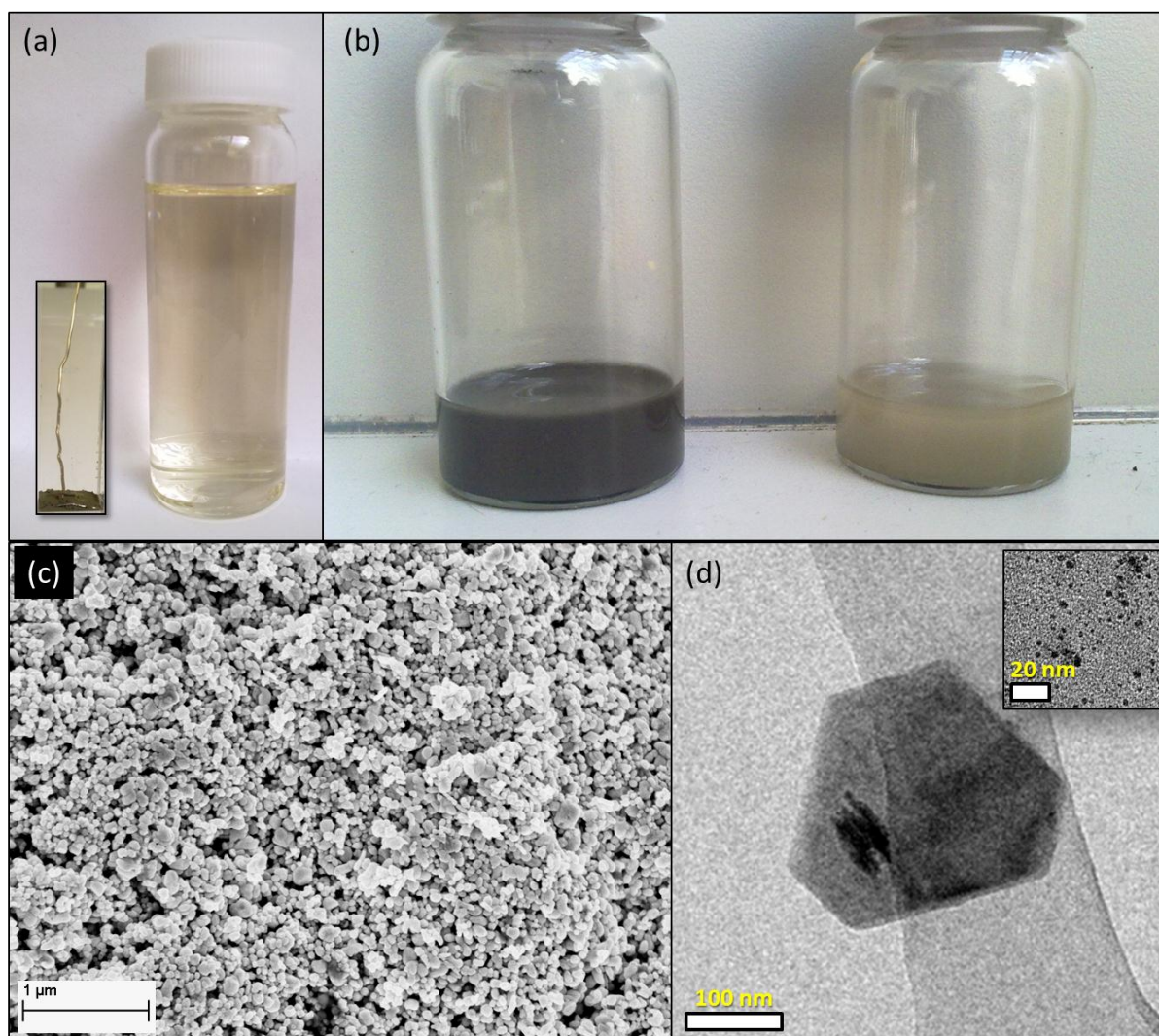
Fig. V-12 Reductive electrochemical dissolution of silver nanoparticles. (a) Silver nanoparticle electrochemical dispersion in 1 mM TBAP/AN at -2.3 V *vs.* Ag/Ag$^+$ for 120 h, giving a mild yellow coloured solution. Inset: inside the electrochemical setup. (b) Raw silver nanopowder sonicated in AN, left, and the undissolved silver nanopowder sonicated in AN, right. A significant colour change from dark grey to pale yellow was observed. (c) SEM image of the raw silver nanopowder, (d) TEM image of a large individualised silver nanoparticle following electrochemical reductive dissolution. Inset: the majority of dissolved silver particles are < 5 nm in size but are highly individualised.

V. 2. 6. Metal chalcogenides

Carbon is not the only species to form nanotube and layered structures, many analogous materials exist with distinct properties; boron nitride (BN) is the closest example but is not suitable for electrochemical dissolutions due to it being insulating with an extremely large band gap (~5.5 eV). Metal chalcogenides (investigated in this section) and oxides can also form both

layered and nanotube structures. Metal chalcogenides consist of hexagonal layers of metal atoms (M) sandwiched between two layers of group 16/chalcogen atoms (X) *e.g.* S, Se, Te, *etc*. Although the bonding within these sheets is covalent, adjacent sheets stack *via* vdW interactions to form a 3D crystal (Fig. V-13), as with graphitic materials. Binary metal chalcogenides occur in more than 40 different types, depending on the M-X combination. Variations in coordination and oxidation state of the metal atoms can infer metallic, semi-metallic, or semi-conducting character.[303]

These materials have been known for many decades, typically synthesised from high-temperature molten salts, and are rapidly gathering interest due to the presence of significant band gaps. Generating a controlled band gap in graphene requires the formation of nanoribbon structures, or covalent functionalisations.[304] Bulk metal chalcogenides have indirect band gaps (momentum in conduction and valence bands are different; consequently optical transitions between free electrons and holes are forbidden) that become direct upon the formation of single layers giving great potential for optoelectronic device applications;[305] other applications include polymer reinforcements, insulators and thermoelectric materials. Currently, liquid-phase exfoliation using sonication[303] or the scotch-tape technique[305] provide monolayer and few layer nanosheets, with minimal damage compared to chemical methods that predominantly rely on alkali metal intercalation followed by exfoliation upon water addition that rapidly generates alkali metal hydroxide and hydrogen gas.[306, 307]

Electrochemistry of metal chalcogenides[308] has primarily been used as both a synthesis (electrodeposition) and characterisation tool. Metal chalcogenides exhibit high electrochemical activity and reversibility as cathodes; intercalation of guest species within the metal chalcogenides is well studied and applied in energy storage applications. The intercalation of alkali metals (A) into dichalcogenide hosts generates A_xMX_2 phases, where $0 < x \leq 1$. Intercalation of 3D lattices ($M_xMo_6X_8$) and 1D structures (MX_3) are also reported.
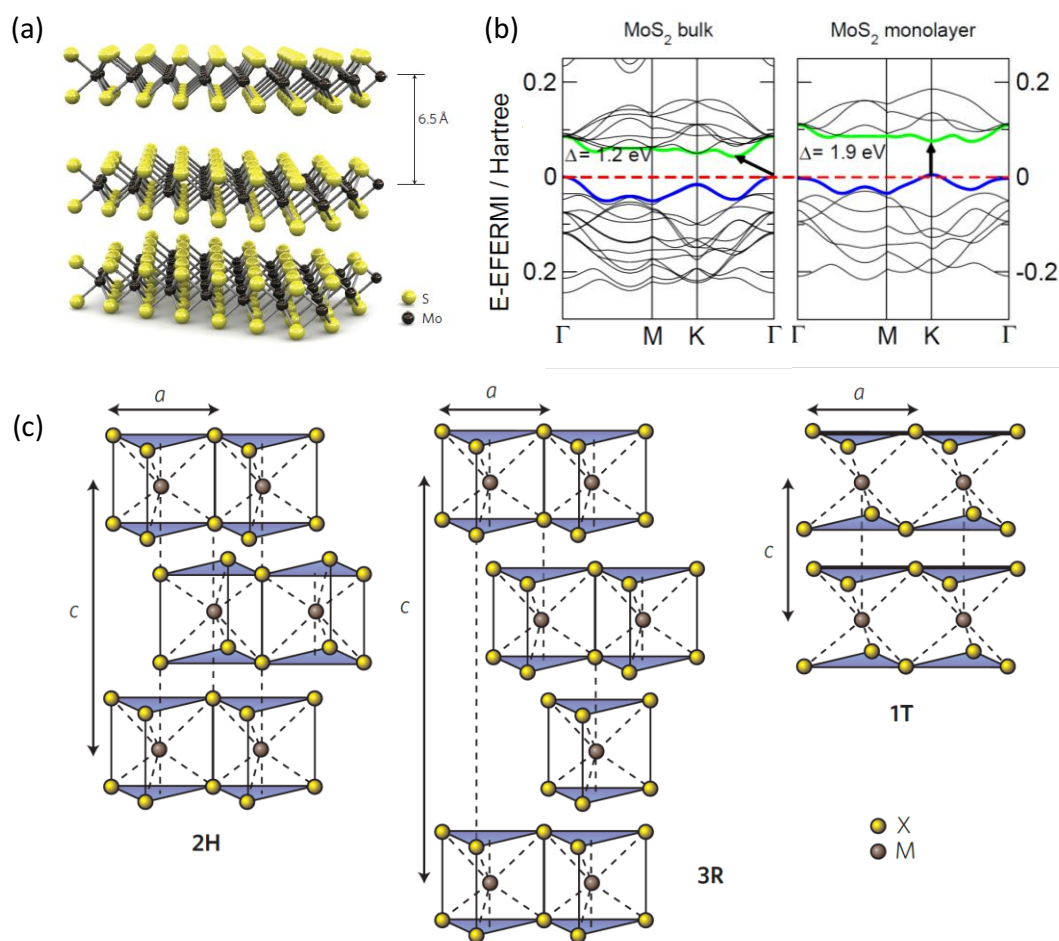
Fig. V-13 A typical transition metal dichalcogenide, MoS_2. (a) Three-dimensional representation of the MoS_2 structure; single layers are 6.5 Å thick. Reproduced from ref. 305. (b) Band structure of MoS_2 as a bulk (indirect band gap) and monolayer (direct band gap) structure. Reproduced from ref. 309. (c) Schematic views of the structural polytypes: 2H (hexagonal symmetry, two layers per repeat unit, trigonal prismatic coordination), 3R (rhombohedral symmetry, three layers per repeat unit, trigonal prismatic coordination) and 1T (tetragonal symmetry, one layer per repeat unit, octahedral coordination). The chalcogen atoms (X) are yellow and the metal atoms (M) are grey. Reproduced from ref. 304.

In this research, the cyclic voltammetry (Fig. V-14) and chronoamperometric dissolution of MoS_2, $MoSe_2$ and Bi_2Te_3 layered metal chalcogenides was studied. CVs were performed using 1 mM STPB/DMF prior to optimising the CV behaviour of SWNT electrodes (0.1 M electrolyte concentration). However, all metal chalcogenides showed strong features related to intercalation of the sodium cations into the lattice at ~-1.2 V, involving the breaking of vdW bonds. In MoS_2, for example, S-S bonds break to form Na-S bonds, while further excessive reducing potentials

would lead to the decomposition of MoS_2 to Mo nanoparticles embedded in a Na_2S matrix.[310] The appearance of a redox cycle centred at ~-0.25 V for both MoS_2 and $MoSe_2$ CVs suggests the redox activity of Mo species.[311] Following reductive electrochemical treatments in 1 mM STPB/DMF at a constant potential of -2.0 V *vs*. Ag/Ag^+ for 24 h, only $MoSe_2$ appeared to spontaneously dissolve, generating a purple coloured solution (Fig. V-15). However, TEM showed no layered materials indicating possible electrode decomposition.
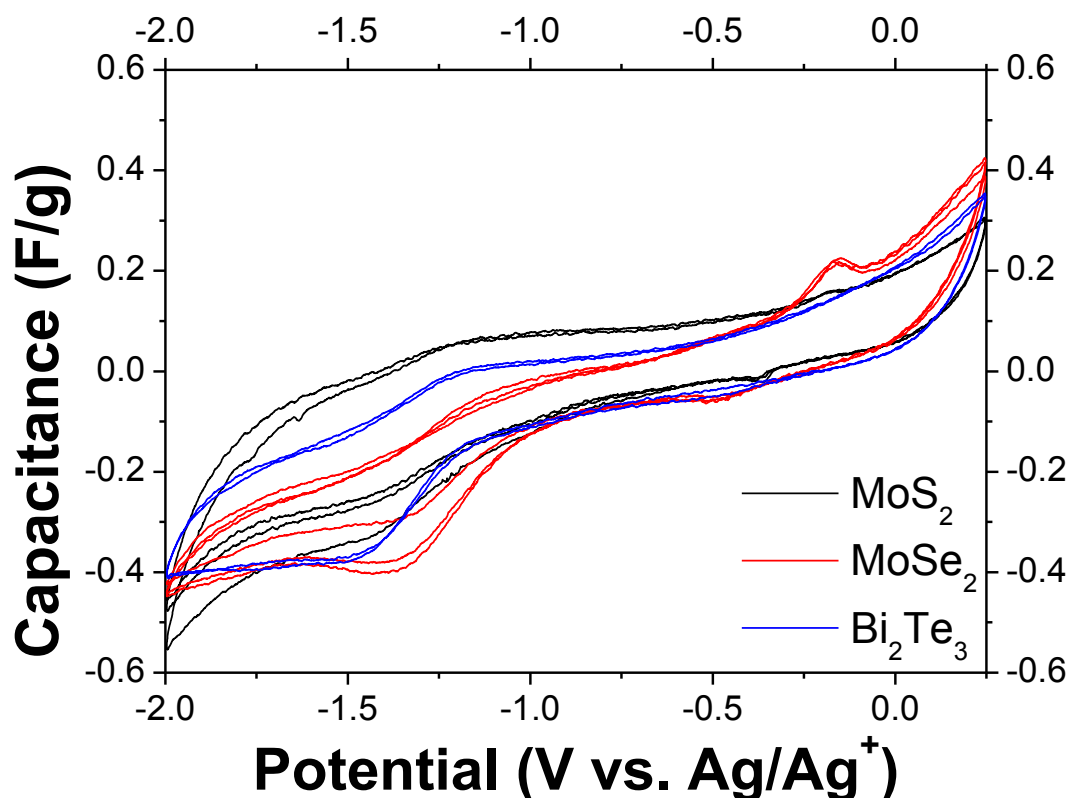
Fig. V-14 Cyclic voltammograms of metal chalcogenide powder electrodes in 1 mM STPB/DMF, 1 mV s^{-1}, 2 cycles.

Dissolution was observed for MoS_2 following water addition in line with the previously observed exfoliation following chemical methods.[306, 307] Chemical approaches involve soaking MoS_2 in *n*-butyllithium/hexane to generate Li_xMoS_2 ($x = 1$); upon water addition (and mild sonication), expansion of the layers occurs following the rapid generation of hydrogen gas and lithium hydroxide leading to exfoliation. Bi_2Te_3 showed no dissolution even after water addition. TEM observations showed small amounts of layered MoS_2 (Fig. V-16); further studies to

evidence monolayer formation should be performed using both electron and X-ray diffraction (XRD).
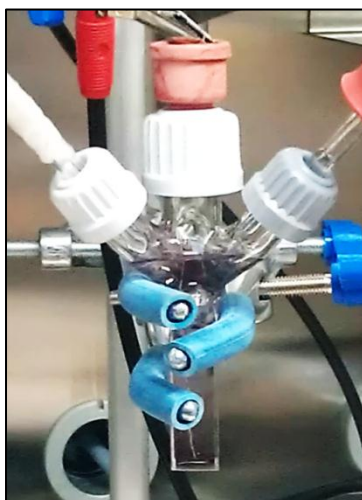
Fig. V-15 Reductive electrochemical dissolution of a MoSe2 powder electrode at -2.0 V vs. Ag/Ag⁺, 24 h. The purple colour generated was presumed as a consequence of electrode decomposition, generating Mo nanoparticles.
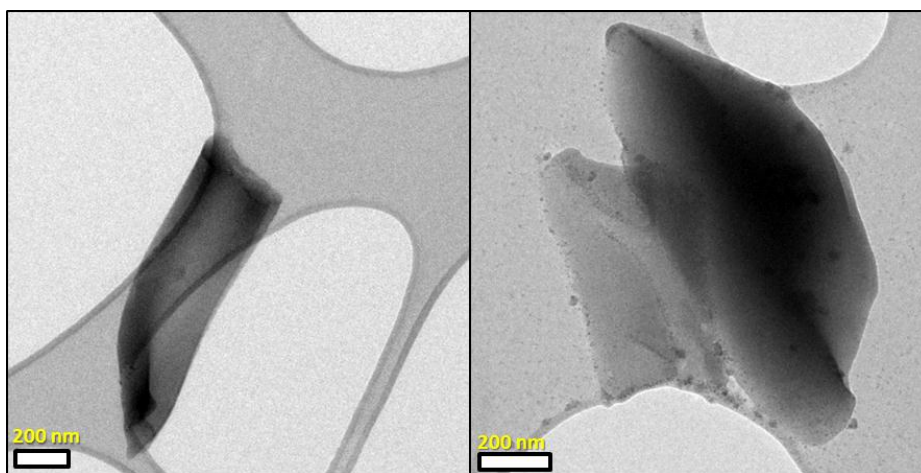
Fig. V-16 Reductive dissolution of MoS_2 following electrochemical charging and water addition. Charging was performed at -2.0 V vs. Ag/Ag⁺, 24 h. The presence of large mono/bilayers is apparent.

V. 3. SUMMARY

The electrochemical reductive dissolution process developed for SWNTs in chapter III has been successfully extended to other carbon-based and inorganic nanomaterials and highlights a promising route for the generalisation of nano-anions. The process developed for SWNTs was not immediately transferrable in many cases, and required alterations to the electrolytic salt and solvent system, as well as the introduction of agitation of MWNT powders due to their slow diffusion and high entanglement, and stirring of charged graphitic electrodes due to a lack of spontaneous dissolution. The dissolution of metal nanoparticles is hindered by oxide layers and needs further exploration of different materials produced using synthesis techniques that don't involve polymer or other long-chain organic molecule stabilisation; further investigation of suitable electrolytes for transition metal dichalcogenide and other small band gap semi-conductor layered and nanotube materials is ongoing.

Fundamentally, the generalisation of this approach to the dissolution of purified nanoparticle ions, will allow specific charge density to be investigated with charged nanoparticles dispersed as discrete objects. To apply this electrochemical approach, particles must be electrochemically-stable, and reasonably electrically conductive; semi-conducting materials with wide band gaps are not suitable for electrochemical processing. There is an abundance of pre-existing literature regarding the electrochemistry and intercalation of many of the nanomaterials investigated, finding the most suitable electrolyte salt and solvent system remains the vital component.

Overall, the potential benefits to general nanomaterial processing are clear. The reductive dissolution of graphene, for example, could revolutionise current bulk processing of graphite that relies heavily on aggressive sonication; introducing an electrodeposition route for graphenide species would also be highly advantageous in developing large scale (opto)electronic devices. It is also hoped that following optimisation of the dissolution of metal chalcogenides, these materials could also be introduced into similar devices, or new applications involving hybrid structures.

VI. CONCLUSIONS AND FUTURE STUDIES

VI. 1. OVERVIEW

This thesis has outlined a new approach for the formation and dissolution of discrete nanotube anions, that has also been generalised to some extent to other electrochemically-stable nanoparticles such as MWNTs, graphene, noble metal nanoparticles and layered metal chalcogenides. Commonly used, commercial, as-received SWNT powders were fully dissolved using mild electrochemical reduction in non-aqueous electrolytic solutions under constant potential control, without the use of ultrasonication, ultracentrifugation, covalent modification, or strongly-bound wrapping agents. The electrochemical aproach offers much greater control over reduction potential than chemical charging routes that use specific reductants or charge transfer agents; the charging current allows independent control of charge:carbon stoichiometry more directly and conveniently than, for example, adjusting the alkali metal:carbon ratio.[123, 131] Careful control of the electrochemical potential offers the removal of carbonaceous impurities, providing a non-destructive strategy for SWNT purification. Between -1.6 and -2.0 V, dissolved fractions contained mostly defective materials, increasing the reduction potential to -2.3 V allowed complete dissolution. Overall, the dissolution and purification technique has been demonstrated at the tens of milligram scale, but offers considerable promise for scaling to larger quantities, whilst avoiding inconvenient reagents such as superacids, liquid ammonia, or alkali metals.

Strong evidence shows the presence of moisture can dramatically alter the character of the dissolved species, a combination of charge quenching and possible selective functionalisations significantly reduced the experimental yield giving the misconception of a selective dissolution process. The move to performing electrochemical dissolutions in a glove box resulted in significantly dryer electrolytes (~5-10 ppm) and complete dissolution, but selectivity for electronic character or diameter was not observed at varying potentials indicating the dissolution

process was not governed by kinetics. Instead, SWNTs and other impurities inherent to all samples, required specific charge densities.

Three different approaches can be used to remove the charge on nanotubide ions: exposure to clean, dry oxygen, deliberate derivatisation, or electrochemical quenching *via* depositions; electrodeposition provides a high level of control and a variety of new processing options. By combining dissolution with electroplating, a semi-continuous purification process can be envisioned, in a similar fashion to the industrial purification of copper.[312] Electrochemical depositions over a -2.2 to -1.2 V range showed slight diameter dependence; entanglement effects are presumed to dominate the dissolution process, whereas the deposition strategy is facilitated by the individualisation of SWNT species. Indeed, this approach may provide a scalable route towards the sorting of specific SWNT species (each representing a distinct molecular structure). However, enhancing the selectivity and overall deposition process yields are essential developments for the near future.

VI. 1. 1. Electrochemcial dissolution of SWNTs and related nanomaterials

The development of an electrochemical dissolution process for single-walled carbon nanotubes has been demonstrated. The spontaneous dissolution process has considerable advantages to commonly used strategies, and could have a dramatic impact upon the general processing of nanomaterials:

- **Mild dissolution** – avoids sonication, centrifugation, strongly-bound wrapping agents, covalent functionalisation. Complete dissolution observed for commercial HiPco and CoMoCAT SWNTs.

- **Non-destructive purification** – preferential dissolution of amorphous carbon, metal catalyst and other defective materials from both SWNT and MWNT samples, without the need for aggressive oxidative treatments.

- **Simple and economical** – dissolution occurs under constant potential control; an expensive potentiostat is therefore not essential.

- **Versatile** – SWNTs reduce and dissolve in a number of different solvents including amides, cyclic carbonates, and sulphoxides.

- **Greater potential control** – other reductive processes are limited to electron potential of solvated electrons in liquid ammonia, or sodium naphthalide, *etc.* and can only vary alkali metal:carbon ratios.

- **Scalable** – dissolution of SWNTs demonstrated at the tens of milligram scale but promises much larger scalability in line with other non-aqueous industrial electrochemical processes.

- **Applications** – reductive chemistries already exist with a huge library of possible modifications; development of transparent conductive film (TCF) devices based on electrochemically dissolved SWNTs without the need for typical sonication and ultracentrifugation has been demonstrated here.

- **Fundamental studies** – cyclic voltammetry has highlighted features relating to the position of SWNT vHS transitions, and could provide a useful characterisation tool in future.

- **Generalisation to nano-anions** – the dissolution process has been extended to other carbon nanomaterials (MWNTs, graphene, fullerene, activated carbon) and non-carbon nanomaterials (metal nanoparticles, metal chalcogenides); there are likely to be many more candidates.

VI. 1. 2. Electrochemical deposition of SWNTs

The electrochemical deposition of SWNTs had not been explored previously; successful electrodeposition of SWNTs over a well-defined potential window has been demonstrated. Similarly, the electrodeposition route provides many benefits to nanomaterial processing:

- **Simple** – deposition occurs under constant potential control, although more complex pulsed waveforms may improve deposition process.

- **Versatile** – deposition demonstrated on a wide range of electrode types including metallic wires, foils and ITO-glass.

- **Charge quenching** – exposure of nanotubides to atmosphere can result in unwanted functionalisations. Electrodeposition provides a route to remove the charge in a convenient way.

- **Sorting** – observed weak diameter dependence due to individualisation of SWNTs. With further process developments it may be possible to further enhance selectivity for other specific SWNT properties, developing a scalable post-synthetic sorting technique.

VI. 2. FUTURE STUDIES

There are still many areas of interest to be explored across all fields of this research. The electrochemical dissolution of SWNTs has already opened up the potential for the creation of many more species with defined charge densities. Scaling up the process beyond the tens of milligram scale will involve the design of different electrochemical cell geometries, larger surface area reference and counter electrodes, and ideally, less toxic solvents. There is still work to be done regarding SWNT modifications, particularly with regard to improving the degree of functionalisation and enhancing the SWNT solubility with many different possible functional moieties still to try. Also, the ability to study the fundamental properties of SWNTs using cyclic voltammetry in identifying the position of the first few vHSs is of great interest.

VI. 2. 1. Electrochemical dissolution

A novel setup for the scale up of the electrochemical dissolution process to at least the gram scale is analogous to a coffee making 'cafetière' (Fig. VI-1a). Here, a fine platinum mesh plunger-type electrode affords good contact with the nanomaterial powder, rises up with the swelling of the charged powder, and limits the mixing of the raw powder with the dissolved fraction. Occasional plunging of the electrode would also allow entangled materials to dissolve without the possibility of mixing with the upper solution. Fig. VI-1b shows a multiple electrode configuration for combined dissolution/deposition in a single step (discussed below).

Other improvements to the dissolution process include using alternative solvent systems, in order to dissolve longer SWNT types (*e.g.* Supergrowth) in larger quantities, improve the dissolution of other nanomaterials, dissolve nanoparticle cations, and improve the degree of functionalisation.
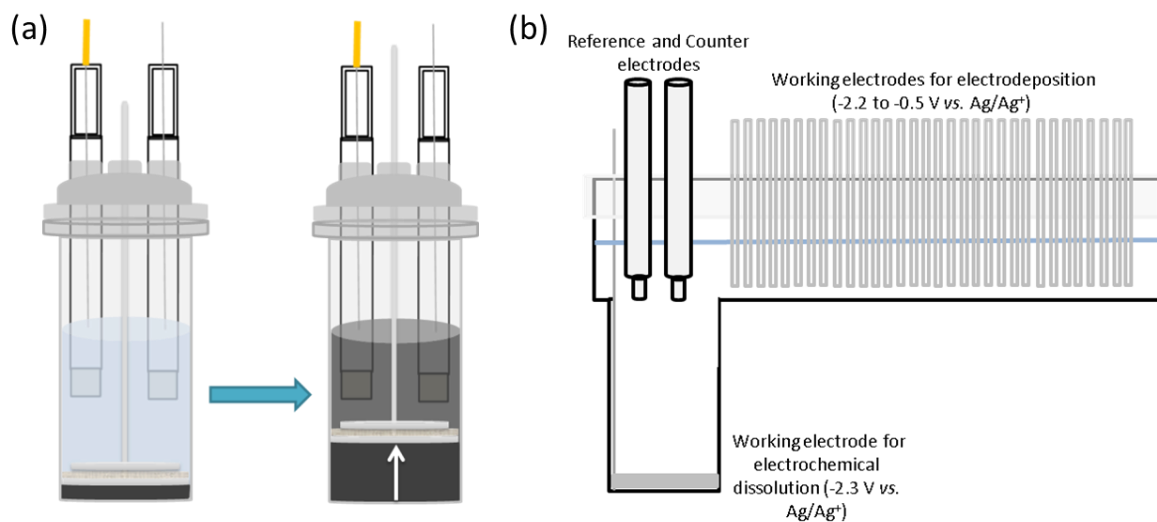
Fig. VI-1 Schematic diagrams of possible future electrochemical cell designs. (a) 'Cafetière' style electrochemical setup for the dissolution of charged nanomaterials. (b) Multi working electrode configuration for combined electrochemical dissolution and selective deposition at finely controlled oxidation potentials. This configuration is discussed in section VI. 2. 2.

VI. 2. 1. 1. Nanoparticle cations

The alternative approach to the electrochemical reductive dissolution is the generation of $SWNT^{n+}$ (nanotube cations), by accessing other electrolytic (salt and solvent) systems that are highly stable to oxidation. Using similar electrolytes used to generate C_{60} cations, potential solvents would include various nitriles (acetonitrile, glutanitrile, adiponitrile, methoxyacetonitrile, 3-methoxypropionitrile), carbonates (propylene carbonate, butylene carbonate), lactones (γ-butyrolactone, γ-valerolactone), nitromethane/ethane, sulpholane, and trimethyl phosphate, although their suitability for dissolving SWNTs is not well known. The use of lithium hexafluoroarsenate ($LiAsF_6$) in propylene carbonate is a well-studied system,[234] although the toxic nature of arsenic compounds may be cause for concern for larger scale studies. Nevertheless, nanotube cations have never been produced (probably in view of the immense difficulty in isolating C_{60}^+, fullerenium cations), but would offer the potential to access a whole new library of possible SWNT functionalisations through various nucleophilic additions. The generation of $SWNT^{n+}$ species would also allow electrodepositions *via* subsequent reduction, and allow the study of the expected vHS features during cyclic voltammetry at oxidising potentials.

Preliminary use of the $LiAsF_6$/PC electrolyte is ongoing, certainly it is more difficult to oxidise the neutral SWNTs since SWNT Fermi levels are reported to be positive *vs.* NHE. The

electrolyte stability window reaches ~+1.5 V *vs.* Ag/Ag$^+$ due to the subsequent degradation of PC at the anode. Chronoamperometric dissolution experiments at this potential should allow the charging of SWNTs to a similar degree as the middle fractions collected in SWNT reduction experiments (Fig. III-16), although not oxidative enough to expect full dissolution. So far, noticeable SWNT^{n+} dissolution has been observed and work will proceed to characterise the nature of this dissolved material. A similar purification trend during the dissolution of these nanotube cations is predicted to develop as observed during the reductive dissolution process.

VI. 2. 1. 2. Isolating single layer graphenes
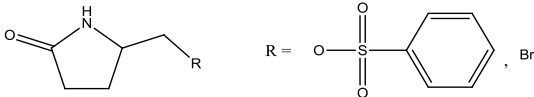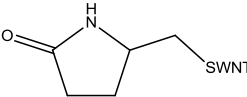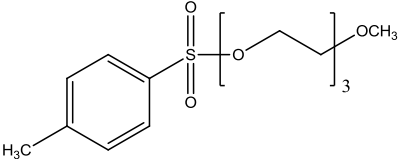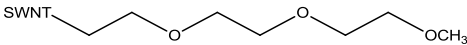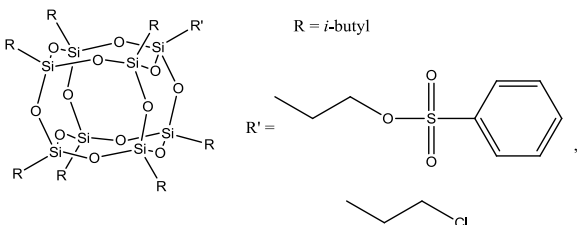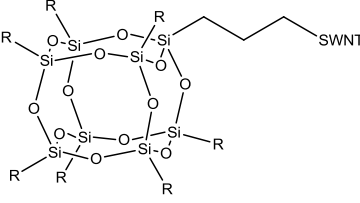
The difficulties witnessed during the application of the dissolution process to graphenes are proposed to be due to poor electrolyte intercalation into the graphene layers. Having attempted with different solvents (DMF, NMP, DMSO) and different salts (NaClO$_4$, LiClO$_4$), the next stage may be to try cationic or anionic intercalation in PC. Many anions are known to intercalate graphite well and are large enough to increase the layer spacing significantly for mild exfoliation.

VI. 2. 1. 3. Nanotubide/Graphenide chemistry

Following the successful dodecyl-grafting of electrochemically reduced SWNTs, the next stage would be to maximise the degree of functionalisation by incorporating side-wall moieties that enhance the solubilisation of SWNTs in the electrolytic solution, avoiding reaggregation. Several possible reagents are shown in Table VI-1, although it is still debatable whether nanotubide reactions proceed *via* electrophilic addition or radical reaction mechanisms. Typically, good "leaving groups" for the electrophilic addition route are bromo, iodo, epoxy, acyl chloride, *etc.* radical based reactions involve peroxides and disulphides, *etc.* as discussed in section I. 3. 3. 2. Other potential reagents of interest that are commercially available include the use of tosylates that have not been reported for reductive functionalisations, and amide containing molecules that should maintain the solubility of functionalised SWNTs in DMF/NMP. Furthermore, for composite applications, short-chain, well-defined oligo/polymers that maintain or enhance solubility would be useful, *e.g.* mono-terminated PEG chains that avoid multiple functionalisation or cross-linking. Polysilsesquioxane (POSS) groups would also be a beneficial attachment due to their high solubility in many organic solvents, large size in providing significant steric hindrance

to nanotubide/graphenide reaggregation, as well as their existing applications in polymer and ceramic composite materials.[313, 314]

Table VI-1 Possible future nanotubide/graphenide chemistries.

Electrophile	Grafting (See Scheme II-2)

Another approach to increasing the degree of functionalisation is to minimize the Bjerrum length, hence, reducing the number of condensed electron sites and freeing up more electrons for reaction. The simplest way to lower the Bjerrum length is to change the solvent for one which has a higher dielectric constant. DMF has a modest dielectric constant (36.7 @ 25°C) but only 1 e⁻ for every 9 sites is available to react; changing the solvent to PC with a significantly higher dielectric constant (66.1 @ 20°C) would increase the number of free electrons to 1 e⁻ in every 3 sites, potentially a factor of three improvement in the degree of functionalisation. However, the degree of condensation is likely to change as charges are consumed, hence, the degree of functionalisation may still be dominated by steric effects.

VI. 2. 2. Electrochemical deposition

Working electrodes for deposition

While ITO-glass electrodes promised simple post-deposition characterisation, in hindsight, significant downfalls exist due to their poor conductivity and surface inhomogeneity compared to metallic electrodes.[284] Experiments are currently underway investigating gold Substratek™

TEM grids (Agar Scientific) as a possible replacement for ITO; these substrates are ultrathin gold layers (2-3 nm) supported on a gold mesh grid (300 mesh), offering high electrochemical stability and conductivity, whilst being electron and optically transparent (~49% transmission) for various forms of microscopy and spectroscopy. Although SWNTs give strong Raman signals, the thin gold layer may also provide a significant surface enhanced Raman scattering (SERS) effect for other types of nanomaterials. It is hoped that the improved conductivity and more homogeneous surface may allow for higher yields, uniform SWNT deposition, and enhanced selectivity over specific SWNT properties. In the future, nanopatterned electrodes[315] or graphene-based flexible electrodes[316] may be useful, especially for device fabrication.

Equipment and electrochemical cell geometries

The long term goal is to deposit SWNTs on multiple electrodes simultaneously using a multi working electrode configuration. Commercial multipotentiostats allow up to 256 simultaneous working electrodes offset by slight potentials, controlled by one reference and counter electrode. Developing a cell geometry that allows for SWNT reduction and dissolution at one end followed by diffusion into another chamber that has multiple electrodes in a linear conformation, would allow SWNTs to deposit at mild to increasingly oxidising potentials as shown in Fig. VI-1b.

VI. 2. 3. Fundamental studies

In terms of fundamental understanding of SWNT properties, there is still a long way to go in determining mechanisms for both SWNT chemical reactivity, as well as the subtle differences in SWNT Fermi level energies and therefore positions of their vHSs. Further cyclic voltammetric studies, as evidenced by *(n,m)* enriched CoMoCAT and Meijo SWNTs, are essential in outlining these features. Only with further enrichment, or the use of single helicity SWNT samples will these features be fully discriminated. Hopefully, this enrichment will be provided by the multi electrode deposition configuration, upon which further CV experiments can be performed on each individual electrode.

VI. 3. CONCLUDING REMARKS

Overall, the development of a fully-optimized electrochemical dissolution procedure for nanomaterials has opened the way for larger scale processing on both an academic and industrial level. The electrochemical process is already patented, and could easily be developed commercially in a similar way to existing industrial electrochemical processes that also require inert environments. In this sense, the research outlined in this thesis could revolutionise the field of nanomaterials. The process is ultimately non-destructive to the exceptional nanotube electronic properties; already the improved performance of electronic devices has been demonstrated in this research. Through the exploration of electrodeposition and the dissolution of a wide range of other carbon and non-carbon nanomaterials, electrochemical strategies have significantly wider implications; the development of electrochemical processes for purification and assembly of nanomaterials will enable both fundamental studies of electronic properties and new applications.

VII. Appendix

VII. 1. Publications

S. A. Hodge, S. Fogden, C. A. Howard, N. T. Skipper, M. S. P. Shaffer, *Electrochemical Processing of Discrete Single-Walled Carbon Nanotube Anions*, **ACS Nano**, doi: 10.1021/nn305919p

S. A. Hodge, M. K. Bayazit, K. S. Coleman, M. S. P. Shaffer, *Unweaving the rainbow: a review of the relationship between single-walled carbon nanotube molecular structures and their chemical reactivity*, **Chem. Soc. Rev.**, 2012, **41**, 4409-4429

S. A. Hodge, M. S. P. Shaffer, *Probing the Van Hove singularities of single-walled carbon nanotubes using cyclic voltammetry*, in preparation, 2012

S. A. Hodge, H. H. Tay, M. K. B. Bayazit, M. S. P. Shaffer, *Nanotubium salts: Novel electrochemical generation of single-walled carbon nanotube cations*, in preparation, 2012

VII. 2. Experimental

VII. 2. 1. Materials

Single-walled carbon nanotubes

HiPco SWNTs (Batches: R0550, R0448, P0261; Carbon Nanotechnologies Inc., USA), CoMoCAT SWNTs (Batches: SG0002, SG0033; SWeNT, USA), CarboLex (AP-grade; CarboLex Inc., USA), Carbon Solutions (AP-183, Carbon Solutions Inc., USA) Hanwha SWNTs (Batch: ASA-100F: A-091230-2; Hanwha Nanotech Corp., South Korea) and Super-Growth SWNTs (Batch: STD2; AIST, Japan) were used as-received without any pre-treatments. See Table III-1 and Appendix VII. 3 for a summary of the characterisation data obtained from these SWNTs.

Other carbon nanomaterials

In-house grown injection CVD MWNTs (IH-MWNTs) were synthesized by Robert Menzel (injection CVD (carbon source: 3 wt % ferrocene/toluene, injection speed: 5 mL h^{-1}; carrier gas: argon, flow rate: 2000 sccm, growth temperature and time: 760°C, 2 h). Nanocyl NC7000

MWNTs were purchased from Nanocyl (Sombreville, Belgium). Vulcan XC72R was purchased from Cabot Corporation (Billerica, MA, USA). CNF-PL was purchased from FutureCarbon GmbH (Bayreuth, Germany), natural crystalline flake graphite (#2369) was purchased from Graphexel Ltd. (Essex, UK). Graphite Oxide powder was purchased from NanoInnova Technologies (Madrid, Spain). Fullerene powder was purchased from SES Research (Houston, TX, USA). All these materials were used as-received without any pre-treatments.

Non-carbon nanomaterials

Silver nanopowder (< 100 nm), iron oxide nanopowder (< 50 nm), MoS_2 and Bi_2Te_3 powders were purchased from Sigma-Aldrich (St. Louis, MO, USA). $MoSe_2$ powder was purchased from Cerac Inc. (Milwaukee, WI, USA) All these materials were used as-received without any pre-treatments.

Other chemicals and materials

N,N-Dimethylformamide/DMF (anhydrous, 99.8%), *N,N*-dimethylacetamide/DMA (anhydrous, 99.8%), 1-methyl-2-pyrrolidinone/NMP (anhydrous, 99.5%), 1,3-dimethyl-2-imidazolidinone /DMEU (puriss., absolute, over molecular sieve ($H_2O \leq 0.04\%$), $\geq$ 99.5%), propylene carbonate/PC (anhydrous, 99.7%), dimethylsulphoxide/DMSO (anhydrous, $\geq$ 99.9%), acetonitrile/AN (anhydrous, 99.8%), 1,2-dimethoxyethane/DME (anhydrous, 99.5%) were all purchased from Sigma-Aldrich and used as-received. 1-cyclohexyl-2-pyrrolidone/CHP (99%) was also purchased from Sigma-Aldrich, but further dried by vacuum distillation over molecular sieves. Tetrahydrofuran/THF was distilled in-house.

The anhydrous electrolytic salts used throughout the research (tetrabutylammonium perchlorate (TBAP), sodium tetraphenylborate (STPB), tetrabutylammonium tetraphenylborate (TBATPB), lithium perchlorate ($LiClO_4$), sodium perchlorate ($NaClO_4$)) were all purchased from Sigma-Aldrich and used as-received. Electrolytic solutions were further dried by 3 Å molecular sieves and kept in a glove box.

Platinum wire electrodes (Laboratory Reagent, 0.5 x 100 mm) were purchased from Fisher Scientific (Loughborough, UK), platinum foil (99.95% purity, 0.125 x 25 x 25 mm) and silver wire (99.99% purity, 0.25 mm x 25 m) were purchased from Advent Research Materials (Oxford, UK). The reference electrode, Ag/Ag^+, containing 0.01 M silver nitrate and 0.1 M TBAP in acetonitrile, and counter electrode parts (sample holders (6 mm O.D.), porous Vycor frits (2.85

mm O.D.) and heat-shrink PTFE tubing) were all purchased from IJ Cambria Scientific (Llanelli, UK).

VII. 2. 2. Equipment and sample preparation

A Solartron 1250 Potentiostat (Solartron Analytical, Farnborough, UK) was used for the cyclic voltammetric (CV) and potentiostatic measurements using CorrWare 2 software. Electrochemistry was performed inside a Labmaster SP nitrogen-filled glove box (mBraun, Garching, Germany) with levels of H_2O and O_2 maintained < 1 ppm.

Raman spectra of were obtained with a LabRAM Infinity instrument (Horiba Jobin-Yvon Ltd., Middlesex, UK) with a 633 nm He-Ne laser (1.96 eV) and 532 nm Nd-YAG laser (2.33 eV). All Raman spectra were recorded using a grating of 1800 grooves mm^{-1}. The maximum powers of the 633 nm and 532 nm lasers at the sample were 8 mW and 24 mW, respectively. The laser power was varied to ensure no damage to samples; typically, 100% intensity was used for the 633 nm laser, 25% intensity for the 532 nm laser. Samples were measured either in raw powder form, as drop-casted dispersions on glass microscope slides, or as electrodeposited films on various electrode surfaces. At least five consistent spectra were measured for each sample at different locations to reduce the effect of sample heterogeneity. Raman spectroscopy of electrochemical dispersions was performed by the author with particular acknowledgement to Mr. Cong Sheng (spectra of starting materials) and Miss. Charlene Lawton (SWNT-ITO deposits).

Transmission electron microscopy (TEM) was carried out using a JEOL2010 TEM (JEOL, Tokyo, Japan) at 200 keV operating voltage. TEM was used to identify the nature of the electrochemically dissolved nanomaterials; sample preparation of electrochemically dispersed SWNTs for TEM has developed from drop-casting on suspended grids (requiring high temperature vacuum oven treatments to remove solvent) to drop-casting on to grids placed on filter paper (to instantly remove the majority of solvent). Samples were typically prepared on 300 copper mesh holey carbon grids (Agar Scientific, Essex) by drop casting on to the grid supported by a filter paper, and left to dry in a nitrogen-filled glove box for several days. Samples were removed from the glove box, washed on filter paper with 2-3 drops of DMF, acetonitrile or water to remove electrolytic salts, then further washed with IPA. All TEM was performed by the author.

SEM was carried out using a Leo Gemini 1525 high resolution field emission gun scanning electron microscope (FEGSEM) using SmartSEM software (Carl Zeiss NTS Ltd., Cambridge, UK). SWNT powders and ITO-glass electrodes were affixed onto aluminium sample stubs using silver dag/carbon tab (all SEM consumables were purchased from Agar Scientific Ltd., Essex, UK). Nanomaterial dispersions were drop-casted directly on to polished Al stubs. All SEM images were recorded by Mr. David B. Anthony.

Atomic Force Microscopy was carried out using a Nanoscope IV Digital Instruments AFM (Veeco, Plainview, NY, USA). AFM sample preparation has also varied somewhat, using different substrates (mica, silica, 3-(iodopropyl)trimethoxysilane-functionalised silica), preparation methods (drop-casting, soaking, spin-coating), different drying techniques (air-dry, vacuum oven dry, dry in inert atmosphere), and washing strategies to remove the electrolytic salts (different solvents, soaking, vigorous washing). The most effective strategy was to drop-cast samples on to silica substrates, dry in the glove box for several days, remove and gently submerge the sample into DMF followed by IPA (avoid heating). AFM images were recorded by Mr. Hin Chun Yau.

UV-vis-nIR spectroscopy was carried out using a Lambda 950 spectrophotometer (Perkin Elmer, Waltham, MA, USA). Photoluminescence spectroscopy was performed using a Nanospectralyzer NS1 (Applied NanoFluorescence, Houston, TX, USA). Samples were prepared either in 1 wt % sodium deoxycholate (DOC)/D_2O by ultrasonication and ultracentrifugation, or as thin films on glass substrates by dispersion drop-casting. Concentrations of electrochemically dissolved SWNTs were measured predominantly be mass measurements, following extensive washing to remove electrolytic salts. Typical SWNT extinction coefficients (3264 mL mg^{-1} m^{-1} @ 660 nm) were found to be consistent with mass measurements and were used at low concentrations.

Ultrasonication was performed using a 750 W ultrasonic processor (Sonic and Materials Inc., Newtown, CT, USA) with probe-type configuration (tapered microtip, 3 mm), operated at 20% power output (150 W) for varying times. Mild sonication was performed using a VWR ultrasonic cleaner bath (VWR, Radnor, PA, USA).

High-speed ultracentrifugation was carried out using a Optima L-90K centrifuge (Beckman Coulter, Brea, CA, USA) with swinging bucket rotor (SW-41Ti) using Beckman Ultra-Clear centrifuge tubes for aqueous based dispersions, and Beckman polyallomer centrifuge tubes for

non-aqueous solvent based dispersions. Typical centrifugation speeds were 31500 rpm (122500g) for 1-4 h. Mild centrifugation was performed using a Sigma 2–16K centrifuge with Sigma 12139-H rotor; typical centrifugation speeds were 5000-10000g for 30 min. Ultracentrifugation was performed by Mr. Hin Chun Yau.

Thermogravimetric Analysis (TGA) was carried out using a Pyris 1 TGA (Perkin Elmer, Waltham, MA, USA). TGA cycles carried out in air (flow rate: 20 mL min^{-1}) were heated from 50°C to 100/170°C at 10°C min^{-1} then held isothermally at 100/170°C for 30 min to remove residual water/DMF. The temperature cycle was then ramped from 100/170°C to 850°C at 10°C min^{-1}. Experiments performed in nitrogen required a flow rate of 60 mL min^{-1} and a significantly longer purge time (90 min) at 100°C to remove all oxygen.

Water contents of electrolytes were measured using a Karl Fischer (KF) titration conducted with a Mettler Toledo DL32 coulometer (Mettler Toledo, Columbus, OH, USA) using HYDRANAL-Coulomat AD reagent (Sigma-Aldrich). Each sample for testing was prepared in the glove box, 12 mL was separated into three flame-dried volumetric flasks sealed with a suba-seal, and further wrapped with Parafilm. A clean syringe was purged with the sample three times before sample injection (~0.8 mL); each flask was used only once as moisture is rapidly absorbed through the punctured suba-seal. KF analysis was performed by the author, or by Miss. Charlene Lawton where stated.

VII. 3. OPTICAL SPECTROSCOPY OF SWNTS

The following SWNT starting materials (Fig. VII-2 to Fig. VII-6) were characterised by Raman, UV-vis-nIR and PL spectroscopy in a controlled manner to ascertain the SWNT helicities present in the samples, approximate SWNT diameter distribution and SWNT purity/graphitic quality.

Raman spectroscopy was performed on the raw powder with no pre-treatment. SWNT helicities were indexed using Kataura plots adjusted for different SWNT types according to reported observations (Fig. VII-1); purity/graphitic quality is given as an intensity ratio of the D and G peaks (I_G/I_D). Samples for UV-vis-nIR and PL were prepared at a starting concentration of 1 mg mL^{-1} in 1 wt % sodium deoxycholate (DOC)/D$_2$O using ultrasonication (power, 30 min) and ultracentrifugation (120000 g, 1 h). The supernatant was carefully decanted and diluted by a factor of 10 to achieve a SWNT concentration between 0.01-0.1 mg mL^{-1}. DOC was chosen as a

surfactant as it is known to be a very effective SWNT dispersant.[90] *(n,m)* indexing of vHSs in UV-vis-nIR spectra was performed using both Weisman's empirical Kataura plot,[41] and Strano's revised, experimental Kataura plot.[317] PL spectra were modelled using ANF SOFT software (Applied NanoFluorescence, Houston, TX, USA) using a user-defined peak excitation/emission template developed for DOC-wrapped SWNTs by Mr. Cong Sheng.
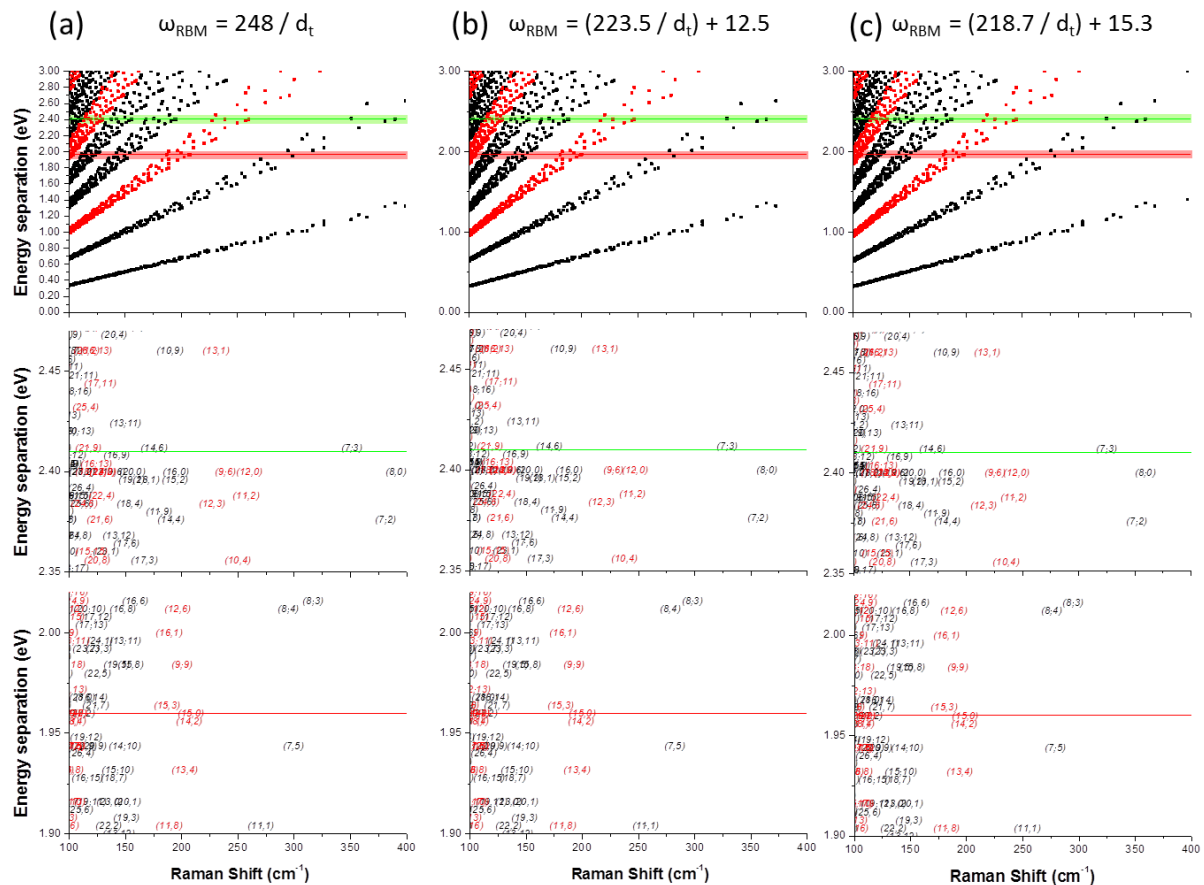
Fig. VII-1 Kataura plots adjusted to different diameter relationships. (a) original Kataura plot, (b) HiPco and (c) CoMoCAT SWNTs. Red and Green lines show the laser energies used in this research. The average resonance window[200] for bundled SWNTs (0.12 eV) is applied to identify the SWNTs that resonate with the particular laser.

VII. 3. 1. 1. HiPco SWNTs
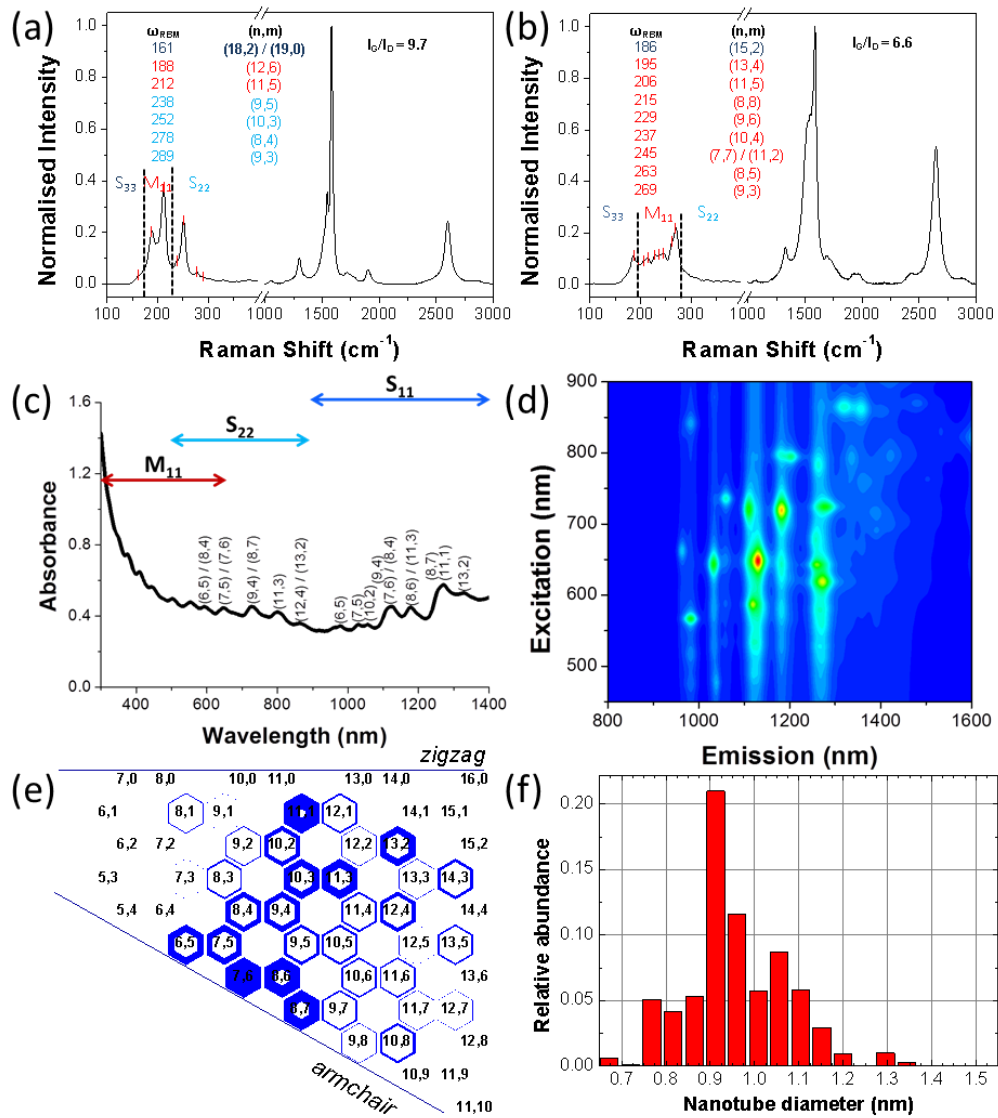
Fig. VII-2 Optical characterisation of as-received HiPco SWNTs, batch #R0550. (a) and (b) Raman spectra of HiPco powder using 633 nm and 532 nm lasers, respectively. RBM assignments and I_D/I_G ratios are labelled. (c) UV-vis-nIR spectrum of HiPco SWNTs (d) PL spectrum of HiPco SWNTs (e) Relative proportion of *(n,m)* SWNTs obtained from the PL spectrum. (f) Histogram of the approximate diameter distribution of the SWNTs in the sample obtained from the PL spectrum.

VII. 3. 1. 2. CoMoCAT SWNTs
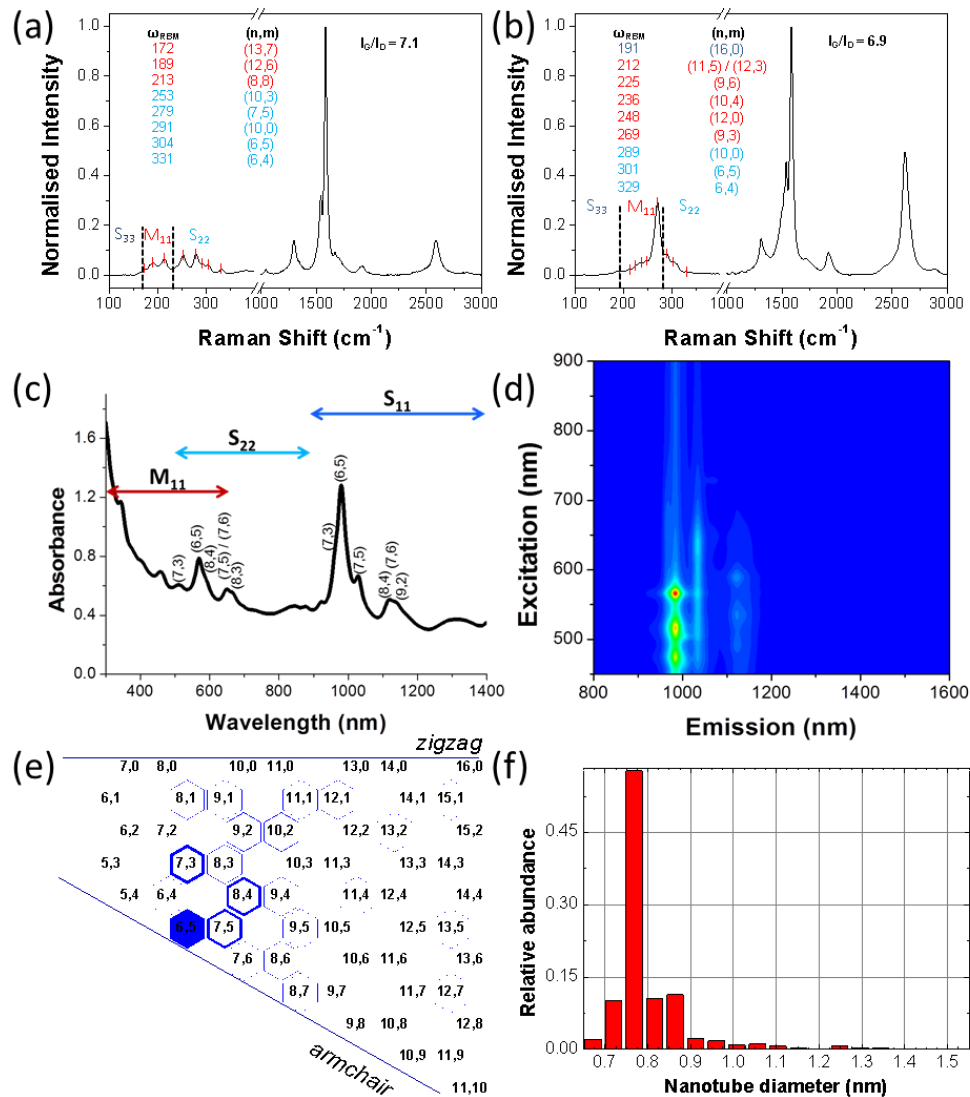
Fig. VII-3 Optical characterisation of as-received CoMoCAT SWNTs, batch #33. (a) and (b) Raman spectra of CoMoCAT powder using 633 nm and 532 nm lasers respectively. RBM assignments and I_D/I_G ratios are labelled. (c) UV-vis-nIR spectrum of CoMoCAT SWNTs (d) PL spectrum of CoMoCAT SWNTs (e) Relative proportion of *(n,m)* SWNTs obtained from the PL spectrum. (f) Histogram of the approximate diameter distribution of the SWNTs in the sample obtained from the PL spectrum.

VII. 3. 1. 3. Supergrowth
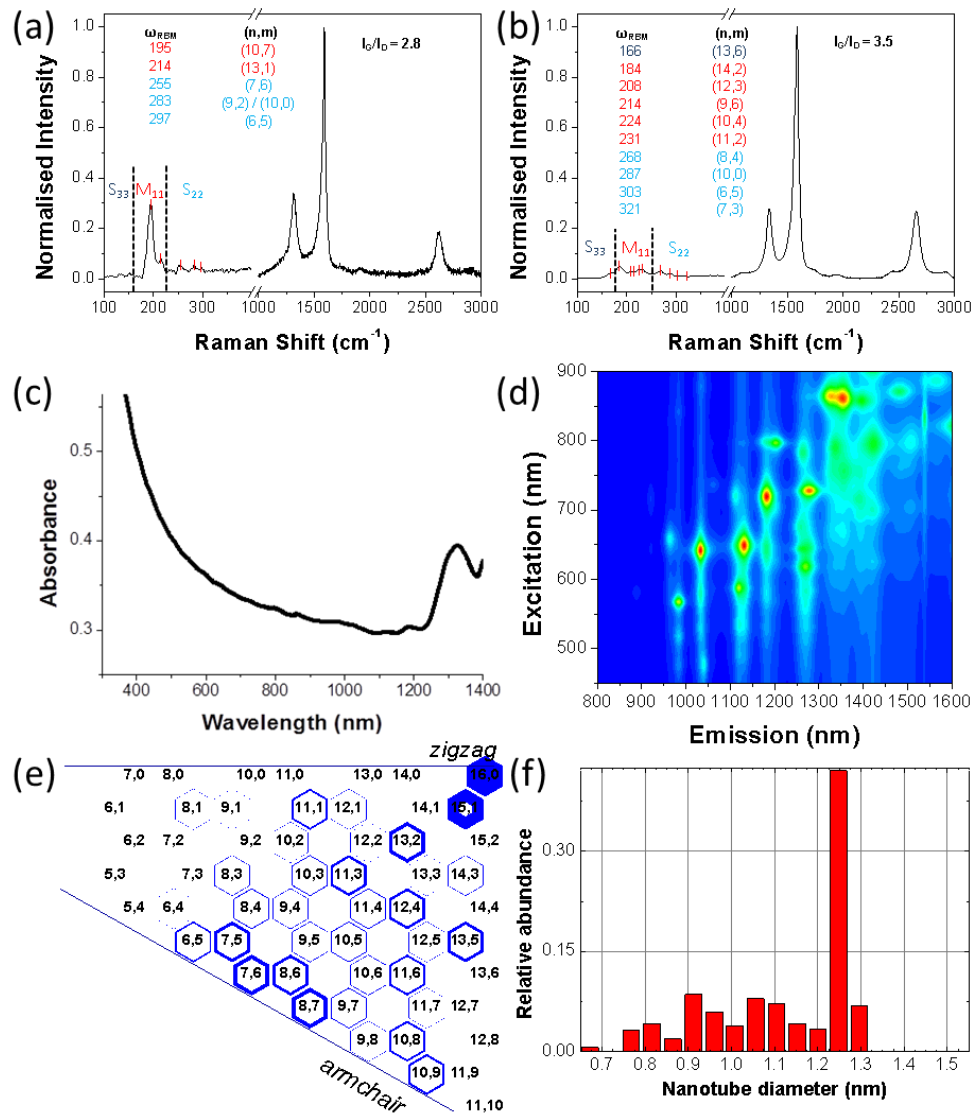
Fig. VII-4 Optical characterisation of as-received SG SWNTs, batch #STD2. (a) and (b) Raman spectra of SG powder using 633 nm and 532 nm lasers, respectively. RBM assignments and I_D/I_G ratios are labelled. (c) UV-vis-nIR spectrum of SG SWNTs. Signals from vHS transitions are very weak as a consequence of the broad diameter distribution of SWNTs in the sample. (d) PL spectrum of SG SWNTs (e) Relative proportion of *(n,m)* SWNTs obtained from the PL spectrum. (f) Histogram of the approximate diameter distribution of the SWNTs in the sample obtained from the PL spectrum.

VII. 3. 1. 4. Carbon Solutions
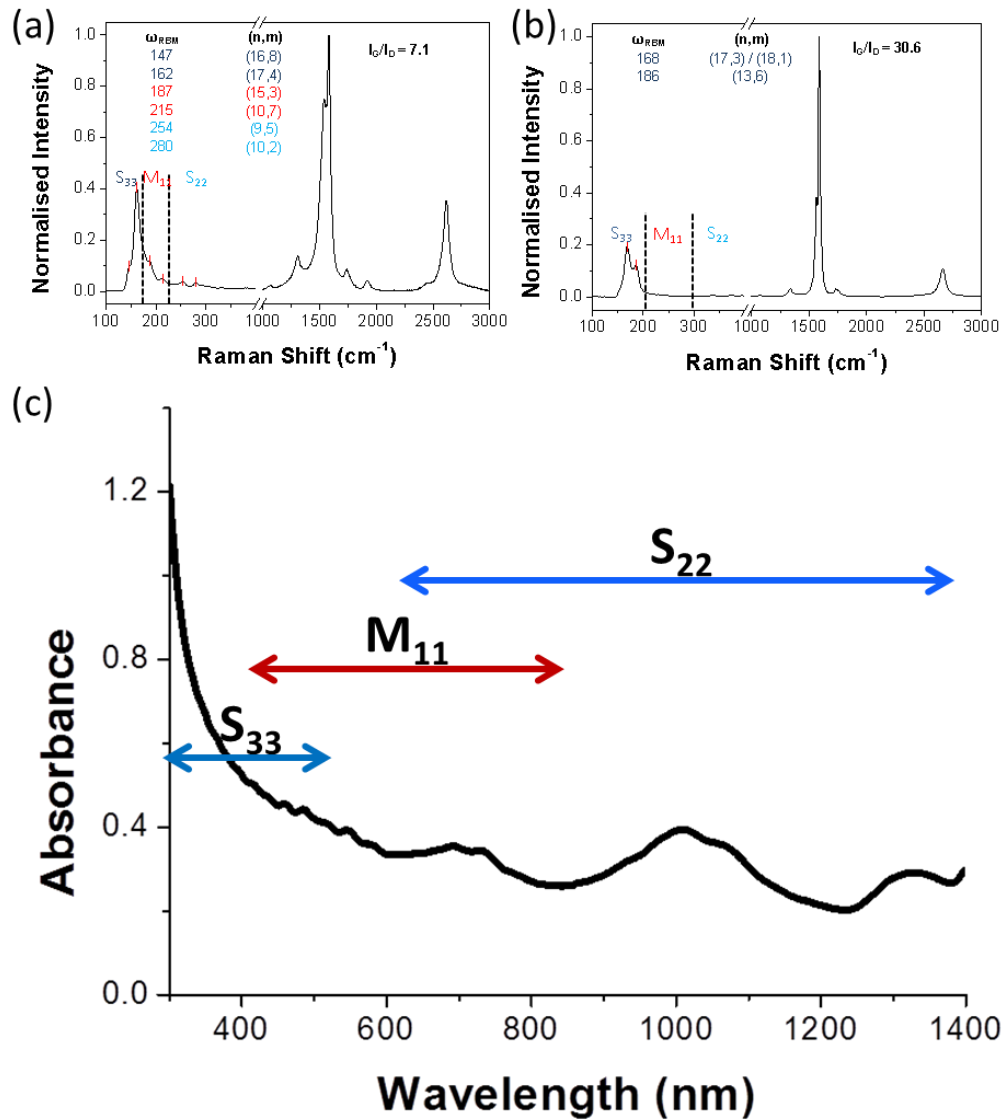
Fig. VII-5 Optical characterisation of as-received Carbon Solutions SWNTs, batch #AP183. (a) and (b) Raman spectra of Carbon Solutions powder using 633 nm and 532 nm lasers, respectively. RBM assignments and I_D/I_G ratios are labelled. (c) UV-vis-nIR spectrum of Carbon Solutions SWNTs. No PL spectra were observed for Carbon Solutions SWNTs.

VII. 3. 1. 5. Hanwha
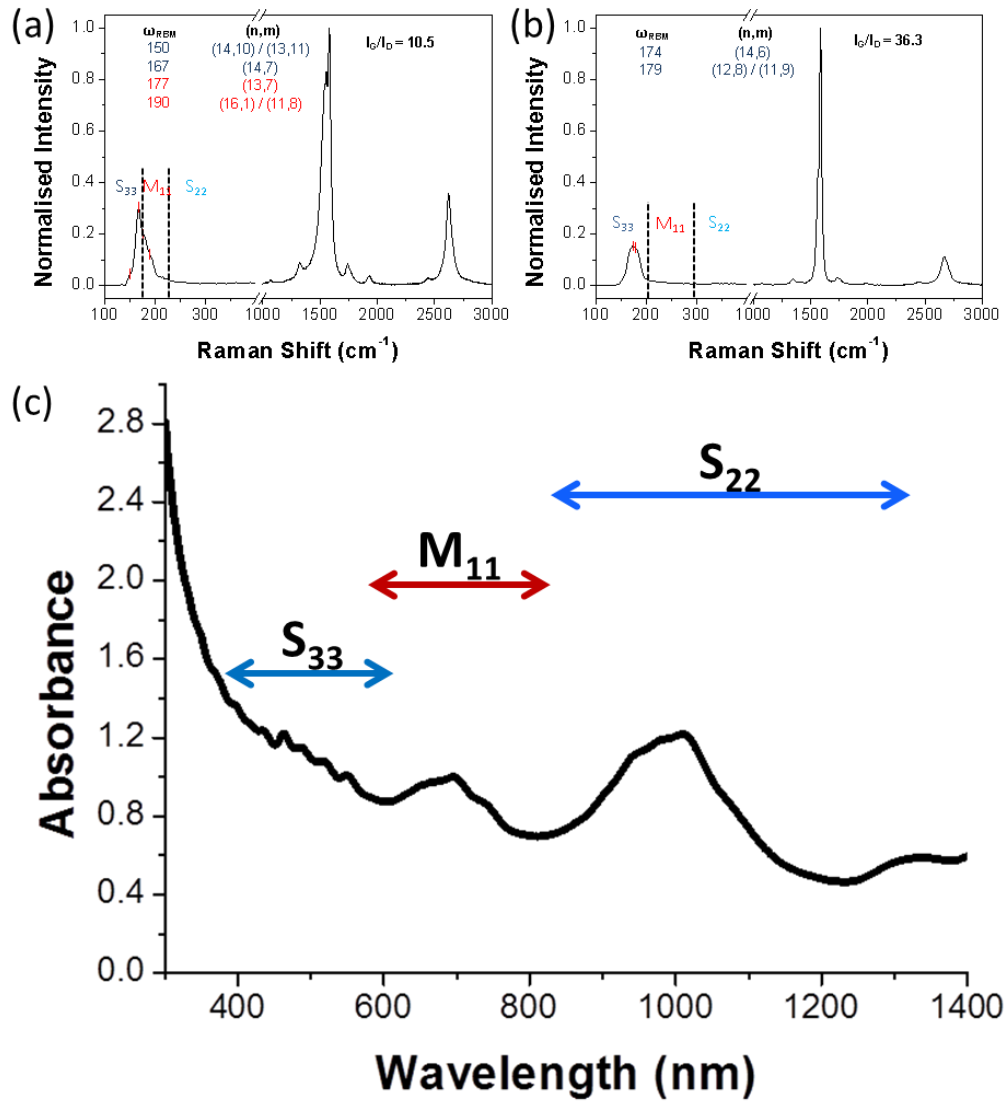
Fig. VII-6 Optical characterisation of as-received Hanwha SWNTs, batch #A-091230-2. (a) and (b) Raman spectra of Hanwha powder using 633 nm and 532 nm lasers, respectively. RBM assignments and I_D/I_G ratios are labelled. (c) UV-vis-nIR spectrum of Hanwha SWNTs. No PL spectra were observed for Hanwha SWNTs.

VIII. BIBLIOGRAPHY

1.   I. Freestone, N. Meeks, M. Sax and C. Higgitt, *Gold Bulletin*, 2007, **40**, 270-277.
2.   K. S. Novoselov, A. K. Geim, S. V. Morozov, D. Jiang, Y. Zhang, S. V. Dubonos, I. V. Grigorieva and A. A. Firsov, *Science*, 2004, **306**, 666-669.
3.   A. A. Green and M. C. Hersam, *The Journal of Physical Chemistry Letters*, 2009, **1**, 544-549.
4.   H. W. Kroto, J. R. Heath, S. C. O'Brien, R. F. Curl and R. E. Smalley, *Nature*, 1985, **318**, 162-163.
5.   L. X. Zheng, M. J. O'Connell, S. K. Doorn, X. Z. Liao, Y. H. Zhao, E. A. Akhadov, M. A. Hoffbauer, B. J. Roop, Q. X. Jia, R. C. Dye, D. E. Peterson, S. M. Huang, J. Liu and Y. T. Zhu, *Nature Materials*, 2004, **3**, 673-676.
6.   J. Meyer, *Artistic impression of a corrugated graphene sheet.*
7.   I. Suarez-Martinez, N. Grobert and C. P. Ewels, *Carbon*, 2012, **50**, 741-747.
8.   L. A. Girifalco, M. Hodak and R. S. Lee, *Physical Review B*, 2000, **62**, 13104-13110.
9.   M. S. Dresselhaus, G. Dresselhaus and P. Avouris, *Carbon nanotubes: Synthesis, structure, properties, and applications*, Springer, New York, 2001.
10.   J. M. Schnorr and T. M. Swager, *Chemistry of Materials*, 2010, **23**, 646-657.
11.   A. Peigney, C. Laurent, E. Flahaut, R. R. Bacsa and A. Rousset, *Carbon*, 2001, **39**, 507-514.
12.   M.-F. Yu, B. S. Files, S. Arepalli and R. S. Ruoff, *Physical Review Letters*, 2000, **84**, 5552-5555.
13.   J. Hone, M. Whitney, C. Piskoti and A. Zettl, *Physical Review B*, 1999, **59**, 2514-2516.
14.   M. Regi, 2007, pp. 113-193.
15.   W. Norimatsu, C. Kawai and M. Kusunoki, *A Close-Packed-Carbon-Nanotube Film on SiC for Thermal Interface Material Applications*, 2011.
16.   S. Hong and S. Myung, *Nature*, 2007, **2**, 207-208.
17.   B. S. Shim, Z. Tang, M. P. Morabito, A. Agarwal, H. Hong and N. A. Kotov, *Chemistry of Materials*, 2007, **19**, 5467-5474.
18.   A. Parish, *Production and applications of carbon nanotubes, carbon nanofibers, fullerenes, graphene and nanodiamonds: A global technology survey and market analysis*, Stamford, CT, USA, 2011.
19.   M. Endo, T. Hayashi, Y. A. Kim, M. Terrones and M. S. Dresselhaus, *Philosophical transactions. Series A, Mathematical, physical, and engineering sciences*, 2004, **362**, 2223-2238.
20.   L. Dai, *Carbon Nanotechnology: Recent Developments in Chemistry, Physics, Materials Science and Device Applications*, Elsevier Science, 2006.
21.   M. C. Hersam, *Nature Nanotechnology*, 2008, **3**, 387-394.
22.   C. Biswas and Y. H. Lee, *Advanced Functional Materials*, 2011, **21**, 3806-3826.
23.   T. Hayashi, Y. A. Kim, T. Matoba, M. Esaka, K. Nishimura, T. Tsukada, M. Endo and M. S. Dresselhaus, *Nano Letters*, 2003, **3**, 887-889.
24.   J. A. Elliott, J. K. W. Sandler, A. H. Windle, R. J. Young and M. S. P. Shaffer, *Physical Review Letters*, 2004, **92**, 095501.
25.   C. N. R. Rao, B. C. Satishkumar, A. Govindaraj and M. Nath, *ChemPhysChem*, 2001, **2**, 78-105.

26. M. Kalbac, A. A. Green, M. C. Hersam and L. Kavan, *Chemistry – A European Journal*, 2011, **17**, 9806-9815.
27. R. Saito, G. Dresselhaus and M. S. Dresselhaus, *Physical Review B*, 2000, **61**, 2981-2990.
28. R. Krupke, F. Hennrich, H. V. Löhneysen and M. M. Kappes, *Science*, 2003, **301**, 344-347.
29. S. Hyung Cheoul and et al., *Nanotechnology*, 2009, **20**, 065707.
30. W. Lu, Y. Xiong, A. Hassanien, W. Zhao, M. Zheng and L. Chen, *Nano letters*, 2009, **9**, 1668-1672.
31. Y. Hirana, Y. Tanaka, Y. Niidome and N. Nakashima, *Journal of the American Chemical Society*, 2010, **132**, 13072-13077.
32. R. Saito, G. Dresselhaus and M. S. Dresselhaus, World Scientific.
33. M. S. Dresselhaus, R. Saito and A. Jorio, *Physics of Semiconductors; Part A*, 2005.
34. T. Ando, *NPG Asia Materials*, 2009, **1**, 17-21.
35. L. Kavan and L. Dunsch, Springer Berlin Heidelberg, Berlin, Heidelberg, 2008, vol. 111, pp. 567-603.
36. R. Saito and H. Kataura, eds. M. Dresselhaus, G. Dresselhaus and P. Avouris, Springer Berlin / Heidelberg, 2001, vol. 80, pp. 213-247.
37. H. Kataura, Y. Kumazawa, Y. Maniwa, I. Umezu, S. Suzuki, Y. Ohtsuka and Y. Achiba, *Synthetic Metals*, 1999, **103**, 2555-2558.
38. A. Jorio, G. Dresselhaus and M. S. Dresselhaus, *Carbon Nanotubes: Advanced Topics in the Synthesis, Structure, Properties and Applications*, Springer, 2008.
39. A. Gaur, *Effects of Substrate and Molecular Adsorption on Raman Scattering from Individual Single-walled Carbon Nanotubes*, University of Illinois at Urbana-Champaign, 2008.
40. I. Heller, J. Kong, K. A. Williams, C. Dekker and S. G. Lemay, *Journal of the American Chemical Society*, 2006, **128**, 7353-7359.
41. R. B. Weisman and S. M. Bachilo, *Nano Letters*, 2003, **3**, 1235-1238.
42. A. Jorio, P. T. Araujo, S. K. Doorn, S. Maruyama, H. Chacham and M. A. Pimenta, *Physica Status Solidi (b)*, 2006, **243**, 3117-3121.
43. S. Maruyama, *Kataura Plot*, http://www.photon.t.u-tokyo.ac.jp/~maruyama/kataura/kataura.html, 2002.
44. S. Suzuki, Y. Watanabe, Y. Homma, S.-y. Fukuba, S. Heun and A. Locatelli, *Applied Physics Letters*, 2004, **85**, 127-129.
45. S. Trasatti, *Journal of Electroanalytical Chemistry and Interfacial Electrochemistry*, 1972, **39**, 163-184.
46. S. Gupta and J. Robertson, *Journal of Applied Physics*, 2006, **100**, 083711-083711.
47. J. Zhao, J. Han and J. P. Lu, *Physical Review B*, 2002, **65**, 193401-193401.
48. S. B. Cronin, R. Barnett, M. Tinkham, S. G. Chou, O. Rabin, M. S. Dresselhaus, A. K. Swan, M. S. Unlu and B. B. Goldberg, *Applied Physics Letters*, 2004, **84**, 2052-2054.
49. K. Okazaki, Y. Nakato and K. Murakoshi, *Physical Review B*, 2003, **68**, 35434-35434.
50. S. Trasatti, *Pure and Applied Chemistry*, 1986, **58**, 955-966.
51. S. Kazaoui, N. Minami, N. Matsuda, H. Kataura and Y. Achiba, *Applied Physics Letters*, 2001, **78**, 3433-3435.
52. V. Ivanovskaya, C. Köhler and G. Seifert, *Physical Review B*, 2007, **75**, 75410-75410.
53. S. Iijima, *Nature*, 1991, **354**, 56-58.
54. S. Iijima and T. Ichihashi, *Nature*, 1993, **363**, 603-605.
55. J. Prasek, J. Drbohlavova, J. Chomoucka, J. Hubalek, O. Jasek, V. Adam and R. Kizek, *Journal of Materials Chemistry*, 2011.
56. K. Hata, *Society of Photo-Optical Instrumentation Engineers*, 2007.

57. P. Nikolaev, M. J. Bronikowski, R. K. Bradley, F. Rohmund, D. T. Colbert, K. A. Smith and R. E. Smalley, *Chemical Physics Letters*, 1999, **313**, 91-97.

58. S. M. Bachilo, L. Balzano, J. E. Herrera, F. Pompeo, D. E. Resasco and R. B. Weisman, *Journal of the American Chemical Society*, 2003, **125**, 11186-11187.

59. D. E. Resasco, W. E. Alvarez, F. Pompeo, L. Balzano, J. E. Herrera, B. Kitiyanan and A. Borgna, *Journal of Nanoparticle Research*, 2002, **4**, 131-136.

60. Y. Li, D. Mann, M. Rolandi, W. Kim, A. Ural, S. Hung, A. Javey, J. Cao, D. Wang, E. Yenilmez, Q. Wang, J. F. Gibbons, Y. Nishi and H. Dai, *Nano Letters*, 2004, **4**, 317-321.

61. Y. Li, S. Peng, D. Mann, J. Cao, R. Tu, K. J. Cho and H. Dai, *The Journal of Physical Chemistry B*, 2005, **109**, 6968-6971.

62. C. Zoican Loebick, R. Podila, J. Reppert, J. Chudow, F. Ren, G. L. Haller, A. M. Rao and L. D. Pfefferle, *Journal of the American Chemical Society*, 2010, **132**, 11125-11131.

63. A. R. Harutyunyan, G. Chen, T. M. Paronyan, E. M. Pigos, O. A. Kuznetsov, K. Hewaparakrama, S. M. Kim, D. Zakharov, E. A. Stach and G. U. Sumanasekera, *Science*, 2009, **326**, 116-120.

64. F. Ding, A. R. Harutyunyan and B. I. Yakobson, *Proceedings of the National Academy of Sciences*, 2009, **106**, 2506-2509.

65. R. M. Sundaram, K. K. K. Koziol and A. H. Windle, *Advanced Materials*, 2011, **23**, 5064-5068.

66. S. Huang, X. Cai, C. Du and J. Liu, *The Journal of Physical Chemistry B*, 2003, **107**, 13251-13254.

67. T.-J. Park, S. Banerjee, T. Hemraj-Benny and S. S. Wong, *Journal of Materials Chemistry*, 2006, **16**, 141-154.

68. Y. Wang, H. Shan, R. H. Hauge, M. Pasquali and R. E. Smalley, *The Journal of Physical Chemistry B*, 2007, **111**, 1249-1252.

69. F. Liang, A. K. Sadana, A. Peera, J. Chattopadhyay, Z. Gu, R. H. Hauge and W. E. Billups, *Nano Letters*, 2004, **4**, 1257-1260.

70. V. C. Moore, M. S. Strano, E. H. Haroz, R. H. Hauge, R. E. Smalley, J. Schmidt and Y. Talmon, *Nano Lett.*, 2003, **3**, 1379-1382.

71. S. D. Bergin, V. Nicolosi, P. V. Streich, S. Giordani, Z. Sun, A. H. Windle, P. Ryan, N. P. P. Niraj, Z.-t. T. Wang, L. Carpenter, W. J. Blau, J. J. Boland, J. P. Hamilton and J. N. Coleman, *Advanced Materials*, 2008, **20**, 1876-1881.

72. F. Hennrich, R. Krupke, K. Arnold, J. A., S. Lebedkin, T. Koch, T. Schimmel and M. M. Kappes, *The Journal of Physical Chemistry B*, 2007, **111**, 1932-1937.

73. S. Niyogi, M. A. Hamon, H. Hu, B. Zhao, P. Bhowmik, R. Sen, M. E. Itkis and R. C. Haddon, *Accounts of Chemical Research*, 2002, **35**, 1105-1113.

74. S. Deng, Y. Zhang, A. H. Brozena, M. L. Mayes, P. Banerjee, W.-A. Chiou, G. W. Rubloff, G. C. Schatz and Y. Wang, *Nature Communications*, 2011, **2**, 382.

75. Y. Miyata, T. Kawai, Y. Miyamoto, K. Yanagi, Y. Maniwa and H. Kataura, *The Journal of Physical Chemistry C*, 2007, **111**, 9671-9677.

76. E. Joselevich, *ChemPhysChem*, 2004, **5**, 619-624.

77. Y. Miyata, Y. Maniwa and H. Kataura, *The Journal of Physical Chemistry B*, 2006, **110**, 25-29.

78. H. Wang and J. Xu, *Chemical Physics Letters*, 2009, **477**, 176-178.

79. M. Yudasaka, M. Zhang and S. Iijima, *Chemical Physics Letters*, 2003, **374**, 132-136.

80. J. Lu, L. Lai, G. Luo, J. Zhou, R. Qin, D. Wang, L. Wang, W. N. Mei, G. Li, Z. Gao, S. Nagase, Y. Maeda, T. Akasaka and D. Yu, *Small*, 2007, **3**, 1566-1576.

81.   C. Ménard-Moyon, N. Izard, E. Doris and C. Mioskowski, *Journal of the American Chemical Society*, 2006, **128**, 6552-6553.
82.   S. Campidelli, M. Meneghetti and M. Prato, *Small*, 2007, **3**, 1672-1676.
83.   R. Krupke and F. Hennrich, *Advanced Engineering Materials*, 2005, **7**, 111-116.
84.   S. A. Hodge, M. K. Bayazit, K. S. Coleman and M. S. P. Shaffer, *Chemical Society Reviews*, 2012.
85.   P. G. Collins, M. S. Arnold and P. Avouris, *Science*, 2001, **292**, 706-709.
86.   M. S. Arnold, A. A. Green, J. F. Hulvat, S. I. Stupp and M. C. Hersam, *Nature Nanotechnology*, 2006, **1**, 60-65.
87.   M. Zheng, A. Jagota, E. D. Semke, B. A. Diner, R. S. McLean, S. R. Lustig, R. E. Richardson and N. G. Tassi, *Nature materials*, 2003, **2**, 338-342.
88.   X. Tu, S. Manohar, A. Jagota and M. Zheng, *Nature*, 2009, **460**, 250-253.
89.   H. Liu, Y. Feng, T. Tanaka, Y. Urabe and H. Kataura, *The Journal of Physical Chemistry C*, 2010, **114**, 9270-9276.
90.   H. Liu, D. Nishide, T. Tanaka and H. Kataura, *Nature Communications*, 2011, **2**, 309.
91.   M. K. Bayazit, L. S. Clarke, K. S. Coleman and N. Clarke, *Journal of the American Chemical Society*, 2010, **132**, 15814-15819.
92.   K. Balasubramanian, R. Sordan, M. Burghard and K. Kern, *Nano Letters*, 2004, **4**, 827-830.
93.   L. An, Q. Fu, C. Lu and J. Liu, *Journal of the American Chemical Society*, 2004, **126**, 10520-10521.
94.   C. Wang, Q. Cao, T. Ozel, A. Gaur, J. A. Rogers and M. Shim, *Journal of the American Chemical Society*, 2005, **127**, 11460-11468.
95.   S. Ghosh and C. Rao, *Nano Research*, 2009, **2**, 183-191.
96.   S. Toyoda, Y. Yamaguchi, M. Hiwatashi, Y. Tomonari, H. Murakami and N. Nakashima, *Chemistry – An Asian Journal*, 2007, **2**, 145-149.
97.   M. S. Strano, C. A. Dyke, M. L. Usrey, P. W. Barone, M. J. Allen, H. Shan, C. Kittrell, R. H. Hauge, J. M. Tour and R. E. Smalley, *Science*, 2003, **301**, 1519-1522.
98.   G. Schmidt, S. Gallon, S. Esnouf, J.-P. Bourgoin and P. Chenevier, *Chemistry – A European Journal*, 2009, **15**, 2101-2110.
99.   F. G. Brunetti, M. A. Herrero, J. d. M. Muñoz, S. Giordani, A. Díaz-Ortiz, S. Filippone, G. Ruaro, M. Meneghetti, M. Prato and E. Vázquez, *Journal of the American Chemical Society*, 2007, **129**, 14580-14581.
100.   F. G. Brunetti, M. A. Herrero, J. d. M. Munoz, A. Diaz-Ortiz, J. Alfonsi, M. Meneghetti, M. Prato and E. Vazquez, *Journal of the American Chemical Society*, 2008, **130**, 8094-8100.
101.   M. K. Bayazit and K. S. Coleman, *Journal of the American Chemical Society*, 2009, **131**, 10670-10676.
102.   M. A. Hamon, K. L. Stensaas, M. A. Sugar, K. C. Tumminello and A. K. Allred, *Chemical Physics Letters*, 2007, **447**, 1-4.
103.   S. Banerjee and S. S. Wong, *Journal of the American Chemical Society*, 2004, **126**, 2073-2081.
104.   S. Banerjee and S. S. Wong, *Nano Letters*, 2004, **4**, 1445-1450.
105.   H. Hu, B. Zhao, M. A. Hamon, K. Kamaras, M. E. Itkis and R. C. Haddon, *Journal of the American Chemical Society*, 2003, **125**, 14893-14900.
106.   C. Liu, Q. Zhang, F. Stellacci, N. Marzari, L. Zheng and Z. Zhan, *Small*, 2011, **7**, 1257-1263.
107.   M. Holzinger, J. Abraham, P. Whelan, R. Graupner, L. Ley, F. Hennrich, M. Kappes and A. Hirsch, *Journal of the American Chemical Society*, 2003, **125**, 8566-8580.

108. T. Hemraj-Benny and S. S. Wong, *Chemistry of Materials*, 2006, **18**, 4827-4839.

109. Y. Lee, K.-S. Jeon, H. Lim, H. S. Shin, S. M. Jin, H. R. Byon, Y. D. Suh and H. C. Choi, *Small*, 2009, **5**, 1398-1402.

110. C.-M. Yang, K. H. An, J. S. Park, K. A. Park, S. C. Lim, S.-H. Cho, Y. S. Lee, W. Park, C. Y. Park and Y. H. Lee, *Physical Review B*, 2006, **73**, 075419.

111. A. Hassanien and et al., *Nanotechnology*, 2005, **16**, 278.

112. G. Zhang, P. Qi, X. Wang, Y. Lu, X. Li, R. Tu, S. Bangsaruntip, D. Mann, L. Zhang and H. Dai, *Science*, 2006, **314**, 974-977.

113. H. Zhang, Y. Liu, L. Cao, D. Wei, Y. Wang, H. Kajiura, Y. Li, K. Noda, G. Luo, L. Wang, J. Zhou, J. Lu and Z. Gao, *Advanced Materials*, 2009, **21**, 813-816.

114. C. Bergeret, J. Cousseau, V. Fernandez, J.-Y. Mevellec and S. Lefrant, *The Journal of Physical Chemistry C*, 2008, **112**, 16411-16416.

115. E. Menna, F. Della Negra, M. Dalla Fontana and M. Meneghetti, *Physical Review B*, 2003, **68**, 193412.

116. J. G. Wiltshire, A. N. Khlobystov, L. J. Li, S. G. Lyapin, G. A. D. Briggs and R. J. Nicholas, *Chemical Physics Letters*, 2004, **386**, 239-243.

117. H. Qiu, Y. Maeda and T. Akasaka, *Journal of the American Chemical Society*, 2009, **131**, 16529-16533.

118. C.-M. Yang, J. S. Park, K. H. An, S. C. Lim, K. Seo, B. Kim, K. A. Park, S. Han, C. Y. Park and Y. H. Lee, *The Journal of Physical Chemistry B*, 2005, **109**, 19242-19248.

119. M. Zhang, M. Yudasaka, Y. Miyauchi, S. Maruyama and S. Iijima, *The Journal of Physical Chemistry B*, 2006, **110**, 8935-8940.

120. T. J. McDonald, J. L. Blackburn, W. K. Metzger, G. Rumbles and M. J. Heben, *The Journal of Physical Chemistry C*, 2007, **111**, 17894-17900.

121. R. Graupner, J. Abraham, D. Wunderlich, A. Vencelová, P. Lauffer, J. Röhrl, M. Hundhausen, L. Ley and A. Hirsch, *Journal of the American Chemical Society*, 2006, **128**, 6683-6689.

122. D. Wunderlich, F. Hauke and A. Hirsch, *Chemistry – A European Journal*, 2008, **14**, 1607-1614.

123. D. Wunderlich, F. Hauke and A. Hirsch, *Journal of Materials Chemistry*, 2008, **18**, 1493-1497.

124. M. K. Bayazit, A. Suri and K. S. Coleman, *Carbon*, 2010, **48**, 3412-3419.

125. S. Deng, A. H. Brozena, Y. Zhang, Y. Piao and Y. Wang, *Chemical Communications*, 2011, **47**, 758-760.

126. Y.-S. Lee and N. Marzari, *Physical Review Letters*, 2006, **97**, 116801.

127. E. Anglaret, F. Dragin, A. Pénicaud and R. Martel, *The Journal of Physical Chemistry B*, 2006, **110**, 3949-3954.

128. A. Pénicaud, P. Poulin, A. Derré, E. Anglaret and P. Petit, *Journal of the American Chemical Society*, 2005, **127**, 8-9.

129. S. Fogden, C. A. Howard, R. K. Heenan, N. T. Skipper and M. S. P. Shaffer, *ACS Nano*, 2011, **6**, 54-62.

130. N. G. Parra-Vasquez, N. Behabtu, M. J. Green, C. L. Pint, C. C. Young, J. Schmidt, E. Kesselman, A. Goyal, P. M. Ajayan, Y. Cohen, Y. Talmon, R. H. Hauge and M. Pasquali, *ACS Nano*, 2010, **4**, 3969-3978.

131. D. Voiry, C. Drummond and A. Penicaud, *Soft Matter*, 2011, **7**, 7998-8001.

132.   S. Ramesh, L. M. Ericson, V. A. Davis, R. K. Saini, C. Kittrell, M. Pasquali, W. E. Billups, W. W. Adams, R. H. Hauge and R. E. Smalley, *The Journal of Physical Chemistry B*, 2004, **108**, 8794-8798.

133.   V. A. Davis, A. N. G. Parra-Vasquez, M. J. Green, P. K. Rai, N. Behabtu, V. Prieto, R. D. Booker, J. Schmidt, E. Kesselman, W. Zhou, H. Fan, W. W. Adams, R. H. Hauge, J. E. Fischer, Y. Cohen, Y. Talmon, R. E. Smalley and M. Pasquali, *Nature Nanotechnology*, 2009, **4**, 830-834.

134.   A. Catheline, C. Valles, C. Drummond, L. Ortolani, V. Morandi, M. Marcaccio, M. Iurlo, F. Paolucci and A. Penicaud, *Chemical Communications*, 2011, **47**, 5470-5472.

135.   F. Oosawa, *Polyelectrolytes*, M. Dekker, 1971.

136.   A. V. Dobrynin, in *Polymer Science: A Comprehensive Reference*, eds. M. Editors-in-Chief: Krzysztof and M. Martin, Elsevier, Amsterdam, 2012, pp. 81-132.

137.   L. Besra and M. Liu, *Progress in Materials Science*, 2007, **52**, 1-61.

138.   I. Szleifer and R. Yerushalmi-Rozen, *Polymer*, 2005, **46**, 7803-7818.

139.   Y. Chen, R. C. Haddon, S. Fang, A. M. Rao, P. C. Eklund, W. H. Lee, E. C. Dickey, E. A. Grulke, J. C. Pendergrass, A. Chavan, B. E. Haley and R. E. Smalley, *Journal of Materials Research*, 1998, **13**, 2423-2431.

140.   F. Liang, L. B. Alemany, J. M. Beach and W. E. Billups, *Journal of the American Chemical Society*, 2005, **127**, 13941-13948.

141.   D. Voiry, O. Roubeau and A. Penicaud, *Journal of Materials Chemistry*, 2010, **20**, 4385-4391.

142.   D. Voiry, C. Vallés, O. Roubeau and A. Pénicaud, *Carbon*, 2011, **49**, 170-175.

143.   A. Mukherjee, R. Combs, J. Chattopadhyay, D. W. Abmayr, P. S. Engel and W. E. Billups, *Chemistry of Materials*, 2008, **20**, 7339-7343.

144.   G. Jingwen, Yadienka Martinez-Rubi, Stéphane Dénommée, Dean Ruth, Christopher T Kingston, Malgosia Daroszewska, Michael Barnes and B. Simard, *Nanotechnology*, 2009, **20**, 245701.

145.   Y. Martinez-Rubi, J. Guan, S. Lin, C. Scriver, R. E. Sturgeon and B. Simard, *Chemical Communications*, 2007, 5146-5148.

146.   F. Liang, J. M. Beach, K. Kobashi, A. K. Sadana, Y. I. Vega-Cantu, J. M. Tour and W. E. Billups, *Chemistry of Materials*, 2006, **18**, 4764-4767.

147.   B. Gebhardt, Z. Syrgiannis, C. Backes, R. Graupner, F. Hauke and A. Hirsch, *Journal of the American Chemical Society*, 2011, **133**, 7985-7995.

148.   B. Gebhardt, F. Hof, C. Backes, M. Müller, T. Plocke, J. Maultzsch, C. Thomsen, F. Hauke and A. Hirsch, *Journal of the American Chemical Society*, 2011, **133**, 19459-19473.

149.   J. Chattopadhyay, S. Chakraborty, A. Mukherjee, R. Wang, P. S. Engel and W. E. Billups, *The Journal of Physical Chemistry C*, 2007, **111**, 17928-17932.

150.   B. Gebhardt, R. Graupner, F. Hauke and A. Hirsch, *European Journal of Organic Chemistry*, 2010, **2010**, 1494-1501.

151.   J. L. Bahr, J. Yang, D. V. Kosynkin, M. J. Bronikowski, R. E. Smalley and J. M. Tour, *Journal of the American Chemical Society*, 2001, **123**, 6536-6542.

152.   S. Fogden, *Purification, Dispersion and Separation of Single Walled Carbon Nanotubes*, Imperial College London, 2009.

153.   S. Lower, *Galvanic cells and electrodes*, http://www.chem1.com/acad/webtext/elchem/ec2.html.

154.   A. Fisher, *Electrochemistry Fundamentals*, http://www.cheng.cam.ac.uk/research/groups/electrochem/teaching.html.

155. Analytical Sciences Digital Library, *Analytical Electrochemistry: The Basic Concepts*, http://www.asdlib.org/onlineArticles/ecourseware/Kelly_Potentiometry/PDF-5-MassTransport.pdf.

156. J. Wang, *Analytical Electrochemistry*, John Wiley & Sons, 2000.

157. A. Fisher, *The Electrical Double Layer*, http://www.cheng.cam.ac.uk/research/groups/electrochem/JAVA/electrochemistry/ELEC/l9html/dl.html.

158. D. C. Grahame, *Chemical Reviews*, 1947, **41**, 441-501.

159. H. B. Mark, *Analyst*, 1990, **115**, 667-678.

160. S. P. Kounaves, in *Handbook of instrumental techniques for analytical chemistry*, ed. F. A. Settle, Prentice Hall PTR, 1997.

161. Gamry Instruments Inc., *Potentiostat Fundamentals*, 2011.

162. J. O. Besenhard and H. P. Fritz, *Angewandte Chemie International Edition in English*, 1983, **22**, 950-975.

163. I. Noviandri, R. D. Bolskar, P. A. Lay and C. A. Reed, *The Journal of Physical Chemistry B*, 1997, **101**, 6350-6358.

164. R. C. Haddon, *Accounts of Chemical Research*, 1992, **25**, 127-133.

165. C. A. Reed and R. D. Bolskar, *Chemical Reviews*, 2000, **100**, 1075-1120.

166. D. Dubois, G. Moninot, W. Kutner, M. T. Jones and K. M. Kadish, *The Journal of Physical Chemistry*, 1992, **96**, 7137-7145.

167. Q. Xie, E. Perez-Cordero and L. Echegoyen, *Journal of the American Chemical Society*, 1992, **114**, 3978-3980.

168. C. Bruno, I. Doubitski, M. Marcaccio, F. Paolucci, D. Paolucci and A. Zaopo, *Journal of the American Chemical Society*, 2003, **125**, 15738-15739.

169. G. Z. Chen, X. Fan, A. Luget, M. S. P. Shaffer, D. J. Fray and A. H. Windle, *Journal of Electroanalytical Chemistry*, 1998, **446**, 1-6.

170. L. Kavan and L. Dunsch, *ChemPhysChem*, 2011, **12**, 47-55.

171. I. Dumitrescu, P. R. Unwin and J. V. Macpherson, *Chemical Communications*, 2009, **7345**, 6886-68901.

172. D. Paolucci, M. M. Franco, M. Iurlo, M. Marcaccio, M. Prato, F. Zerbetto, A. Penicaud and F. Paolucci, *Journal of the American Chemical Society*, 2008, **130**, 7393-7399.

173. Y. Tanaka, Y. Hirana, Y. Niidome, K. Kato, S. Saito and N. Nakashima, *Angewandte Chemie*, 2009, **48**, 7655-7659.

174. M. J. O'Connell, E. E. Eibergen and S. K. Doorn, *Nature materials*, 2005, **4**, 412-418.

175. K. Murakoshi and K. Okazaki, *Electrochimica Acta*, 2005, **50**, 3069-3075.

176. C.-y. Liu, A. J. Bard, F. Wudl, I. Weitz and J. R. Heath, *Electrochemical and Solid-State Letters*, 1999, **2**, 577-578.

177. M. Hahn, M. Baertschi, O. Barbieri, J. C. Sauter, R. Kotz and R. Gallay, *Electrochemical and Solid-State Letters*, 2004, **7**, A33-A36.

178. P. W. Ruch, R. Kötz and A. Wokaun, *Electrochimica Acta*, 2009, **54**, 4451-4458.

179. L. Kavan, P. Rapta, L. Dunsch, M. J. Bronikowski, P. Willis and R. E. Smalley, *The Journal of Physical Chemistry B*, 2001, **105**, 10764-10771.

180. A. Al-zubaidi, T. Inoue, T. Matsushita, Y. Ishii, T. Hashimoto and S. Kawasaki, *The Journal of Physical Chemistry C*, 2012.

181. C. J. Warren, R. C. Haushalter and A. B. Bocarsly, *Journal of Alloys and Compounds*, 1995, **229**, 175-205.

182. D. Pletcher and F. Walsh, *Industrial Electrochemistry*, Chapman and Hall, 1990.

183. W. G. Davenport, *Extractive Metallurgy of Copper*, Pergamon, 2002.
184. E. Peled and E. Gileadi, *Journal of The Electrochemical Society*, 1976, **123**, 15-19.
185. T. Belin and F. Epron, *Materials Science and Engineering: B*, 2005, **119**, 105-118.
186. S. Arepalli, S. W. Freiman, S. A. Hooker and K. D. Migler, *Measurement issues in single-wall carbon nanotubes*, 2008.
187. C. Engtrakul, M. F. Davis, K. Mistry, B. A. Larsen, A. C. Dillon, M. J. Heben and J. L. Blackburn, *Journal of the American Chemical Society*, 2010, **132**, 9956-9957.
188. S. Cambré, W. Wenseleers, J. Culin, Sabine, A. Fonseca, J. B. Nagy and E. Goovaerts, *ChemPhysChem*, 2008, **9**, 1930-1941.
189. Y. Sato, K. Yanagi, Y. Miyata, K. Suenaga, H. Kataura and S. Iijima, *Nano Letters*, 2008, **8**, 3151-3154.
190. A. Vijayaraghavan and et al., *Nanotechnology*, 2011, **22**, 265715.
191. J. W. G. Wilder, L. C. Venema, A. G. Rinzler, R. E. Smalley and C. Dekker, *Nature*, 1998, **391**, 59-62.
192. J. F. Colomer, L. Henrard, P. Launois, G. Van Tendeloo, A. A. Lucas and P. Lambin, *Physical Review B*, 2004, **70**, 075408.
193. A. Jorio, I. O. Maciel, P. T. Araujo, P. B. C. Pesce and M. A. Pimenta, *Physica Status Solidi (b)*, 2007, **244**, 4011-4015.
194. E. B. Wilson, J. C. Decius and P. C. Cross, *Molecular Vibrations: The Theory of Infrared and Raman Vibrational Spectra*, Dover Publications, 1980.
195. Horiba Scientific, *What is Raman Spectroscopy?*, http://www.horiba.com/uk/scientific/products/raman-spectroscopy/tutorial-faqs/raman-faqs/what-is-raman-spectroscopy/.
196. M. S. Dresselhaus, G. Dresselhaus, R. Saito and A. Jorio, *Physics Reports*, 2005, **409**, 47-99.
197. S. K. Doorn, D. A. Heller, P. W. Barone, M. L. Usrey and M. S. Strano, *Applied Physics A: Materials Science & Processing*, 2004, **78**, 1147-1155.
198. L. Grigorian, S. Colbern, I. O. Maciel, M. A. Pimenta, F. Plentz and A. Jorio, *Nanotechnology*, 2007, **18**, 435705-435705.
199. P. T. Araujo, I. O. Maciel, P. B. C. Pesce, M. A. Pimenta, S. K. Doorn, H. Qian, A. Hartschuh, M. Steiner, L. Grigorian, K. Hata and A. Jorio, *Physical Review B*, 2008, **77**, 241403.
200. C. Fantini, A. Jorio, M. Souza, M. S. Strano, M. S. Dresselhaus and M. A. Pimenta, *Physical Review Letters*, 2004, **93**, 147406.
201. S. Heeg, E. Malić, C. Casiraghi and S. Reich, *Physica Status Solidi (b)*, 2009, **246**, 2740-2743.
202. J.-Y. Mevellec, C. Bergeret, J. Cousseau, J.-P. Buisson, C. P. Ewels and S. Lefrant, *Journal of the American Chemical Society*, 2011, **133**, 16938-16946.
203. D. A. Heller, P. W. Barone, J. P. Swanson, R. M. Mayrhofer and M. S. Strano, *The Journal of Physical Chemistry B*, 2004, **108**, 6905-6909.
204. S. D. M. Brown, A. Jorio, P. Corio, M. S. Dresselhaus, G. Dresselhaus, R. Saito and K. Kneipp, *Physical Review B*, 2001, **63**, 155414.
205. R. Graupner, *Journal of Raman Spectroscopy*, 2007, **38**, 673-683.
206. Thermo Spectronic, *Basic UV-Vis Theory, Concepts and Applications,* 2011.
207. W.-J. Kim, M. L. Usrey and M. S. Strano, *Chemistry of Materials*, 2007, **19**, 1571-1576.
208. J.-H. Lee, U. Paik, J.-Y. Choi, K. K. Kim, S.-M. Yoon, J. Lee, B.-K. Kim, J. M. Kim, M. H. Park, C. W. Yang, K. H. An and Y. H. Lee, *The Journal of Physical Chemistry C*, 2007, **111**, 2477-2483.

209.   T. Hasan, V. Scardaci, P. H. Tan, A. G. Rozhin, W. I. Milne and A. C. Ferrari, *The Journal of Physical Chemistry C*, 2007, **111**, 12594-12602.

210.   S. D. Bergin, Z. Sun, D. Rickard, P. V. Streich, J. P. Hamilton and J. N. Coleman, *ACS Nano*, 2009, **3**, 2340-2350.

211.   S. Giordani, S. D. Bergin, V. Nicolosi, S. Lebedkin, M. M. Kappes, W. J. Blau and J. N. Coleman, *The Journal of Physical Chemistry B*, 2006, **110**, 15708-15718.

212.   B. Zhao, M. E. Itkis, S. Niyogi, H. Hu, J. Zhang and R. C. Haddon, *The Journal of Physical Chemistry B*, 2004, **108**, 8136-8141.

213.   S. M. Bachilo, M. S. Strano, C. Kittrell, R. H. Hauge, R. E. Smalley and R. B. Weisman, *Science*, 2002, **298**, 2361-2366.

214.   L. Cognet, D. A. Tsyboulski, J.-D. R. Rocha, C. D. Doyle, J. M. Tour and R. B. Weisman, *Science*, 2007, **316**, 1465-1468.

215.   Y. Qian, C. Wang, G. Ren and B. Huang, *Applied Surface Science*, 2010, **256**, 4038-4041.

216.   Materials Evaluation and Engineering Inc., *Handbook of Analytical Methods for Materials: Scanning Electron Microscopy,* 2009.

217.   Measurements and Characterization division, *Measurements and Characterization: Analytical Microscopy*, National Renewable Energy Laboratory, 2000.

218.   A. Rao and K. McGuire, in *Carbon Nanotubes*, CRC Press, 2004, pp. 117-136.

219.   D. B. Williams and C. B. Carter, *Transmission Electron Microscopy: A Textbook for Materials Science*, Springer, 2009.

220.   B. W. Smith and D. E. Luzzi, *Journal of Applied Physics*, 2001, **90**, 3509-3515.

221.   V. H. Crespi, N. G. Chopra, M. L. Cohen, A. Zettl and S. G. Louie, *Physical Review B*, 1996, **54**, 5927-5931.

222.   G. Binnig, C. F. Quate and C. Gerber, *Physical Review Letters*, 1986, **56**, 930-933.

223.   G. Binnig, G. Ch, E. Stoll, T. R. Albrecht and C. F. Quate, *Europhysics Letters*, 1987, **3**, 1281.

224.   Materials Evaluation and Engineering Inc., *Handbook of Analytical Methods for Materials: Atomic Force Microscopy,* 2009.

225.   S. Bellucci, G. Gaggiotti, M. Marchetti, F. Micciulla, R. Mucciato and M. Regi, *Journal of Physics: Conference Series*, 2007, **61**, 99.

226.   H. Li, *The Common AFM Modes*, 1997.

227.   E. T. Vandenberg, L. Bertilsson, B. Liedberg, K. Uvdal, R. Erlandsson, H. Elwing and I. Lundström, *Journal of colloid and interface science*, 1991, **147**, 103-118.

228.   P. Kissinger and W. R. Heineman, *Laboratory Techniques in Electroanalytical Chemistry, Second Edition, Revised and Expanded*, Taylor & Francis, 1996.

229.   D. Harvey, *Modern Analytical Chemistry*, McGraw-Hill, 1999.

230.   S. P. Satsangee, *Analytical and Virtual Instumentation Applications Lab: Cyclic Voltammetry,* 2012.

231.   Bank Elektronik - Intelligent Controls GmbH, *Electrochemical Techniques*.

232.   K. Byungwoo, C. Haegeun and K. Woong, *Nanotechnology*, 2012, **23**, 155401.

233.   P. Bruttel and R. Schlink, *Water determination by Karl Fischer Titration*.

234.   D. Aurbach, *Nonaqueous Electrochemistry*, CRC Press, 1999.

235.   K. B. Shelimov, R. O. Esenaliev, A. G. Rinzler, C. B. Huffman and R. E. Smalley, *Chemical Physics Letters*, 1998, **282**, 429-434.

236.   C. A. Furtado, U. J. Kim, H. R. Gutierrez, L. Pan, E. C. Dickey and P. C. Eklund, *Journal of the American Chemical Society*, 2004, **126**, 6095-6105.

237.   R. R. Gagne, C. A. Koval and G. C. Lisensky, *Inorganic Chemistry*, 1980, **19**, 2854-2855.

238. J. Rosenfarb, H. L. Huffman and J. A. Caruso, *Journal of Chemical & Engineering Data*, 1976, **21**, 150-153.
239. P. Kneisl and J. W. Zondlo, *Journal of Chemical & Engineering Data*, 1987, **32**, 11-13.
240. E. Q. Lawson, A. J. Sadler, D. Harmatz, D. T. Brandau, R. Micanovic, R. D. MacElroy and C. R. Middaugh, *Journal of Biological Chemistry*, 1984, **259**, 2910-2912.
241. H. Normant, *Angewandte Chemie International Edition in English*, 1967, **6**, 1046-1067.
242. Knovel, *Knovel Critical Tables (2nd Edition),* 2003.
243. J. A. Dean, McGraw-Hill, 1999.
244. K. Izutsu, in *Electrochemistry in Nonaqueous Solutions*, Wiley-VCH Verlag GmbH & Co. KGaA, 2003, pp. 85-106.
245. Pine Instrument Company, *Educator's Reference Guide for Electrochemistry*, 2000.
246. N. Priyantha and A. Bandara, *Journal of the National Science Council of Sri Lanka*, 1997, **25**, 193-202.
247. ESPI Metals, *Safe Handling of Lithium Metal.*
248. Thermo Fisher Scientific Inc., *AcroSeal® Extra Dry Solvents for Moisture Sensitive Applications,* 2008.
249. C. A. Goss, J. C. Brumfield, E. A. Irene and R. W. Murray, *Analytical Chemistry*, 1993, **65**, 1378-1389.
250. Y. Hui and R. D. Webster, *Analytical Chemistry*, 2011, **83**, 976-981.
251. Unidym Inc., *Unidym Product Sheet: Unidym™ Carbon Nanotubes,* 2012.
252. O. Kimizuka, O. Tanaike, J. Yamashita, T. Hiraoka, D. N. Futaba, K. Hata, K. Machida, S. Suematsu, K. Tamamitsu, S. Saeki, Y. Yamada and H. Hatori, *Carbon*, 2008, **46**, 1999-2001.
253. P. Ruch, L. Hardwick, M. Hahn, A. Foelske, R. Kotz and A. Wokaun, *Carbon*, 2009, **47**, 38-52.
254. Y. Yamada, T. Tanaka, K. Machida, S. Suematsu, K. Tamamitsu, H. Kataura and H. Hatori, *Carbon*, 2012, **50**, 1422-1424.
255. M. Zheng and B. A. Diner, *Journal of the American Chemical Society*, 2004, **126**, 15490-15494.
256. A. Jorio, A. Santos, H. Ribeiro, C. Fantini, M. Souza, J. Vieira, C. Furtado, J. Jiang, R. Saito, L. Balzano, D. Resasco and M. Pimenta, *Physical Review B*, 2005, **72**, 075207-075207.
257. S. Maruyama, *One-dimensional DOS for each chirality*, http://www.photon.t.u-tokyo.ac.jp/~maruyama/kataura/kataura.html#DOS, 2002.
258. J. Israelachvili, *Intermolecular and Surface Forces*, Second edn., Academic Press, San Diego, 1991.
259. H. Lund and O. Hammerich, *Organic electrochemistry*, M. Dekker, 2001.
260. A. Jorio and et al., *New Journal of Physics*, 2003, **5**, 139.
261. J. Muzart, *Tetrahedron*, 2009, **65**, 8313-8323.
262. N. G. Connelly and W. E. Geiger, *Chemical Reviews*, 1996, **96**, 877-910.
263. U. Schindewolf, *Pure and Applied Chemistry*, 1981, **53**, 1329-1344.
264. N. Fakhri, F. C. MacKintosh, B. Lounis, L. Cognet and M. Pasquali, *Science*, 2010, **330**, 1804-1807.
265. M. J. Green, A. N. G. Parra-Vasquez, N. Behabtu and M. Pasquali, *The Journal of Chemical Physics*, 2009, **131**, 084901-084910.
266. R. H. Baughman, C. Cui, A. A. Zakhidov, Z. Iqbal, J. N. Barisci, G. M. Spinks, G. G. Wallace, A. Mazzoldi, D. De Rossi, A. G. Rinzler, O. Jaschinski, S. Roth and M. Kertesz, *Science*, 1999, **284**, 1340-1344.

267. S. Shiraishi, H. Kurihara, K. Okabe, D. Hulicova and A. Oya, *Electrochemistry Communications*, 2002, **4**, 593-598.
268. G. S. Manning, *The Journal of Chemical Physics*, 1969, **51**, 924-933.
269. Z. Syrgiannis, B. Gebhardt, C. Dotzer, F. Hauke, R. Graupner and A. Hirsch, *Angewandte Chemie*, 2010, **49**, 3322-3325.
270. J. M. Achord and C. L. Hussey, *Analytical Chemistry*, 1980, **52**, 601-602.
271. R. Battino, T. R. Rettich and T. Tominaga, *Journal of Physical and Chemical Reference Data*, 1983, **12**, 163-178.
272. D. T. Sawyer, G. Chiericato, C. T. Angelis, E. J. Nanni and T. Tsuchiya, *Analytical Chemistry*, 1982, **54**, 1720-1724.
273. S. A. Hodge, M. K. Bayazit, K. S. Coleman and M. S. P. Shaffer, *Chemical Society Reviews*, 2012, **41**, 4409-4429.
274. K. Kamarás, Á. Pekker, B. Botka, H. Hu, S. Niyogi, M. E. Itkis and R. C. Haddon, *Physica Status Solidi (b)*, 2010, **247**, 2754-2757.
275. Y.-B. Park, L. Hu, G. Gruner, G. Irvin and P. Drzaic, *SID Symposium Digest of Technical Papers*, 2008, **39**, 537-540.
276. D. Hecht, L. Hu and G. Gruner, *Applied Physics Letters*, 2006, **89**, 133112-133113.
277. A. N. Khlobystov, D. A. Britz and G. A. D. Briggs, *Accounts of Chemical Research*, 2005, **38**, 901-909.
278. F. Endres, D. MacFarlane and A. Abbott, *Electrodeposition from Ionic Liquids*, Wiley, 2008.
279. R. Ghodssi and P. Lin, *MEMS Materials and Processes Handbook*, Springer, 2011.
280. J. W. Dini, *Electrodeposition - The Materials Science of Coatings and Substrates*, William Andrew Publishing/Noyes, 1993.
281. L. Oniciu and L. Mureşan, *Journal of Applied Electrochemistry*, 1991, **21**, 565-574.
282. D. A. Tsyboulski, S. M. Bachilo, A. B. Kolomeisky and R. B. Weisman, *ACS Nano*, 2008, **2**, 1770-1776.
283. H. Wang, C. Zhong, J. Li and Y. Jiang, Electronic Packaging Technology & High Density Packaging, 2008. ICEPT-HDP 2008. International Conference on, 2008.
284. C.-G. Wu, P.-Y. Chen and S.-S. Chang, *International Journal of Nanoscience*, 2004, **03**, 859-868.
285. Nanocyl, *NC7000 Technical Datasheet*, 2009.
286. R. Menzel, *Developing gas-phase methodologies for the modification and characterisation of carbon nanotube surfaces*, Imperial College London, 2010.
287. M. Q. Tran, C. Tridech, A. Alfrey, A. Bismarck and M. S. P. Shaffer, *Carbon*, 2007, **45**, 2341-2350.
288. C. Skidmore, *Graphite Report: April 2012*, 2012.
289. E. M. Milner, N. T. Skipper, C. A. Howard, M. S. P. Shaffer, D. J. Buckley, K. A. Rahnejat, P. L. Cullen, R. K. Heenan, P. Lindner and R. Schweins, *Journal of the American Chemical Society*, 2012, **134**, 8302-8305.
290. M. S. Dresselhaus and G. Dresselhaus, *Advances in Physics*, 1981, **30**, 139-326.
291. M. Inagaki and O. Tanaike, *Synthetic Metals*, 1995, **73**, 77-81.
292. J. M. Englert, C. Dotzer, G. Yang, M. Schmid, C. Papp, J. M. Gottfried, H.-P. Steinrück, E. Spiecker, F. Hauke and A. Hirsch, *Nature Chemistry*, 2011, **3**, 279-286.
293. H. C. Schniepp, J.-L. Li, M. J. McAllister, H. Sai, M. Herrera-Alonso, D. H. Adamson, R. K. Prud'homme, R. Car, D. A. Saville and I. A. Aksay, *The Journal of Physical Chemistry B*, 2006, **110**, 8535-8539.
294. X.-Y. Peng, X.-X. Liu, D. Diamond and K. T. Lau, *Carbon*, 2011, **49**, 3488-3496.

295. X. Ji, C. E. Banks, G. Hu, A. Crossley and R. G. Compton, *Electroanalysis*, 2006, **18**, 2141-2147.

296. S. Nitin and H. Scott, in *Handbook of Nanophysics*, CRC Press, 2010, pp. 1-10.

297. L. A. Bulavin, I. I. Adamenko, V. M. Yashchuk, T. Y. Ogul'chansky, Y. I. Prylutskyy, S. S. Durov and P. Scharff, *Journal of Molecular Liquids*, 2001, **93**, 187-191.

298. K. Jobst, L. Sawtschenko, G. Paasch and J. Fink, *Synthetic Metals*, 1993, **56**, 3179-3184.

299. A. Hirsch, *The Chemistry of the Fullerenes*, John Wiley & Sons, 2008.

300. Cabot Corporation, *VULCAN® XC72R Product Data Sheet,* 2002.

301. L. Ji, Z. Tan, T. R. Kuykendall, S. Aloni, S. Xun, E. Lin, V. Battaglia and Y. Zhang, *Physical Chemistry Chemical Physics*, 2011, **13**, 7170-7177.

302. U. Kreibig and M. Vollmer, *Optical properties of metal clusters*, Springer, 1995.

303. J. N. Coleman, M. Lotya, A. O'Neill, S. D. Bergin, P. J. King, U. Khan, K. Young, A. Gaucher, S. De, R. J. Smith, I. V. Shvets, S. K. Arora, G. Stanton, H.-Y. Kim, K. Lee, G. T. Kim, G. S. Duesberg, T. Hallam, J. J. Boland, J. J. Wang, J. F. Donegan, J. C. Grunlan, G. Moriarty, A. Shmeliov, R. J. Nicholls, J. M. Perkins, E. M. Grieveson, K. Theuwissen, D. W. McComb, P. D. Nellist and V. Nicolosi, *Science*, 2011, **331**, 568-571.

304. Q. H. Wang, K. Kalantar-Zadeh, A. Kis, J. N. Coleman and M. S. Strano, *Nat Nano*, 2012, **7**, 699-712.

305. B. Radisavljevic, A. Radenovic, J. Brivio, V. Giacometti and A. Kis, *Nature Nanotechnology*, 2011, **6**, 147-150.

306. P. Joensen, R. F. Frindt and S. R. Morrison, *Materials Research Bulletin*, 1986, **21**, 457-461.

307. H. S. S. Ramakrishna Matte, A. Gomathi, A. K. Manna, D. J. Late, R. Datta, S. K. Pati and C. N. R. Rao, *Angewandte Chemie International Edition*, 2010, **49**, 4059-4062.

308. M. Bouroushian, *Electrochemistry of Metal Chalcogenides*, Springer, 2010.

309. A. Kuc, N. Zibouche and T. Heine, *Physical Review B*, 2011, **83**, 245213.

310. G. Du, *Nanostructured anode materials for lithion-ion batteies*, University of Wollongong, 2011.

311. G. Hautier, A. Jain, S. P. Ong, B. Kang, C. Moore, R. Doe and G. Ceder, *Chemistry of Materials*, 2011, **23**, 3495-3508.

312. C. R. Bayliss, *Electronics and Power*, 1976, **22**, 773-776.

313. C. McCusker, J. B. Carroll and V. M. Rotello, *Chemical Communications*, 2005, 996-998.

314. D. Gnanasekaran, K. Madhavan and B. S. R. Reddy, *Journal of Scientific and Industrial Research*, 2009, **68**, 437-464.

315. P. B. Catrysse and S. Fan, *Nano Letters*, 2010, **10**, 2944-2949.

316. M. He, J. Jung, F. Qiu and Z. Lin, *Journal of Materials Chemistry*, 2012.

317. M. S. Strano, *Journal of the American Chemical Society*, 2003, **125**, 16148-16153.